UNIVERSITY OF SOUTHAMPTON

FACULTY OF ENGINEERING, SCIENCE AND MATHEMATICS

School of Chemistry

Preparation, Characterisation and Evaluation of Core-Shell Electrocatalyst for PEMFCs

by

Béatrice Claire Tessier

Thesis for the degree of Doctor of Philosophy

December 2009

ACKNOWLEDGEMENTS

To start with, I would like to express my gratitude to my supervisors Professor Andrea Russell and Dr. Brian Theobald, for their continuous support and motivation throughout my PhD. I am grateful to Dr. Dave Thompsett for his valuable advice and enthusiasm for my PhD project.

Besides my supervisors, I would like to thank the members of the ECP group at JMTC, who provided me assistance in a number of ways and made me feel part of their group.

My sincere thanks also go to the people in the Analytical department at JMTC who helped me characterising my catalysts: Dr. Don Ozkaya, Dr. Richard Smith, Steve Spratt, James McNaught, Paul Fisher, Dr. Sarennah Longworth, Dr. Hoi Jobson, Junior Godson, Ian Briggs and Brian Moore. I am very grateful for the time they took to explain to me the principle of the characterisation techniques and for their patience.

I would like to thank the staff of Tascon GmbH Analytical Services and Consulting (Münster, Germany), for the HS-LEIS analyses. In addition, I would like to acknowledge Haibo E. for the aberration-corrected STEM analyses.

I would like to show my gratitude to the members of the Russell group for welcoming me and helping during my visits to the University of Southampton. They provided significant contributions in the acquisition of the EXAFS data. They were Gaël Chouchelamane, Anna Wise, Dr. Peter Wells, Prabalini Kannan, Stephen Price and Jon Speed.

Lastly, I offer my regards and blessings to all of those who supported me in any respect during the completion of the project, in particular my friends and my family.

UNIVERSITY OF SOUTHAMPTON

ABSTRACT

FACULTY OF ENGINEERING, SCIENCE AND MATHEMATICS

School of Chemistry

Doctor of Philosophy

Preparation, Characterisation and Evaluation of Core-Shell Electrocatalyst for PEMFCs

By Béatrice Claire Tessier

For oxygen reduction catalysis it has been shown that thin layers of platinum (shell) over a non-Pt core enhance the activity. In addition surface science studies have found that overlayers of one metal on another strongly modifies the electrocatalytic properties of the surface metal. The aim of this project is to develop this concept by the preparation of practical fuel cell catalysts based on the core-shell model and gain a fundamental understanding of their properties and behaviour. A key aspect of the work is to establish the physical characteristics required for a catalyst to show long-term stability as well as improved activity.

Chapter 1 introduces the PEM fuel cells, ORR electrocatalysts and the preparation and characterisation of core-shell type electrocatalysts. The experimental techniques, procedures and apparatus used for this work will be described in Chapter 2. The mechanism of the synthetic controlled-surface reaction (CSR) used to prepare the core-shell electrocatalysts was studied in Chapter 3. Then the focus will be on the palladium-core and platinum-shell system in Chapter 4 and 5, where the effects of the Pt shell and the Pd core size on the electrocatalysts properties are investigated. The electrocatalysts prepared for these studies were assessed for their electrochemical stabilities and their ORR activities. Finally, Chapter 6 presents preliminary results on the iridium-core and platinum-shell system.

The deposition of Pt on Pd and Ir cores using the CSR did not lead to a complete Pt coverage as Pt tended to deposit preferentially at the edges and corners on the core surface and then on Pt. Whereas an enhancement in the electrochemical stability of the Pt/Pd core-shell electrocatalysts was observed compared to a pure Pt electrocatalyst, the Pt/Ir core-shell showed poorer stability than Pt. Benefits in the ORR activity were gained with both the Pt/Pd and Pt/Ir core-shell electrocatalysts. This demonstrates that, due to the original properties of the core-shell-structured electrocatalysts, it is possible to use less Pt and still obtain an improvement in the ORR activity.

TABLE OF CONTENTS

COMMONLY USED ABBREVIATIONS AND SYMBOLS

Acac	acetylacetone
ADF	annular dark field
BF	bright field
Cs	aberration correction
D	metal dispersion (%)
DFT	density functional theory
d_s	surface atomic density (number atoms per m^2)
E	potential vs a reference electrode (V or mV)
E°	standard electrode potential (V or mV)
E^0_{cell}	E_C-E_A (V or mV)
E_b	binding energy (eV)
ECA	electrochemical area (m^2 g^{-1})
EDX	energy dispersive X-rays
E_e	equilibrium potential (V or mV)
E_F	Fermi level (eV)
EPSA	electrochemical platinum surface area (cm^2_{Pt} cm^{-2})
ESCA	Electron Spectroscopy for Chemical Analysis
EXAFS	extended X-ray absorption fine structure
F	Faraday constant (96 485 C mol^{-1})
FT	fourier transform
FWHM	full width at half maximum
h	Planck's constant (6.63×10^{-34} m^2 kg s^{-1})
HAADF	high angle annular dark field
HS-LEIS	High-Sensitivity Low Energy Ion Scattering
I, i	current (A, mA or μA)
i_0	exchange current (A, mA or μA)
ICP-AES	Inductively coupled plasma atomic emission spectroscopy
I_k	kinetic current (A, mA or μA)
I_L	limiting current (A, mA or μA)

j	current density (A cm^{-2} or mA cm^{-2})
k	photo-electron wave vector (Å-1)
MEA	membrane-electrode assembly
MM	molar mass (g mol^{-1})
N	EXAFS coordination number
N_A	Avogadro's constant (6.02×10^{23} mol^{-1})
ORR	oxygen reduction reaction
P^0	standard pressure (1 atm)
PEMFC	proton exchange membrane fuel cell
PGM	platinum group metal
PTFE	Polytetrafluoroethylene
Q	charge (C)
R	gas constant (8.314 J K^{-1} mol^{-1})
	or EXAFS interatomic distance (Å)
RDE	rotating disc electrode
RH	relative humidity (%)
RHE	reversible hydrogen electrode
S	surface area (m^2 g^{-1})
STEM	scanning transmission electron microscopy
T^0	standard temperature (273 K)
TEM	transmission electron microscopy
UV	ultra-violet
V_m	molar volume (24.789 dm^3 mol^{-1} at 25 °C)
W	weight (g or mg)
XPS	X-ray photoelectron spectroscopy
XRD	X-ray diffraction
Z	atomic number
δ	thickness of diffusion layer (m)
ε_d	d-band center (eV)
ε_F	Fermi level (eV)
η	overpotential, $E-E_e$ (V or mV)
λ	wavelength (nm)
μ	absorption coefficient (m^2 mol^{-1})
ν	kinematic viscosity (m^2 s^{-1})

	or potential scan rate (V s^{-1} or mV s^{-1})
σ^2	mean-square disorder of neighbour distance
χ	EXAFS function
ω	rotation speed (rad s^{-1} or rpm)

CHAPTER 1

INTRODUCTION

CHAPTER 1: Introduction

1.1. General introduction

1.1.1. History of fuel cell development

The discovery of the fuel cell operating principle was attributed to Sir William Grove in 1839, although it appears that a Swiss scientist Christian F. Schoenbein independently discovered the same phenomenon at about the same time (1). Knowing that sending an electric current through water splits it into hydrogen and oxygen, Grove tried and succeeded in reversing the reaction by combining hydrogen and oxygen to produce electricity and water. The cell consisted of two platinum strips surrounded by closed tubes containing hydrogen and oxygen, respectively, formed by preliminary electrolysis of the electrolyte.

After this discovery followed nearly a century of research attempts to improve Grove's cell into a practical device. It was Francis Thomas Bacon, who started researching alkali electrolyte fuel cells (with potassium hydroxide) in the late 1930s, that demonstrated in the late 1950s the first large scale fuel cell stack. Bacon's fuel cells attracted the attention of Pratt & Whitney who licensed his work to power the Apollo spacecraft (2).

In the meantime, William White Jacques introduced the phosphoric acid fuel cell (PAFC) in the late 19th century, but PAFCs were slower to develop than other types of fuel cells because of the poor electric conductivity of phosphoric acid (3). But in 1967, it was reintroduced by the American Gas Association and United Technology Corp. (UTC) as part of the Target program and rapid progress was made thereafter in the production of PAFC power units (4).

Low-temperature proton-exchange membrane fuel cell (PEMFC) technology was invented later at General Electric in 1955, through the work of Thomas Grubb and Leonard Niedrach (2). The PEMFC was the first type of fuel cell to have an application. It was used as a power source for NASA's Gemini space flights in the 1960s (5). The formation of the California fuel cell partnership for the development and commercialisation of zero-emission vehicles stimulated the research on PEMFCs.

Although the cell as developed by General Electric was compact and portable, it was highly expensive to produce as the catalyst electrodes used Pt 'blacks' (unsupported catalysts) and the Pt loading could be as high as 30 mg Pt cm^{-2} (6). In the early 1990s, the cathode Pt loading was dramatically reduced to approximately 0.5 mg Pt cm^{-2} by supporting the Pt particles on a graphitic carbon support, which greatly increased the catalytic surface area and then the performance (7). Subsequently, Los Alamos National Laboratory and Texas A&M University developed an electrode assembly technique that enabled the reduction of the Pt loading by one order of magnitude and the conservation of the performances (8). The electrode Pt loading was lowered from 4 to 0.1 mg Pt cm^{-2} by using carbon supported platinum particles in a catalyst layer. The catalyst layer was directly bonded to the membrane, with a separate gas diffusion structure used as backings. This breakthrough combined with the rise of the energy cost led to active research and development on PEM fuel cells, which continues today. In the early 1990s, Ballard developed its Mark 5 fuel cell stack with a total power output of 5kW. With the contribution of Daimler Chrysler, this product was further developed and a total output of 75 kW was achieved. In 1993, Ballard demonstrated a PEMFC-powered van, showing that PEMFC were able to meet the performance targets for transportation applications. Since then, PEM technology has remained the choice of the automotive industry

1.1.2. The ecological and energy context

Global warming is one of the most serious challenges to be faced today. To protect the health and economic well-being of current and future generations, greenhouse gas emissions have to be reduced by using more sustainable sources of energy. Fossil fuels, including natural gas and coal, are by far the main source of energy for the functioning of factories, for the electricity production, and for everything that sustains the modern world. The dependency of modern societies on fossil fuel energy resources, which are inherently limited and becoming scarce, is another major challenge that needs to be addressed.

Many countries are actively working to reduce their gas pollutant emissions. California, known as the most air polluted state in the USA, was the first to integrate fuel cells into its program. In fact, the development of cleaner motor vehicle was a leading factor for the improvement in air quality, considering that transportation accounts for 38% of California's greenhouse gas emissions (9). The California Fuel Cell Partnership was formed in 1999 with the objective to demonstrate and promote the feasibility of making

zero-emission fuel cell vehicles as clean, safe and practical alternative to vehicles powered by internal combustion engines (10). This alliance was composed of two state government agencies, California Air Resources Board (CARB) and California Energy Commission (CEC) and six private sector companies, Ballard Power Systems, DaimlerChrysler, Ford Motor Company, BP, Shell Hydrogen and ChevronTexaco. Numerous active hydrogen demonstration programs have also been developed in Korea, Japan, China, Singapore, France, Germany, Italy, Spain, Norway and Iceland (9). Since 1999, policies on clean energy, such as the Zero Emission Vehicle Program, have required zero emission transportation as a key component and fuel cell vehicles are a solution that will enable the reduction of greenhouse gases (9).

1.2. Proton exchange membrane fuel cell (PEMFC)

There is great interest in the development of H_2 fueled PEM fuel cells to power automobiles replacing the internal combustion engine and as stationary power sources. They are potentially highly energy efficient power source while emitting little or no pollutants (CO, NO_x,..) or the greenhouse gas CO_2 (10-12).

1.2.1. General principles

A fuel cell converts chemical energy directly into electrical energy as long as fuel is supplied. The proton exchange membrane (PEM) fuel cells operate at 60-80 °C. The heart of the PEM fuel cell is the membrane-electrode assembly (MEA) (Figure 1-1). The membrane is a solid polymer electrolyte layer, which is bonded to catalysed porous electrodes (anode and cathode) placed on each side. Both the anode and the cathode are usually composed of a Pt-containing catalyst on conductive carbon. Typically, hydrogen gas is fed to the anode and is electrocatalytically oxidised into protons (H^+) and electrons (e^-). While protons migrate through the electrolyte to the cathode, electrons are forced to travel in an external circuit because the polymer electrolyte is electrically insulating. The resulting electric current can be utilised to provide power before returning to the cathode by the external circuit. At the cathode, oxygen is electrocatalytically reduced and combined with the protons to form water. H_2 and O_2 are delivered to the MEA through channels in

the electrically conductive gas impermeable bi-polar plates. The reactions occurring in the fuel cell are as follows:

Anode (Oxidation half reaction): $2H_2 \rightarrow 4H^+ + 4e^-$ (1. 1)

Cathode (Reduction half reaction): $O_2 + 4H^+ + 4e^- \rightarrow 2H_2O$ (1. 2)

Overall (Fuel cell reaction): $2H_2 + O_2 \rightarrow 2H_2O + energy$ (1. 3)

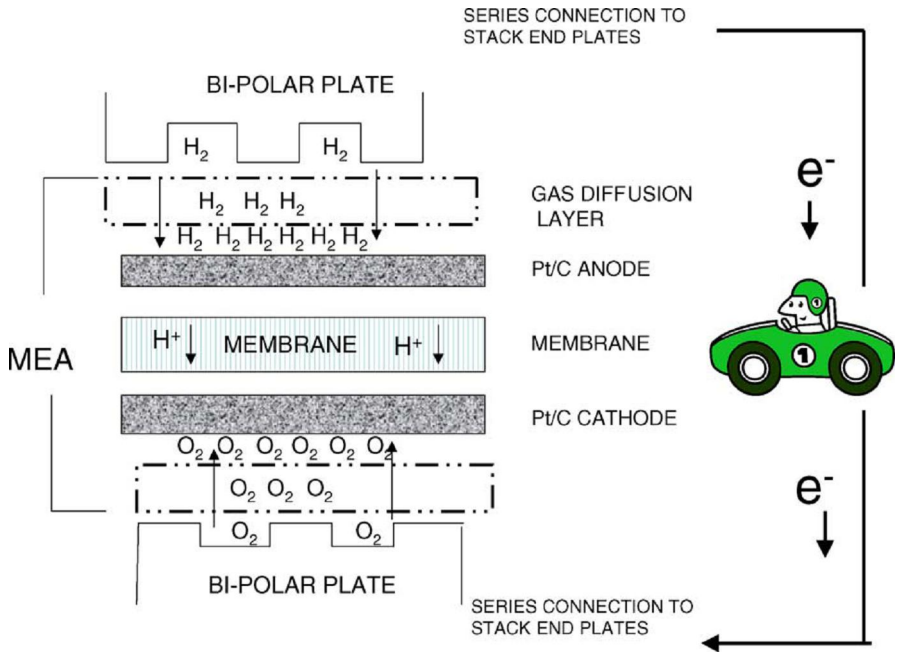

Figure 1- 1 Membrane electrode assembly arranged in a stack (11)

The gases are dispersed through the anode and cathode layers through gas diffusion layers, typically composed of a porous carbon fabric. The five-layer sandwich forms a single cell. The MEAs are stacked in series to increase the voltage output. When current flows through the cell, the voltage decreases due to the existence of different resistances within the cell: the diffusion of the gas to the electrodes, the kinetics of the reactions occurring at the anode and the cathode and the flow of protons through the membrane (Figure 1-2). The sharp decrease in the voltage at low current density is due to the sluggish kinetics of the oxygen reduction reaction. As more current is drawn, there is an additional resistance due to the transport of the protons through the membrane. At high current densities, the voltage is mainly limited by the transport of O_2 to the cathode layer. At low

and high currents, the reaction is said to be kinetically and mass-transfer controlled, respectively.

Major improvements have been applied to PEMFCs since the first example of a membrane fuel cell in the 1960s (5). Nowadays, PEMFCs have specific powers of 800 mW/cm^2, while using less than 0.4 mg/cm^2 of platinum catalyst (13). This was achieved mainly by using new Nafion-type proton-exchange membranes and developing ways of better utilisation of the platinum catalysts in the electrodes.

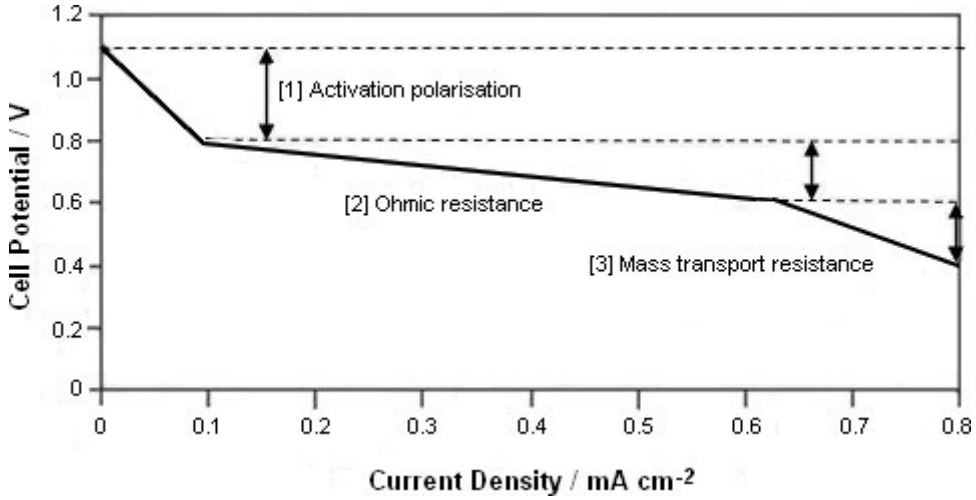

Figure 1- 2 Typical PEM Fuel Cell polarisation curve.

Polymer electrolyte membrane

The electrolyte is an ion conducting polymer, able to carry mobile protons. The polymer electrolyte membrane is a solid, organic polymer, usually poly[perfluorosulfonic] acid (5). A typical membrane material, such as Nafion^{TM}, consists of three regions, as shown in Figure 1-3:

- the Teflon-like, fluorocarbon backbone, with the $–CF_2$-CF-CF_2,
- the side chains, -O–CF_2-CF-O-CF_2- CF_2, which connect the molecular backbone to the third region,
- the ion clusters consisting of sulfonic acid ions, $SO_3^-H^+$.

The membrane must be humidified to enable proton conduction. The negative ions, SO_3^-, are not mobile and are attached to the side chain. However, they form hydrophilic channels within the membrane because they absorb water strongly. Once hydrated, being negatively charged, they allow the transport of protons. Bonded to water molecules,

protons hop from SO_3^- site to SO_3^- site within the membrane. Because of this mechanism, the solid hydrated electrolyte is an excellent conductor of hydrogen ions.

A major limitation of Nafion® and fluorosulphonated ionomers is the operating temperature (6): when the temperature increases above 100 °C, without increasing the pressure, the polymer membrane dehydrates and thus looses proton conductivity.

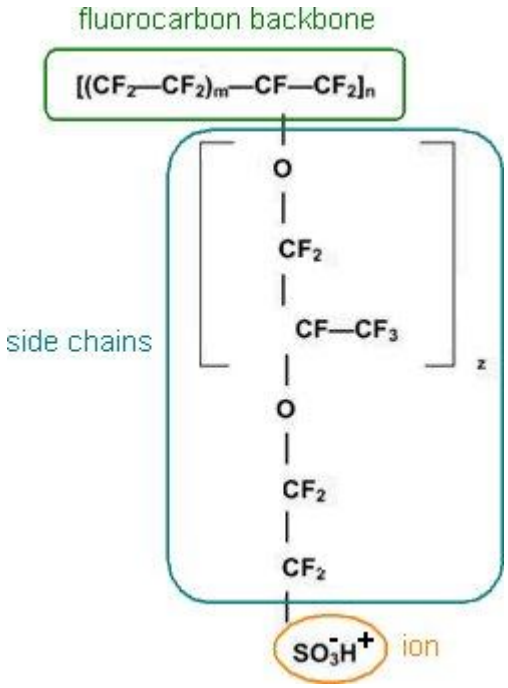

Figure 1- 3 Chemical structure of Nafion™ (by Dupont) membrane material

Electrocatalysts in PEMFC

In the PEM fuel cell, two half-reactions take place simultaneously, the oxidation of hydrogen at the anode, and the reduction of oxygen at the cathode. Catalysts are used both at the anode and at the cathode to increase the rates of each reaction, which would normally be very slow. Pt based catalysts are the best catalysts for these reactions because Pt binds H_2 and O_2 molecules strongly enough to dissociate them but not too strongly so that the H and O intermediates can be released to form the final products (14).

In the first membrane-type fuel cells, the dispersed platinum catalyst was pure metal, with a specific area as low as 10 to 15 $m^2 g^{-1}$. Strategies for a more efficient utilization of the platinum catalyst have been developed, both for reasons of cost and Pt supply limitations (15). First, the platinum was deposited on a high surface area carbon support, which considerably increased the available catalytic surface area. The platinum

concentrations loaded on to the carbon blacks are typically between 10 and 40 wt%, sometimes even higher (16, 17). A further decrease in Pt consumption without performance loss was also achieved by introducing a certain amount (30 to 40 wt%) of a proton-conducting polymer into the catalyst layer of the electrode (8). The catalyst surface area that is in contact with the electrolyte increases considerably, due to the ionomer present in the active catalyst layer.

While lowering the Pt-loading for the anode is straightforward due to the high activity of Pt toward H_2 oxidation, the reduction of the Pt-loading for the cathode is limited due to the poor activity of Pt towards O_2 reduction. A reduction of Pt loadings has been mainly attempted through a decrease of the size of the Pt nanoparticles. This, however, is not sufficient and the eventual use of alloys, although very active, have not brought a significant decrease of Pt loading since they are usually Pt rich. A promising approach to solving this problem is to design electrocatalysts having monolayer amounts of Pt on the surface of suitable metal nanoparticles.

1.2.2. Performance loss in PEMFC

The equilibrium cell voltage (E^0_{cell}) is defined as the difference between the reduction potentials of the cathode and anode reactions (18). The cathode and anode potentials can be obtained from the Nernst equation. For a PEM fuel cell operating at standard conditions (25 °C, 1 atmosphere) the reversible cell emf is 1.23 V. In an ideal (reversible) fuel cell, the cell voltage is independent of the current drawn. In practice, the reversible cell voltage is not realised even under open-circuit (zero current) conditions due to various phenomena that arise during fuel cell operation. The difference between actual cell voltage at a given current density (current per unit active electrode area) and the reversible cell voltage for the reaction is termed overvoltage (overpotential when referring to a single electrode). The major sources of overvoltage in a fuel cell are schematically represented in Figure 1-2.

- Voltage loss due to activation resistance [1]:

Activation polarisation arises from charge-transfer and is present when the reaction kinetics at an electrode surface are sluggish. In the PEMFC, this is due to the sluggish oxygen reduction kinetics at the cathode. The effects of these losses are most pronounced at low current densities (~1 to 100 mA cm^{-2}). The corresponding voltage drop can be

expressed by the Tafel equation, here shown as the activation polarisation, η_A, defined in equation (1-1):

$$\eta_A = \frac{RT}{\alpha nF} \ln\left(\frac{i}{i_0}\right) \quad \textbf{(1- 1)}$$

Where R is the gas constant, T is the temperature, F the Faraday constant, i the current, α is the transfer coefficient of the reaction at the electrode being studied, n is the number of electrons transferred during the reaction, and i_0 is the partial cathodic exchange current, which is the current that can be extracted at the equilibrium potential.

- Voltage loss due to ohmic resistance [2]:

The ohmic resistance arises from the internal resistances of the fuel cell components, such as the electrode materials, the electrolyte membrane and the various interconnections. The ohmic potential drop η_o increases with the current I as shown in equation (1-2):

$$\eta_O = I \times R \quad \textbf{(1- 2)}$$

Where I is the current flowing through the cell, and R is the total internal resistance.

- Voltage loss due to mass transport [3]:

Mass transport resistance arises from the inability of the surrounding materials to continuously supply reactant as it is consumed at the electrode. Slow transport of reactants/products to/from the electrochemical reaction site can generate considerable potential loss:

$$\eta_M = \frac{RT}{nF} \ln\left(1 - \frac{I}{I_L}\right) \quad \textbf{(1- 3)}$$

Where I_L is the limiting current, which is the maximum rate at which a reactant can be supplied to an electrode.

The combined contributions of these sources of overvoltage cause the cell voltage output to decrease with increasing current density. The power output of the fuel cell (in mW cm^{-2}) is given by the product of voltage and current density.

1.3. The ORR mechanism

To investigate the metal surface activity towards the ORR, it is necessary to understand the ORR mechanism. The electrochemical reduction of oxygen on platinum electrodes has been studied for about 40 years and the mechanistic details are still not fully understood. ORR is a multi-electron reaction, which may consist of several elementary steps involving different intermediates. Several pathways for O_2 reduction in acidic media have been proposed (19):

- The direct four-electron pathway (Reaction 1-1) where the oxygen is reduced to water
- The indirect pathway (Reactions 1-4 and 1-5), where oxygen is first reduced to form hydrogen peroxide by a two-electron reduction, which is then followed by a second two-electron reduction to form water:

$$O_2 + 2H^+ + 2e^- \rightarrow H_2O_2 \quad \textbf{(1- 4)}$$

$$H_2O_2 + 2H^+ + 2e^- \rightarrow 2H_2O \quad \textbf{(1- 5)}$$

The basic difference between the two pathways resides in the fate of the O–O bond in the original oxygen molecule, which in the first pathway is broken in the initial reaction step. The resulting oxygen atoms are adsorbed on the surface of the metal and then are reduced electrochemically. In the reaction following the second pathway, the O–O bond is not broken while the first two electrons are added; the O–O bond is preserved in the H_2O_2 produced as an intermediate, and breaks in a later step, when the hydrogen peroxide is reduced or catalytically decomposed (20). Rotating-ring disc electrode studies provided evidence that, on Pt, the ORR proceeds mainly through the four-electron pathway (19, 21), although the details of the mechanism are not clear. The four-electron reduction to water is the desired reaction in the fuel cell cathode and the two-electron reduction to hydrogen peroxide is to be avoided as hydrogen peroxide causes damage to the polymer membrane.

As reviewed by Yeager (19), the rate determining (RD) step was proposed to be the O_2 dissociative adsorption on a clean Pt surface. However, at potentials where an oxide film is formed on the Pt surface, both the O_2 adsorption and O-H bond formation steps were proposed to be RD steps. Damjanovic demonstrated that at low overpotentials the O-O bond breaking did not occur before the RD chemical step, which occurred after the fast electron transfer following either of the mechanisms shown in equations 1-6 and 1-7 (22):

Mechanism 1:

$$O_2 + e^- \leftrightarrow O_2^-$$
$$O_2^- + H \leftrightarrow [O_2 H] \qquad \textbf{(1- 6)}$$

Mechanism 2:

$$O_2 + H^+ + e^- \leftrightarrow O_2 H$$
$$O_2 H \leftrightarrow [OH + O] \qquad \textbf{(1- 7)}$$

A more simplistic approach was to consider that, despite the discrepancies with the ORR mechanism, the four-electron pathway must involve the breaking of the O-O bond and the formation of an O-H bond. From that point, two representative elementary steps were singled out and their activation energies on different metal surfaces were calculated using DFT (14). Moreover, the relationship between the theoretical electronic state of the surfaces (d-band centre model) and the experimental ORR activities was examined. It was found that to obtain an optimal ORR activity the metal surface should strike a balance between the energy barriers of O_2 dissociation and OH bond formation, like Pt.

It is also accepted that one of the major barriers to ORR kinetics is the strong adsorption of OH and O species. This is supported by the kinetic model for the four-electron ORR in acidic media proposed by Wang *et al.* (23). In this model, four elementary reactions were proposed and can be schematically summarised in equation 1-8 as follows:

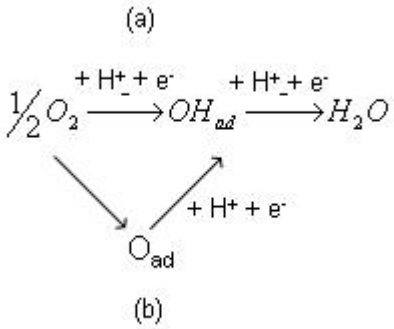

(1- 8)

The mains conclusions drawn from the calculations showed that at low overpotentials, the dominant pathway on Pt(111) is that of the dissociative adsorption of O_2 (b). However, this was followed by very slow kinetics for O and OH desorption, which are trapped on the surface, causing the decline in ORR activity.

1.4. Core-shell electrocatalysts for the ORR

1.4.1. Origin of the activity

When going through the periodic table, the oxygen adsorption properties vary significantly from one pure metal to another, due to a change in the electronic structure of the metal surfaces. This is why the understanding of a metal catalyst activity towards a reaction relies on the understanding of its electronic structure. Such atomic-scale study has been made possible thanks to modern density functional theory (DFT) calculations (24-26). Extensive work has been done to provide understanding of which surface properties of metals determine their activities. One would like to make a connection between the reactivity parameter and the properties of a metal or alloy surface.

An important development was the model proposed by Hammer and Nørskov (24). Their model singles out three surface properties contributing to the ability of the surface to make and break adsorbate bonds: the center, ε_d, of the d-band; the degree of filling f_d of the d-band; and the coupling matrix element, V_{ad}, between the adsorbate states and the metal d-states. These quantities have been calculated from extensive DFT calculations for a significant portion of the periodic table. The basic idea of the Hammer–Nørskov model is that trends in the interaction and reactivity are governed by coupling of the adsorbate states with the metal d-states.

Further on, they developed the d-band model (25), where they described how the d-band properties of a metal surface determine the bonding strength with adsorbates. From the rationalisation of what makes a transition metal surface reactive the possibility of changing this reactivity arose. For example, the reactivity can be modified by changing the surface structure, through “electronic” and “geometric” effects. This can be achieved by alloying or by introducing adsorbates on the metal surface (26, 27).

The adsorption properties of molecules on transition metals can be tuned by changing the d-band structure (27). Two critical factors contribute to the modification of the electronic properties of a metal in a bimetallic system: the strain effect that arises from the lattice mismatch between the two metals, and the ligand effect that arises from the electronic interaction between the metals. Based on Hammer and Norskov’s work (25), it was demonstrated that the use of the d-band center as a parameter to describe the d-band structure was more appropriate than the filling or the width of the d-bands, as it gives a general description. In this work, the ligand effect was shown to influence the d-band

width. The "rectangular band model" (25) predicts that if the band widens, then its energy must decrease to conserve the Pt d-band filling, and so does the density of state (DOS) at the Fermi level. When a surface undergoes compressive or tensile strains, the overlap of the metal d states will either increase or decrease and so will the d bandwidths. A linear correlation between the d-band center energy and the O_2 dissociative adsorption energy was established. A decrease in the d-band centre leads to a decrease in the O_2 adsorption energy, which is favourable to a reduction in the adsorbed OH coverage and therefore to a better ORR activity.

The ligand effect theory was further developed by Bligaard and Norskov on the basis of the d-band model (28). The d-band model was reviewed in order to rationalise the trends in reactivity in heterogeneous catalysis and electrochemistry. The results showed that d-band centre shifts are observed when the atoms surrounding Pt change, such as in Pt alloys, but also depending on the coordination number (differences between a kink and a plane surfaces).

The tunable reactivity of the core-shell catalysts comes from the originality of its structure, where a monolayer of one metal is deposited on top of another one. A strain is created in the surface due to the difference in bulk lattice parameter between the substrate and the overlayer elements. The metal overlayer may be subjected to mechanical compressive or tensile strains, which, by modifying the d-state overlap, leads to the downshift or upshift of its ε_d. Figure 1-4 shows the effect of a tensile strain on the d-band centre. The d-band width is narrowed upon the application of the tensile strain (Figure 1-4(b)), which then leads to an upshift of the d-band centre (Figure 1-4(c)) to allow the conservation of the d-states at the Fermi level. This is also combined with the ligand effect. This new approach to nanoparticle surface modification has been applied to develop more active fuel cell electrocatalysts with a Pt overlayer deposited on a late transition metal.

The d-band centre of Pt surface atoms and the binding energy of atomic oxygen on these surfaces were both shown to correlate well with their experimentally measured ORR activity (14). The enhancement of the ORR activity mostly relies on the choice of the substrate or core metal, which should not induce too large a d-band shift for the Pt in the overlayer, as this would lead to a drop of the activity due to far too strongly or too labile bonded reactants/products (14).

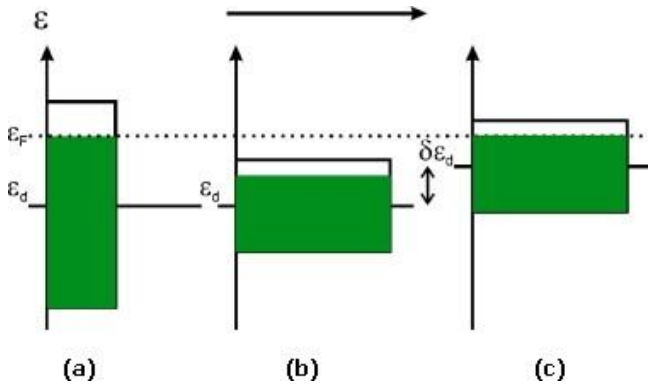

Figure 1- 4 Illustration of the effect of tensile strain on the d band centre (25).

The ORR activity of a series of Pt monolayers supported on close-packed metal surfaces (such as Au(111), Rh(111), Ir(111), Pd(111), etc.) was evaluated and plotted with respect to the shift of the Pt monolayer d-band centre energy $\epsilon_d - \epsilon_F$ as calculated by DFT. A volcano-type plot was obtained with the Pt_{ML}/Pd(111) system at the top of the volcano (29-31) as shown in Figure 1-5. A Pd(111) substrate, by inducing a slight downshift of ϵ_d, enhances greatly the activity so that Pt/Pd(111) is more active than Pt(111). The geometric and electronic effects are such that there is a balance between the energy barriers of O_2 dissociation and OH bond formation. More in-depth work was performed on carbon-supported Pt_{ML}/Pd nanoparticles to better understand the origin of its remarkable activity (5-8 times higher to that of Pt nanoparticles) and it was found that it could partly be attributed to the decrease in PtOH coverage, leaving more free sites for the ORR (31). The large ϵ_d upshift of the Pt monolayer in Pt_{ML}/Au(111) led to an increase in the O-metal bond strength, hence causing the build up of oxygenated species on the surface. In contrast, the large ϵ_d downshift of the Pt monolayer on Ru(0001), Rh(111) and Ir(111) leads to a weakening of the O-Pt bond, making the O-O bond scission more difficult (14).

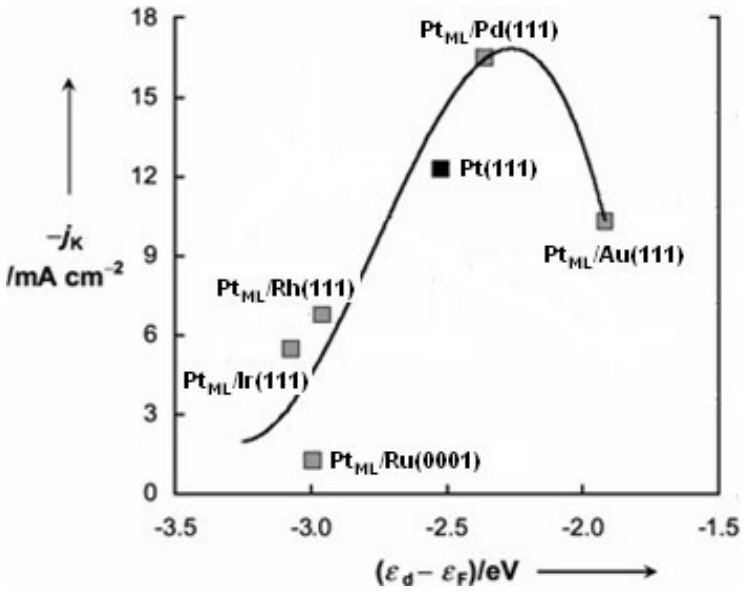

Figure 1- 5 Kinetic current densities (j_K) at 0.8 V for O_2 reduction on the Pt monolayers supported on different crystals in a 0.1M $HClO_4$ solution as functions of calculated d-band centre (ϵ_d - ϵ_F ; relative to the Fermi level) of the respective clean Pt monolayers (14).

As the high OH coverage on Pt has been shown to inhibit the ORR (32), the Pt monolayer was mixed with late transition metals M (M = Ir, Ru, Os, Rh, Au, Re) which, by adsorbing oxygenated species more strongly, induce a decrease of the OH coverage on Pt by lateral repulsion (29, 33, 34). An optimal ORR activity was obtained with a monolayer composition of 80% Pt and 20% M for $Pt_{0.8}Ir_{0.2}$/Pd/C and $Pt_{0.8}Ru_{0.2}$/Pd/C, yielding a three fold improvement compared to a Pt_{ML}/Pd/C. A multi-layer core-shell structure, with non-noble metal core (Co, Ni), a noble metal protective shell (Au, Pd, Pt) and a Pt overlayer, has also proved to greatly enhance the Pt-mass activity. For example, the carbon-supported $Pt_{ML}/Pd_{shell}/Co_{core}$/C showed a Pt-mass activity at 0.9 V of 6.5 times higher than that of Pt/C. Figure 1-6 summarises the different core-shell structures mentioned above.

.

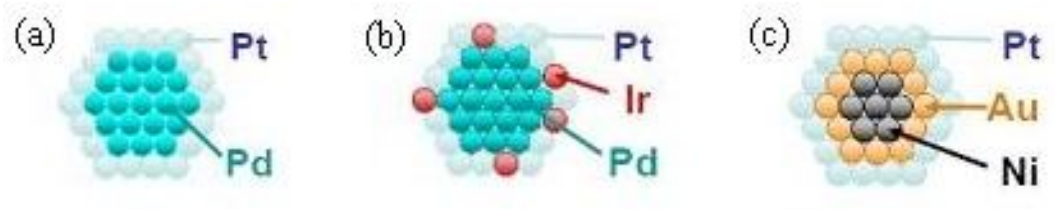

Figure 1- 6 Core-shell structures. (a) Pt monolayer on a Pd core (b) Mixed-metal Pt and Ir monolayer on a Pd core (c) Pt monolayer on a noble/non-noble core-shell nanoparticles (35).

1.4.2. Synthesis

Colloidal methods

Core-shell synthetic routes consist of sequential reduction processes to first form the core colloids and then establish the shell. To achieve this, various strategies are employed, such as the selective reduction of the precursor on the core nanoparticles. The polyol process, in which a polyol is used as both the solvent and the reductant, is commonly used but it does not always allow control over the deposition of the shell. To avert nucleation and growth of the shell metal in the solution, Sastry *et al.* had the idea to immobilize the reducing agent on the surface of the core nanoparticles (36). When the second metal ions were exposed to the surface, they were reduced forming a thin metallic layer. Phase pure core-shell nanoparticles were successfully synthesised: Au@Ag, Au@Pd and Au@Pt core-shell, where Au is the core and Ag, Pd and Pt form the shell. Another strategy for shell formation is to combine the polyol process with the controlled thermal decomposition of the precursor. The idea is to determine the reduction temperature at which the shell element precursor would reduce to the metal in the presence of the metallic core colloids. For example, it was found that the reduction of H_2PtCl_4 by 1,2-propanediol occurs at 118 °C in the presence of Ni particles instead of 158 °C (37). Son reported the preparation of Pd_{shell}/Ni_{core} nanoparticles from the thermal decomposition of Pd and Ni precursors (38). The generation of the Pd shell was possible because the metal-surfactant complexes employed, Pd and Ni- trioctylphosphine (TOP), decompose at different temperatures, which allowed the successive reduction of the Ni core and then the Pd shell. Evidence of the core-shell structure was given by field-emission Auger electron spectroscopy.

Surface organometallic chemistry methods

For the preparation of core-shell catalysts, a controlled deposition method of the Pt layer is desirable. The method must allow the deposition of Pt on the metal particles constituting the core only and prevent the deposition of isolated Pt particles on the carbon support. With conventional methods such as deposition-precipitation, impregnation, Pt may be deposited at different sites on the support. Over recent years, a new method for the preparation of bimetallic catalysts, the surface organometallic chemistry method (SOMC), has been developed. This is a new field of chemistry that studies the reactivity of organometallic complexes with surfaces (39-41). The surfaces may be highly dispersed oxides or zero-valent metallic particles. In SOMC on metals, the metallic surfaces are

those of highly dispersed metallic particles, supported or unsupported (42). SOMC has the possibility of controlling the relative location of the metal components of a bimetallic catalyst (M_1 and M_2). The activity and stability of the catalyst can sometimes depend drastically on how the two metals of a bimetallic are distributed with respect to one another (43). The reaction is believed to occur selectively between the organometallic precursor (M_1) and pre-adsorbed H on the core metal surface (M_2). This way, an intimate contact of both metals can be assured. Crabb *et al.* successfully prepared modified carbon-supported Pt catalysts for fuel cells (PtMo/C (44), PtSn/C (45)). Renouprez *et al.* (46) prepared silica-supported Pd-Ni catalysts by both SOMC and a coexchange methods and showed that catalysts with a more uniform surface composition were obtained using the first method. Qian *et al.* synthesised a wide range of carbon supported Pt-based bimetallic catalysts using the surface organometallic route (47). The PtM/C catalysts were prepared by reducing the second metal M (M = Co, Fe, Cr, Ni) as metallocene complexes $M(C_5H_5)_2$ on a Pt/C surface. The following reaction mechanism was proposed:

$$\mathrm{Pt/C} + \frac{1}{2}\mathrm{H_2} \rightarrow \mathrm{H\text{-}Pt/C} \qquad \textbf{(1- 9)}$$

$$\mathrm{H\text{-}Pt/C} + \mathrm{M(C_5H_5)_2} + 2\mathrm{H_2} \rightarrow \mathrm{C_5H_5\text{-}M\text{-}Pt/C} + \mathrm{C_5H_{10}} \qquad \textbf{(1- 10)}$$

$$\mathrm{C_5H_5\text{-}M\text{-}Pt/C} + \frac{5}{2}\mathrm{H_2} \rightarrow \mathrm{M\text{-}Pt/C} + \mathrm{C_5H_{10}} \qquad \textbf{(1- 11)}$$

The precursor was decomposed following a stepwise hydrogenolysis assisted by the preadsorbed hydrogen in the first step and H_2 gas in the second step. No evidence for the presence of the second metal, M, by itself was found, which confirms that M deposition occurred selectively on the Pt sites.

The preparation of Pt/Pd and Pd/Pt core-shell catalysts using CSR was attempted by Wells *et al.* (48). For the Pd monolayer-catalysts, Pd was exclusively found at the surface of the Pt particles whereas for the Pt monolayer-catalysts, the surface had more alloy character due to Pt diffusion into the Pd near surface.

Electrochemical methods

A new metal deposition method, involving a redox replacement of UPD (underpotential) adlayers by more noble metal cations which are reduced and simultaneously deposited, was developed by Brankovic *et al* (49). UPD is the deposition of

about one monolayer of a metal onto a foreign metal electrode at potentials more positive than those necessary for bulk deposition. The deposition of Pt monolayers on metal nanoparticles has been successfully achieved by Cu UPD replacement with no preferential deposition along the steps and the defect sites. The underpotentially deposited Cu adlayer on a noble metal substrate (such as Au) was obtained by immersion of the substrate in a Cu solution. The overall electroless deposition process of Pt can be described by the following equation:

$$Cu^{0}{}_{UPD} + \frac{m}{z} Pt^{z+} \rightarrow Cu^{m+} + \frac{m}{z} Pt^{0} \qquad \textbf{(1- 12)}$$

Using this method, Pt ML were obtained and characterised as interconected two-dimensional islands with holes of a monoatomic depth (50, 51). The advantage of this technique is that the total amount of deposited metal is controlled by the stoichiometry of the redox reaction.

The idea of depositing a noble metal monolayer at the expense of a non- or less noble metal adlayer is similar to the redox transmetalation process (52). If the shell metal (M_2) has a higher redox potential than the core metal (M_1), then a shell can be easily established, providing the deposited atoms can remain stable on the surface without migrating into the core. The process, which occurs through the sacrificial oxidation of M_1 to produce M_2 deposition on M_1, can be expressed as follows.

$$xM_1 + M_2^{n+} \rightarrow M_{1,x-1}M_2 + M_1^{n+} \qquad \textbf{(1- 13)}$$

The transmetalation process can also proceed through a ligand exchange between the metal core surface and the metal shell, when the latter is a metal-ligand complex. A number of core-shell materials, with Co as core metal, were successfully prepared using the redox-transmetalation route (52-54).

In the case where the redox potential between the two metals is not favourable, a strategy called the hydrogen sacrificial protective method was designed to ensure the formation of a controllable shell (55). The principle of this method is similar to that of the CSR. This strategy is based on the fact that, when they adsorb hydrogen, noble metals acquire a very strong reducing ability, which facilitates the reduction of foreign noble metal ions. Unlike the redox-transmetalation process, this method sacrifices the hydrogen

atom instead of the core metal atom. Following the hydrogen sacrificial protective process, a Pt shell was established on Pd nanoparticles (55) and Ru nanoparticles (56, 57). As the shell metal reduction and the core metal oxidation are simultaneous processes, the original size of the particles constituting the shell remains the same after the process.

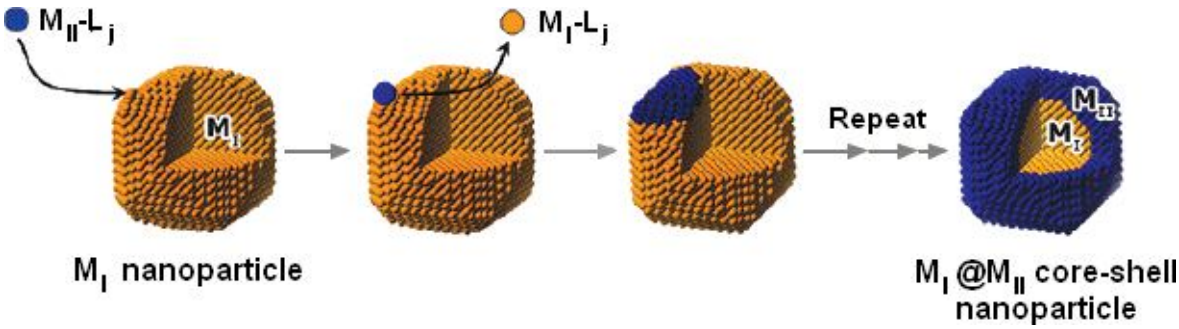

Figure 1- 7 Metal ions of reactant metal complexes (M_{II}-L_i) are reduced on the surface of M_I core nanoparticles while M_I atoms are oxidised to My+ by forming a M_I-ligand complex (M_I-L_j) (52).

Segregation effect in alloys

From alloys materials, core–shell structures can be achieved by high-temperature annealing, chemical leaching of the non-noble material, or electrochemical deposition techniques. All of these methods, however, exhibit significant disadvantages including the loss in active surface area and material and/or the formation of an incomplete noble metal shell.

Depending on the heat of segregation and the surface mixing energy, the composition of the surface of a bimetallic system can be very different from the bulk. This effect is additionally dependent upon the nature of the gas atmosphere in which the catalyst is in contact with, since the strong bonding of certain adsorbates will result in a gain in energy of the system. As a consequence, for bimetallic systems, an enrichment at the surface of the component that binds a certain adsorbate more strongly may occur. For example, the adsorption enthalpy of CO on Pt is higher than on Co, therefore a Pt-rich shell can be formed by CO-annealing of PtCo alloy nanoparticles (58). Similar results were also obtained by applying potential cycling to a PtCo alloy electrocatalyst in acid electrolyte, which led to the dissolution of Co surface atoms (59).

1.5. Project aims and objectives

The brief review of fuel cell technology presented in this chapter has described a number of challenges faced by the development of PEMFCs for future commercial use. The work presented in this thesis will focus on the development of core-shell cathode catalysts with improved oxygen reduction activity compared to pure Pt. A range of techniques will be used in order to elucidate the catalyst structure and test their activity and stability.

For oxygen reduction catalysis, it has been shown that thin layers of a platinum shell on a non-Pt core can enhance the activity of the Pt. In addition surface science studies have found that overlayers of one metal on another strongly modifies the electrocatalytic properties of the surface metal. The aim of this project is to develop this concept by the preparation of practical fuel cell catalysts based on the core-shell model and to gain a fundamental understanding of their properties and behaviour. A key aspect of the work is to establish the physical characteristics required for a catalyst to show long-term stability as well as improved activity.

Chapter 1 introduces the PEM fuel cells, ORR electrocatalysts and the preparation and characterisation of core-shell type electrocatalysts. The experimental techniques, procedures and apparatus used for this work will be described in Chapter 2. The mechanism of the synthetic controlled-surface reaction (CSR) used to prepare the core-shell electrocatalysts was studied in Chapter 3. Then the focus will be on the palladium-core and platinum-shell system in Chapter 4 and 5, where the effects of the Pt shell and the Pd core size on the electrocatalysts properties are investigated. The electrocatalysts prepared for these studies were assessed for their electrochemical stabilities and their ORR activities. Finally, Chapter 6 presents preliminary results on the iridium-core and platinum-shell system.

References

1. F. Barbir, in *PEM fuel cells: Theory and Practice*, p. 4, Elsevier Academic Press (2005).

2. http://americanhistory.si.edu/fuelcells/index.htm, Smithsonian Institution.

3. A. E. Institute and K. K. Smith, in *Powering Our Future: An Energy Sourcebook for Sustainable Living*, p. 111, iUniverse (2005).

4. L. J. M. J. Blomen and M. N. Mugerwa, in *Fuel Cell Systems*, L. J. M. J. Blomen and M. N. Mugerwa Editors, p. 19, Springer (1993).

5. S. Srinivasan and P. Costamagna, *Journal of Power Sources*, **102**, 242 (2001).

6. G. Hoogers and D. Thompsett, *Cattech*, **3**, 106 (2000).

7. N. Giordano, E. Passalacqual, L. Pino, A. S. Arico, V. Antonucci, M. Vivaldi and K. Kinoshita, *Electrochimica Acta*, **36**, 1979 (1991).

8. M. S. Wilson and S. Gottesfeld, *Journal of Applied Electrochemistry*, **22**, 1 (1992).

9. C. F. C. Partnership, http://www.fuelcellpartnership.org/benefits/global-warming-and-fcvs.

10. A. C. Lloyd, *Journal of Power Sources*, **86**, 57 (1999).

11. R. J. Farrauto, *Applied Catalysis B: Environmental*, **56**, 3 (2005).

12. K. Joon, *Journal of Power Sources*, **71**, 12 (1998).

13. V. S. Bagotsky, *Fundamentals of Electrochemistry*, John Wiley & Sons (2006).

14. J. Zhang, M. B. Vukmirovic, Y. Xu, M. Mavrikakis and R. R. Adzic, *Angewandte Chemie International Edition*, **44**, 2132 (2005).

15. G. A. H. C. Jaffray, in *Handbook of Fuel Cells – Fundamentals, Technology and Applications*, A. L. W. Vielstich, H. Gasteiger Editor, John Wiley & Sons Ltd, Chichester, UK (2003).

16. T. R. Ralph, G. A. Hards, J. E. Keating, S. A. Campbell, D. P. Wilkinson, M. Davis, J. St-Pierre and M. C. Johnson, *Journal of Electrochemical Society*, **144**, 3845 (1997).

17. H. A. Gasteiger, S. S. Kocha, B. Sompalli and F. T. Wagner, *Applied Catalysis B: Environmental*, **56**, 9 (2005).

18. D. Pletcher, *A First Course in Electrode Processes*, The Electrochemical Consultancy (1991).

19. E. Yeager, *Electrochimica Acta*, **29**, 1527 (1984).

20. V. S. Bagotsky, in *Fundamentals of Electrochemistry*, p. 275, John Wiley & Sons (2006).

21. Y. H. Shih, G. V. Sagar and S. D. Lin, *Journal of Physical Chemistry C*, **112**, 123 (2008).

22. A. Damjanovic and P. G. Hudson, *Journal of the Electrochemical Society*, **135**, 2269 (1988).

23. J. X. Wang, J. Zhang and R. R. Adzic, *Journal of Physical Chemistry A*, **111**, 12702 (2007).

24. B. Hammer and J. K. Norskov, *Surface Science*, **343**, 211 (1995).

25. B. Hammer and J. K. Norskov, *Advances in Catalysis*, **45**, 71 (2000).

26. A. Ruban, B. Hammer, P. Stoltze, H. L. Skriver and J. K. Norskov, in *1st Francqui Colloquium on Molecular Heterogeneous Catalysis*, p. 421, Brussels, Belgium (1996).

27. J. R. Kitchin, J. K. Norskov, M. A. Barteau and C. J. G., *Journal of Chemical Physics*, **120**, 10240 (2004).

28. T. Bligaard and J. K. Norskov, *Electrochimica Acta*, **52**, 5512 (2007).

29. R. Adzic, J. Zhang, K. Sasaki, T. Huang, J. Wang and M. Vukmirovic, in *DOE Hydrogen Program Review, May 23-26* (2005).

30. J. Zhang, M. B. Vukmirovic, K. Sasaki, F. Uribe and R. R. Adzic, *Journal of the Serbian Chemical Society*, **70**, 513 (2005).

31. J. Zhang, Y. Mo, M. B. Vukmirovic, R. Klie, K. Sasaki and R. R. Adzic, *Journal of Physical Chemistry B*, **108**, 10955 (2004).

32. J. X. Wang, N. M. Markovic and R. R. Adzic, *Journal of Physical Chemistry B*, **108**,. 4127 (2004).

33. J. Zhang, M. B. Vukmirovic, K. Sasaki, A. U. Nilekar, M. Mavrikakis and R. R. Adzic, *Journal of the American Chemical Society*, **127**, 12480 (2005).

34. M. B. Vukmirovic, J. Zhang, K. Sasaki, A. U. Nilekar, F. Uribe, M. Mavrikakis and R. R. Adzic, *Electrochimica Acta*, **52**, 2257 (2007).

35. R. Adzic, J. Zhang, K. Sasaki, M. Vukmirovic, J. Wang and M. Shao, in *DOE Hydrogen Program Review, May 16 - 19* (2006).

36. M. Sastry, A. Swami, S. Mandal and P. Selvakannan, *Journal of Materials Chemistry*, **15**, 3161 (2005).

37. Y. M. Chen, F. Yang, Y. Dai, W. Q. Wang and S. L. Chen, *Journal of Physical Chemistry C*, **112**, 1645 (2008).

38. S. U. Son, Y. Jang, J. Park, B. H. Na, H. M. Park, H. J. Yun, J. Lee and T. Hyeon, *Journal of the American Chemical Society*, **126**, 5026 (2004).

39. H. Mxura, H. Taguchi, K. Sugiyama, T. Matsuda and R. D. Gonzalez, *Journal of Catalysis*, **124**, 194 (1990).

40. J. P. Candy, B. Didillon, E. L. Smith, T. B. Shay and J. M. Basset, *Journal of Molecular Catalysis*, **86**, 179 (1994).

41. V. D. Stytsenko, *Applied Catalysis A: General*, **126**, 1 (1995).

42. C. E. Lee, P. B. Tiege, Y. Xing, J. Nagendran and S. H. Bergens, *Journal of the American Chemical Society*, **119**, 3543 (1997).

43. F. Humblot, J. P. Candy, F. Le Peltier, B. Didillon and J. M. Basset, *Journal of Catalysis*, **179**, 459 (1998).

44. E. M. Crabb, M. K. Ravikumar, Y. Qian, A. E. Russell, S. Maniguet, J. Yao, D. Thompsett, M. Hurford and S. C. Ball, *Electrochemical and Solid State Letters*, **5**, A5 (2002).

45. E. M. Crabb, R. Marshall and D. Thompsett, *Journal of the Electrochemical Society*, **147**, 4440 (2000).

46. A. Renouprez, J. F. Faudon, J. Massardier, J. L. Rousset, Delichère, P. and G. Bergeret, *Journal of catalysis*, **170**, 181 (1997).

47. Y. Qian, Preparation of Pt-based Bimetallic Catalysts for the Oxygen Reduction Reaction in PEM Fuel Cells, in *Department of Chemistry*, Open University, Milton Keynes (2004).

48. P. P. Wells, E. M. Crabb, C. R. King, R. Wiltshire, B. Billsborrow, D. Thompsett and A. E. Russell, *Physical Chemistry Chemical Physics*, **27**, 5773 (2009).

49. S. R. Brankovic, J. X. Wang and R. R. Adzic, *Surface Science*, **474**, L173 (2001).

50. K. Sasaki, J. X. Mo, M. Balasubramanian, F. Uribe, J. Mcbreen and R. R. Adzic, *Electrochimica Acta*, **48**, 3841 (2003).

51. J. Zhang, Y. Mo, M. B. Vukmirovic, R. Klie, K. Sasaki and R. R. Adzic, *Journal of Physical Chemistry B*, **108**, 10955 (2004).

52. W. R. Lee, M. G. Kim, J. R. Choi, J. I. Park, S. J. Ko, S. J. Oh and J. Cheon, *Journal of the American Chemical Society*, **127**, 16090 (2005).

53. M. Shao, K. Sasaki, N. S. Marinkovic, L. Zhang and R. R. Adzic, *Electrochemistry Communications*, **9**, 2848 (2007).

54. J. I. Park, M. G. Kim, Y.-w. Jun, J. S. Lee, W.-r. Lee and J. Cheon, *Journal of the American Chemical Society*, **126**, 9072 (2004).

55. Y. Wang and N. Toshima, *Journal of Physical Chemistry B*, **101**, 5301 (1997).

56. S. R. Brankovic, J. X. Wang and R. R. Adzic, *Electrochemical and Solid-State Letters*, **4**, A217 (2001).

57. K. Sasaki, J. X. Wang, M. Balasubramanian, J. McBreena, F. Uribe and R. R. Adzic, *Electrochimica Acta*, **49**, 3873 (2004).

58. K. J. J. Mayrhofer, V. Juhart, K. Hartl, M. Hanzlik and M. Arenz, *Angewandte Chemie International Edition*, **48**, 3529 (2009).

59. F. H. B. Lima, J. F. R. de Castro, L. G. R. A. Santos and E. A. Ticianelli, *Journal of Power Sources*, **190**, 293 (2009).

CHAPTER 2

EXPERIMENTAL TECHNIQUES: THEORY AND PRACTICE

CHAPTER 2: Experimental Techniques: Theory and Practice

This chapter describes the theory and experimental procedures of the techniques used to prepare and characterise the electrocatalysts. The description of the synthesis techniques will comprise the materials and chemical reagents used and the synthesis route employed to prepare precursor and catalyst materials. Then will follow the techniques to characterise the electrocatalyst's physical and electrochemical properties.

2.1. Reagents

Table 2-1 Chemical reagents and materials

Chemical reagent/material	Supplier
High surface area black carbon	Johnson Matthey
Pd nitrate	Johnson Matthey
Sodium hydroxide	Aldrich
Acetylacetone	Fluka Chemika
K_2PtCl_4 (Pt assay: 46.56%)	Johnson Matthey
Potassium hydroxide	Alfa Aesar
Toluene	Sigma-Aldrich
Platinum bis-acetylacetone	Johnson Matthey
40% Pt/C	Home-prepared by B. Theobald
40% Ir/C	Home-prepared by E. Christian
Teflonised carbon paper	Toray
1 M sulphuric acid	VWR International Ltd
Isopropanol	Sigma-Aldrich
Nafion solution (6.43 wt%)	Home-prepared at JMTC
Concentrated perchloric acid (70%)	GFS Chemicals
O_2	Air Products
N_2	Air Products
H_2	Air Products

2.2. Preparation of the Pd/C core catalyst

40 g of 20%Pd/C catalyst were prepared using a precipitation-deposition route followed by a hydrogen-reduction step at 200 °C. 34 g carbon support (6% moisture) were dispersed in distilled water for 30 min at 5000 rpm using a Maelstrom mixer. The carbon slurry was then further diluted in demineralised water in a large vessel. Meanwhile 56.5 g Pd nitrate (Pd assay: 14.6%) precursor were diluted in demineralised water. The base (1 M NaOH) and the Pd solution were simultaneously added to the stirred carbon slurry by means of an autotitrator and a peristaltic pump (pump setting: 10 ml min^{-1}) respectively. The addition was slow enough to maintain the pH at 7. After the addition was complete, the solution was stirred at room temperature for 90 mins to ensure all the Pd reacted to form Pd oxide. The catalyst was then filtered and washed free of sodium and nitrate ions until the filtrate conductivity went down below 10 μS, which indicates most of the nitrate and sodium ions are washed away. The catalyst was dried at 100 °C prior to reduction in 5%H_2/N_2 at 200 °C for 1 hr in a controlled atmosphere furnace.

2.3. Preparation of bis-acetylacetone Pt precursor ($Pt(acac)_2$)

2.3.1. Apparatus

$Pt(acac)_2$ was formed in a 3-neck rounded bottom flask fitted with a condenser, a N_2 gas inlet glass tube and a magnetic stirring heating mantle. $Pt(acac)_2$ was purified using a Soxhlet apparatus, shown in Figure 2-1, that consisted of a rounded bottom flask, a soxhlet extractor and a condenser fitted in series. A thimble was placed inside the extractor to collect the impurities from the reaction mixture. Once purified, $Pt(acac)_2$ was crystallised using a rotary evaporator.

2.3.2. Preparation procedure

21.3 g potassium tetrachloroplatinate(II) salt (K_2PtCl_4 [Pt assay: 46.56%]) were dissolved in 500 mL demineralised water in the 3-neck flask to give a red solution. The solution was then dearated by gently bubbling N_2 through. 79 mL acetylacetone (acacH) was mixed with 153.9 mL of 1M KOH base (molar ratio $C_5H_8O_2$:KOH 5:1), to form the

conjugate base acetylacetonate $C_5H_7O_2^-$ (1). The reaction equation is shown in Figure 2-2. Acetylacetonate is a bidentate ligand that can bind to Pt^{II} via both oxygen atoms. A large excess of acacH was used to improve the yield of the reaction (molar ratio acacH:Pt 15:1).

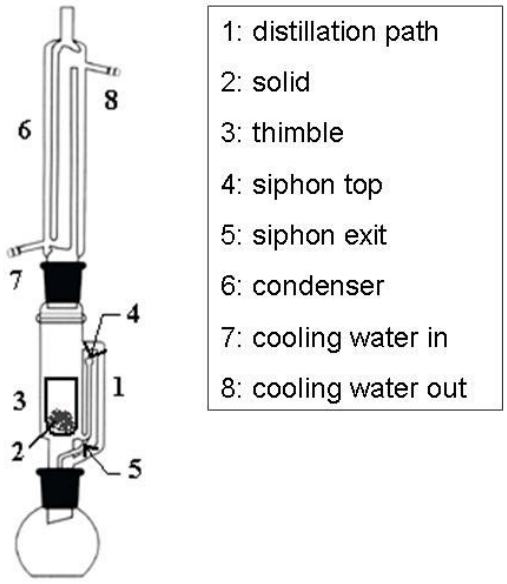

Figure 2- 1 A schematic representation of a Soxhlet extractor.

The yellow $C_5H_8O_2$:KOH mixture was then transferred to the flask and the reaction mixture was refluxed until the colour turned orange, which is an indication of the presence of $Pt(acac)_2$. If the reflux is maintained too long, it can cause the precipitation of Pt with the excess of KOH. The reaction was cooled down under N_2 and left to settle to allow the crystallisation of $Pt(acac)_2$. The yellow crystalline product was collected by suction filtration using a funnel and washed with demineralised water. It was then dried in vacuum conditions at 40 °C for 12 h.

The product was purified by Soxhlet extraction using toluene as the solvent. The product was placed in a thimble in Soxhlet extractor, while toluene was loaded in the flask below. The solvent was heated up until boiling point. The solvent vapor travelled through the product containing-thimble and condensed in the extractor. The extractor compartment was filled up slowly with toluene and dissolved $Pt(acac)_2$ that were led back to the flask through the distillation path, leaving the product impurities in the thimble. This reflux process was carried out for at least a day. $Pt(acac)_2$ was then separated from toluene using a rotary evaporator.

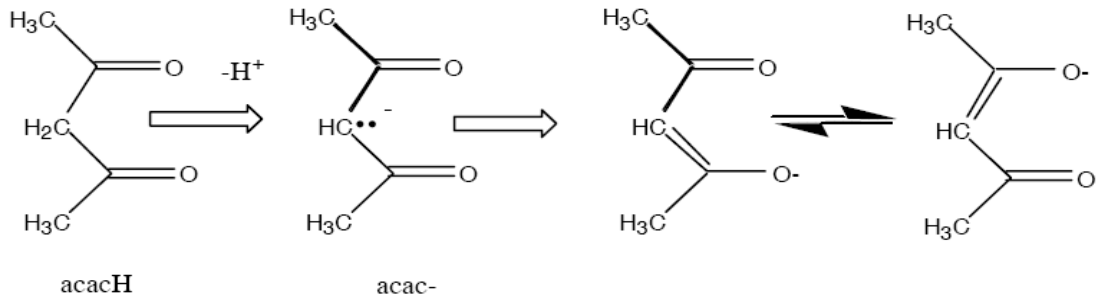

Figure 2- 2 In the presence of base, acetylacetone (acacH), readily loses a proton to form the acetylacetonate anion, acac.

2.4. Preparation of $Pt_{shell}/M_{core}/C$ catalyst using CSR

2.4.2.2.4.1. Apparatus

The reaction set up was constructed in the laboratory for the preparation of $Pt_{shell}/M_{core}/C$ (M = Pd, Ir) core-shell electrocatalysts (Figure 2-3). A 5-neck rounded bottom flask was fitted with a temperature probe, a gas inlet tube for H_2 and N_2, a condenser to minimise loss of solvent, and a dropper. The flask and the dropper were connected to a T-junction by the means of rubber tubing. The third T-junction exit was connected to another T-junction attached to a gas control box, which was used to select which gas between N_2 and H_2 to deliver. The gas control box had two functions: controlling the gas flow (ml cm^{-3}) and avoiding over pressurisation in the reaction system. Two bubblers were connected to the top of the condenser in series and were used to check the state of the gas flow through the system.

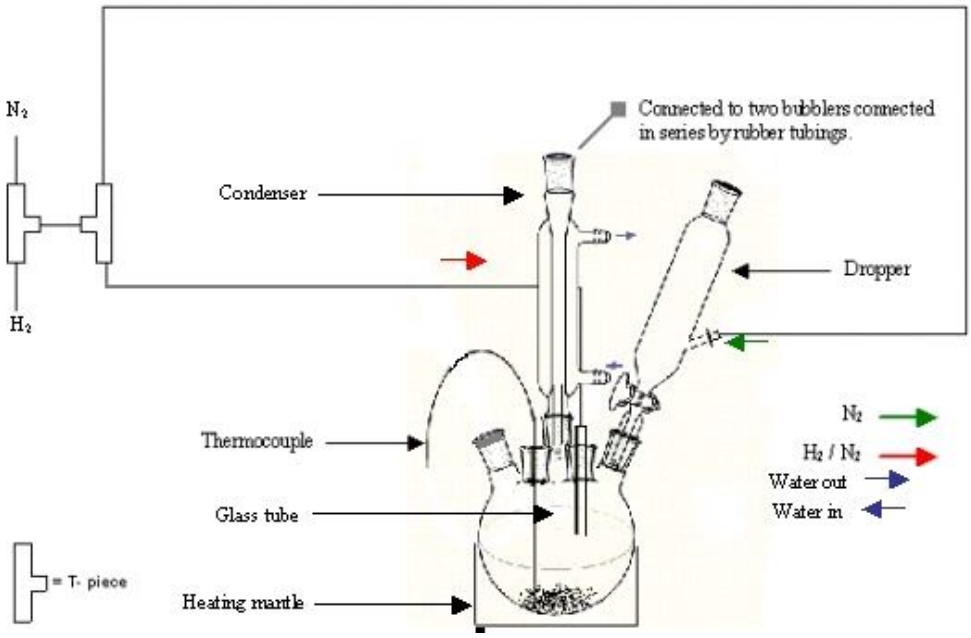

Figure 2- 3 Schematic diagram of the reactor used for CSR

2.4.3.2.4.2. Preparation procedure for $Pt_{shell}/Pd_{core}/C$ catalysts

The Pd/C core catalyst was first loaded in the vessel. The vessel was purged with nitrogen for 30 min. The catalyst was reduced under H_2 flow at 200 °C for 1 h to form the hydrogen sites and then was allowed to cool down. Then the condenser valve was closed to maintain the hydrogen atmosphere in the vessel. The $Pt(acac)_2$ precursor was dissolved in toluene and transferred to the dropper, where it was purged with N_2 for about 30 min. The dropper was then closed to avoid air coming in and H_2 was flowed again in the vessel. The precursor was added to the flask and the temperature was raised to 90 °C. The reaction was stirred under H_2 flow at 90 °C for 6 h. The deposition of Pt onto Pd is thought to occur through the displacement of the hydrogen preadsorbed on Pd. The vessel was then allowed to cool down under N_2 flow. The catalyst was filtered off by gravity, washed with toluene and allowed to dry in the fume cupboard. To remove the adsorbed organic species from the catalyst surface, a heat treatment was carried out at 100 °C for 1 hr in $5\%H_2/N_2$. To avoid self-ignition, the catalyst was passivated before exposure to air. Passivation of the catalyst was obtained by first evacuating the furnace and then introducing an oxygenated-N_2 gas flow with gradually increasing O_2:N_2 ratio.

The required amount of $Pt(acac)_2$ was calculated using the equation below:

$$\text{Mass precursor} = \frac{\text{wt\% Pd} \times \text{mass Pd/C} \times \text{D} \times x \times \text{RMM Pt(acac)}_2}{\text{MM Pd}} \quad \textbf{(2- 1)}$$

wt% Pd: Pd loading of the Pd/C catalyst (g)
D: dispersion of Pd measured by CO chemisorption (%)
x: number of monolayers to be deposited
MM: molar mass (g mol^{-1})

2.5. Techniques for physical characterisation

2.5.1. Surface area and metal dispersion of M/C core catalyst

The accessible metal surface area (S) and the dispersion (D) of the Pd particles on the carbon support were determined using an automatic CO chemisorption instrument developed at the Johnson Matthey Technology Centre. The catalyst sample is placed in a glass u-tube, which is connected to the gas inlet and outlet ports of the instrument. For carbon-supported noble metal catalysts, the sample (typically 20 mg, to ensure all catalyst is accessible to the gas) is first reduced with hydrogen at 50 ˚C for 30 min, and then the reduced metal surface is saturated with carbon monoxide at room temperature by flowing CO(g) through the cell.

Two detectors at both ends of the tube measure the amount of CO going in and out of the cell after several 0.25 mL injections of CO until the amount of CO coming out of the cell becomes constant. Two sets of peaks are recorded: the peaks corresponding to CO injections before the gas comes into contact with the catalyst (Peak 2), and the peaks corresponding to the amount of CO left after adsorption on the catalyst (Peak 1). The measurement stops when the area of Peak 1 becomes constant, which is the indication the catalyst surface is saturated. The catalyst surface area is automatically calculated following:

$$S(m^2.g_{catalyst}^{-1}) = \frac{T^0}{P^0} \times \frac{T}{P} \times \frac{V}{w} \times \frac{\sum A(h) - A}{A(h)} \times \frac{N_A}{V_m \cdot d_s} \quad \textbf{(2- 2)}$$

$$S'(m^2.g_{metal}^{-1}) = \frac{S(m^2.g_{catalyst}^{-1})}{wt\%Metal} \quad \textbf{(2- 3)}$$

Where T^0 and P^0 are the standard temperature and pressure respectively (273 K, 760 mbar); T and P are the temperature and pressure of the experiment; V is the injection volume of CO (0.25 mL); w is the weight of the catalyst sample (g); $\Sigma A(h) - A$ is the sum of the areas of the Peaks 1 subtracted to the largest peak area $A(h)$ ($A(h)$ is assumed to be equivalent to the injection volume V and $V \times \frac{\sum A(h) - A}{A(h)}$ corresponds to the volume of adsorbed CO in mL); N_A is the Avogadro constant (6.023×10^{23}); V_m is the molar volume (2.2414×10^4 cm^3); d_s is the number of metal atoms per cm^2.

The metal catalyst dispersion can also be calculated. It is the proportion of surface atoms with respect to the total number of atoms and can be calculated following equation (2-4):

$$D(\%) = \frac{\frac{V}{w \cdot V_m} \times \frac{\sum A(h) - A}{A(h)}}{\frac{wt\%Metal}{MM(Metal)}} \quad \textbf{(2- 4)}$$

Where the numerator corresponds to the amount of adsorbed CO in mmol $g_{catalyst}^{-1}$, wt%Metal is the metal loading on the carbon support and MM(Metal) is the molar mass of the metal catalyst.

Equations 2-2 and 2-4 assume that the metal-CO bonding type is single (1:1), which is the case for CO adsorbed on Pt. However, it can also be 2, corresponding to adsorption at bridging sites, M:CO ratio of (2:1), which is more appropriate for Pd. In the latter case the dispersion calculated via equation 2-1 must be doubled (2).

2.5.2. Transmission Electron Microscopy (TEM) and Scanning TEM (STEM)

The TEM and STEM have very high spatial resolution allowing the observation of features of atomic size. The main uses of this technique in the analysis of catalyst samples are to examine catalyst particle size, localised atomic structure, composition and interactions with the support.

Principle

The scheme of a typical electron transmission microscope is shown in Figure 2-4. An electron beam is accelerated by 100-400 kV to obtain a wavelength of the order of 10^{-3} to 10^{-2} nm (3). The beam is directed through a thin specimen under high vacuum and the sample image is produced by the scattered electrons when they hit the fluorescent screen placed at the end of the column. The electron beam is focused and magnified by electromagnetic lenses.

Several parameters can affect the resolution of the image, such as:

- the size of the objective aperture,
- the accelerating voltage applied to the electrons,
- aberrations (chromatic and spherical)
- astigmation of the beam

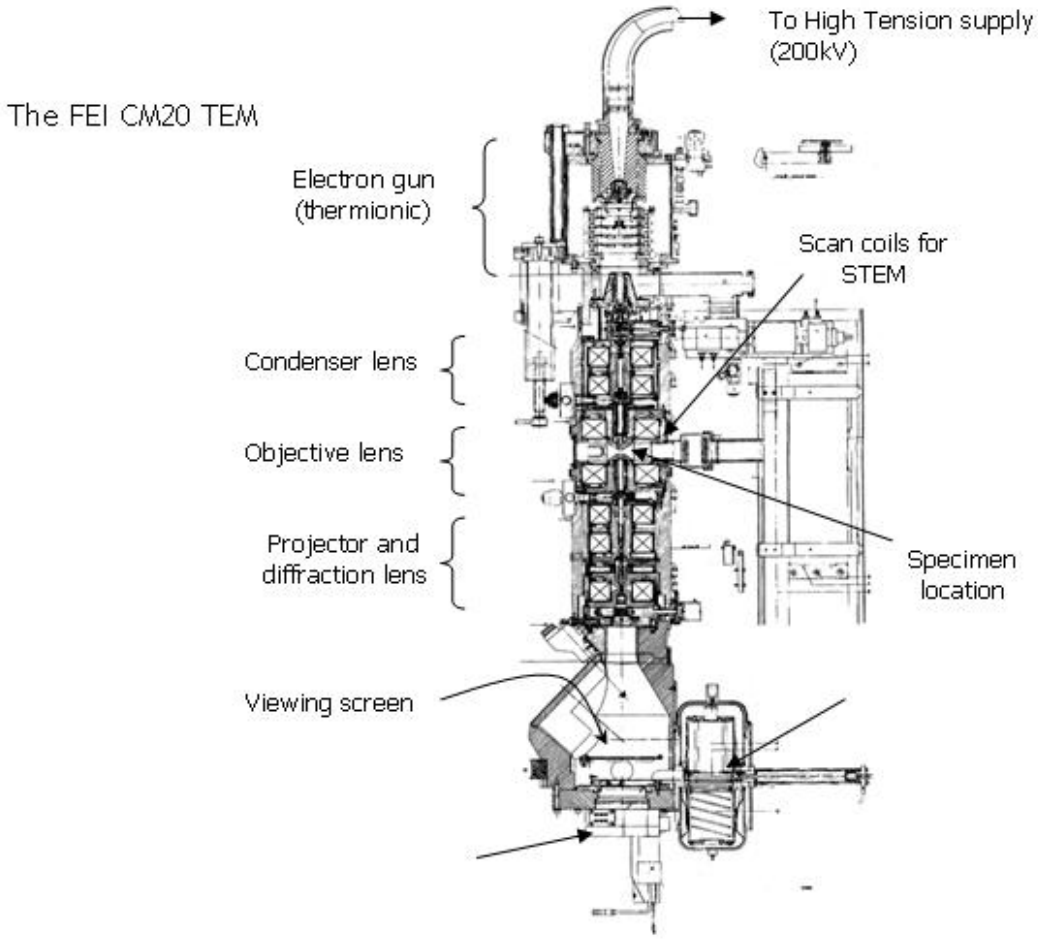

Figure 2- 4 Transmission electron microscope similar to the one used in this study.

In the STEM mode, a fine electron probe is focussed and scanned over the sample, and transmitted electrons are detected by either a bright field (BF) or an annular dark field detector (ADF). If the inner angle of the annular dark field detector is set to sufficiently high angles (50 mrad or more), it is called high angle annular dark field detector (HAADF). In this mode due to fine spot size combined with high beam currents it can be used to characterise nanoparticle compositions with high spatial resolution when combined with an energy dispersive X-ray (EDX) detector or electron energy loss detector (EELS). EDX analysis was the preferred method as it is more efficient in detecting high atomic number elements like PGM's.

Instrumentation and experimental procedure

The TEM analyses were carried out by Dr. D. Ozkaya, Dr S. Spratt and Dr S. Longworth at Johnson Matthey Technology Centre, Sonning Common (UK). A small portion of the sample was crushed and dusted onto a holey carbon film on a TEM copper grid prior to analysis. The sample was examined in a Tecnai F20 field emission Transmission Electron Microscope using the following parameters:

- the accelerating voltage 200 kV,
- the condenser lens aperture was set to 30 or 50 μm,
- the objective lens had an aberration correction Cs of 1.2 mm

The images were acquired using a number of modes in the microscope. Most of the direct imaging and particle size analysis was carried out in the BF mode, using the methodology described by L. Cervera Gontard (4) and D. Ozkaya (5). The intensities at the image are formed by a combination of the transmitted beam and the Bragg diffracted beams. An objective aperture at the back focal plane is used to choose which beams are allowed through the objective aperture. If it is set to the straight through beam this imaging mode is called bright field imaging, if any of the Bragg diffracted beams are chosen it is called Dark field imaging (DF). For most catalyst nanoparticles the atomic number is sufficiently different compared to the support to allow the particle image contrast to be differentiated from the support in the bright field mode. The support is usually bright and the particles are dark. However the Bragg scattering sometimes disrupts this proportional contrast behavior. This mode however is good enough in most cases to perform a particle size analysis.

The annular Dark Field imaging (HAADF) used in the STEM mode is based on a Z^2-contrast mechanism that makes heavy atoms appear bright and because it only detects the electrons scattered to large angles, Bragg diffracted beams do not interfere with the images. Thus, it is a better way of determining distributions of particles on the support. At high resolutions high angle annular dark field imaging reveals the atomic structure as a function of atomic number. This aspect has been exploited and used to image the core-shell structure for Pd/Pt system. The difference in atomic number is sufficiently high to be able to see interatomic columns of Pt and Pd as separate entities.

High-resolution micrographs of the core-shell catalysts were obtained using an aberration-corrected TEM/STEM instrument. Aberration correction is a recent development in transmission electron microscopy and it corrects for the spherical aberration. Spherical aberration limits resolution by focusing electrons from the sides of the lens to a different point compared to the electrons scattered from the center of the lens. By using a set of coils driven by computers it has been possible to limit this aberration and obtain less than 0.1 nm resolution in the aberration corrected microscopes (6). Aberration correction in the STEM mode creates a smaller electron beam with higher current density.

The analyses were performed by L. Cervera Gontard at the Center for Electron Nanoscopy Department of Technical University of Denmark electron microscopy, and by Haibo E at the Department of Materials at the University of Oxford.

2.5.3. Powder x-ray diffraction (XRD)

The primary use of XRD in this work is to identify metallic phases in the catalysts by comparison of their diffraction patterns with known standards. It includes the determination of the crystal structure of identified metals and the determination of the average crystallite size of the metal particles.

The application of X-ray diffraction technique is restricted due to the limited crystallinity of most supported metal catalyst systems. Another limitation is that only relatively large particles can be examined due to severe X-ray line broadening in the case of small particles. However, in favourable circumstances, where the catalyst displays a degree of crystallinity and where the phases under investigation are present in sufficient

quantities, it is possible to extract structural information, such as phase composition and crystallite size, from an XRD pattern.

Principle

X-rays are electromagnetic radiations of wavelength ~ 1 Å. They occur in that part of the electromagnetic spectrum between γ-rays and the ultraviolet.

When a crystal is bombarded with x-rays of a fixed wavelength (similar to spacing of the atomic-scale crystal lattice planes) and at certain incident angles, intense reflected x-rays are produced when the wavelengths of the scattered x-rays interfere constructively. In order for the waves to interfere constructively, the differences in the travel path must be equal to integer multiples of the wavelength. When this constructive interference occurs, a diffracted beam of x-rays will leave the crystal at an angle equal to that of the incident beam.

To illustrate this feature, consider a crystal with crystal lattice planar distances d as shown in Figure 2-5. When the travel path length difference between the ray paths 1 and 2 is an integer multiple of the wavelength, constructive interference will occur for a combination of that specific wavelength, crystal lattice planar spacing and angle of incidence θ. Each rational plane of atoms in a crystal will undergo refraction at a single, unique angle (for x-rays of a fixed wavelength).

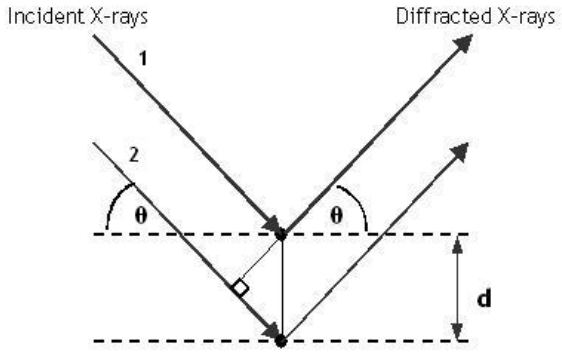

Figure 2- 5 Deriving Bragg's Law reflection geometry.

The general relationship between the wavelength of the incident x-rays, angle of incidence and spacing between the crystal lattice planes of atoms is known as Bragg's Law, expressed as:

$$n\lambda = 2d\sin\theta \quad \textbf{(2- 5)}$$

λ: wavelength of the X-rays,

d: distance between two lattice planes,

θ: angle between the incoming X-rays and the normal to the reflecting lattice plane,

n: integer called the order of the reflection.

Analysis methods

Several X-ray diffraction methods for crystallite size determination are available. These include the widely used, but less accurate, single-peak Scherrer method and the popular Rietveld refinement.

The Debye-Scherrer method corrects only for the peak broadening effect observed for sub-micrometre particles. This is achieved by the use of a shape factor K for the determination of the average crystalline size in the Debye-Scherrer formula:

$$< L >= \frac{K\lambda}{\beta\cos\theta} \quad \textbf{(2- 6)}$$

<*L*>: measure of the dimension of the particle in the direction perpendicular to the reflecting plane,

B: full width at half maximum, FWHM, of the peak (radians) corrected for instrumental broadening,

K: constant that depends on the crystallite shape and is comprised between 0.9 and 1.

The Debye-Scherrer equation can only be applied to the diffraction peaks individually, which may lead to some inaccuracy in the calculation of the crystallite.

In contrast, the Rietveld method uses structure data for the calculation of a full diffraction pattern and compares this with measured data. It also corrects for the instrument effects such as optics effects. By least squares fitting, the algorithm calculates (by varying different parameters such as peak shape or lattice constants) the minimum difference between calculated and measured patterns. Small crystallite sizes well below 1 μm show a peak broadening in the diffraction pattern, which results in different profile parameters.

These are then used to calculate the crystallite size and the lattice parameter based on the assumption of a Gaussian size distribution.

Instrumentation

The sample powder is spread over a glass holder and then pressed to obtain a flat coverage. The XRD pattern of the sample is measured with a Bruker AXS D-500 diffractometer using a stationary X-ray source Cu Kα and a movable detector, which scans the intensity of the diffracted radiation as a function of the angle between the incoming and the diffracted beams ($10° < 2\theta < 90°$). The measurements were performed by H. Jobson and J. McNaught from the Analytical department at JMTC.

2.5.4. X-ray Photoelectron spectroscopy (XPS)

XPS, also called electron spectroscopy for chemical analysis, ESCA, can provide information such as the elemental composition and the oxidation state of the surface region.

Principle

Surface analysis is accomplished by irradiating the sample with short wavelengths from Mg Kα (1253.6 eV) or Al Kα (1486.3 eV) X-ray sources. As the photons have limited penetrating power, they interact only with atoms in the surface region, which makes XPS a surface sensitive technique.

The absorption of a photon of energy $h\upsilon$ by an atom induces the emission of electrons following two processes: the photoelectric effect and the Auger process (Figure 2-6). The incoming photon ejects a photoelectron of binding energy E_b from its atomic orbital. The kinetic energy E_k of the ejected photoelectron is given by:

$$E_k = E_b - h\nu - \varphi \qquad \textbf{(2- 7)}$$

Where ν is the frequency of the exciting radiation, E_b is the binding energy of the photoelectron with respect to the Fermi level of the sample and φ is the work function of the spectrometer. As the vacancy is filled from a higher orbital, an Auger electron carries away the energy equal to the difference in the orbitals.

The resulting spectrum is a plot of the number of electrons (I) versus electron binding energy over a small fixed energy interval. Slight differences in orbital energies in different compounds give rise to a chemical shift in the peak position and a change in the peak shape, allowing differentiation of chemical species. The peak areas can be used (with appropriate sensitivity factors) to determine the composition of the material's surface.

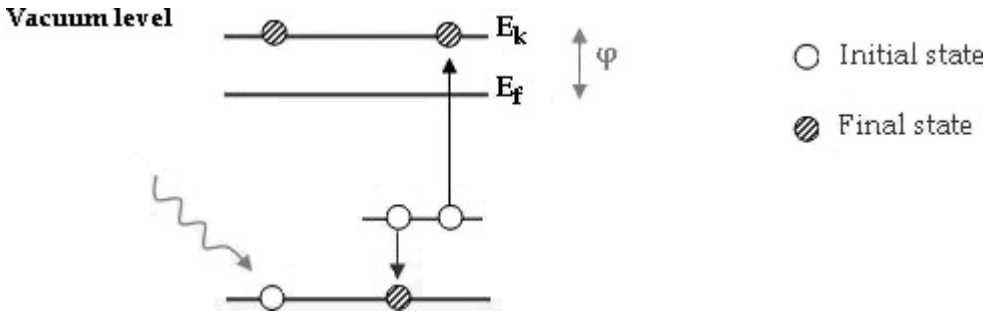

Figure 2- 6 XPS emission processes for a model atom

Instrumentation and experimental procedure

The powder was dusted onto carbon tape, which is then mounted on a standard sample stub. The XPS analyses were carried out in an ESCALAB 250. The exciting radiation used in the studies was for the monochromatised aluminium Kα radiation focused in a 650 μm spot at 200 W power. The analyses were performed by Dr R. Smith at Johnson Matthey Technology Centre, Sonning Common (UK).

2.5.5. High Sensitive-Low Energy Ion Scattering Spectroscopy (HS-LEIS)

LEIS spectroscopy uses primary energies in the range of 100 eV to 10 keV. Due to its extreme sensitivity, LEIS is used to provide quantitative information on the atomic composition of the top surface layer or two monolayers. It was used to estimate the Pt coverage for core-shell catalysts.

Theory

When a monoenergetic ion beam hits a solid surface part of the projectiles will be scattered back into the vacuum after one or more collisions with target atoms of the top

few layers. Measurement of the energy of the backscattered particles can be used to identify the mass of the atoms.

Instrumentation and experimental procedure

The samples were analysed with the Calipso LEIS instrument. The catalyst samples were placed in a sample cup, mounted on a specimen holder and transferred to the pre-treatment chamber of the instrument. There, the catalyst samples were reduced for 10 minutes with 100 mbar H_2 at room temperature. After the reduction treatment, the samples were transferred to the analysis chamber.

For an overview of all elements, the samples are usually analysed with 3keV $^4He^+$. For a more specific study of heavy atoms, like Pt-Pd catalysts, the samples were analysed with 3keV $^{20}Ne^+$ ions. In a case where the atoms have similar *Z* (atomic number), like Pt and Ir, high mass resolution at high masses is required to separate the Pt peak from the Ir peak. This can be achieved with heavy primary ions ($^{84}Kr^+$) and the Qtac100 instrument.

The samples were typically analysed at 6 different spots with a size of 1.7 x 1.7 mm^2. These spectra were averaged to obtain improved statistics. With the Qtac100 instrument, the samples were typically analysed at 6 different spots with a size of 2 x 2 mm^2. This made it possible to keep the sputter damage to the samples limited to less than 1% of a monolayer.

The analyses were performed by Dr. Rik ter Veen at Tascon GmbH Analytical Services and Consulting, Münster (Germany).

2.5.6. Inductively Coupled Plasma (ICP) analytical techniques

Principle

Elemental analysis is obtained by decomposing the sample upon intense heat into a cloud containing free atoms and ions. When they return to their ground state, the excited atoms release energy in the form of light radiation at a characteristic wavelength. Because this process is element-specific, the intensity of the light emitted is used to determine the concentration of that particular element in the sample. ICP sources are used to excite atoms for atomic-emission spectroscopy and to ionize atoms for mass spectrometry. ICP Atomic

Emission Spectrometry (ICP-AES) can detect concentrations in the order of µg - mg/L (ppb – ppm) (7). For lower detection limits (ng/L to µg/L), ICP Mass Spectrometry (ICP-MS) is preferred.

ICP source

A scheme of the ICP source used at JMTC is shown in Figure 2-7. RF electric and magnetic fields are created in the region of the top of a torch by passing 0.7 – 1.5 kW of radiofrequency energy through a coil wrapped round the torch carrying argon gas. A spark is applied to the gas causing electrons to be stripped out of the Ar atoms resulting in a very hot plasma, up to 10,000 °C. The sample is sprayed through a nebulizer and the sample droplets pass up the torch into the plasma where they are atomised and then emit their characteristic wavelengths.

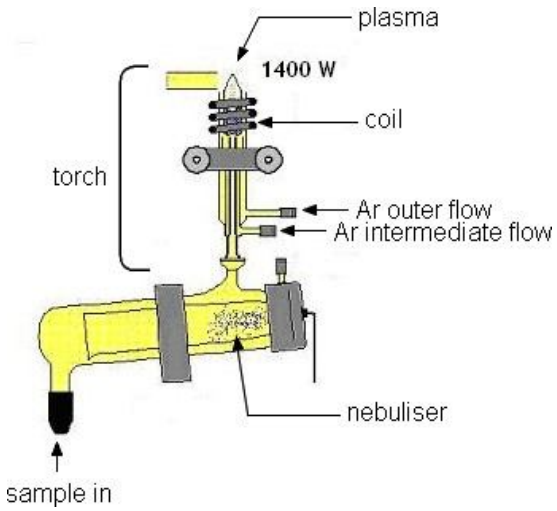

Figure 2- 7 Scheme of an ICP source.

ICP-ES

The different emitted wavelengths are separated into individual wavelengths by a monochromator or polychromator. Once separated, the wavelengths are detected by a photosensitive detector. The nature of the elements is obtained by identification of the emission lines and the concentration of the elements is determined from the line intensity.

ICP-MS

Mass spectrometers use the difference in mass-to-charge ratio (m/e) of ionised atoms to separate them from each other and then measure the quantity of ions of each mass-to-charge ratio.

Experimental procedure

- Determination of PGM catalyst assay

About 50 mg of catalyst was weighed and placed in a quartz microwave vessel. A mixture of 30:70 hypochloric acid and nitric acid was added to the vessel, which was then placed in a Multiwave 3000 microwave system at 1200 W for 99 min. The role of nitric acid is to oxidise all the carbon support into CO_2 whereas hypochloric acid helps solvating PGM atoms in the solution. 10 mL of the resulting suspension was diluted in a 100 mL-flask with demineralised water. The flask was then placed in a water bath to be equilibrated at 20 ^{o}C to ensure accuracy of the volume. In the ICP instrument, the sample was compared against standard solution of the atomic species to be analysed (typically 1 mg dm^{-3} to 10 mg dm^{-3}). The sample was continuously pumped into the sprayer and then to the plasma for about 90 s prior to the measurement, to ensure stability of the plasma. A blank measurement is run between every measurement to confirm the stability and cleanliness of the system.

- Determination of PGM traces in solution

Depending on the nature of the solution sample, different preparation procedures are applied. For aqueous solutions, the sample is diluted in water by about ten times and analysed by ICP.

The analyses were performed by James McNaught, Ian Briggs, Paul Fischer and Junior Godson at Johnson Matthey Technology Centre, Sonning Common (UK).

2.5.7. Extended X-ray Absorption Fine Structure (EXAFS)

X-ray absorption fine structure (XAFS) is an x-ray absorption technique that gives a global view of a material structure. Information about the number, type and distance of the

absorbing atom neighbours can be obtained. It is important to note that EXAFS provides an average picture of the environment of a particular atom and the sample does not need to have an ordered structure.

Principle

In high-energy accelerators, electrons are injected into an electron storage ring and accelerated to energies above the MeV range to emit synchrotron radiation. In this energy range, the electron is close to the speed of light.

In an EXAFS experiment, the (usually synchrotron based) x-ray radiation passes through a material and is absorbed by the material, giving rise to a loss of intensity in the transmitted signal. According to the Beer's Law, the loss of intensity can be expressed as follows:

$$dI = -\mu(E)Idt \quad \textbf{(2- 8)}$$

$$I = I_0 e^{-\mu(E)t} \quad \textbf{(2- 9)}$$

dI: loss in intensity of an x-ray beam through the path length dt,
$\mu(E)$: absorption coefficient of a specific material,
I: intensity of the transmitted (attenuated) beam,
I_0: intensity of the initial x-ray beam,
t: material thickness

The absorption of a monochromatic x-ray of energy $h\nu \geq E_b$ by an atomic core-level of binding energy E_b, causes the ejection of a photoelectron from its quantum level to the continuum with a kinetic energy $E_k = h\nu - E_b$ (Figure 2-8). This is represented by a sharp increase in the absorption function spectrum, also referred as absorption edge. The oscillations or wiggles of the EXAFS signal are due to the scattering of photoelectrons on neighbouring atoms. The outgoing and backscattered electrons can interfere constructively or destructively, depending on their mean free path, λ, the distance between the absorbing atom and the scattering atom, r, and the phase shift, φ, caused by the scattering event. The maxima and minima of the EXAFS plot correspond to constructive and destructive wave interferences (Figure 2-9) respectively.

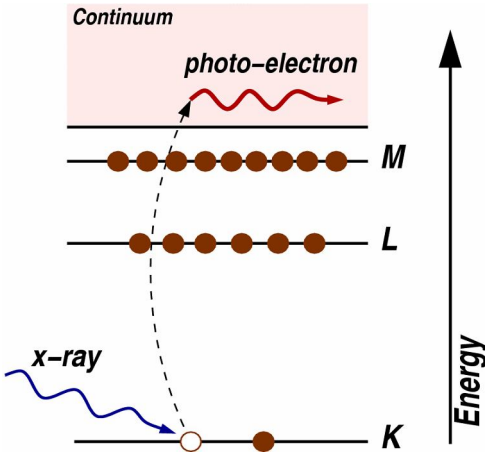

Figure 2- 8 Photoelectron emission mechanism

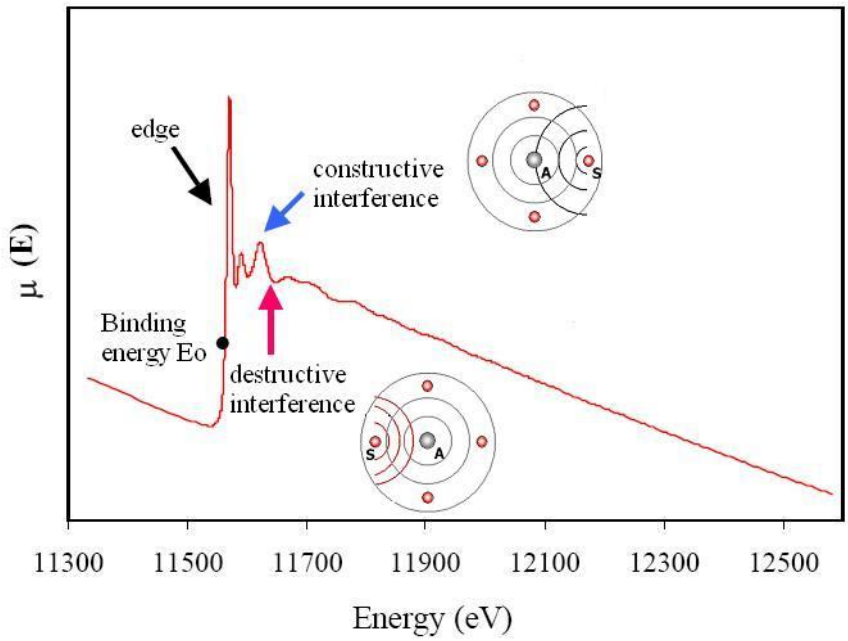

Figure 2- 9 EXAFS spectrum for an atomic species. The constructive interference corresponds to a maxima, whereas a a destructive interference corresponds to minima in the EXAFS plot. They are represented by the inference between the waves coming from the absorbing atom (A) and the scattering atom (S).

An x-ray absorption spectrum is generally divided into four regions (8):

- The pre-edge $(E < E_0)$. The minor features in the pre-edge region are usually due to the electron transitions from the core level to the higher unfilled or half-filled orbitals (e.g, s → p, or p → d).

- The x-ray absorption near edge structure (XANES), where the energy of the incident x-ray beam is $E = E_0 \pm 10eV$. Here the photoelectrons have a low kinetic energy that does not allow them to be released in the continuum. Instead, they interact with valence electrons. In the XANES region, transitions of core electrons to non-bound levels with close energy occur. Because of the high probability of such transition, a sudden increase of absorption is observed.

- The near edge x-ray absorption fine structure (NEXAFS), in the region between 10 eV up to 50 eV above the edge. In NEXAFS, the ejected photoelectrons have low kinetic energy (E-E_0 is small) and experience strong multiple scattering by the first and even higher coordinating shells.

- The extended x-ray absorption fine structure (EXAFS), which starts approximately from 50 eV and continues up to 1000 eV above the edge. In the EXAFS region, the photoelectrons have high kinetic energy (E-E_0 is large), and single scattering by the nearest neighbouring atoms normally dominates.

Data analysis

After obtaining the XAS spectrum, the information about the local structure around the absorber atom must be extracted from the EXAFS data. The EXAFS function $\chi(k)$ is defined by the following equation:

$$\chi = \frac{\mu - \mu_0}{\mu} \qquad \textbf{(2- 10)}$$

With $\mu_0(E)$ the linear absorption coefficient of the isolated atom.

To obtain $\chi(k)$, the raw data is processed following consecutive steps (9):

- The first step is the pre-edge subtraction to remove the absorption of the x-rays from shells other than the one under study and from other elements in the sample (Figure 2-10(a)). This involves the fitting of a function to the pre-edge and the extrapolation of this function over the whole data range.
- Then the edge position E_0, which corresponds to the zero point of k ($Å^{-1}$), is obtained from the peak position of the maximum in the first derivative of the spectrum (Figure 2-10(b)).

- Once the edge position is determined, the atomic background (μ_0) should be determined and subtracted from the data. The background subtraction involves fitting a cubic spline function as expressed in the following equation:

$$\sum_{i=1}^{NPTS} \frac{\left(\mu x_i - BCK_i\right)^2}{e^{-WEk_i^2}} \leq SM \qquad \textbf{(2- 11)}$$

SM: smoothing parameter

WE: weighing factor

i: NPTS defines the start and end energy of the background.

These parameters have to be defined to determine the number of points. To do so, they are varied until an optimum signal-to-noise ratio is obtained.

- Since the EXAFS signal reflects the contribution of all the target element atoms in the irradiated volume, the experimental spectrum must be normalised to take in account the element atom concentrations. The spectrum is then normalised giving an edge jump of one, placing the measured spectrum on a per absorber atom basis.
- After the above-mentioned steps, the $\chi(k)$ spectrum is converted into k-space according to equation (2-12):

$$k = \sqrt{\frac{2m_e\left(h\nu - E_0\right)}{\hbar^2}} \qquad \textbf{(2- 12)}$$

m_e: electron mass

$\hbar = \frac{h}{2\pi}$: reduced Planck's constant.

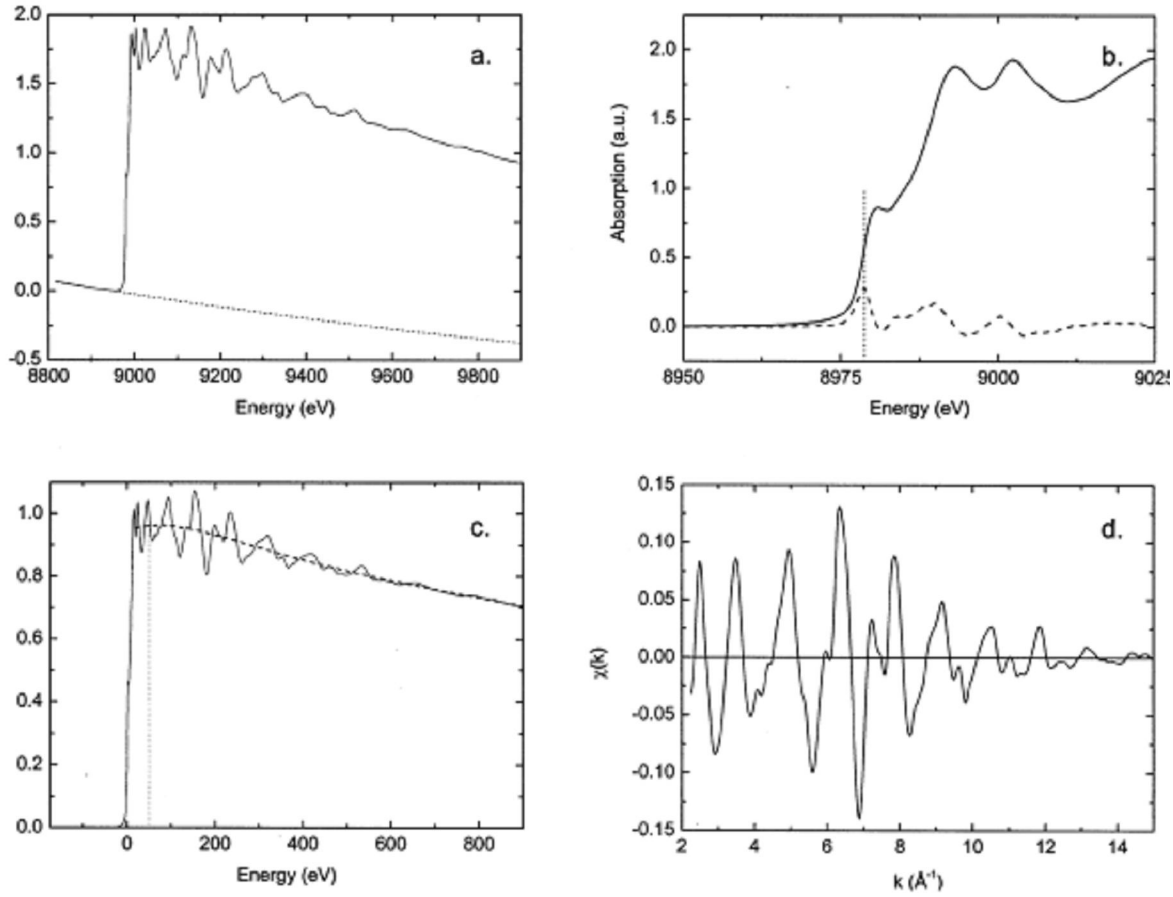

Figure 2- 10 EXAFS data analysis scheme. (a) Subtraction of Pre-edge. (b) Determination of the absorption edge. (c) Subtraction of the background and normalisation. (d) Produced EXAFS data.

The Fourier Transform

To analyse the EXAFS oscillations, Sayer *et al.* (10) proposed a Fourier transform, which is defined by:

$$FT(r) = \frac{1}{2\pi} \int_{k\,\min}^{k\,\max} k^n \cdot \chi(k) \cdot e^{2ikr}\, dk \qquad \textbf{(2- 13)}$$

The Fourier transform (FT) of the EXAFS function represents the atomic radial distribution function around the absorber atom. It is a complex function defined by an imaginary part, used for the determination of interatomic absorber-scatterer distances, and a real part, used for the determination of the number of neighbouring atoms and disorder parameter (Debye-Waller factor). When performing a Fourier transform, k^n-weighing can be used to emphasize the role of light or heavy atoms. A light element (like O) scatters mainly at low *k*-value, whereas a heavy element (like Pt) scatters significantly at high *k*-values.

Data analysis programs

The EXAFS spectra collected at the Synchrotron Radiation Source (S.R.S.) in Daresbury Laboratory (Warrington, UK) and at the National Synchrotron Light Source (N.S.L.S.) in Brookhaven National Laboratory (New York, USA) were analysed with computer programs available on the XRSSERV1 computer (Unix operating system) at Daresbury Laboratory. The dataset collected consists of values taken by different detectors at each point of the spectrum. These points are defined by the position of the monochromator in millidegrees. The data is first calibrated with the EXCALIB program: the millidegree x-scale is converted into eV-scale, and the *I* (reading signal) y-scale is converted into absorption-scale. The analysis of the data, described previously (pre-edge removal, inner potential determination, background substraction and spectrum normalisation), is performed with the EXBROOK program. Finally, the curve fitting of the data and the determination of the coordination number (*N*), the distance to the neighbouring atoms, the Debye-Waller term ($2\sigma^2$) and the shift in the Fermi energy (E_f) were performed with the EXCURV98 program. The EXAFS function can be described as (11):

$$\chi(k) = \sum_j \frac{N_j f_j(k) e^{-2k^2\sigma_j^2}}{kR_j^2} \sin\left[2kR_j^2 + \delta_j(k)\right] \qquad \textbf{(2- 14)}$$

f(k): scattering amplitude,
δ(k): phase-shift,
R: distance to neighbouring atom,
N: coordination number of neighbouring atom,
σ^2: mean-square disorder of neighbour distance
j: neighbour atom

f(k) and *δ(k)* are photo-electron scattering properties of the neighbouring atom. As they depend on the atomic number *Z* of the scattering atom, the species of the neighbouring atom can be determined.

The goodness of the fit can be assessed with an R_{EXAFS} factor:

$$R_{EXAFS} = \sum_i^N \frac{\left(\left|\chi_i^{\exp}(k) - \chi_i^{th}(k)\right|\right)}{\sigma_i} \times 100\% \qquad \textbf{(2- 15)}$$

Where $\chi^{exp}(k)$ and $\chi^{th}(k)$ are the experimental and theoretical EXAFS, N the number of data points, k the magnitude of the photoelectron wave vector and σ the variation in the path length. A value of $\leq 30\%$ for R_{EXAFS} is considered to a good fit.

Experimental procedure

The EXAFS measurements at the Pt L_{III}-edge were carried out using SRS at the double crystal Si(111) harmonic monochromator on station 9.3 at SRS at Daresbury Laboratory. The storage ring was operated at 2.0 GeV energy with an average current of about 125 mA. In Figure 2-11, the x-ray beam enters from the left, passes through a slit to adjust its size, and then through the monochromator. The amount of x-rays before and after the sample are measured by ionization chambers. For transmission detection mode, a third ion chamber is placed at the end of the setup to measure the transmitted beam Ir following a reference material or foil. For fluorescence detection mode, the fluorescence radiation resulting from the absorption of x-ray photons, is detected by a solid-state detector. The transmission detection mode is suitable for the investigation of concentrated samples whereas the fluorescence mode is for dilute sample.

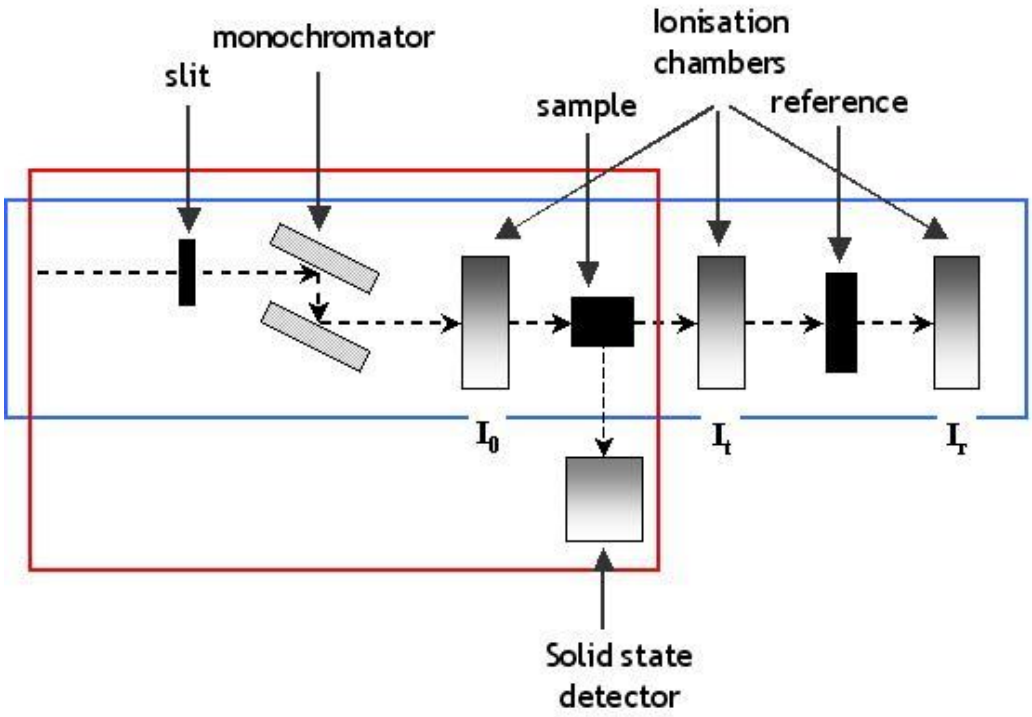

Figure 2- 11 Scheme of the set-ups for the transmission detection mode (inside blue rectangle) and for the fluorescence detection mode (inside red rectangle). The dashed line represents the pathway of the beam.

The carbon supported catalyst samples were prepared as pellets. The preparation of pellets involves grinding a set amount of catalyst and boron nitride to form a homogenous mixture and then compacting this in a purpose built press to form a self-supporting wafer. The pellet holder used in the pressing process can then be transferred to a gas treatment cell shown in Figure 2-12.

The gas treatment cell contains a gas inlet and gas outlet port so that different gases can be purged through the cell. The gas can be contained within the cell by shutting the outlet and inlet ports. The cell consists of a series of Kapton windows to allow for the entry and exit of the X-ray beam. As the sample holder is mounted into a removable arm, the angle of the arm with respect to the cell can be varied for both transmission and fluorescence experiment set-ups. When exposing the sample to different gas environments, the cell was purged with the desired gas for ~ 1 hour before closing the gas taps. At the end of an experiment the cell was purged with $N_2(g)$ for 30 min before opening to air.

All the XAS data was collected by members of the Russell group which included myself and K.B. Blaney, S. Burton, G. Chouchelamane, P. Kanan, S. Price, J. Speed, A. Wise, and Prof. A.E. Russell.

Figure 2- 12 EXAFS gas treatment cell.

2.6. Electrochemical characterisation

2.6.1. Cyclic voltammetry

Principle

Cyclic voltammetry is a very useful tool for catalyst surface characterisation. In cyclic voltammetry, the potential applied to the working electrode is swept back and forth between two chosen limits, at a steady potential scan rate, υ, while the current response is monitored. The working electrode is the electrode where oxidation and reduction processes are studied. The obtained voltammogram is a plot of the current, i, versus the potential, E, which is time-dependent.

To carry out cyclic voltammetry measurements, a three-electrode cell configuration shown schematically in Figure 2-13 is usually used. It consists of three electrodes immersed in an electrolyte: the working electrode (WE), the counter electrode (CE) and the reference electrode (RE). The potential of the WE is measured against the RE and the current is passed between the WE and the CE. The counter electrode makes a connection to the electrolyte so that a current can flow between the working and the counter electrodes when a potential is applied to the working electrode.

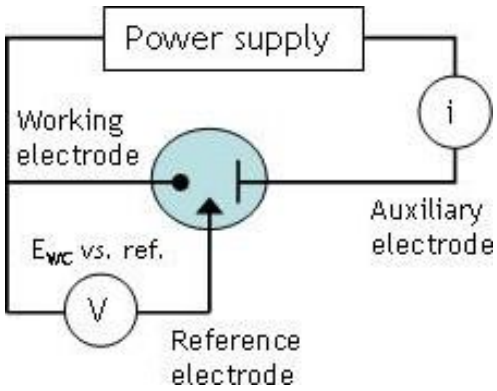

Figure 2- 13 Electrical circuit for a three-electrode cell

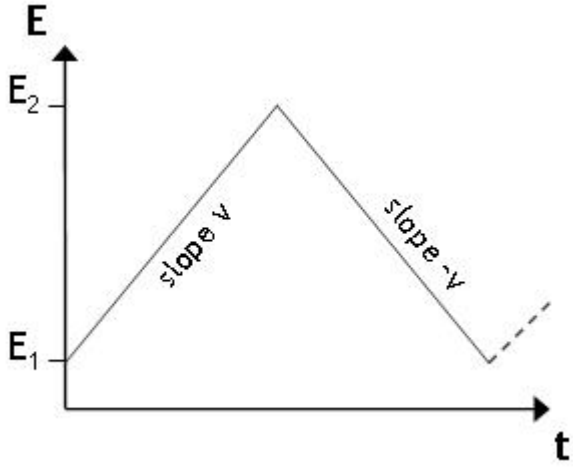

Figure 2- 14 Potential - time profile used in cyclic voltammetry

Characterisation of metal surfaces

As a surface sensitive technique, cyclic voltammetry is very useful for catalyst surface characterisation. When the potential is ramped to the upper limit, oxidation processes occur at the electrode. When the potential is reversed to the lower limit, reduction processes. In acidic aqueous electrolyte, noble metals adsorb hydrogen and oxygen by charge transfer. However, the shape and the potential of the corresponding features are characteristic of the metal.

Figure 2-14 shows the cyclic voltammogram of a Pt electrode in aqueous H_2SO_4 (12). Three different regions can be distinguished. Between 0 and 0.4 V, hydrogen is adsorbed on the cathodic sweep and oxidised on the anodic sweep, giving rise to two pairs of peaks. These peaks have been assigned to weakly and strongly bound hydrogen (13). The desorption-adsorption of hydrogen occurs through the reaction:

$$M - H \leftrightarrow M + H^{+} + e^{+} \qquad \textbf{(2- 16)}$$

In the double-layer region, between 0.4 and 0.8 V, no electrochemical reaction occurs and the current recorded is due to the accumulation of charges from the electrolyte at the polarised interface. Above 0.8 V, oxygen starts to be chemisorbed and oxides are formed. As the potential increases above 0.8 V, the oxygen adsorption becomes increasingly irreversible due to rearrangement of the oxygen species layer into two dimensional lattice of O species and metal atoms (14). At the onset of the oxide formation, the Pt surface

interacts with the O-containing species present in the electrolyte (H_2O, OH^-) and as the process progresses a 3-dimensional oxide lattice develops.

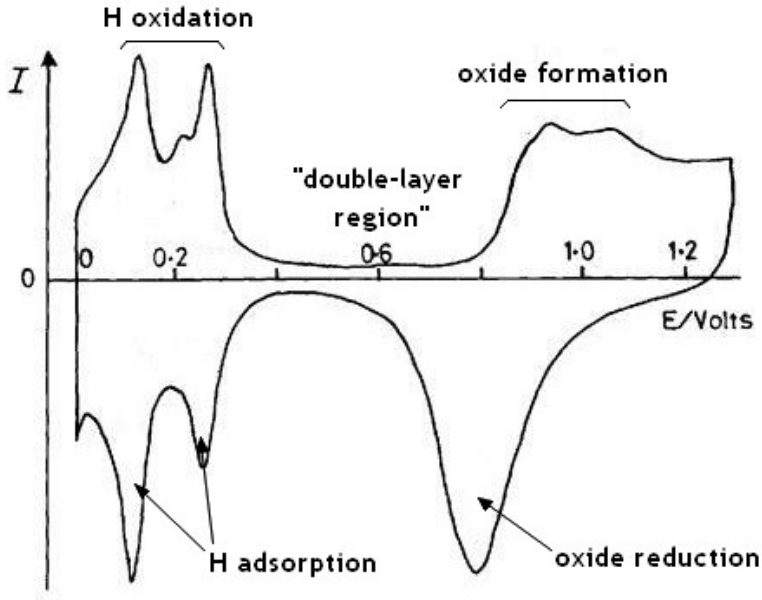

Figure 2- 15 Cyclic voltammogram of a Pt electrode in 0.5 M H_2SO_4 at 25 °C at 100 mV s^{-1}

The active surface area of a metal can be evaluated from cyclic voltammetry in acidic media. Assuming one surface Platinum atom has the ability to adsorb one hydrogen atom, the integration of the charge passed to form a hydrogen monolayer (Q_H) allows evaluation of the electrochemical Pt surface are (EPSA):

$$EPSA(cm^2{}_{Pt}cm^{-2}) = \frac{Q_H}{A \times 210 \times 10^{-6}} \qquad \textbf{(2- 17)}$$

Where Q_H is the charge passed to form a monolayer of adsorbed hydrogen (C), A is the geometric are of the electrode (cm^2) and 210×10^{-6} is the charge it takes to oxidise one hydrogen monolayer on one centimetre square of Pt in C $cm^{-2}{}_{Pt}$.

The electrochemical surface area is:

$$ECA(m^2 g^{-1}{}_{Pt}) = \frac{EPSA}{L_{Pt}} \qquad \textbf{(2- 18)}$$

Where L_{Pt} is the loading of Platinum in the electrode in g m^{-2}.

This is not the preferred method to determine the electrochemical surface area of Palladium and Iridium-based catalysts. The ECA is overestimated in the first case and

underestimated in the latter, due to hydrogen absorption and poor hydrogen adsorption respectively.

Another way to determine the catalyst electrochemical area is by CO electrooxidation voltammetry. Prior to the electrochemical measurements, CO is adsorbed on the catalyst and then a cyclic voltammogram is performed. CO is oxidised into CO_2 by increasing the potential following the reactions:

$$H_2O \rightarrow OH_{ad} + H^+ + e^- \quad \textbf{(2-19a)}$$

$$CO_{ad} + OH_{ad} \rightarrow CO_2 + H^+ + e^- \quad \textbf{(2- 19b)}$$

Experimental

I completed all of the electrochemical characterisation measurements myself at the Johnson Matthey Technology Centre laboratories.

- Preparation of the electrodes

3.14 cm^2 disk-electrodes were prepared by brush-coating an aqueous based catalyst ink containing between 80 and 110 wt% Nafion solids with respect to the carbon onto teflonised carbon paper to yield a carbon loading of 0.6 mg_C cm^{-2}. Prior to electrochemical measurement, the electrodes were boiled in water with a few drops of sulphuric acid until wet.

- Electrochemical measurement

The electrochemical study was carried out in a standard three-electrode cell, using an Autolab potentiostat/galvanostat PGSTAT 30. The reference electrode used was H_2 purged Pd/C electrode (Pd/H ref.). A Pt coil served as the counter electrode.

A cyclic voltammogram was typically run in 1 M H_2SO_4 between 0.01 and 1.0 V at 10 mV s^{-1}.

2.6.2. Rotating-disk electrode

Principle

The rotating disc electrode (RDE) is the classical hydrodynamic electroanalytical technique used to limit the diffusion layer thickness. The RDE consists of a disc (such as Pt or glassy carbon) set into an insulating (PTFE) surround. The electrode is rotated about its vertical axis (Figure 2-17), typically between 400 and 10,000 rpm. Similar to cyclic voltammetry, in rotating disk voltammetry, the potential of the working electrode is swept back and forth between two potential limits. The difference in rotating disk voltammetry is that the working electrode is rotated at a very high speed. This motion induces a well-defined flow pattern of the electrolyte, where it is pumped up from the bulk towards the electrode surface and then flung out centrifugally. The layer of liquid adjacent to the electrodes is motionless with respect to the electrode and rotates at the same velocity. The concentration of the reactant is consequently uniform in the electrolyte bulk and decreases linearly from the edge of the stagnant layer, also called Nernst diffusion layer, to the electrode. The theory for the hydrodynamics at the RDE (15) assumes that the electrode is uniformly accessible and affords a precise and reproducible control of the convection and diffusion of reactant to the electrode.

The theoretical treatment yields the concentration profile of reactant towards the RDE and defines a layer with thickness δ where diffusion is the sole mode of mass transport.

$$\delta = \left[1.61 \nu^{1/6} D^{1/3}\right] \omega^{-1/2} \qquad \textbf{(2- 20)}$$

ω: is the rotation speed (rad s^{-1}),

v: kinematic viscosity (m^2 s^{-1})

D: diffusion coefficient of the reacting species in the liquid (m^2 s^{-1})

It can be seen that δ can be controlled by the rotation speed. From the concentration profile is derived an expression for the limiting current I_L, know as the Levich equation:

$$I_L = 0.62 nFD^{0.67} \nu^{-0.166} c w^{0.5} \qquad \textbf{(2- 21)}$$

v: kinematic viscosity (m^2 s^{-1})

c: concentration of reacting species (mol m^{-3})

n: number of transferred electrons

Classically, the limiting current is reached by recording a linear sweep voltammogram at a low scan rate (1–10 mV s^{-1}). At high overpotentials, the reaction kinetics is very fast and the reaction is limited by the diffusion of the reactant through the Nernst diffusion layer. The current reaches a limit I_L that increases with the rotation speed, which controls the thickness of δ.

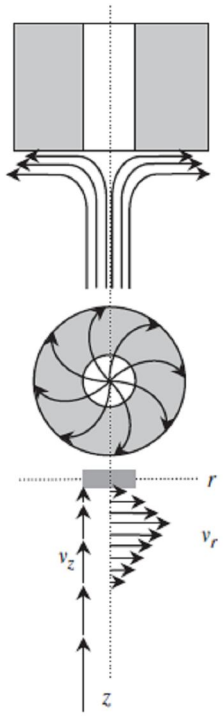

Figure 2- 16 Streamlines for flow and vector representation of fluid velocities near a rotating disc electrode (16).

For an irreversible redox process such as the reduction of oxygen, the measured current I can be expressed as a contribution of the kinetic current I_k and the limiting current I_L, as shown in the Koutecký-Levich equation (16):

$$\frac{1}{I} = \frac{1}{I_k} + \frac{1}{0.201FAD_0^{2/3}\nu^{-1/6}C_0\omega^{1/2}} \qquad \textbf{(2- 22)}$$

The kinetic current is extracted from equation (2-22) and given by:

$$I_K = \frac{I \times I_L}{I_L - I} \qquad \textbf{(2- 23)}$$

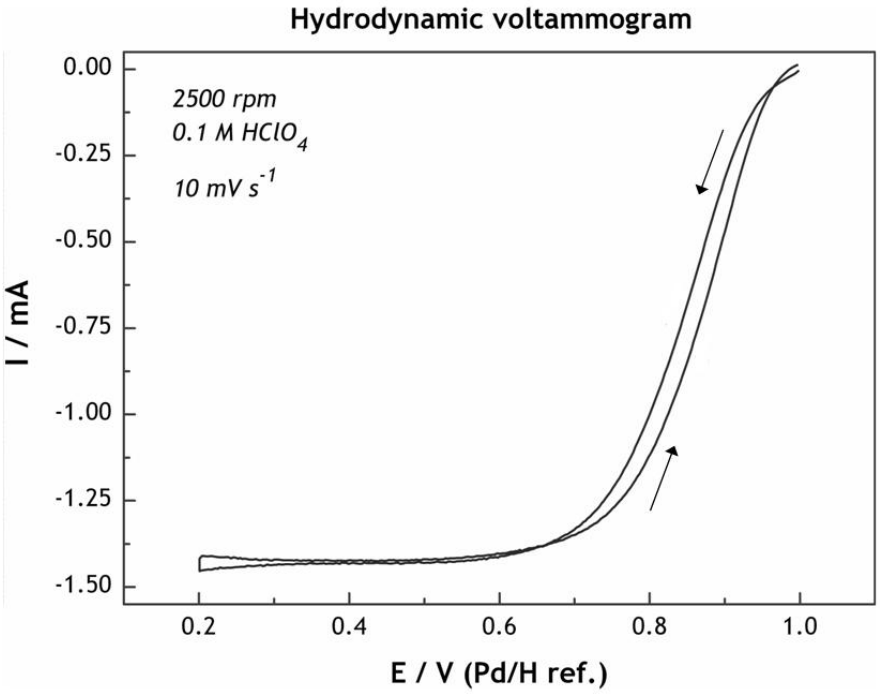

Figure 2- 17 Typical rotating disk voltammogram for a carbon-supported Pt catalyst in 0.1 M $HClO_4$, at 10 mV s^{-1}, from 1.0 V to 0.2 V at a rotating speed of 2500 rpm.

Set up

The electrochemical measurements were conducted in a standard sealed three-electrode cell with a Pine disc electrode as the working electrode. The electrode was made of a glassy carbon disk embedded in Teflon. An Autolab potentiostat/galvanostat PGSTAT 30 and a rotation control were also used. The reference electrode consisted of a carbon-supported Pd catalyst electrode near hydrogen bubbling and the counter electrode of a Pt coil. The electrolyte was prepared using distilled water and concentrated $HClO_4$ to give a concentration of 0.1 M.

Electrode preparation

The electrode surface was polished with a 0.05 μm alumina paste, rinsed with Millipore water, ultrasonically cleaned in water and then rinsed again prior to use. The catalyst was dispersed ultrasonically in a mixture of isopropyl alcohol, water and Nafion®. Thin films of the electrocatalysts were prepared by placing a defined amount of catalyst suspension, onto a flat glassy carbon electrode (5 mm diameter, Pine Instruments). To ensure the thickness of the catalyst layer was thin enough to allow optimum accessibility of the catalyst by the reactant, one should aim for the following catalyst loadings:

20-25μg/cm^2 for catalysts containing 45-50 wt% metal

15-20μg/cm^2 for catalysts containing 30-40 wt% metal

10-15μg/cm^2, for catalysts containing less than 30% metal

The electrode was then partially dried under an infrared lamp.

Experimental procedure

The cell was purged with nitrogen or argon prior to the introduction of the working electrode in the cell. The electrode was cycled between 0.02 and 1.2 V (vs Pd/H ref.) at 20 mV s^{-1}, until a well-defined and stable voltammogram was recorded, (typically 10 cycles were required). The electrochemically active surface area was calculated from the charge it takes to adsorb a layer of hydrogen in the H_{UPD} region (between 0.04 and 0.4 V (vs Pd/H)). O_2 was then bubbled into the electrolyte for 20-30 minutes to ensure saturation of the electrolyte. Before evaluating the catalyst activity, the electrode was conditioned by running 2 cycles at a rotation rate of 400 rpm, between 1 and 0.2 V at 10 mV s^{-1}. Then two scans were run at the following rotation speeds, whilst O_2 was bubbled into the electrolyte: 400, 900, 1600 and 2500 rpm. The experiment was repeated 3 times for each catalyst to ensure reproducibility of the results.

2.6.3. Activity measurements in miniature PEMFC

A single cell PEM was designed at Johnson Matthey for rapid screening of MEA performances. The electrocatalysts developed in this project were tested as cathodes and a standard 40%Pt/C electrocatalyst was used as the anode.

MEA preparation

The anode and the cathode constituting the MEA were prepared by brush-painting inks onto teflonised carbon paper disks of an area of 3.14 cm^2. All catalysts investigated in the fuel cell were used as cathodes.

The inks were prepared using between 85 to 100 wt % Nafion® with respect to the carbon mass of the catalyst used. This was achieved by adding the required amount of 11.9 wt% Nafion® aqueous solution to 0.5 g of catalyst. The ink containing plastic pots were then placed in a Speedy Mixer apparatus set at 2000 rpm for 2 min. A few drops of water were added to the pot to dilute the ink. The ink was processed another time in presence of four ceramic balls in the Speedy Mixer at 2000 rpm for 2 min to help break down the

catalyst particles. Each carbon paper disk was first wetted with 35 % IPA solution in water before the catalyst ink was brush-painted on them. After each coat the electrode was dried on a hot plate at 90 ^{o}C and painted again until the target mass was reached. The metal loading was chosen so that the carbon loading was 0.6 mg cm^{-2} for every catalyst.

To produce the MEAs the membrane was sandwiched between the cathode and anode, with the catalyst layers facing the membrane. The MEAs were hot pressed between PTFE and paper sheets at 150 ^{o}C, at 90 psi for 2 min as shown in Figure 2-18.

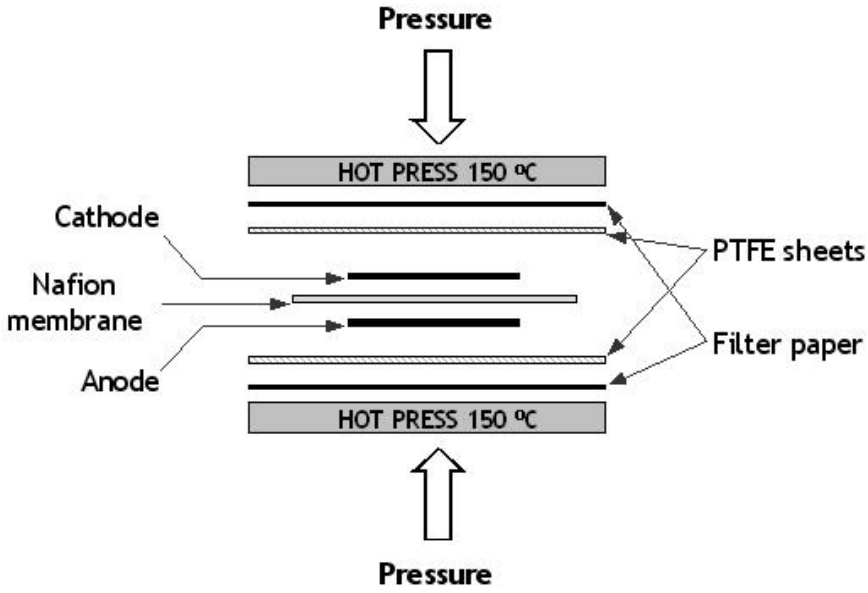

Figure 2- 18 Arrangement used for hot pressing MEAs.

Description of the cell

For performance testing, the MEAs were assembled within a miniature PEMFC (Figure 2-19). In the fuel cell assembly, the MEA sat between two graphite current collector plates. It was compressed to 80 % thickness by tightening the bolts used to hold the plates together and measuring the distance between the plates until the desired compression was achieved. The graphite plate design consisted of a single serpentine channel through which the gas reactants travelled to the electrode catalyst layers. The MEA/graphite plate body was sandwiched between two membrane substrate assembly components (MSA), whose role was to humidify the fuel and oxidant gases to prevent the membrane from drying out. Water was pumped through tubes from a water bath at 80 ^{o}C. A temperature probe was

placed between the graphite plates to control the temperature at the MEA. Two thick plastic plates and screws held the cell together. A scheme of the single cell PEM is shown in Figure 2-20.

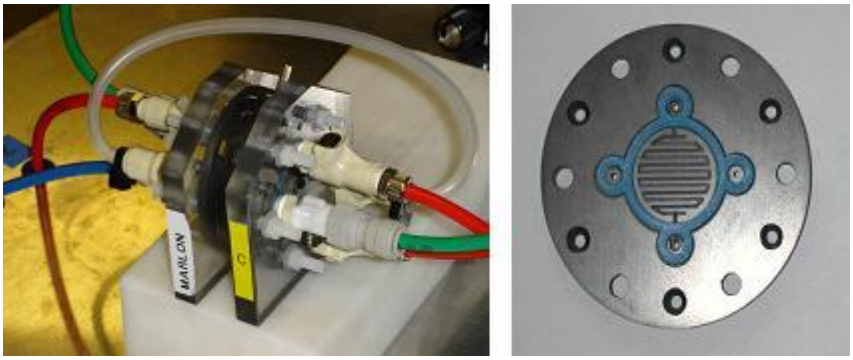

Figure 2- 19 Miniature PEMFC on the left. Graphite plate current collector on the right.

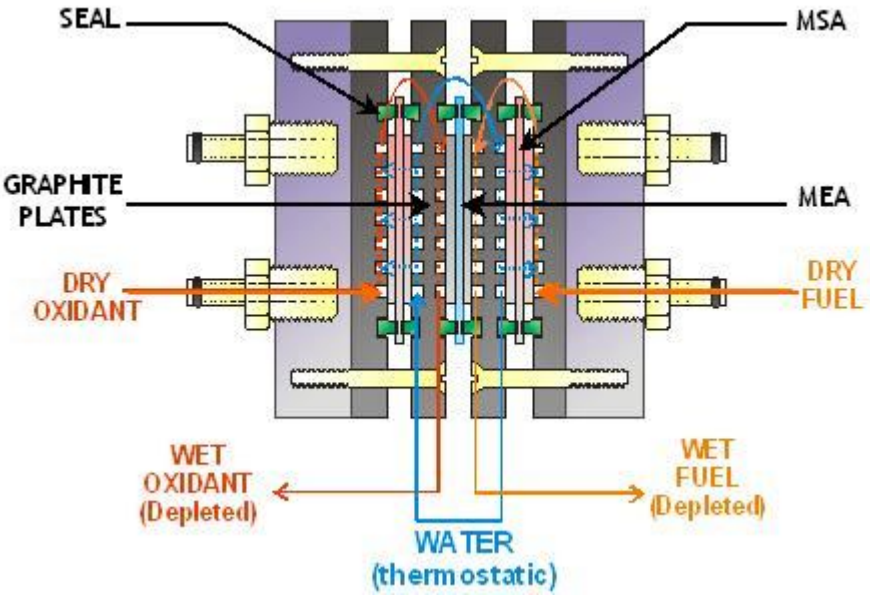

Figure 2- 20 Scheme of single cell PEM

Experimental procedure

Gas flow rates of 60 ml min^{-1} were used for the cathode and anode, and both sides of the cell were pressurised at 10 pounds per square inch gauge (psig). After ensuring the system leak proof, it was first purged with nitrogen gas at a pressure of 10 psig. Setting the cathode as the working electrode and the anode as the counter/reference electrode,

the anode gas was switched to hydrogen while nitrogen is flowing at the cathode. Once the open circuit potential was stable, the cell was polarised to 0.3 V vs RHE. This current quantified the hydrogen crossing over the membrane from the anode to the cathode. If the membrane had no hole, this current was expected to be below 20 mA.Leak check

N2/N2 heat cell (water bath at 80 □C) set pressure to 10 psi

H2/N2 measure crossover at 10 psi

Measure cathode CVA cyclic voltammogram was recorded at the cathode to ensure the resistance across the cell was reasonable. A CO stripping measurement was performed to determine the catalyst electrochemical area. The potential was held at 0.15 V vs RHE for 15 mins while CO flowed over the cathode, after which the gas was switched to nitrogen for 30 min. Three CVs were then measured by cycling from 0.01 V to 1.0 V vs. RHE at a scan rate of 10 mV s^{-1}.

Switch to H2/O2 & measure OCVTo perform steady state polarisation measurements, oxygen was flowed to the cathode whereas hydrogen was flowed to the anode. Twenty fast polarisation curves were recorded in order to condition the cell. The potential was stepped by 0.05 V every 5 s from 0.95 V to 0.65 V vs. RHE. An example of the 1^{st}, 5^{th} and 10^{th} scans is shown in Figure 2-21(a). Then two slow polarisation curves were recorded from 0.95 V to 0.65 V vs. RHE, at a step potential of 0.026 V and a time interval of 30 s. An example is shown in Figure 2-21(b).

Current interrupt measurements are carried out to correct the performance data for ohmic losses. The technique involves holding the potential until the current response is stable and measuring the potential-time curve after the current is switched off. The curve obtained is characterised by a jump of the potential followed by a slow equilibration to the open circuit voltage. The potential jump divided by the initial current gives the ohmic drop. Current interrupt measurements are performed at different currents to obtain an average of the resistance value.

N2/N2 turn cell round to get correct gases

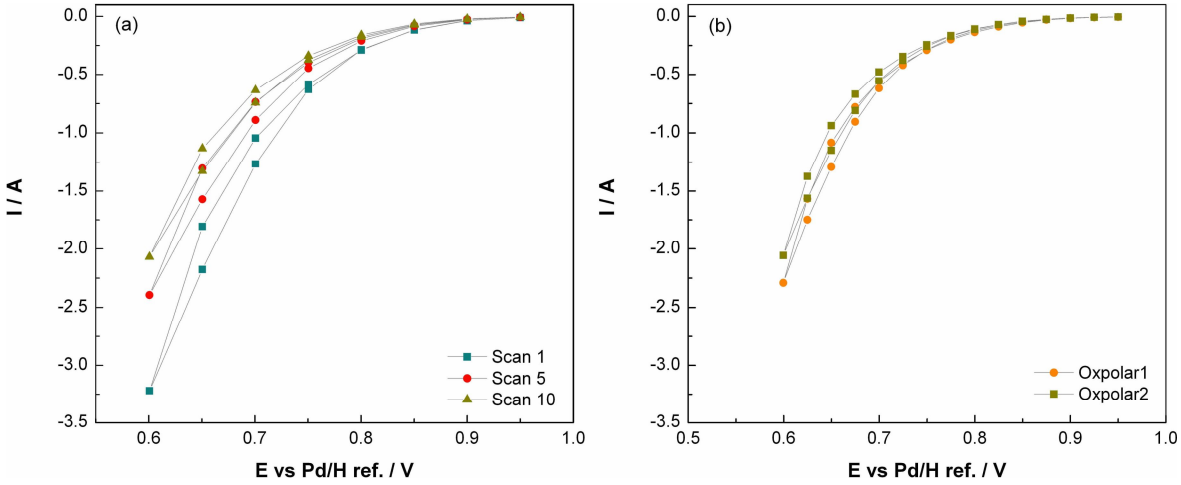

Figure 2- 21 Cell pre-conditioning with fast polarisation scans at a step potential of 50 mV per 5 s (a). Slow polarisation scans at a potential step of 50 mV per 30 s.

References

1. Z. Szafran, R. M. Pike and M. M. Singh, *Microscale Inorganic Chemistry: A Comprehensive Laboratory Experience*, p. 384, Wiley, New York (1991).

2. P. Canton, G. Fagherazzi, M. Battagliarin, F. Menegazzo, F. Pinna and N. Pernicone, *Langmuir*, **18**, 6530 (2002).

3. P. J. Goodhew, J. Humphreys and B. Richard, *Electron Microscopy And Analysis*, p. 254, Taylor & Francis; 3 edition (November 30, 2000), London & New York (2001).

4. L. Cervera Gontard, R. E. Dunin-Borkowski, D. Ozkaya, T. Hyde, P. A. Midgley and P. Ash, *Journal of Physics: Conference Series*, **26**, 367 (2006).

5. D. Ozkaya, *Platinum Metals Review*, **52**, 61 (2008).

6. N. Tanaka, *Science and Technology of Advanced Materials*, **9** (2008).

7. C. B. Boss and K. J. Fredeen, *Concepts, Instrumentation and Techniques in Inductively Coupled Plasma Optical Emission Spectrometry*, p. 125, Perkin Elmer, U.S. (2004).

8. F. Jalilehvand, http://www.chem.ucalgary.ca/research/groups/faridehj/xas.pdf.

9. J. A. van Bokhoven, T. Ressler, F. M. F. de Groot and G. Knopp-Gericke, *In-Situ Spectroscopy of Catalysts*, American Scientific Publishers (2004).

10. D. E. Sayers, E. A. Stern and F. W. Lytle, *Physical Review Letters*, **27**, 1204 (1971).

11. M. Newville, in *Consortium for Advanced Radiation Sources*, University of Chicago (2004).

12. P. A. Christensen and A. Hamnett, *Techniques and mechanisms in electrochemistry*, p. 396, Springer (1994).

13. F. G. Will, *Journal of the Electrochemical Society*, **112**, 451 (1965).

14. D. R. Lowde, J. O. Williams and B. D. McNicol, *Applied Surface Science*, **1**, 215 (1978).

15. A. L. Bard and L. R. Faulkner, in *Electrochemical methods - Fundamentals and Applications*, p. 331, John Wiley & Sons (2001).

16. C. G. Zoski, in *Handbook of Electrochemistry*, C. G. Zoski Editor, p. 451, Elsevier (2007).

CHAPTER 3

UNDERSTANDING THE MECHANISM OF THE CONTROLLED SURFACE REACTION FOR THE PREPARATION OF CORE-SHELL ELECTROCATALYSTS

CHAPTER 3: Understanding of the mechanism of the Controlled Surface Reaction (CSR) for the preparation of core-shell electrocatalysts

3.1. Introduction

To precisely control the preparation of the Pt/Pd core-shell materials, it is necessary to understand the reaction pathway during the hydrogenolysis of $Pt(acac)_2$ in the vicinity of the reduced Pd surface. This chapter is dedicated to the study of the mechanism of the CSR used to prepare carbon-supported Pt/Pd core-shell catalysts, from the decomposition of $Pt(acac)_2$ to the Pt shell formation.

This chapter will try to determine whether the reaction between $Pt(acac)_2$ and Pd/C proceeds via stepwise hydrogenolysis of the acetylacetonate (acac) ligands or simultaneous hydrogenolysis of both ligands. The following final products can be envisaged:

(1) Pt organometallic fragments are coordinated to the surface Pd atoms, or

(2) Pt organometallic fragments are completely decomposed into Pt "adatoms", which are then incorporated onto the Pd surface.

(3) Applicable if situation (2) occurs; Pt organometallic fragments are coordinated to previously deposited Pt atoms

$Pt^{II}(acac)_2$ could be fully hydrogenolysed using two Pd-H sites (reaction 3-1). Another possibility is first the formation of Pd-Pt-acac, which is then further reduced to Pd-Pt + acacH by H_2 (reaction 3-2).

$$Pt(acac)_2 + 2Pd_S - H \rightarrow Pt - Pd_2 + 2acacH \quad \textbf{(3- 1)}$$

$$2Pt(acac)_2 + 2Pd_S - H \rightarrow 2Pd - Pt - acac + 2acacH \xrightarrow{H_2} 2Pd - Pt + 4acacH \quad \textbf{(3- 2)}$$

To understand how the reaction proceeds, the parameters of the reaction were varied and the reaction products were monitored by gas chromatography and UV-visible spectroscopy. The results will be discussed in Section 3.2. Evidence of the Pt shell formation is given in Section 3.3 using XRD, cyclic voltammetry, aberration-corrected

STEM, and EXAFS analyses. Finally, the study was supported by a comparison with acarbon-supported PtPd/C alloy of same composition.

3.2. Mechanism of the CSR

3.2.1. Change of reaction parameters

To understand the nature of the reaction between $Pt(acac)_2$ and Pd-H sites, the effect of the key parameters of the CSR were evaluated one at a time. Four carbon supported Pt/Pd core-shell catalysts were prepared by CSR (described in Section 2) using the same Pd/C core. The importance of the temperature, the hydrogen atmosphere, the Pd sites on which hydrogen was preadsorbed and the nature of the Pt precursor compound were examined (Table 3- 1).

- Experiment 1 aimed to determine the stoichiometry of the reaction between the Pd-H and $Pt(acac)_2$ as indicated in reactions 3-1 and 3-2. If the final catalyst has a composition of Pd_2Pt, then mechanism 3-1 would be indicated. A final product with Pd_1Pt_1 would suggest formation of a Pt-acac fragment on the Pd surface.

2 g 18% Pd/C (Pd dispersion of 49%) were loaded in the vessel and reduced at 200 °C for 30 min by flowing H_2. 0.67 g $Pt(acac)_2$ (equivalence of one Pt monolayer) were diluted in 300 mL toluene and dearated in the dropper. The precursor was then transferred to the vessel and the mixture was stirred and heated at 90 °C for 6 hr under N_2 flow. 6 hr were sufficient to reach the completion of the reaction.

- Experiment 2 explores if the pre-reduction of the Pd core is necessary before introducing flowing H_2 to generate sites for the reduction of $Pt(acac)_2$.

As described previously, 2 g of the same 18% Pd/C were loaded in the vessel and N_2 was flowed to remove the air. 0.67 g $Pt(acac)_2$ were diluted in 300 mL toluene and dearated in the dropper. The precursor was then transferred to the vessel and the mixture was stirred and heated at 90 °C for 6 hr under H_2 flow.

- Experiment 3 aimed to determine the effect of temperature on the reaction.

2 g of the same 18% Pd/C were loaded in the vessel and reduced at 200 °C for 30 min by flowing H_2. 0.67 g $Pt(acac)_2$ were diluted in 300 mL toluene and dearated in the dropper.

The precursor was then transferred to the vessel and the mixture was stirred at room temperature for 6 h under H_2 flow.

- In Experiment 4, the Pt precursor was changed to dimethyl(1,5-cyclooctadiene) platinum (II) ($Pt(COD)Me_2$) (Figure 3-1). This choice was based on the fact that this precursor was expected to be more reactive than $Pt(acac)_2$. It contains COD, which is a labile ligand, and should be easily hydrogenolysed during the reaction. The methyl ligands, although more strongly bonded to the metal may form methane under the reducing conditions of the CSR. In contrast, $Pt^{II}(acac)_2$ forms two six-membered chelated rings, which should make it more stable.

2 g of 18% Pd/C were loaded in the vessel and reduced at 200 °C for 30 min by flowing H_2. 0.58 g $Pt(COD)Me_2$ were diluted in 300 mL toluene and dearated in the dropper. The precursor was then transferred to the vessel and the mixture was stirred and heated at 90 °C for 6 h under H_2 flow.

As a control experiment, $Pt(acac)_2$ was reacted with the carbon support only in the presence of flowing H_2. A qualitative assessment indicated no $Pt(acac)_2$ reduction had occurred, confirming that $Pt(acac)_2$ reduces exclusively in the presence of Pd particles.

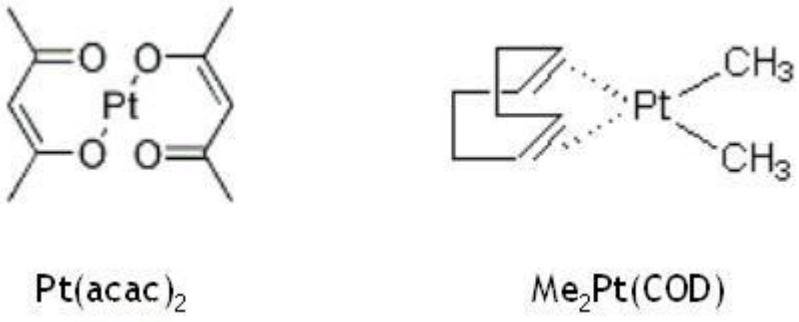

Figure 3 - 1 Pt precursor compounds used in CSR reaction to deposit Pt.

Table 3- 1 Parameters of CSR evaluated.

Experiment	Pd-H[a]	H_2[b]	Temperature[c]	Precursor[d]
1	√	X	90 °C	$Pt(acac)_2$
2	*X*	√	90 °C	$Pt(acac)_2$
3	√	√	20 °C	$Pt(acac)_2$
4	√	√	90 °C	$Pt(COD)Me_2$

[a] Pre-adsorption of hydrogen on Pd/C core performed (√) or not performed (X)
[b] Continuous hydrogen flow after addition of precursor (√) or no hydrogen flow (X)
[c] Temperature of the reaction after addition of precursor

The metal content in the filtrate of the reaction mixtures and in the resulting catalysts was determined by ICP (Table 3- 2).

The result of Experiment 1 presented in Table 3-2, showed that only half the $Pt(acac)_2$ reacted, under nitrogen, with the Pd surface on which hydrogen had been preadsorbed. This suggests that two Pd-H sites are needed to fully reduce one molecule of $Pt(acac)_2$, which agrees with the oxidation state of Pt in the compound. No Pt deposition on Pt could occur since no Pt-H sites were formed.

The result of Experiment 2 showed that the pre-formation of Pd-H sites before the addition of the precursor is not a prerequisite condition for the complete decomposition of $Pt(acac)_2$. In the presence of a continuous hydrogen flow, new Pd-H sites can constantly be created and are thus available for the $Pt(acac)_2$ decomposition. In addition, once Pt(0) has been deposited on the Pd surface, it is possible that, in the presence of H_2, the Pt itself may become a site at which $Pt(acac)_2$ then reacts.

Experiment 3 gave a similar outcome to Experiment 1. This indicates that it was primarily the preadsorbed hydrogen that participated in the reaction on the Pd surface despite being carried out under constant hydrogen flow. Examination of the Temperature-Programmed Reduction plot in Figure 3-2 shows that the reduction of Pd/C starts around 35 °C. This suggests that the temperature may have been too low to allow the formation of a significant number of new Pd-H sites.

The use of $Pt(COD)Me_2$ instead of $Pt(acac)_2$ under the same conditions gave the same metal composition of the catalysts, indicating that the reactivities of $Pt(acac)_2$ and $Pt(COD)Me_2$ were similar. Exploring the effect of the precursor at lower temperature would be an interesting experiment to provide further differentiation.

Table 3- 2 Results of the four CSR experiments as described in Table 3-1

Experiment	Evaluated parameter	Remaining Pt in filtrate / ppm	% Non-deposited Pt	Pt assay in catalyst / wt %
1	H_2 flow	800	51	7.61
2	Pd-H	0.6	0	13.3
3	Temperature	960	56	6.59
4	Precursor	0.8	0	13.3

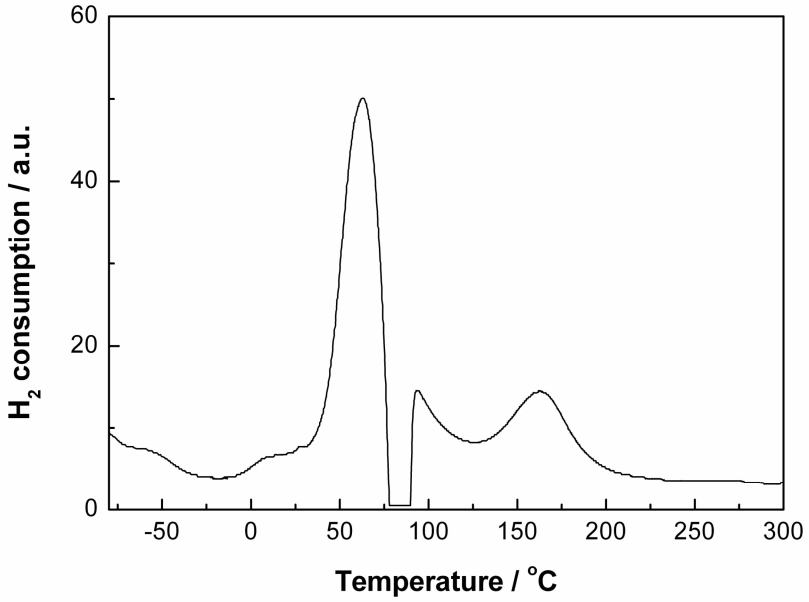

Figure 3 - 2 H_2-TPR 20%Pd/C.

3.2.2. Identification of the $Pt(acac)_2$ decomposition products

Gas chromatography was used to identify the main decomposition products of $Pt(acac)_2$ at different times during the CSR. For this experiment, the GC chromatograph was equipped with a capillary column CP-WAX52 (50 m x 0.53 mm x 2 m) and the oven was set at 170 ^oC. The main products of $Pt(acac)_2$ decomposition are likely to be acetylacetone, acetone and ethanol since the reaction was carried out under hydrogen. Acetone may be further reduced forming isopropanol. Prior to the analysis of the reaction mixture, pure samples of the possible products of $Pt(acac)_2$ decomposition were diluted in toluene, the

reaction solvent and identified by GC. The retention times obtained for these reference compounds are listed in Table 3-3. The chromatograms of the quenched and diluted reaction mixtures are shown in Figure 3-3 and peak areas are given in Table 3-4. As for most acetylacetonate complexes, the main decomposition products of $Pt(acac)_2$ were acetone and acetylacetone (acacH) (3). Although acetone was not the only product from the reduction of acetylacetone, it was the only species detected and identified by GC. The formation of acetone suggests that total hydrogenation had occurred although this might be subsequent to the deposition of the platinum. This is consistent with the fact that the reaction was carried out under flowing hydrogen.

Acetone and acetylacetone appeared simultaneously after 20 min of reaction time. The amount of acetylacetone increased slowly from 20 min to 1 h and then decreased. This was accompanied by a rapid increase of the level of acetone in the reaction mixture. This suggests that the rate of decomposition of acetylacetone into acetone is slower than the rate of formation of acetylacetone. As shown in Table 3-4, ethanol was detected at t = 0, before $Pt(acac)_2$ was added in the vessel. It is more likely that ethanol was present as an impurity in toluene and was not a decomposition product since it was not detected in the subsequent reaction samples.

Table 3- 3 Retention time for possible decomposition products

	Ethanol	**Isopropanol**	**Acetone**	**Acetylacetone**	**Toluene**
Retention time / min	2.78	2.95	2.71	3.94	3.11

Although no decomposition products were detected by GC before 20 min during which the $Pt(acac)_2$ level in solution was decreasing, acetylacetone and acetone may have been present but at such low levels that they were not detectable by the GC.

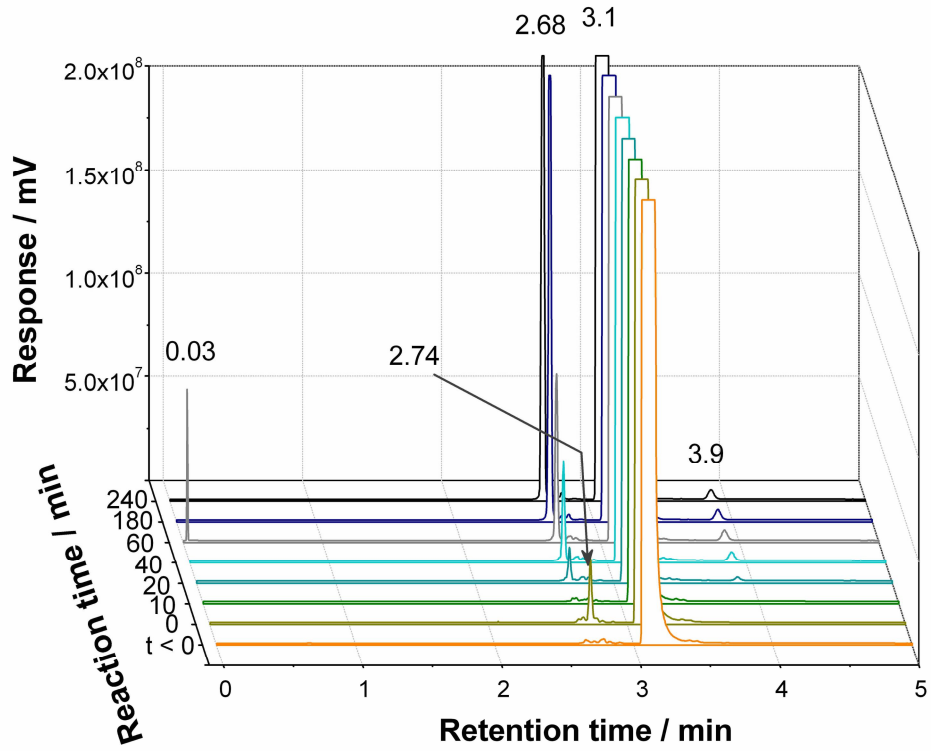

Figure 3 - 3 Evolution of the reaction mixture composition during the reaction as formed by GC. Retention times are identified in Table 3-3.

Table 3- 4 Peak areas of the compounds present in the reaction mixture.

		Unknown	Acetone	Ethanol	Toluene	Acetylacetone
		0.03 min	2.68 min	2.74 min	3.1 min	3.9 min
Reaction time / min	0	0	0	2.84	97.16	0
	10	0	0	0.1	99.9	0
	20	0	1.56	0	98.1	0.33
	40	0	4.05	0	95.19	0.76
	60	2.12	6.27	0	90.78	0.84
	180	0	18.06	0	81.19	0.75
	240	0	19.96	0	79.35	0.68

3.2.3. Kinetics of $Pt(acac)_2$ decomposition

The kinetics of $Pt(acac)_2$ decomposition were followed by UV-visible spectroscopy. To achieve this, about 5 ml of the reaction mixture was withdrawn at various times during the core-shell synthesis and the reaction quenched by cooling the sample in ice. The carbon

was separated from the liquid by filtration. To avoid saturation of the transmitted signal in the spectroscopic analysis, the solutions were diluted 100 times with toluene. The reaction kinetics were derived from the $Pt(acac)_2$ absorbance at 344 nm, which is characteristic of $Pt(acac)_2$ in toluene. The spectra were recorded between 200 and 500 nm using a spectrometer in transmission mode. The samples are shown in Figure 3-4.

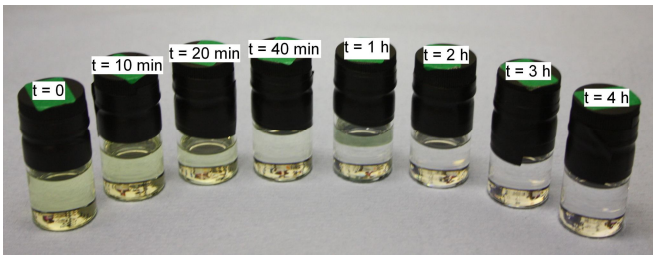

Figure 3 - 4 Filtrates withdrawn from the reaction mixture at 0, 10, 20, 40, 60, 120, 180, 240 min.

From the GC studies, the principle products of the reaction were acetylacetone and acetone. The UV spectrum obtained for $Pt(acac)_2$ in toluene (Figure 3-5) is in agreement with that published by Womes et al (1). It contains two main absorption bands with maxima at 292 nm, 344 nm and a shoulder around 400 nm, the peak at 344 nm is attributed to an intraligand $\pi \rightarrow \pi^*$ transitions (2). The absorption band at 292 nm coincides with that of pure acetylacetone and is assigned to the acac-ligands. The peak arising from the $Pt(acac)_2$ component of the spectrum decreased significantly within the first 10 mins of the reaction as shown in Figure 3-6. The absorption band at 280 - 310 nm sharpened at 284 nm, while the absorption band at 341 nm disappeared in less than 1 h. This may be explained by the decomposition of $Pt(acac)_2$ and the release of acacH ligands, which are readily decomposed to form acetone. The production of acetone is shown by the increase of the peak intensity at 284 nm.

The concentration of $Pt(acac)_2$ in Figure 3-7 was determined from the intensity of the peak at 344 nm from Figure 3-6. It can be seen that at t = 40 min, about 90 % of the precursor had reacted. Kinetics for the reaction between $Pt(acac)_2$ and a pre-reduced metal surface on this timescale was also observed by M. Womes, for which the process of $Pt(acac)_2$ decomposition on reduced platinum was complete within half an hour (1).

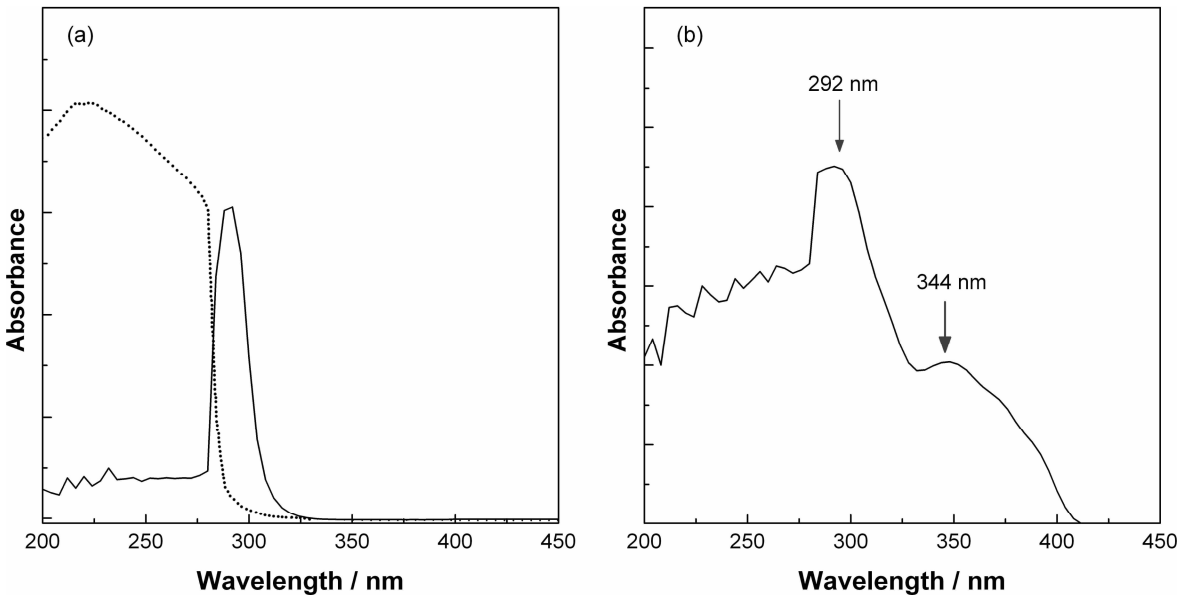

Figure 3 - 5 UV spectra for (a) toluene (dotted line) and acetylacetone diluted in toluene (solid line) and (b) for $Pt(acac)_2$ dissolved in toluene.

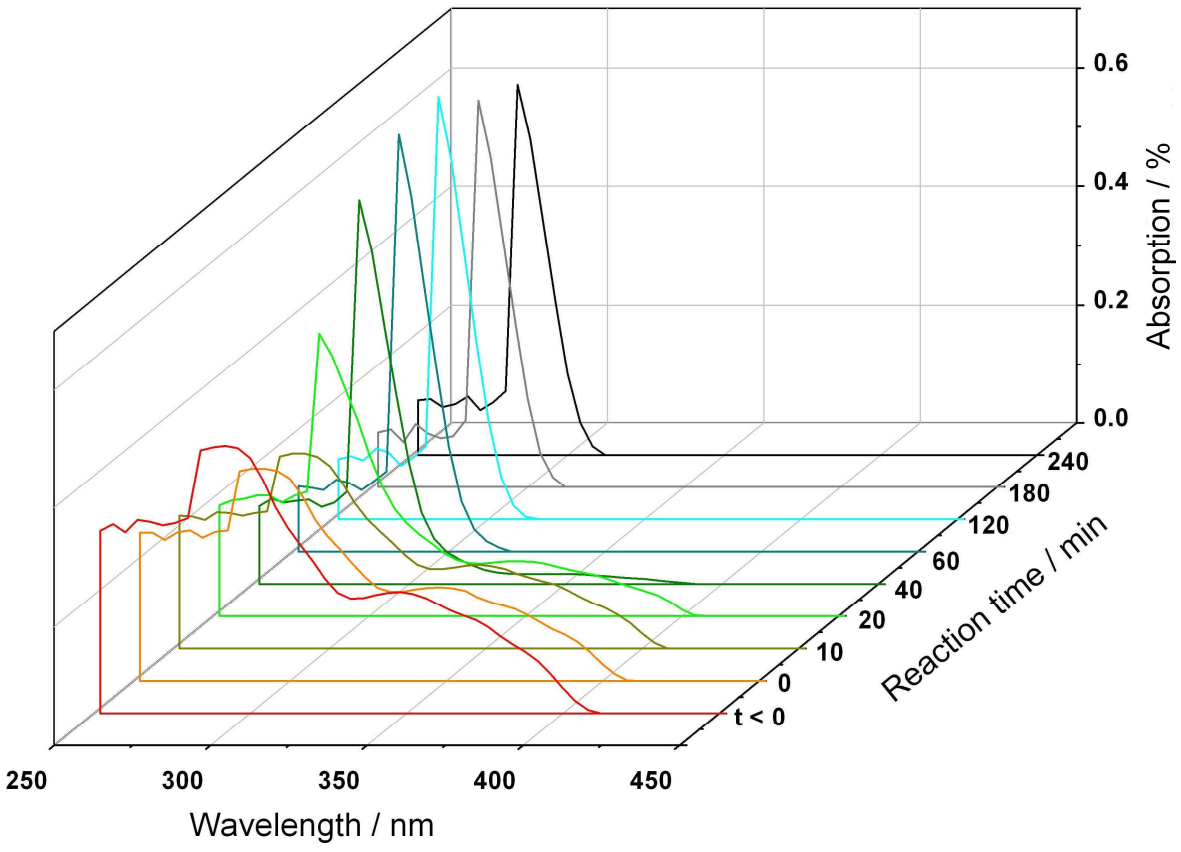

Figure 3 - 6 UV spectra following the CSR reaction between Pd/C and $Pt(acac)_2$ as a function of time.

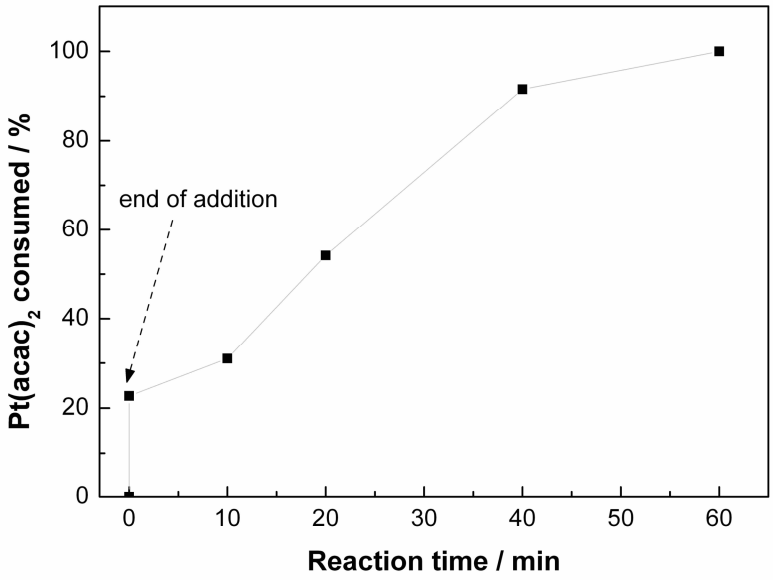

Figure 3 - 7 Consumption of $Pt(acac)_2$ during CSR. The reaction time t = 0 corresponds to the end of the precursor addition to the vessel.

3.3. Characterisation of the Pt shell. Comparison between the alloy and core-shell structure

3.3.1. Catalysts studied

To find the evidence for the Pt shell formation, a carbon-supported core-shell catalyst was compared with a carbon-supported PtPd alloy of the same composition. Both materials were prepared using the CSR synthetic method. Prior to the preparation of the core-shell, the Pd core particles were annealed at 600 °C in $10\%H_2/90\%N_2$. An amount of Pt precursor equivalent to two Pt monolayers was then deposited onto the large Pd core particles. To form the alloy, the Pt was deposited onto a non-sintered Pd core and annealed at 850 ^oC for 3 h in $10\%H_2/90\%N_2$ atmosphere to ensure complete mixing of the Pt and Pd components (5). Physical characterisation data are shown in Table 3-5.

Table 3- 5 Physical characterisation data for Pt/Pd/C core-shell and PtPd/C alloy.

Catalyst	Pd core		Heat treatment	Pt:Pd atomic ratio
	TEM size / nm	Dispersion* / %		
Core-shell	10.5	18.6	100 ^{o}C in H_2	25.5 : 74.5
Alloy	3	43	850 ^{o}C in H_2	26.6 : 73.4

* measured by CO chemisorption

3.3.2. XRD analysis

The XRD diffraction patterns of Pd/C, the Pt/Pd/C core-shell and PtPd/C alloy electrocatalysts are shown in Figures 3-8(a), (b) and (c), respectively. The crystallite sizes and the lattice parameters of the identified phases are presented in Table 3-6.

Face-centered cubic (fcc) Pd is characterised by peaks at 40.11° (111), 46.66° (200) and 68.12° (220). As the carbon contribution to the signal interferes least with the (220) peak, it is appropriate to use this peak to determine the crystallite size of the Pd core using the Debye-Scherrer equation (Section 2, equation 2-6). The (220) peak for the core-shell was analysed by the Rietveld method and was best described by the presence of two cubic phases with lattice parameters of 3.92 Å and 3.90 Å (Figure 3-9). These phases were attributed to Pt [a = 3.9231 Å] and Pd [a = 3.8902 Å]. A mean crystallite size of 9.7 nm was calculated for the Pd phase. Figure 3-10 shows an expanded view of the (220) peak for Pd/C core and Pt/Pd/C core-shell. The slight negative shift of the core-shell (220) peak (67.95°) relative to that of Pd/C (68.12°) suggests an expansion of the Pd lattice parameter at the core/shell interface due to the larger size of the Pt atoms (6).

The crystallite size of the PtPd alloy was found to be 3 nm, which is only slightly larger than the crystallite size of the Pd core used (about 2 nm). Surprisingly, no significant growth in the alloy crystallite size was observed after annealing at 800 °C. From the lattice parameter (3.896 Å) the Pt:Pd atomic composition can be calculated using a polynomial fit of combined data of PtPd alloys of various compositions (7).

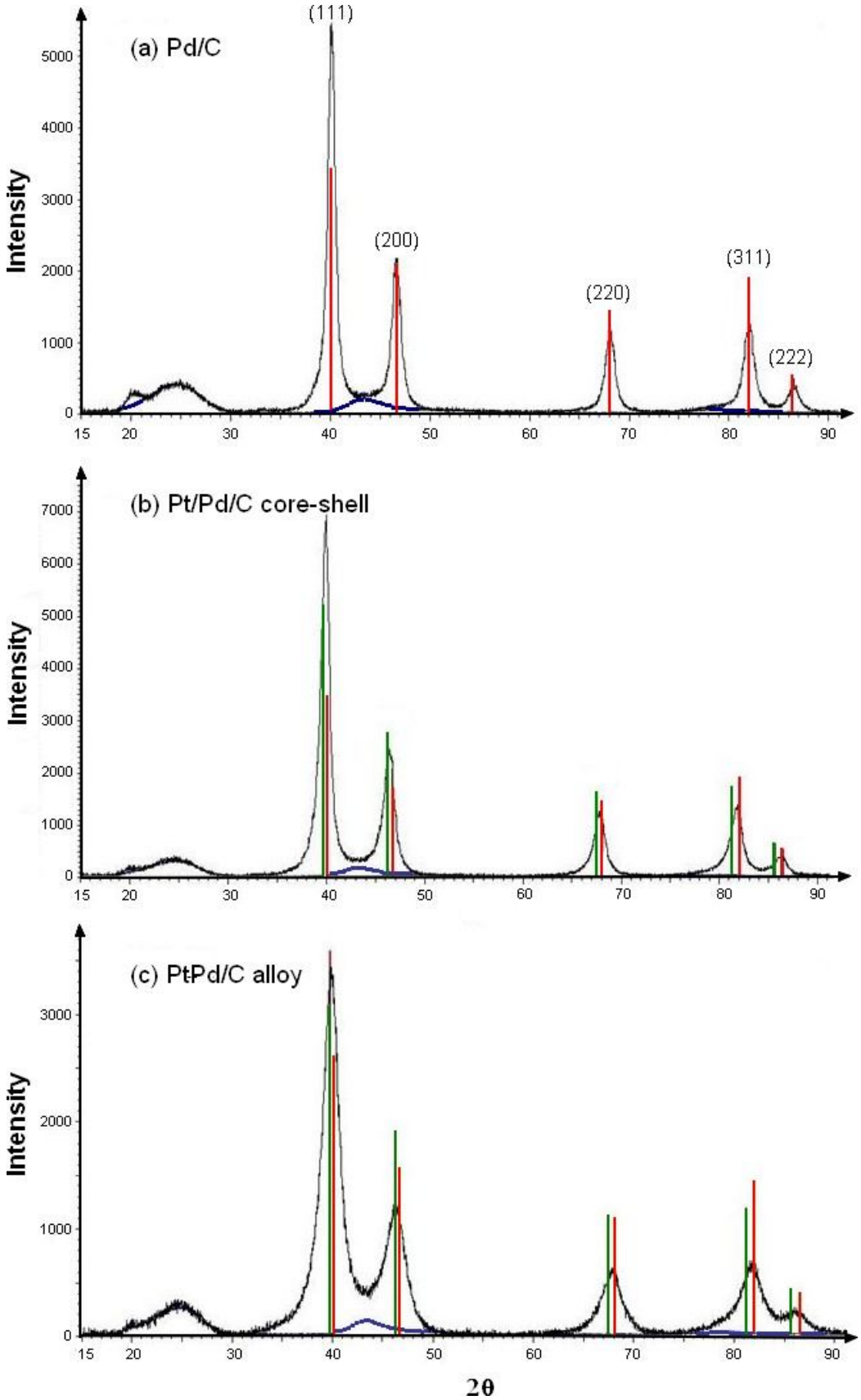

Figure 3 - 8 XRD patterns for Pd/C core catalyst (a), the Pt/Pd/C core-shell catalyst (b) and the PtPd/C alloy. The red and green lines represent the documented diffraction peaks of Palladium and Platinum respectively. The blue pattern is the contribution of the carbon support.

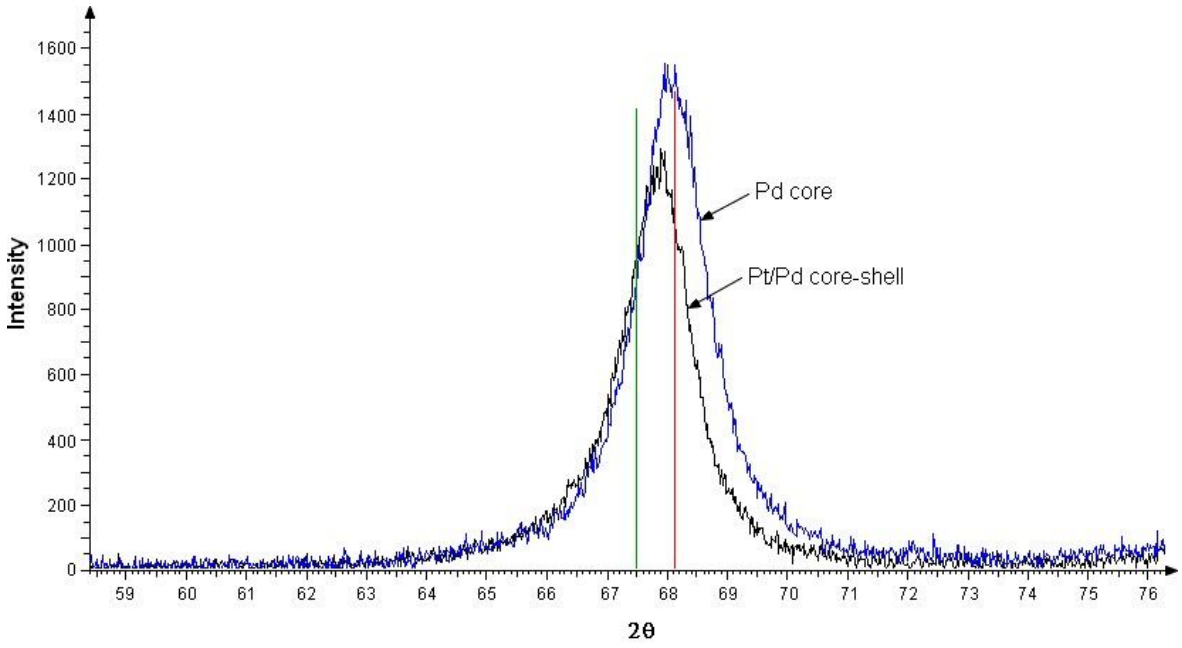

Figure 3 - 9 Representation of (220) diffraction for the Pd core and the Pt/Pd core-shell.

Table 3- 6 XRD parameters

	Phases	Crystallite size / nm	Lattice parameter / Å
Pd	-	-	3.890
Pt	-	-	3.923
Pd/C	Pd	5.3	3.890
Pt/Pd core-shell	Pd	9.7	3.900
Pt/Pd alloy	PtPd	3.0	3.896

3.3.3. Aberration-corrected STEM

The use of STEM enables the observation of the Pt shell in the bright field mode due to the Z-contrast between Pt and Pd. Aberration corrected STEM images of Pt/Pd core-shell particles are shown in Figure 3-11. The micrographs of the same core-shell nanoparticles can also be seen in Figure 3-12(a). The red line corresponds to the scanned region and the total emission signal, measured in counts, is plotted with respect to the scanned distance and is shown in Figure 3-12(b). The variation of the EDX signals specific to Pt and Pd across the particles is presented in Figure 3-12(d). As the counts emitted by an element are proportional to the amount of this element, the EDX line profile is a reliable way for

determining particle structures, provided that the element emission energies are sufficiently far apart. In Figure 3-12(c), the counts for all the emission energies at the position P are shown. It can be seen that the EDX profiles of the Pt/Pd core-shell (Figure 3-12(b)) and the Pt-Pd alloy (Figure 3-13(b)) were derived from the variation of the intensity of the Pt $M_{\alpha 1}$ (2.05 keV) and Pd $L_{\alpha 1}$ (2.84 keV) emission lines.

Figure 3-10 shows the EDX profiles expected for a core-shell particle with a complete and uniform shell and a well-alloyed particle. The shell element signal should be more intense at the edges due to the higher proportion of this element at those points. In contrast to the shell element, the core element EDX profile should not vary much across the particle. In the profile obtained for an alloy catalyst, both element signals follow each other since the elements are randomly distributed.

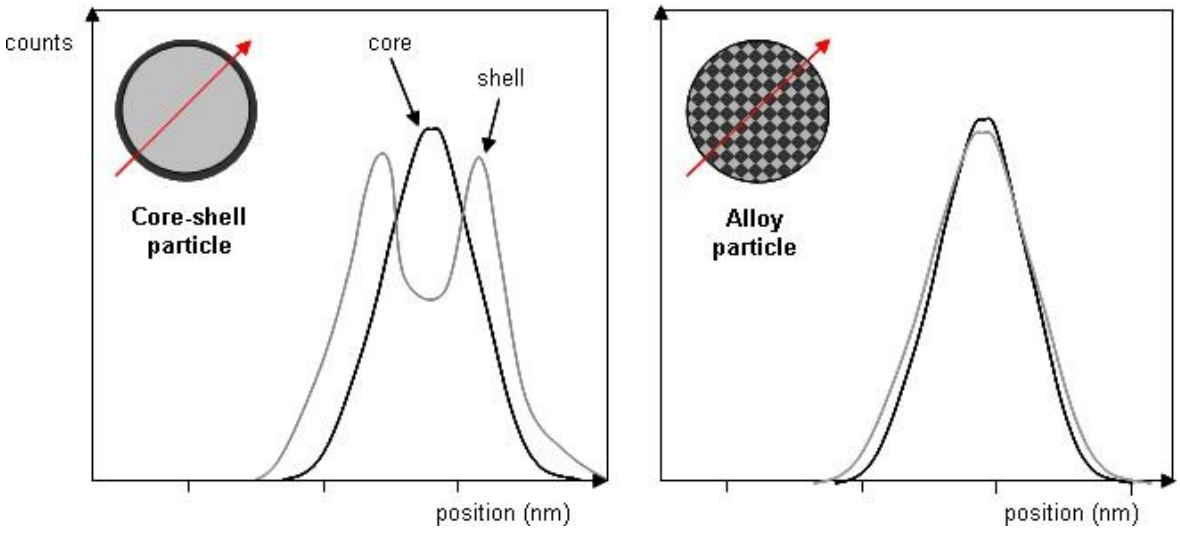

Figure 3 - 10 Models of the EDX line profile for core-shell and alloy particles along red scan line, as depicted in Figures 3-12 and 3-13.

For the core-shell particles, the relative intensities of the Pt and Pd signals along the scan line confirmed the presence of a Pt rich region on the outside of the Pd particles. However, it can be seen on the micrograph that the Pd core is not completely covered by the Pt shell. In fact, the Pt signal decreases to the noise level between 3 and 5 nm and between 10 and 15 nm indicating a discontinuity in the Pt shell. As the intensity of the Pt peaks at around 1, 6 and 16 nm is just a few counts higher than the noise level, it is possible that the real Pt contribution to the signal is lower than what is observed. The

determination of the width of the main Pt peaks at half height indicated that the Pt shell was approximately 1.8 nm thick, which is equivalent to 3.2 atomic layers of Pt, whereas 2 Pt atomic layers were expected. In contrast, the Pt and Pd EDX profiles of the alloy particles followed each other, indicating statistical distribution of both elements.

The above observations suggest that there may have been accumulation of Pt on some areas of the Pd surface during the formation of the shell. Both H-Pt and H-Pd sites could have been formed during the reaction. However, the difference in energy between Pd-H and Pt-H bonds is not significant enough to conclude that there is a preferential site for the precursor reduction (8). In Figure 3-13, it can be seen that the Pt shell is thicker on the small cores than on the large cores. It is also clearly visible that some areas are not covered with Pt. The apparent selective deposition of the Pt suggests Pt may deposit preferentially on the edges and corners of the Pd particles as demonstrated by Coq et al. for the deposition of germanium on rhodium (9). The same observation was made for the deposition of tin on rhodium (10). The difference with the Pt-Pd system is that tin and germanium stacks can not form as they can not adsorb hydrogen. The fact that a complete coverage was not obtained with an equivalent of two Pt monolayers implies that Pt built up around the low coordination sites of the Pd core. A representation of the structure of the obtained Pt/Pd core-shell particles is shown in Figure 3-16.

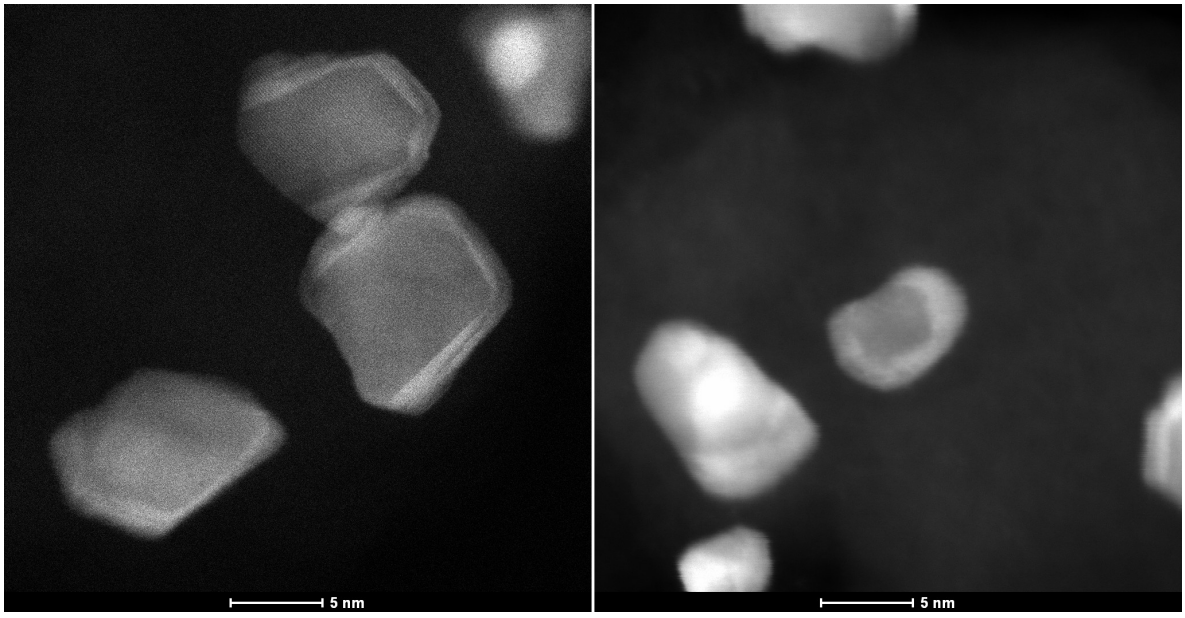

Figure 3 - 11 Aberration corrected STEM images of Pt/Pd/C core-shell.

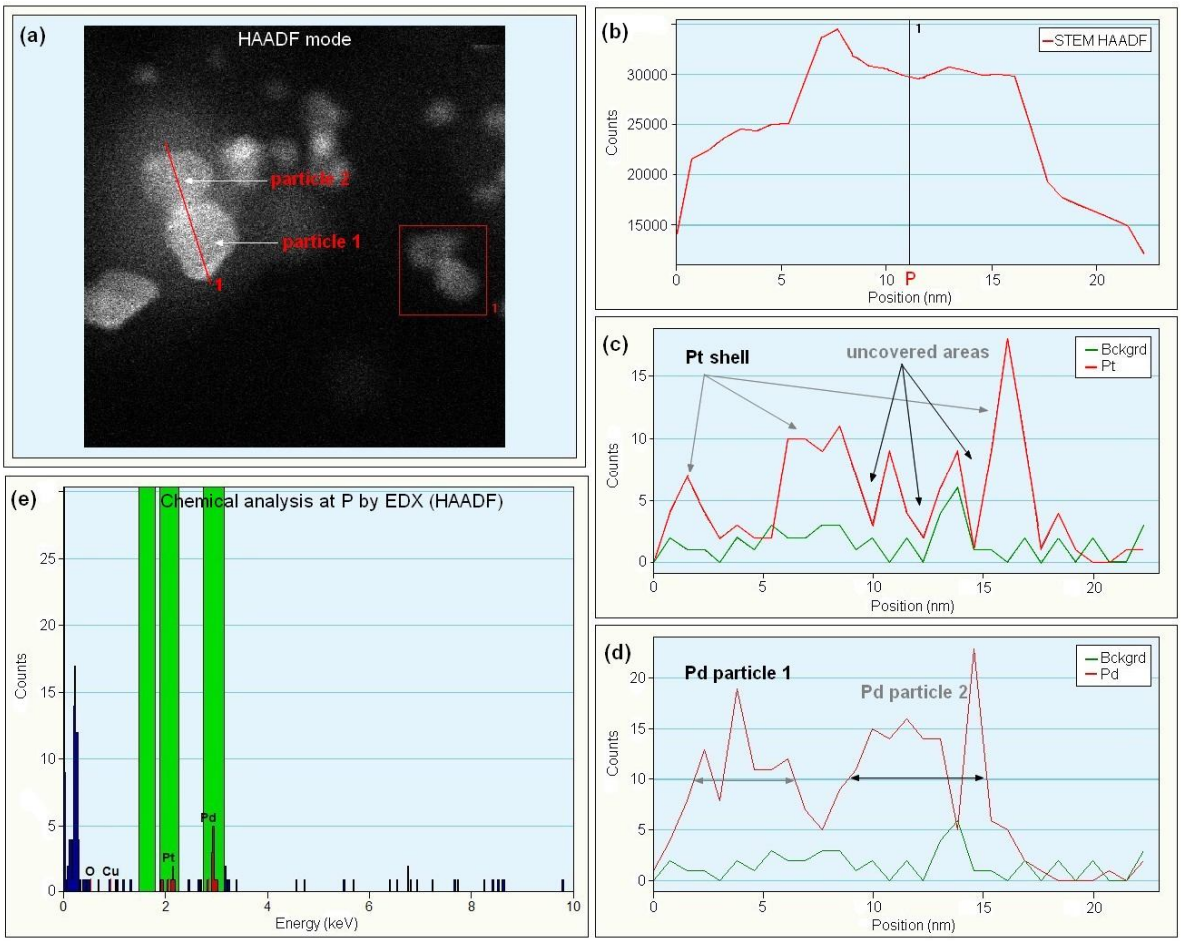

Figure 3 - 12 (a) HRTEM micrographs of Pt/Pd core-shell particles in bright field. (b) EDX sum profile across two core-shell particles following the red line in picture (a). (c) Chemical analysis at position P. (d) EDX Pt and Pd profiles across the two core-shell particles.

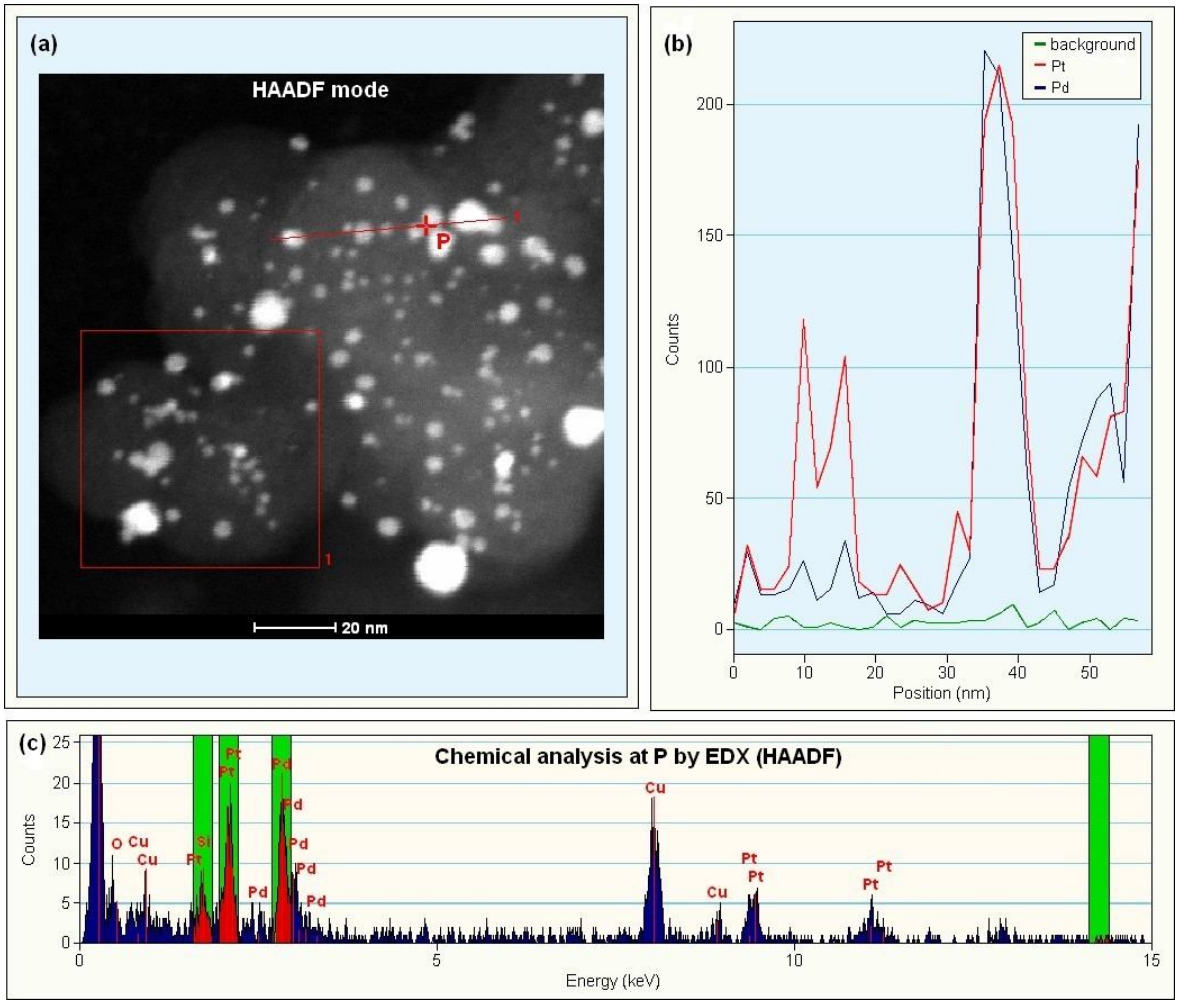

Figure 3 - 13 (a) HRTEM micrographs of Pt-Pd alloy particles in bright field. (b) EDX Pt and Pd profiles across the alloy particles following the red line in picture (a). (c) Chemical analysis at position P.

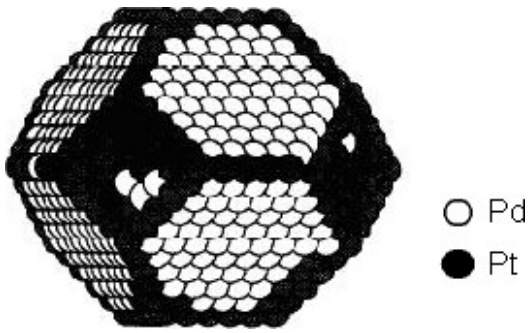

Figure 3 - 14 Representation of a cubooctahedral Pd particle covered with Pt only at the corners and edges.

3.3.4. EXAFS analysis

To further validate the core-shell structure of the synthesized Pt-Pd nanoparticles, EXAFS analyses were performed. For comparison, a well alloyed Pt-Pd catalyst was also examined by EXAFS. The core-shell structure of the Pt-Pd nanoparticles is supported by the analysis of the Fourier transforms (FTs) of the EXAFS spectra shown in Figure 3-17 and Figure 3-18. The presence of Pd and Pt at the Pt L_{III} edge confirmed that Pt was co-located with Pd. Pt-only nanoparticles show a symmetric FT peak at 2.75 Å (11), while this FT peak is split into two peaks around 2.9 Å and 2.3-2.4 Å for the Pt-Pd/C core-shell and alloy nanoparticles. These FT peak features suggest that the first shell around the central Pt atom includes two different kinds of neighbouring atoms (12).

Examination of the fitting parameters for first shell-neighbours in Table 3- 7, shows that the Pt atoms (on average) are in a more Pt rich environment than would be expected from the elemental composition of the catalyst (N(Pt):N(Pd) = 4.7:1 compared to the predicted 0.35:1). Such coordination numbers are consistent with the formation of a core-shell structure rather than a well-mixed alloy with some clustering of the Pt atoms in the shell as indicated by the HRTEM images shown in Figure 3 - 12 and Figure 3 – 12 (13). In contrast, the PtPd/C alloy coordination environment of Pt is equally made of Pt and Pd.

The acquisition of data at the Pd edge could have provided more information about the geometric effect of the Pt shell on the Pd lattice (Pd-Pd distances) and the presence of Pd atoms at the surface (14). But due to the lack of beamtime, this experiment was not performed. The Pt-Pd bond distance was expected to be slightly contracted due to the small lattice parameter mismatch existing between Pt and Pd. The Pt-Pt bond distances appeared slightly smaller for both catalysts than the Pt-Pd distances. For example, there is difference of almost 0.02 Å between Pt-Pt and Pt-Pd distances in the core-shell. This suggests that the Pt shell is not pseudomorphic to the Pd core.

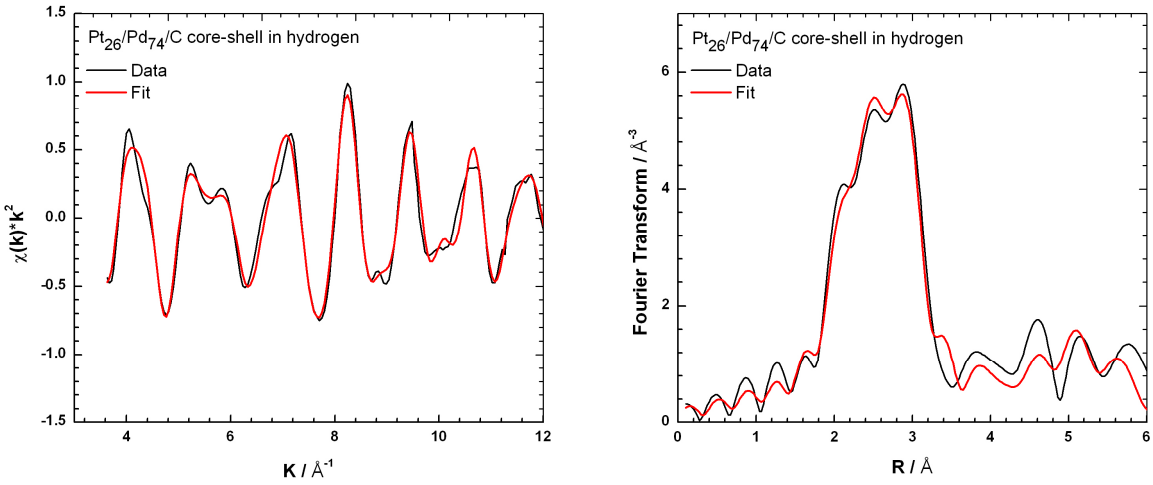

Figure 3 - 15 Pt/Pd core-shell: k^2-weighed $\chi(k)$ spectrum collected at Pt L_{III} edge obtained in H_2 atmosphere; (right) k^2-weighed Fourier transform of the $\chi(k)$ data.

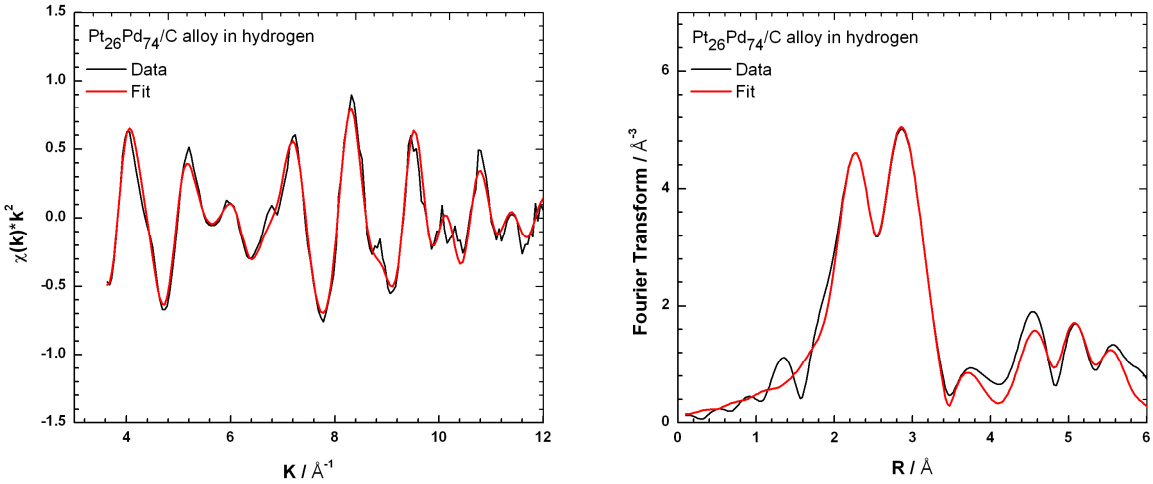

Figure 3 - 16 Pt-Pd alloy: k^2-weighed $\chi(k)$ spectrum collected at Pt L_{III} edge obtained in H_2 atmosphere; (right) k^2-weighed Fourier transform of the $\chi(k)$ data.

Table 3- 7 EXAFS fit parameters at Pt L_{III} absorption edge.

Catalysts	Coordination number	Distance / Å	Debye-Waller factor $2\sigma^2$ / $Å^2$	E_f / eV	R_{exafs} / %
Pt/Pd	Pt = 6.88 ± 0.54	2.76 ± 0.01	0.013 ± 0.002	-12.71 ± 1.47	21.0
core-shell	Pd = 1.45 ± 0.38	2.77 ± 0.02	0.014 ± 0.004		
PtPd	Pt = 3.82 ± 0.32	2.76 ± 0.01	0.012 ± 0.002	-11.64 ± 0.56	21.2
alloy	Pd = 3.31 ± 0.23	2.77 ± 0.01	0.014 ± 0.001		

3.3.5. CO electrooxidation voltammetry

The electrooxidation of a saturated monolayer of CO is a quick method to probe the surface composition of Pt:Pd bimetallic catalysts, as described in Chapter 2. Figure 3-19 shows the CO stripping voltammograms of the Pt-Pd alloy and Pt/Pd core-shell electrocatalysts along with a Pt-only and a Pd-only electrocatalysts for comparison.

It can be seen that the position of the peaks was intermediate between the CO peaks of Pt (632 mV) and Pd (834 mV) for both the core-shell and the alloy, which is evidence of the modification of Pd with Pt (15). The maxima of the core-shell and the alloy main CO peaks appeared at very close potentials, suggesting both structures lead to the same type of electronic interaction (16). The core-shell CV exhibited a single peak for the electrooxidation of CO. The absence of a shoulder or second peak at lower potentials for the core-shell CO peak suggested that there were no isolated Pt particles on the carbon support and that the Pt shell and the Pd core together behaved as one phase. In contrast, the alloy CV presented two CO peaks at 692 mV and 820 mV. The appearance of a second peak at a potential close to that of the Pd CO peak may result from Pd segregation during the thermal treatment. It is worth noticing that the potential of the oxide removal peak of the core-shell CV appears more positive than that of the alloy. This is indicative of the stronger Pt character of the core-shell surface.

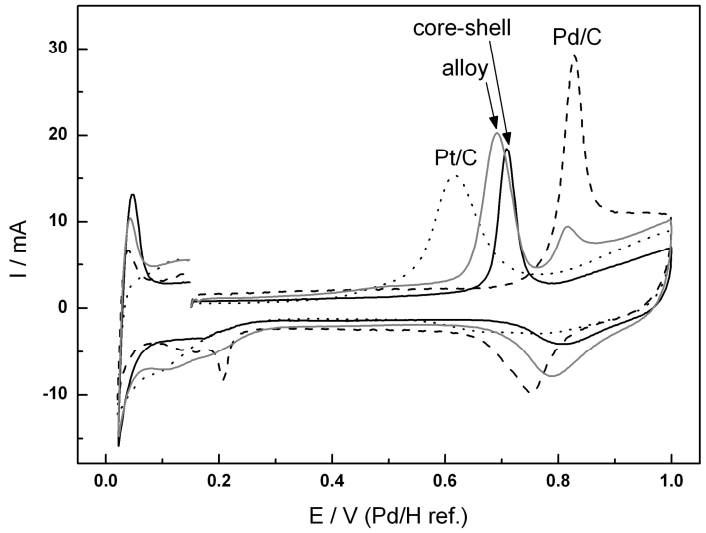

Figure 3 - 17 CV of carbon-supported Pt (dotted line), Pt_{26}/Pd_{74}/C core-shell (dark grey line), $Pt_{26}Pd_{74}$/C alloy (light grey line) and Pd (dashed line), after CO saturation, in 1 M H_2SO_4 at 80 °C. Scanning rate 10 mV s^{-1}, 0.01 - 1.0 V (Pd/H ref.).

3.4. Conclusions

In this chapter, the deposition mechanism of $Pt(acac)_2$ on carbon-supported Pd was investigated. The variation of the reaction parameters including monometallic catalyst preconditioning, gas atmosphere, temperature and Pt precursor compound were evaluated to determine how they influenced the outcome of the reaction. The interpretation of these results was supported by the GC and UV-visible analyses. The data suggests that the hydrogenolysis of $Pt(acac)_2$ on carbon-supported Pd is a rapid stepwise process, which leads to surface organometallic fragments that undergo complete hydrogenolysis to Pt. Under the CSR conditions employed, the deposition of one Pt monolayer occurs within one hour. The elevated temperature and the presence of a hydrogen atmosphere are necessary for the completion of the reaction to form one Pt monolayer, as these conditions are required for the constant formation of Pd-H sites. Without an elevated temperature and flowing hydrogen, only half a monolayer of Pt can be formed on the pre-formed Pd-H sites. It may be that in the absence of hydrogen flow, there are insufficient Pd-H sites present to fully reduce $Pt(acac)_2$.

The characterisation of the Pt shell by XRD, EXAFS, voltammetry and STEM confirmed the absence of isolated Pt clusters on the carbon support and differentiated the core-shell structure from that of an alloy. The extent of the Pt coverage was not quantified in this chapter but will be discussed in Chapters 4 and 5. However, the images obtained by aberration-corrected STEM clearly indicated Pt was localised on the outside of the Pd particles and also indicated the presence of uncovered Pd areas. The images strongly suggested that Pt deposited preferentially at the low-coordination sites of the Pd particles (edges, corners) and built up there before starting to cover the facets.

To conclude, the use of CSR to prepare Pt/Pd core-shell catalysts is an effective and promising route and gives some control over the Pt location. The availability of adsorbed H atoms seems to be the limiting factor in determining the Pt coverage.

References

1. M. Womes, T. Cholley, F. Le Peltier, S. Morin, B. Didillon and N. Szydlowski-Schildknecht, *Applied Catalysis a-General*, **283**, 9 (2005).

2. F. D. Lewis, G. D. Salvi, D. R. Kanis and M. A. Ratner, *Inorganic Chemistry*, **32**, 1251 (1993).

3. J. Von Hoene, R. G. Charles and W. M. Hickam, *Journal of Physical Chemistry*, **62**, 1198 (1958).

4. Y. Qian, Preparation of Pt-based Bimetallic Catalysts for the Oxygen Reduction Reaction in PEM Fuel Cells, in *Department of Chemistry*, Open University, Milton Keynes (2004).

5. H. Okamoto, *Journal of Phase Equilibria*, **12**, 617 (1991).

6. J. H. Yang, J. Y. Lee, Q. B. Zhang, W. J. Zhou and Z. L. Liu, *Journal of the Electrochemical Society*, **155**, B776 (2008).

7. I. Moysana, V. Paul-Boncourb, T. S., E. Sciorac, J. M. Fournierd, R. Cortese, S. Bourgeois and A. Percheron-Guégan, *Journal of Alloys and Compounds*, **322**, 14 (2001).

8. R. R. Squires, *Journal of the American Chemical Society*, **107**, 4385 (1985).

9. A. G. Bernard Coq, Touria Tazi, Francois Figueras, Dennis R. Salahub, *Journal of the American Chemical Society*, **113**, 1485 (1991).

10. J.-P. Candy, B. Didillon, E. L. Smith, T. B. Shay and J.-M. Basset, *Journal of Molecular Catalysis*, **86**, 179 (1994).

11. A. E. Russell, S. Maniguet, R. J. Mathew, J. Yao, M. A. Roberts and D. Thompsett, in *22nd International Power Sources Symposium*, p. 226, Manchester, England (2001).

12. W. R. Lee, M. G. Kim, J. R. Choi, J. I. Park, S. J. Ko, S. J. Oh and J. Cheon, *Journal of the American Chemical Society*, **127**, 16090 (2005).

13. A. Renouprez, J. L. Rousset, A. M. Cadrot, Y. Soldo and L. Stievano, in *5th International School and Symposium on Synchrotron Radiation in Natural Science (ISSRNS)*, p. 50, Poland (2000).

14. P. P. Wells, E. M. Crabb, C. R. King, R. Wiltshire, B. Billsborrow, D. Thompsett and A. E. Russell, *Physical Chemistry Chemical Physics*, **27**, 5773 (2009).

15. D. C. Papageorgopoulos, M. Keijzer, J. B. J. Veldhuis and F. A. de Bruijn, *Journal of the Electrochemical Society*, **149**, A1400 (2002).

16. A. Ruban, B. Hammer, P. Stoltze, H. L. Skriver and J. K. Norskov, in *1st Francqui Colloquium on Molecular Heterogeneous Catalysis*, p. 421, Brussels, Belgium (1996).

17. V. D. Stytsenko, *Applied Catalysis a-General*, **126**, 1 (1995).

CHAPTER 4

EFFECT OF THE Pt COVERAGE ON THE PROPERTIES OF THE Pt_{SHELL}/Pd_{CORE} ELECTROCATALYSTS

CHAPTER 4: Effect of Pt coverage on the properties of the Pt_{shell}/Pd_{core} electrocatalysts

4.1. Introduction

This chapter discusses the surface structure and the electrochemical properties of Pt/Pd core-shell catalysts as a function of the Pt coverage. The catalysts will be denoted as $Pt_{0.5}$/Pd, $Pt_{1.0}$/Pd, $Pt_{1.5}$/Pd, $Pt_{2.0}$/Pd, with the subscript indicating the number of equivalent monolayers. The particle morphology and structure were studied by TEM, XRD and EXAFS. Attempts to quantify the coverage and thickness of the Pt shell were made using mainly HS-LEIS and XPS. Segregation effects were also examined. The stability of the catalysts in oxidising conditions was assessed by cyclic voltammetry and their ORR activity was measured first using the thin film method and then in a miniature PEM single cell.

4.2. Preparation of Pt_{xML}/Pd/C core-shells

The core-shell catalyst $Pt_{1.0}$/Pd was prepared by a single deposition of Pt onto 18.5 wt% Pd/C core catalyst with a dispersion (measure by CO chemisorption) of 56 %. $Pt_{1.5}$/Pd and $Pt_{2.0}$/Pd were obtained by depositing half and one Pt monolayer onto $Pt_{1.0}$/Pd, respectively. $Pt_{0.5}$/Pd was prepared from a 19.5 wt% Pd/C core with a dispersion of 43%. The quantities used in the preparations are summarised in Table 4-1. The required amount of $Pt(acac)_2$ was calculated using equation 2-1 in Section 2.

Table 4- 1 Quantities of starting materials and ICP-ES analysis of reaction filtrates.

Catalyst	Pd/C	Pd/C / g	Required $Pt(acac)_2$ / g	In filtrate / ppm	
				Pt	Pd
$Pt_{0.5}$/Pd	19.5 wt%	3.9	0.59	0.68 ± 0.05	1.19 ± 0.09
$Pt_{1.0}$/Pd	18.5 wt%	6	2.3	< 0.1 ± 0.01	0.2 ± 0.02
$Pt_{1.5}$/Pd	18.5 wt%	2.2	0.42	0.3 ± 0.02	1.1 ± 0.09
$Pt_{2.0}$/Pd	18.5 wt%	2.2	0.84	N/A	N/A

At the end of the Pt deposition reaction, the filtrates were all colourless, indicating that most of the $Pt(acac)_2$ had reacted. The amount of Pt and Pd remaining in the filtrates were determined by ICP-AES, as shown in Table 4-1, and the very low levels of Pt and Pd confirmed that the Pt precursor reacted with the reduced Pd surface and that the CSR reaction did not involve the dissolution of Pd.

The amounts of platinum and palladium in each catalyst prepared for this study were quantitatively analysed by ICP and the results are given in Table 4-2. For all the Pt_x/Pd core-shell catalysts, it can be seen that there is not a significant difference between the experimental and the theoretical metal content data, confirming all the Pt precursor reacted.

Table 4- 2 Catalyst compositions measured by ICP-ES.

Catalyst	Pt assay wt%	Nominal assay	Pd assay wt%	Nominal assay	Pt:Pd atomic ratio
$Pt_{0.5}/Pd$	6.7 ± 0.5	7	17.0 ± 1.4	18	18:82
$Pt_{1.0}/Pd$	12.4 ± 1.0	16	14.8 ± 1.2	15	30:70
$Pt_{1.5}/Pd$	19.8 ± 1.6	23	13.3 ± 1.1	14	46:54
$Pt_{2.0}/Pd$	25.8 ± 2.1	29	12.2 ± 1.0	12	54:46

4.3. Characterisation of the Pt shell

4.3.1. Structural characterisation

XRD

X-ray diffraction analysis was used to characterise the nature of the core-shell catalysts, including evidence for alloying or segregation. Rietveld analysis was employed to try and profile the metallic phases present. The metallic phase of carbon-supported fuel cell catalysts tend to be present as a poorly crystalline phase, which can make the analysis difficult. This arises from the highly dispersed nature of those catalysts. The XRD patterns for $Pt_{1.0}/Pd$ and $Pt_{2.0}/Pd$ are shown in Figure 4-1.

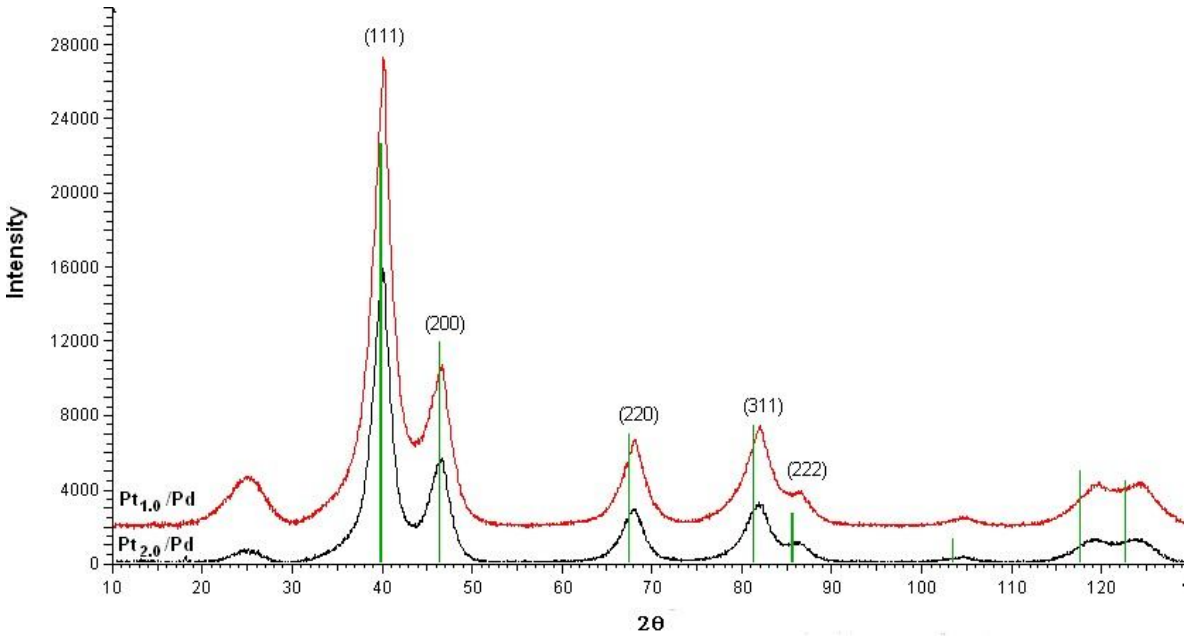

Figure 4- 1 XRD patterns of $Pt_{1.0}/Pd$ (red spectrum) and $Pt_{2.0}/Pd$ (black spectrum). The green vertical lines represent the documented diffraction peaks of Platinum.

Both XRD patterns in Figure 4-1 have a profile typical of fcc Pd. Although $Pt_{1.0}/Pd$ contained 12.4 wt% of Pt, no evidence of a Pt phase was observed. Rietveld profile fitting was unable to confirm the presence of a Pt phase. In a core-shell structure, the shell element is likely to be non-crystalline and thus, unable to be detected by XRD. This suggests that Pt is probably present as an amorphous phase possibly attributed to stress/strain and dislocation defects in the shell. A closer examination of the $Pt_{1.0}/Pd$ profile shows a slight shift of the diffraction peaks from those of Pd towards lower 2θ. This would suggest some alloying of the Pt with the Pd has occurred. In comparison, the $Pt_{2.0}/Pd$ XRD pattern (Figure 4-1) exhibits more Pt character as the diffraction peaks are slightly shifted towards lower 2θ, which is evidence of lattice expansion of the Pd lattice. The diffraction peaks (220), (311) and (222), exhibit a shoulder on the lower 2θ side, which can be assigned to a contribution from Pt. A Rietveld profile was fitted on this pattern revealing that the catalyst was mainly composed of a Pd-rich PtPd alloy phase (Figure 4-2). The residual peaks at 25.05° and 38.97° are too minor to be clearly assigned to a specific phase. The crystallite size associated to this phase was 2.36 nm which is smaller than the mean particle measured by TEM (Section 4.3.1.C). The calculated lattice parameter was 3.8981 Å, which shows an expansion of the Pd lattice (3.890 Å) upon addition of Pt at the surface. Such an expansion was also observed by J. Yang et al. (1) who suspected Pt diffusion occurred into the Pd core in $Pt_{shell}/Pd_{core}/C$.

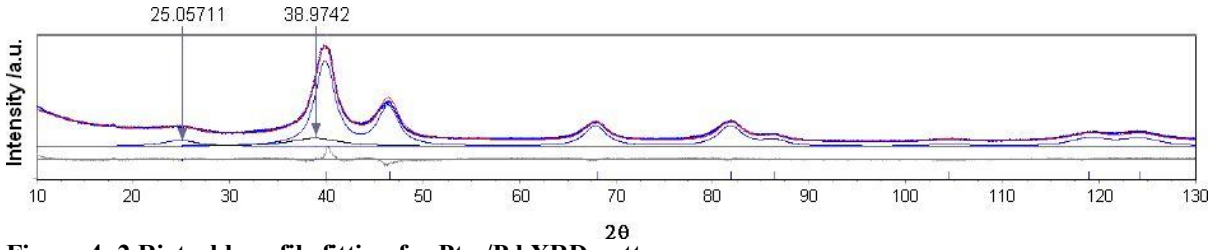

Figure 4- 2 Rietveld profile fitting for $Pt_{2.0}/Pd$ XRD pattern.

Table 4- 3 XRD parameters.

	Phases	Crystallite size / nm	Lattice parameter / Å	Cell volume / $Å^3$
Pd	-	-	3.890	58.87
Pt	-	-	3.923	60.38
$Pt_{1.0}/Pd$		Identification failed		
$Pt_{2.0}/Pd$	PtPd	2.36	3.898	59.23

EXAFS

EXAFS experiments were performed at SRS (Daresbury Laboratory, UK) and at the NSLS (Brookhaven National Laboratory, New York, USA). Owing to a lack of available beamtimes, only experiments at the Pt L_{III} edge were performed. The data was collected in air (as prepared) and following reduction at room temperature in hydrogen gas. Experiments on the Pd K edge would have been desirable for $Pt_{0.5}/Pd$, $Pt_{1.0}/Pd$, $Pt_{1.5}/Pd$ and $Pt_{2.0}/Pd$, under both hydrogen and air atmospheres. The corresponding chi and Fourier transform plots in hydrogen and in air are shown in Figure 4-3 and Figure 4-4, respectively. The structure of the core-shell and evidence for segregation were investigated. The fit parameters for a two-shell fitting model are presented in Table 4-4.

The total coordination numbers were lower than the 12 found in the face-centred cubic bulk structure and this is attributed to the high proportion of surface atoms for particles of such small diameters. In a hydrogen atmosphere, the total first shell ($R \leq 2.9$ Å) coordination number ($N_{Pt} + N_{Pd}$) remained about the same (~ 8) independent of the Pt coverage. However, the proportion of Pt-Pt neighbours increased from 61% to 75% as the Pt coverage increased, which can be interpreted as evidence of Pt deposition onto Pt. While the Pt-Pt distance in $Pt_{0.5}/Pd$ and $Pt_{1.0}/Pd$ was the same as in Pt/C (2.75 Å), it expanded by about 0.03 Å for $Pt_{1.5}/Pd$ and $Pt_{2.0}/Pd$, suggesting some kind of change in the shell structure

with higher Pt coverage. Likewise, the Pt-Pd distance was expanded from 2.74 to 2.78 Å as the Pt content increased. In a PtPd alloy where Pd is the host, the Pt-Pt distances are expected to contract since the Pt atom is larger than the Pd atom. In fact, the Pt-Pd distance in small PtPd alloy aggregates of Pt:Pd atomic composition 35:65 was found to be 2.74 Å (2). If the Pt shell was pseudomorphic to the Pd core particle, a small compressive strain on the Pt monolayer should be expected. It was shown that the Pt_xPd core-shell catalysts prepared by CSR presented a discontinuous Pt shell, which consisted of Pt 3D-islands. The fact that the Pt-Pt distance increases with the Pt coverage does not indicate the formation of non-strained Pt islands. However, it suggests that for the Pt_xPd series the degree of alloying of the catalyst surface decreases as the Pt coverage increases.

The effect of the oxide layer on the structure was determined by collecting the EXAFS in air (the as-prepared catalysts left to age in air for several weeks prior to collecting the EXAFS data). Changes were observed both in metal-metal bond distances and the coordination numbers as shown in Table 4-4. Unfortunately, it was not possible to perform EXAFS measurements on Pt0.5/Pd in air. The total coordination number generally decreased and Pt-O neighbours at 2.02 Å were formed upon exposure of the catalysts to air. It can be noticed that the proportion of Pt-Pd neighbours decreased dramatically compared to Pt-Pt neighbours, which may signify a change in the structure. The biggest changes were observable for $Pt_{1.5}$/Pd and $Pt_{2.0}$/Pd, for which the Pt-Pt distances contracted by up to 0.05 Å whereas the Pt-Pd distances expanded by 0.02 Å. This suggests that as $N_{Pt\text{-}Pt}$ goes down the Pd core has more influence on the Pt-Pt interactions.

Measurements at the Pd K edge in hydrogen atmosphere would have possibly given more information about the alloy character of the core-shell surfaces. Measurements in air atmosphere would have provided more information about the structure and the extent of the Pt coverage for the Pt_xPd catalysts. This would have been indicated by the number of Pd-O neighbours. Comparison of the data in both atmospheres would have possibly helped to identify the effect of the atmosphere on the surface composition.

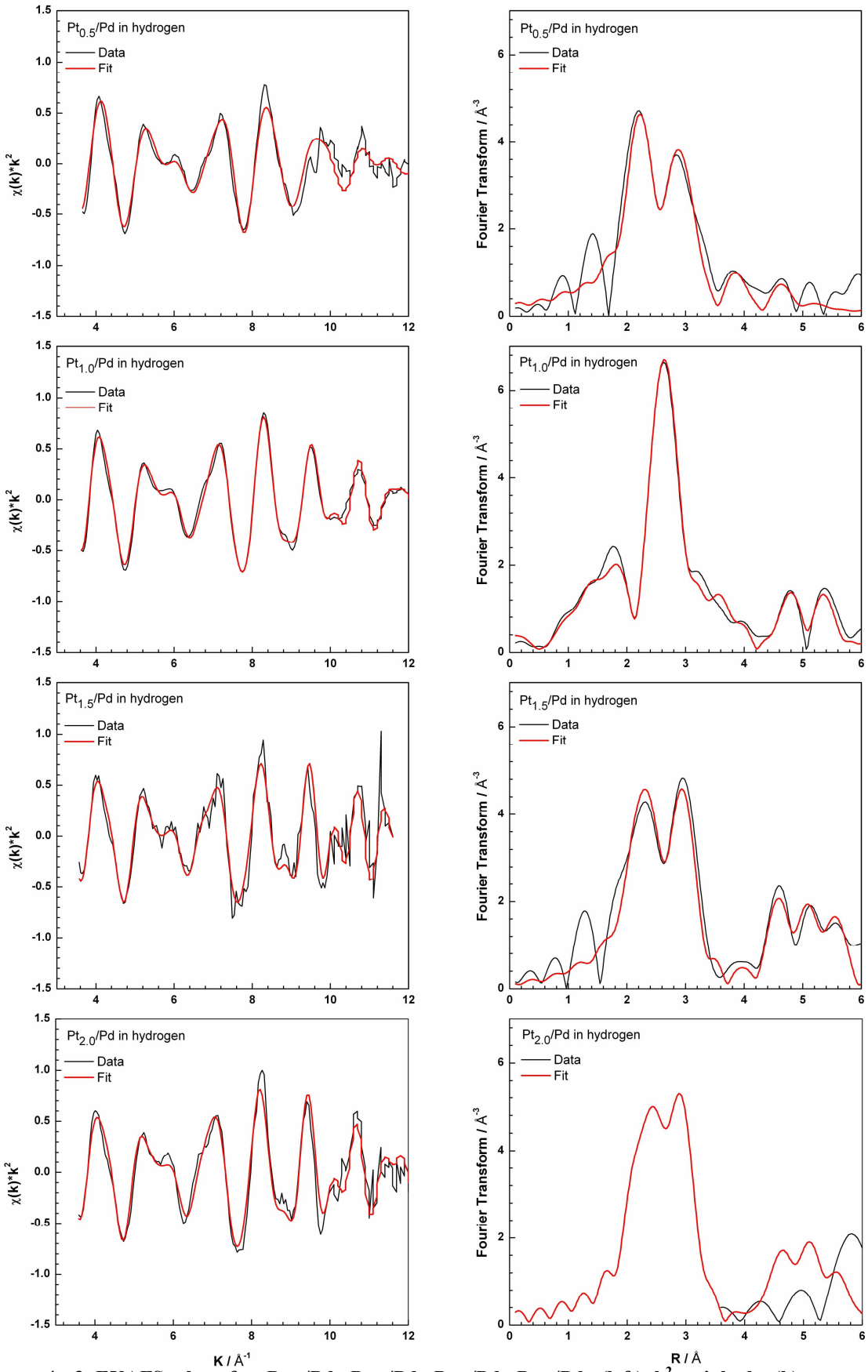

Figure 4- 3 EXAFS plots for $Pt_{0.5}/Pd$, $Pt_{1.0}/Pd$, $Pt_{1.5}/Pd$, $Pt_{2.0}/Pd$. (left) k^2-weighed χ(k) spectrum collected at Pt L_{III} edge obtained in hydrogen; (right) k^2-weighed Fourier transform of the χ (k) data.

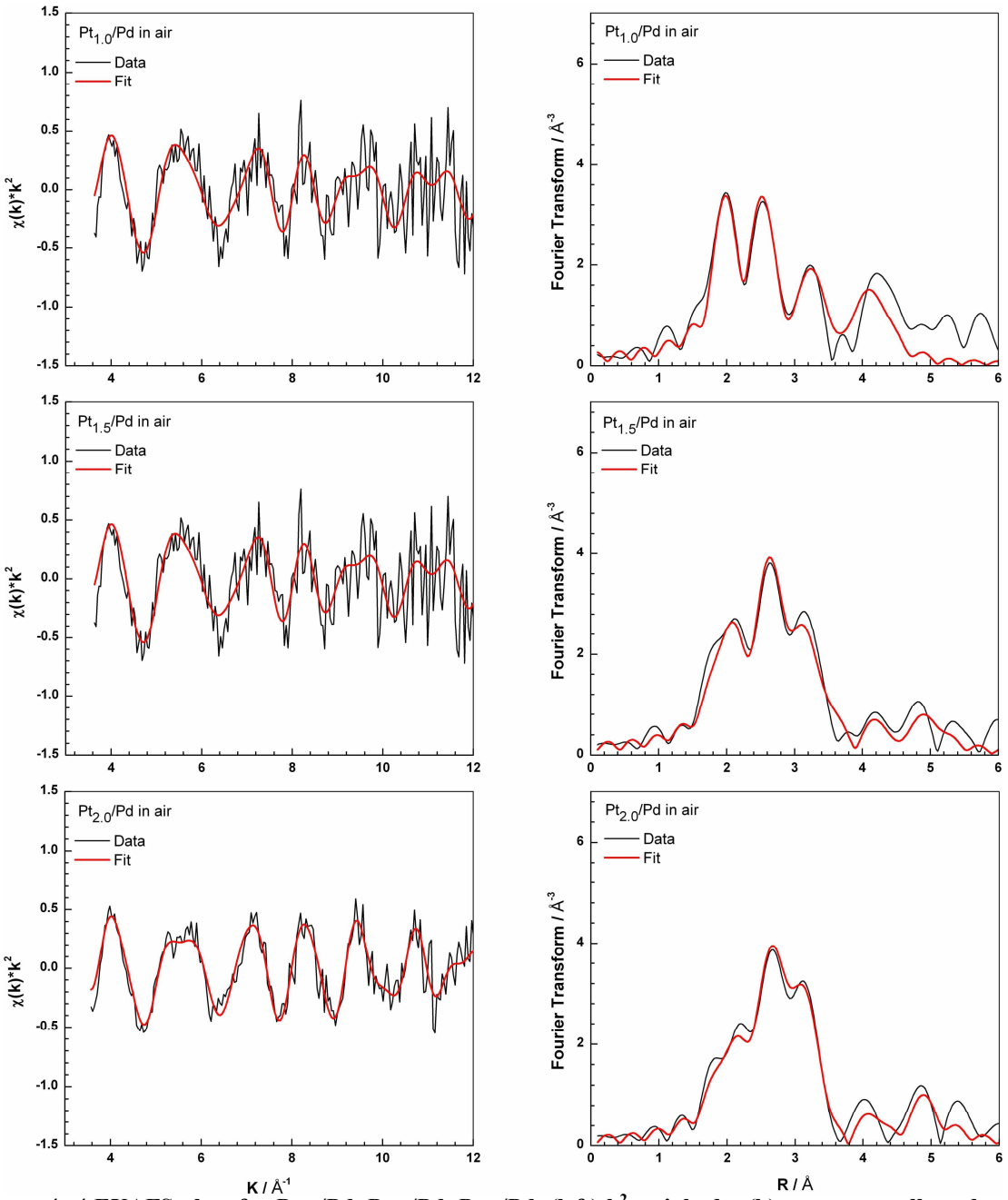

Figure 4- 4 EXAFS plots for $Pt_{1.0}/Pd$, $Pt_{1.5}/Pd$, $Pt_{2.0}/Pd$. (left) k^2-weighed χ (k) spectrum collected at Pt L_{III} edge obtained in air; (right) k^2-weighed Fourier transform of the χ (k) data.

Table 4- 4 EXAFS fit parameters in hydrogen and air atmospheres at the Pt L_{III} edge.

Catalysts	Coordination number	Distance (Å)	Debye-Waller factor $2\sigma^2$ ($Å^2$)	E_f / eV	R_{EXAFS} / %
			In hydrogen		
$Pt_{0.5}/Pd$	Pt = 4.9 ± 0.5	2.75 ± 0.01	0.016 ± 0.003	-9.75 ± 0.98	35.7
	Pd = 3.1 ± 0.3	2.75 ± 0.01	0.014 ± 0.002		
$Pt_{1.0}Pd$	Pt = 5.4 ± 0.2	2.75 ± 0.24	0.013 ± 0.001	-10.98 ± 0.46	15.5
	Pd = 2.9 ± 0.2	2.77 ± 0.01	0.016 ± 0.001		
$Pt_{1.5}Pd$	Pt = 4.9 ± 0.8	2.78 ± 0.02	0.011 ± 0.004	-11.62 ± 1.56	33.0
	Pd = 2.3 ± 0.6	2.78 ± 0.03	0.013 ± 0.005		
$Pt_{2.0}Pd$	Pt = 5.7 ± 0.7	2.77 ± 0.01	0.011 ± 0.002	-12.00 ± 1.25	29.0
	Pd = 1.9 ± 0.4	2.78 ± 0.02	0.011 ± 0.003		
			In air		
$Pt_{0.5}/Pd$	Not measured				
$Pt_{1.0}Pd$	O = 0.7 ± 0.2	2.02 ± 0.20	0.012 ± 0.003	-13.42 ± 4.22	67.0
	Pt = 3.7 ± 1.0	2.76 ± 0.03	0.014 ± 0.006		
	Pd = 1.1 ± 0.4	2.75 ± 0.03	0.011 ± 0.005		
$Pt_{1.5}Pd$	O = 0.8 ± 0.2	2.02 ± 0.03	0.011 ± 0.007	-11.10 ± 2.44	46.3
	Pt = 7.0 ± 1.6	2.73 ± 0.03	0.031 ± 0.005		
	Pd = 1.0 ± 0.3	2.80 ± 0.02	0.010 ± 0.003		
$Pt_{2.0}Pd$	O = 0.7 ± 0.2	2.03 ± 0.03	0.014 ± 0.007	-13.48 ± 2.52	37.4
	Pt = 4.4 ± 0.8	2.74 ± 0.02	0.018 ± 0.003		
	Pd = 1.1 ± 0.3	2.80 ± 0.02	0.013 ± 0.004		

High Resolution TEM and STEM

The effect of the Pt coverage on the particle size was investigated by TEM measurements. Assuming that the Pd core particles were spherical and the Pt shell covered the Pd core uniformly, the expected sizes for $Pt_{1.0}/Pd$ and $Pt_{2.0}/Pd$, starting from a Pd core of 2.9 nm, would be 3.4 nm and 4 nm respectively. Histograms of the particle size distribution (Figure 4-5) establish that the average particle size of the core-shell catalysts increased with the amount of Pt deposited on the Pd core surface. The results were fairly consistent with the predicted particle diameters within the error of the measurement.

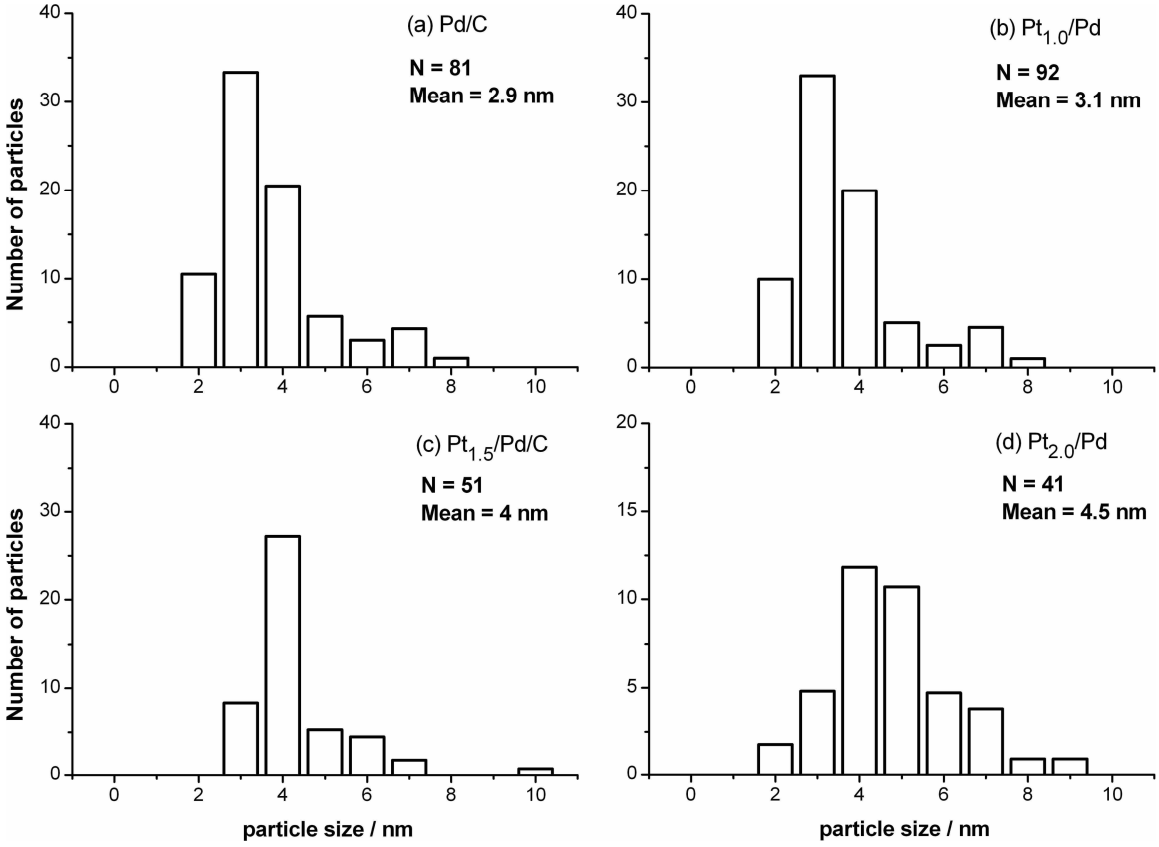

Figure 4- 5 Particle size distribution bar charts for (a) Pd/C, (b) $Pt_{1.0}/Pd$, (c) $Pt_{1.5}/Pd$ and (d) $Pt_{2.0}/Pd$

Figure 4-6 shows the aberration corrected STEM micrographs of $Pt_{2.0}/Pd$. The lighter outer areas show the Pt shell and the darker centre the Pd core. It can be seen that there is a variation in the thickness of the Pt shell. Some regions of the Pd were not covered at all. A study of their micrographs indicates that there was more accumulation of Pt at the edges of

the Pd particle compared to the planes. These observations suggest the chemistry used resulted in a preferential deposition of Pt onto the Pd core particle edges.

Unfortunately, there was no opportunity to examine the other core-shell catalysts under the same conditions to allow a comparison to be made.

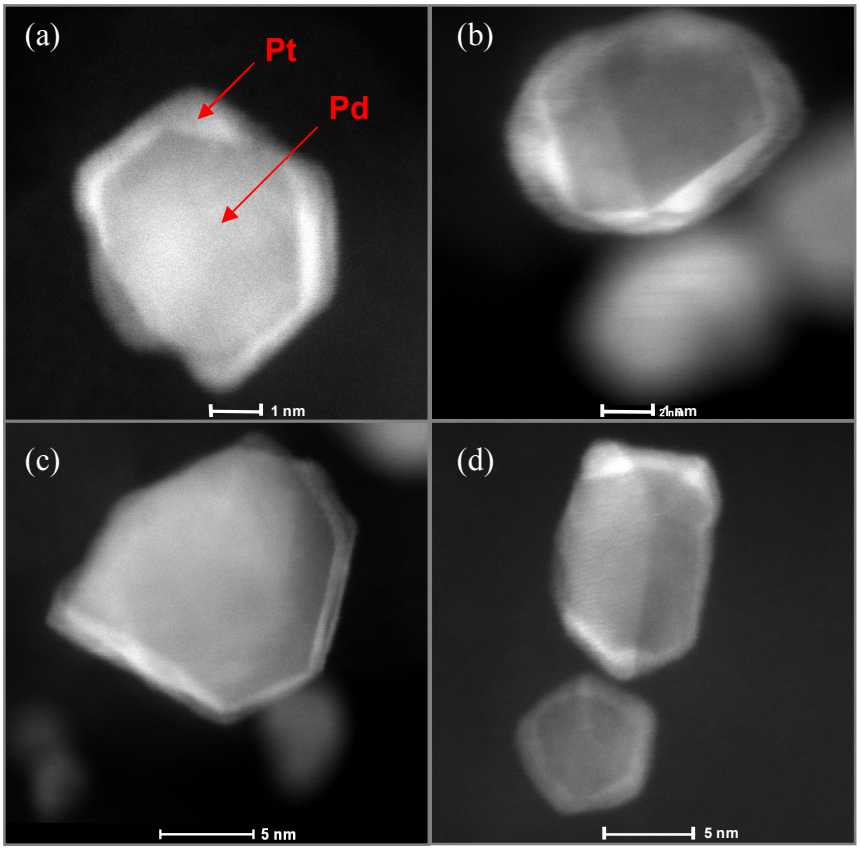

Figure 4- 6 Aberration-corrected STEM images of $Pt_{2.0}$/Pd core-shell catalyst.

4.3.2. Quantification of the Pt shell

HS-LEIS

This method is a probe of the composition of the outermost atomic layer of a material and it was hoped to gain information about the surface of the catalyst particles. It was only possible to obtain HS-LEIS data for the $Pt_{2.0}$/Pd catalyst due to the cost of the experiment. The LEIS spectrum for $Pt_{2.0}$/Pd was collected after conditioning the catalyst in hydrogen at ambient temperature, as was done for the EXAFS spectra obtained in hydrogen. The resulting LEIS spectrum is shown in Figure 4-7. The spectrum was recorded with $^{20}Ne^{+}$ rather than He^{+} to obtain better mass resolution between Pt and Pd. The area of the HS-

LEIS peak for each element is proportional to its surface fraction. Pure Pt and Pd references were analyzed so that the peak areas for the core-shells can be expressed as a fraction of the reference peak areas (3). The Pd and Pt signals are observed at 1.3 and 1.9 keV, respectively. The measured surface fraction (m^2 covered / total m^2) for Pd was 0.16 % and that of Pt was 0.30 %. Removing the contribution of the carbon surface, this corresponds to a Pt surface coverage of 65 %. Since a Pt atom occupies about 2 % more surface area than a Pd atom, the corresponding atomic ratios are 35.4 at % Pd and 64.6 at % Pt. The bulk Pt:Pd atomic composition for $Pt_{2.0}/Pd$ of 53.6:46.4 confirms the previous TEM observations that once Pt has been deposited, further Pt deposition on Pt is just as likely to occur as that on uncovered Pd.

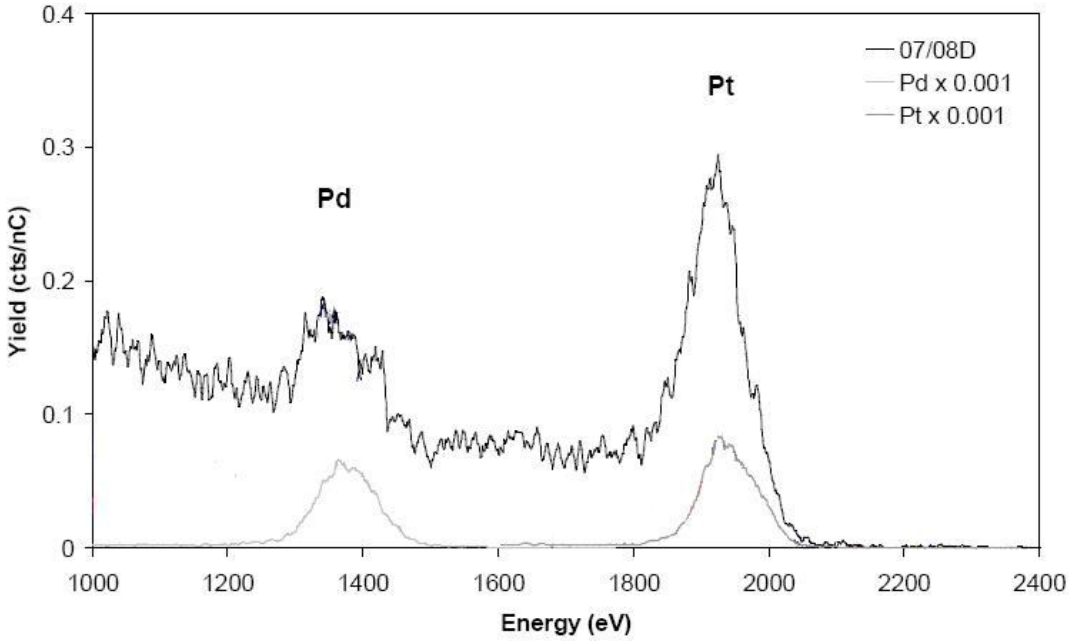

Figure 4- 7 The 3keV $^{20}Ne^+$ spectrum of $Pt_{2.0}/Pd$ after the reduction treatment, compared to the spectra for the Pd and Pt reference. The spectra for the references have been multiplied by 0.001 to facilitate comparison.

XPS

To explore their electronic properties and surface composition, the Pt/Pd core-shell catalysts, were examined by XPS. The catalyst samples were not pre-reduced for the analysis. Figure 4-8(a) shows XPS spectra of the Pt_x/Pd core-shell catalysts in the binding energy ranges for Pd 3d and Pt 4d. The corresponding binding energies together with the XPS derived atomic ratios are summarized in Table 4-5. As shown in Figure 4-8 (a), the

curves exhibit four main peaks assigned to Pd $3d_{3/2}$, Pd $3d_{5/2}$, Pt $4d_{3/2}$ and Pt $4d_{5/2}$. The spectra were normalized to the Pd 3d peaks and demonstrates the Pt enrichment of the core-shell surface with increasing amounts of deposited Pt. The observed binding energies are close to those of metallic Pd and Pt, with binding energies of 340.4 eV, 335.1 eV, 332 eV and 315 eV for Pd $3d_{5/2}$ Pd $3d_{3/2}$, Pt $4d_{5/2}$ and Pt $4d_{3/2}$ respectively (4). This indicates that the Pt_x/Pd core-shells exist mostly in their metallic state. The Pd 3d lines are slightly shifted to higher energies compared to the metallic Pd peaks, which can be attributed to the interaction between Pt and Pd (5, 6). Figure 4-8 (b) shows a closer view of the Pd $3d_{5/2}$ peaks, in which a shoulder on the high binding energy side (~337 eV) can be observed. This feature, decreasing as the Pt coverage increased, can be ascribed to Pd oxide (Pd[II]) at the surface and may correspond to Pd that was not decorated with Pt. The Pt 4f peaks, as shown in Figure 4-9(c), also tended to shift to higher binding energies as the Pt coverage decreases, which indicate a modification of the Pt electronic structure.

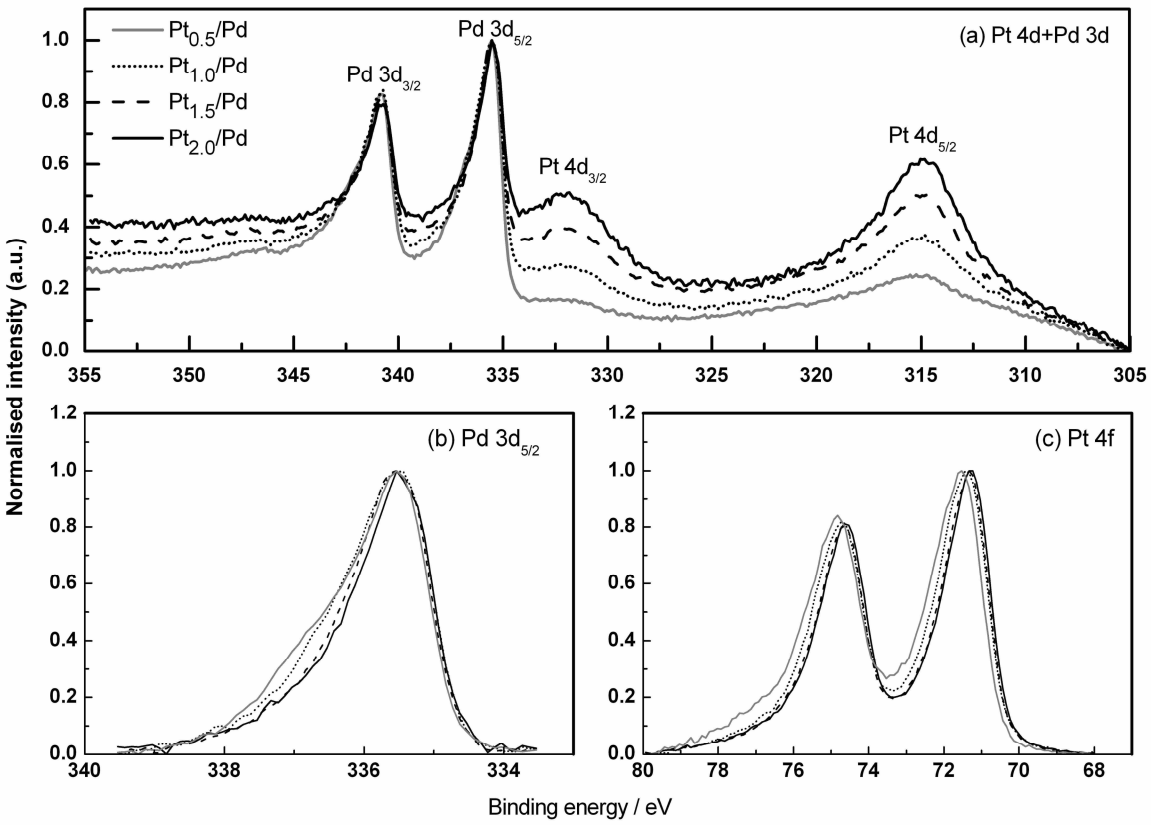

Figure 4- 8 Intensity normalised (a) Pt 4d and Pd 3d and (b) Pd 3d and (c) Pt 4f (background substracted) XPS spectra for $Pt_{1.0}$/Pd, $Pt_{1.5}$/Pd, $Pt_{2.0}$/Pd.

XPS was also used to analyze the Pt/Pd near surface ratios. The Pt:Pd atomic ratios were determined from a quantitative analysis of the areas of the Pd 3d and Pt 4f peaks. They were compared to the bulk ratios to characterize the Pt shell. The results, presented in Table 4-5, confirmed that the catalyst near surface regions were Pt-rich compared to the bulk composition. The HS-LEIS derived Pt:Pd atomic ratio of 63:35 obtained for $Pt_{2.0}/Pd$ is lower than the XPS derived 71:29 ratio. Two reasons may explain this observation. First of all, a bimetallic catalyst surface composition can be affected by segregation effects. According to the DFT calculations, in the case of Pt/Pd system where Pd is the host element, a moderate antisegregation of Pd is expected (7). Secondly, the high resolution TEM images presented earlier showed that the Pt shell does not cover the entire surface but tend to concentrate around the edges of the Pd particles. Unlike HS-LEIS, XPS is able to probe below the surface to a depth of ~ 2 nm. This means that compared to LEIS, XPS will detect more Pt.

Table 4- 5 Binding energies of Pd and Pt XPS lines XPS derived and bulk Pt:Pd atomic ratios.

Catalysts	Pd $3d_{5/2}$	Pt $4f_{5/2}$	Pt $4f_{7/2}$	$(Pt:Pd)_{XPS}$	$(Pt:Pd)_{Bulk}$
Pd/C	335.5	-	-	0:100	
Pt/C	-	74.7	71.7	100:0	
$Pt_{0.5}/Pd$	335.5	74.8	71.5	25:75	18:82
$Pt_{1.0}/Pd$	335.6	74.7	71.4	43.5:56.5	31.4:68.6
$Pt_{1.5}/Pd$	335.6	74.6	71.3	60:40	44.8:55.2
$Pt_{2.0}/Pd$	335.6	74.6	71.3	75:25	53.6:46.4

CO metal area

The uptake of CO (per gram of catalyst including the carbon support) was measured by CO chemisorption (see Chapter 2 Section 2.5.1). The dispersion (D) represents the ratio between the number of surface metal atoms over the total number of atoms (Equation 4-1). To take into account the surface composition, the dispersion was corrected using the XPS Pt:Pd atomic ratios (Equation 4-2). It was assumed that there was one CO molecule per Pt surface atom and one CO molecule per two Pd surface atoms.

$$D = \frac{CO(mol/g)}{\frac{Pd_{wt\%}}{MM(Pd)} + \frac{Pt_{wt\%}}{MM(Pt)}} \quad \textbf{(4- 1)}$$

$$D_{CORR} = D \times \left(2 \times Pd_{at\%} + Pt_{at\%}\right) \quad \textbf{(4- 2)}$$

The surface area (S) was calculated using equation 4-3:

$$S = \frac{CO(mol/g) \times N_A}{d_S} \times \left(2 \times Pd_{at\%} + Pt_{at\%}\right) \quad \textbf{(4- 3)}$$

(where $d_s = 1.27 \times 10^{19}$ atoms per cm^2 for Pt)

The results are shown in Table 4-6. The amount of adsorbed CO corrected by the mass of Pd tends to increase with the Pt coverage. This confirms the surface was modified by the addition of Pt. The increase of the amount of adsorbed CO per gram of Pd may be caused by an increase in the surface roughness and in the number of single-bonded CO. Since the surface area per gram of catalyst remains constant for the core-shell catalysts, a decrease is observed in the surface area per gram of Pt with increasing the Pt content.

Table 4- 6 Calculated dispersion and surface areas determined from the amount of adsorbed CO.

	CO / mmol g^{-1}	CO / mmol g_{Pd}^{-1}	Surface area /	
			$m^2\ g^{-1}$	$m^2\ g_{Pt}^{-1}$
18.5%Pd/C	0.487	2.63	46	-
$Pt_{1.0}$/Pd	0.410	3.51	30	245
$Pt_{1.5}$/Pd	0.467	3.42	31	157
$Pt_{2.0}$/Pd	0.494	4.05	30	116

4.4. Electrochemical properties

4.4.1. Surface characterisation

Pt voltammetry

Figure 4-9 shows the CV of a carbon-supported Pt catalyst in 1 M H_2SO_4. The voltammetric features appear less sharp than in the bulk Pt electrode CV presented in Section 2.6.1. The peak for "strongly" adsorbed hydrogen (H_S) is small compared to that of

"weakly" (H_W) adsorbed hydrogen and is attributed to the Pt size and dispersion on the carbon support, which may change the ratio of the number of adsorption sites.

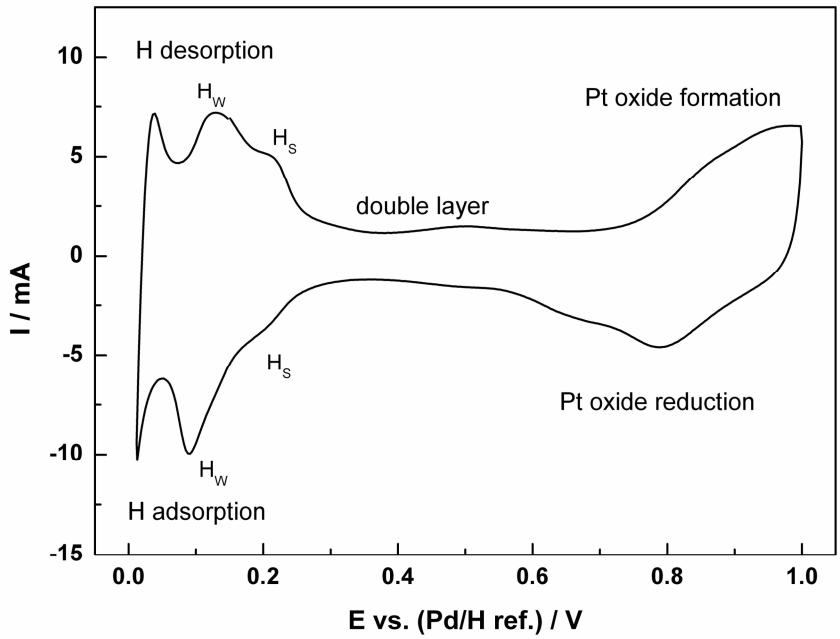

Figure 4- 9 Cyclic voltammogram of 40% Pt/C (0.4 mgPt/cm^2) in 1 M H_2SO_4, 80°C.

Pd voltammetry

Figure 4-10 shows the cyclic voltammogram of a carbon-supported Pd electrode in 1 M H_2SO_4. As can be seen, the Pd CV is distinctive from that of Pt in the hydrogen and oxide regions. The shape of the voltammogram in the hydrogen sorption/desorption region (0.0 – 0.25 V vs Pd/H ref.) shows two sets of peaks that are consistent with the two types of sorption (8). The adsorption of hydrogen starts around 0.25 V. First, a sharp peak at 0.23 V was observed. Such a peak was also identified both on thin Pd film electrodes in 0.5 M H_2SO_4 and on Pd(111) and Pd(100) single crystals in 0.1 M H_2SO_4 (9) and was attributed to the adsorption of strongly bonded hydrogen accompanied by the desorption of (hydrogen) sulfate anions. Between 0.08 V and 0.18 V followed a flat peak, which was also observed on Pd thin film electrodes (10). This flat peak may be due to hydrogen absorption in the α-phase. At more negative potentials, a large peak is observed and is attributed to the formation of the β-Pd-H phase and hydrogen evolution (11). The absorption of hydrogen into the Pd lattice can proceed following either an indirect or a direct mechanism, involving the transfer of one electron (10, 12, 13).

Indirect mechanism:

$$M + H^+ + e^- \leftrightarrow M - H_{ads} \quad \textbf{(4- 4)}$$

$$M - H_{ads} + M_{subsurface} \leftrightarrow M_{surface} + M - H_{abs} \quad \textbf{(4- 5)}$$

Direct mechanism:

$$M + H^+ + e^- \leftrightarrow M - H_{abs} \quad \textbf{(4- 6)}$$

Where $M\text{-}H_{ads}$ is hydrogen atom adsorbed on the Pd electrode and $M\text{-}H_{abs}$ is hydrogen absorbed in the subsurface Pd layer. $M\text{-}H_{abs}$ then diffuses into the Pd lattice.

The onset of the Pd oxide formation is at 0.72 V, which is similar to that of Pt.

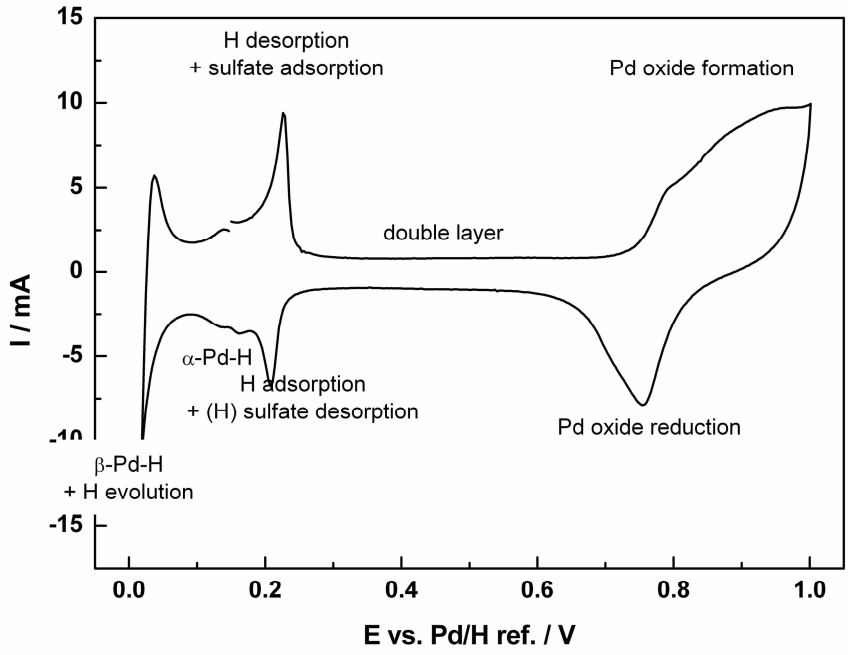

Figure 4- 10 Cyclic voltammogram of 20% Pd/C (0.18 mgPt/cm^2) in 1 M H_2SO_4 at 80 °C

Pt/Pd core-shell voltammetry

The cyclic voltammograms of $Pt_{0.5}$/Pd, $Pt_{1.0}$/Pd, $Pt_{1.5}$/Pd and $Pt_{2.0}$/Pd in 1 M H_2SO_4 at 80 ^oC are presented in Figure 4-11. All except $Pt_{2.0}$/Pd show broad features at low potentials very different to that observed for Pd and attributed to hydrogen adsorption/desorption. A similar CV profile was observed for a PtPd alloy catalyst (Figure 4-13). Additional contributions from bisulfate anion adsorption and from hydrogen absorbed into the Pd lattice were also anticipated in this potential region.

In contrast to the other core-shell catalysts, $Pt_{2.0}$/Pd exhibits features characteristic of Pd at low potentials, although the Pt coverage was estimated to be 65 % by HS-LEIS. Two sharp peaks at 0.16 V on the cathodic sweep and 0.19 V on the anodic sweep, followed by two flat peaks and then hydrogen evolution/absorption at more negative potentials. Similar peaks were also observed by Solla-Gullon et al. for a Pd-rich PtPd alloy (Pt:Pd 20:80 atomic ratio) (14). The negative potential shift of the hydrogen adsorption/desorption peaks relative to that of Pd may originate from the interaction between Pt and Pd. In the oxide region, there is no major difference between the Pt/Pd core-shell and the Pt-only CVs, and the onset of the oxide formation and the potential of the oxide removal peaks are similar. The reasons why such a strong Pd character was observed on the core-shell catalyst with the highest Pt coverage is not well understood.

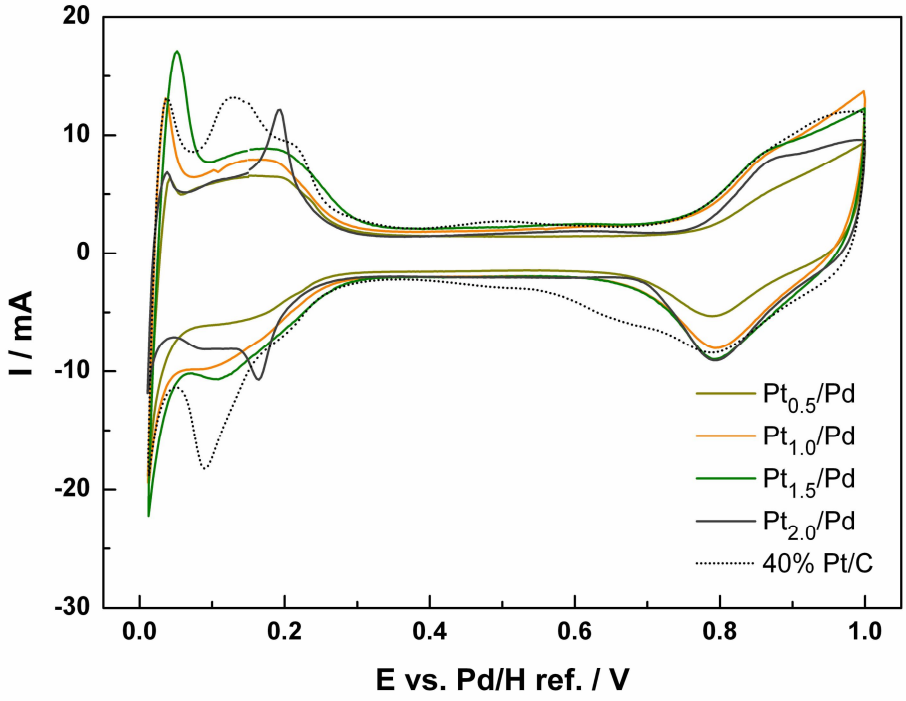

Figure 4- 11 Cyclic voltammogram of Pt/Pd/C core-shell painted button electrodes (0.6 mg carbon/cm^2) in 1 M H_2SO_4, at 10 mV/s at 80^{o}C. Electrode area: 3.14 cm^2.

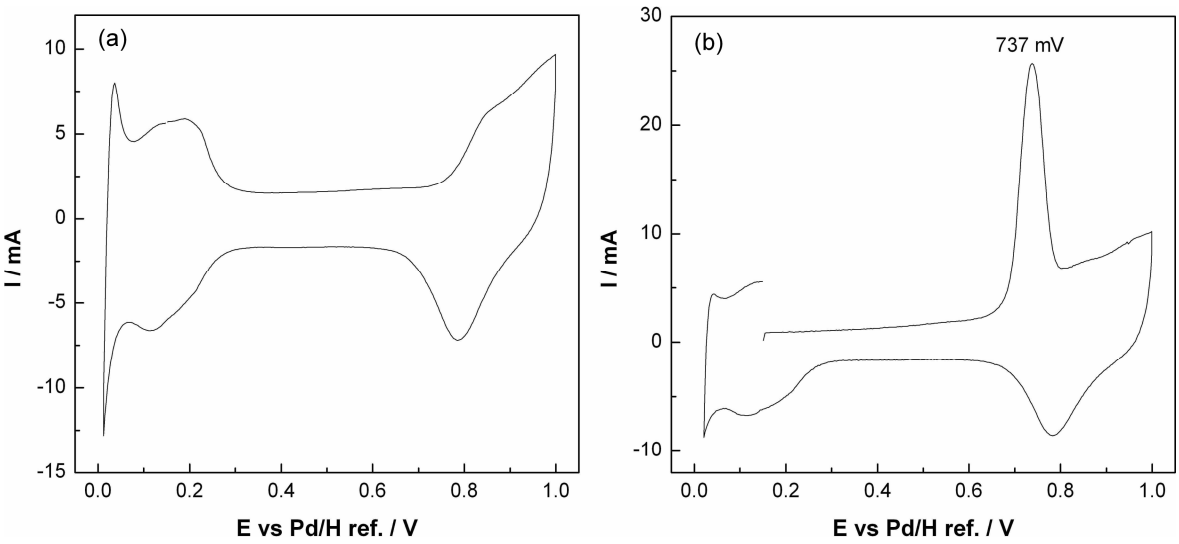

Figure 4- 12 Cyclic voltammogram (a) and CO electrooxidation voltammograms (b) of PtPd/C alloy painted button electrode in 1M H_2SO_4, at 10 mV/s, at 80°C. Electrode area: 3.14 cm^2.

The charge under the hydrogen sorption peaks of the core-shell catalyst was calculated by integration between the onset potential of the hydrogen evolution (~ 0.05 V) and the potential at the start of the double layer region (~ 0.35 V). These are shown in Table 4-7. The charge per gram of total metal is higher for the core-shell catalysts than for the Pd/C core catalyst. This can be explained by a higher surface area which is due to an increase in the roughness of the surface. Assuming the absorption of hydrogen was negligible, the catalyst ECA was calculated by integration of the amount of sorbed hydrogen following Equation 2-16 and the results are shown in Table 4-7.

Figure 4-13 shows cyclic voltammograms of the core-shell catalysts for the oxidation of carbon monoxide measured using the procedure described in Section 2.6.1. The CO cyclic voltammograms of Pt/C and Pd/C are shown for comparison. The charges under the CO oxidation peaks and the peak potential are given in Table 4-7. Similar single CO electrooxidation peaks are found for the core-shell catalysts. All core-shell catalysts except $Pt_{0.5}/Pd$ were positioned at a potential intermediate (701-725 mV) between that of Pt (629 mV) and that of Pd (834 mV) and exhibit a peak shape similar to that of Pt. In contrast, $Pt_{0.5}/Pd$ CO peak was more Pd-like in terms of peak potential and shape.

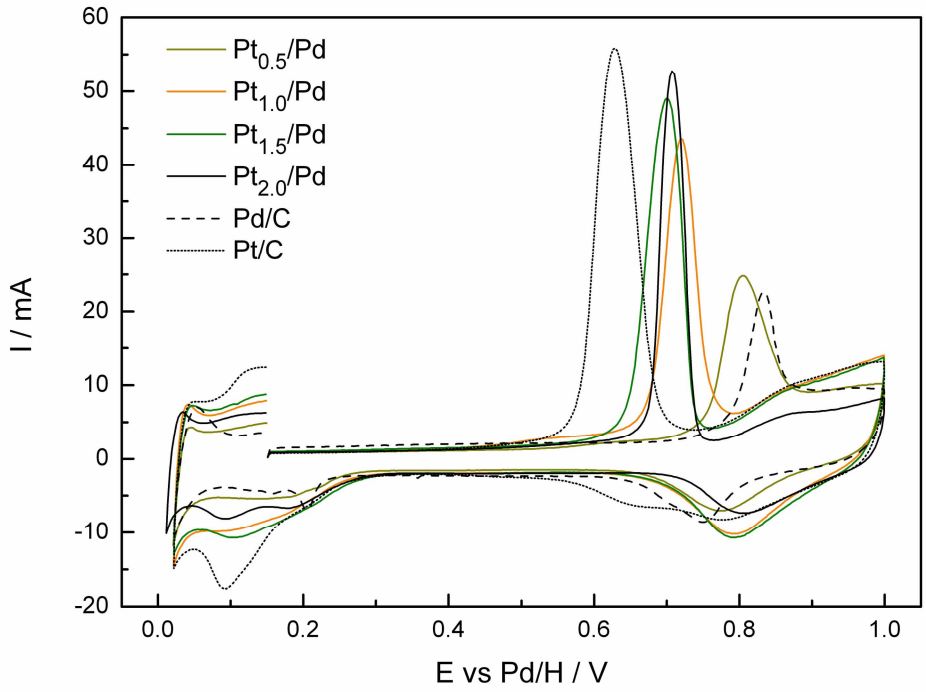

Figure 4- 13 CO cyclic voltammograms of 20% Pd/C, $Pt_{0.5}$/Pd, $Pt_{1.0}$/Pd, $Pt_{1.5}$/Pd, $Pt_{2.0}$/Pd and 40% Pt/C in 1 M H_2SO_4 at 80 °C

During CO oxidation on the core-shell catalysts, it is assumed that CO originated from both Pt and Pd atoms. However the CO peak was observed mainly as a single uniform peak rather than a mixture of Pt and Pd-like CO peaks. The peak was not simply an addition of the fractional contributions of Pt and Pd sites. This would imply an electronic modification of the CO oxidation characteristics on the two metals, due to bimetallic formation at the surface of the particles. The intermediate position of the core-shell catalyst CO peaks is due to the presence of Pt, which triggers the water activation and consequently the oxidation of CO at a lower potential than Pd. There is a tendency for the CO oxidation peak potential to shift to lower potentials as the Pt coverage increased. Thus, the CO peak potential of the core-shell catalysts may, to a certain extent, give some indication of how complete the Pt shell coverage is. However, the electronic effect arising from the Pt/Pd "ligand effect" characteristic to bimetallics, may have also influenced the potential at which the CO electrooxidation occurred. The significant increase in the CO charges per gram of total metal generated on the core-shell surfaces compared to that of Pd may result from an increase in the proportion of single-bonded CO species as well as an increase in the surface area.

The ratios between the CO and H charges (Q_{CO}:Q_H) were calculated for the core-shell catalysts and the Pd/C and Pt/C catalysts. For Pt, this ratio is close to 2 since the oxidation of CO is a two-electron process whereas the adsorption of H is one-electron process. It can be noticed that Q_{CO}:Q_H for Pd/C is higher than 2, suggesting that H was not absorbed in the Pd lattice. The absorption of H would have been indicated by an excess of H charges, and consequently a Q_{CO}:Q_H ratio lower than 2. This observation can be attributed to the highly dispersed character of the supported Pd catalyst, which may not be favourable to the formation of hydride phase (15). However, this does not explain the excess of CO charges observed for Pd/C and $Pt_{0.5}$/Pd. The other core-shell catalysts have a similar Q_{CO}:Q_H ratio to that of Pt/C.

Table 4- 7 Charges for the hydrogen adsorption and CO electrooxidation processes.

Catalysts	Q_H charge / $C.mg_{(Pt+Pd)}^{-1}$	Q_{CO} charge / $C.mg_{(Pt+Pd)}^{-1}$	CO peak potential / mV	CO/H	ECA / m^2 $g^{-1}_{(Pt+Pd)}$
20% Pd	0.06	0.15	834	2.8	50.5
$Pt_{0.5}$/Pd	0.11	0.30	804	2.6	86.4
$Pt_{1.0}$/Pd	0.11	0.22	719	2.0	83.7
$Pt_{1.5}$/Pd	0.13	0.28	701	2.2	92.7
$Pt_{2.0}$/Pd	0.10	0.19	725	2.1	67.3
40% Pt	0.13	0.28	629	2.1	61.6

4.4.2. Electrochemical stability

The electrochemical stability of the core-shell catalysts was assessed by cycling the electrodes 1000 times between 0.6 and 1.0 V at 20 mV s^{-1} at 80 ^oC in 1 M H_2SO_4. To follow the changes at the catalyst surfaces upon cycling, CV and CO oxidation voltammograms were performed after every 200 cycles. The successive voltammograms recorded after 0, 200, 600 and 1000 cycles are shown in Figure 4-14. The electrolyte (100 mL) was sampled (~5 mL) with the same regularity, then analyzed by ICP-ES to evaluate the rate of metal dissolution during the stability test. The volume of the electrolyte solution was kept constant by addition of the same volume of fresh sulfuric acid (1 M).

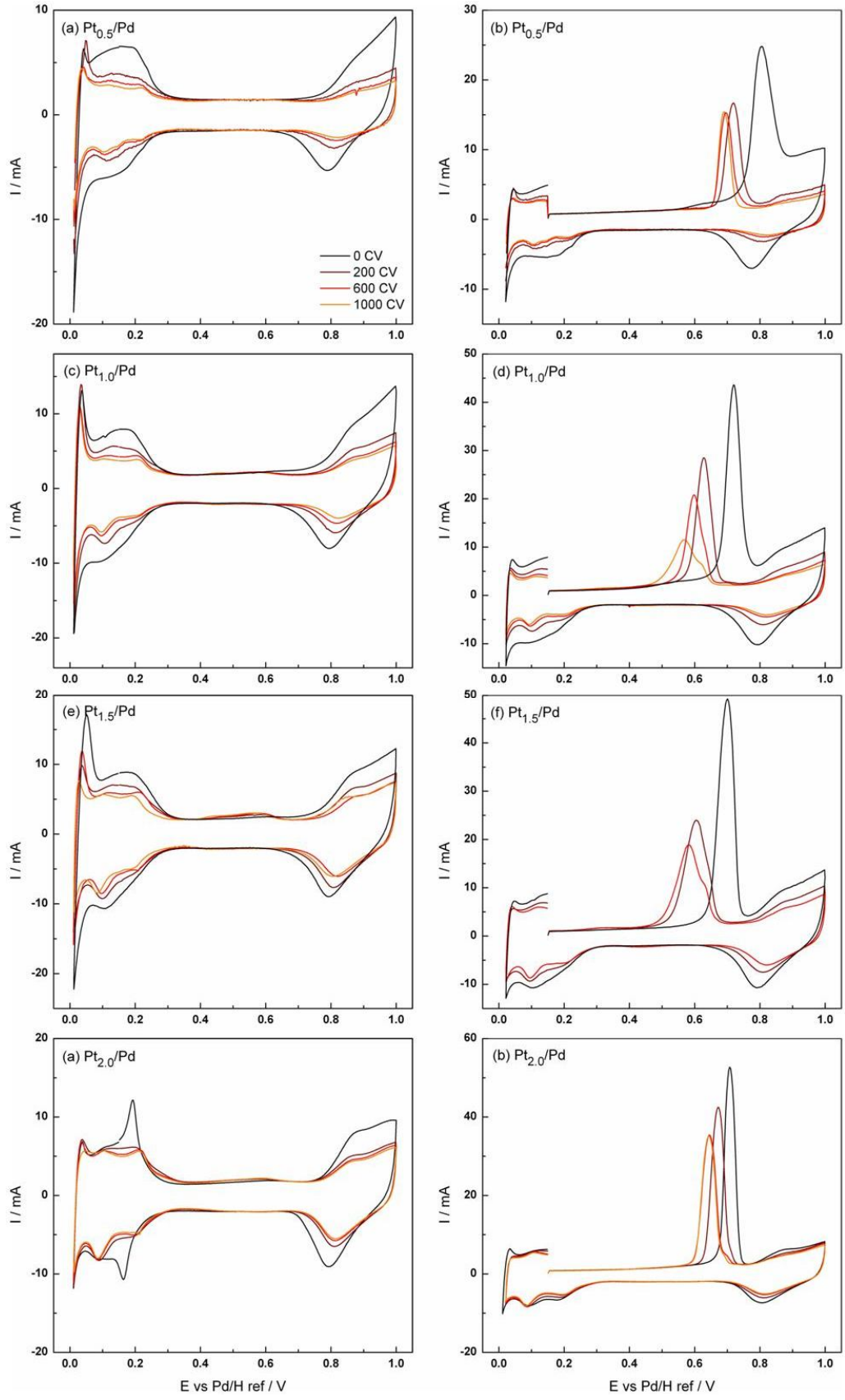

Figure 4-14 CV (on the left) and CO electrooxidation voltammograms (on the right) of $Pt_{0.5}/Pd$, $Pt_{1.0}/Pd$, $Pt_{1.5}/Pd$ and $Pt_{2.0}/Pd$ recorded after 0, 200, 600 and 1000 polarisation scans (0.6-1.0 V) in 1 M H_2SO_4, υ = 10 mV s^{-1}, at 80 °C.

It can be seen that during the cycling regime the shape of the core-shell CVs changed progressively becoming more Pt-like. The Pt characteristic features in the hydrogen adsorption region became more and more pronounced, while the oxide reduction peak shifted to higher potentials. This was accompanied by a loss in the CV areas. Changes are apparent in the CO oxidation peaks. These moved towards negative potentials and the corresponding oxidation charges decreased with the number of cycles.

The rate of electrochemical area loss was determined from the depletion rate of the sorbed H charges and CO oxidation charges. The H and CO charges decreased at a similar rate for all catalysts, as shown in Figure 4-16. This once again indicates that the contribution of the hydrogen absorption to the sorbed H charge is not significant. In fact, for the core-shells as well as for Pt/C, the CO:H ratio of the charges remained close to 2 during the cycling regime, as shown in Figure 4-15(b). As expected, Pd/C was the most unstable and most of the Pd was dissolved within 50 cycles. The electrochemical stability of the tested catalysts was expressed through the H and CO charge losses during the cycling regime. The stability of the core-shell catalysts was evaluated after 1000 cycles and the results are shown in Figure 4-14(a). It can be seen that the association of Pt with Pd considerably improved the cycling stability and that there was a systematic dependence between the Pt coverage and the stability. $Pt_{1.5}/Pd$ and $Pt_{2.0}/Pd$ showed even better stability than Pt/C.

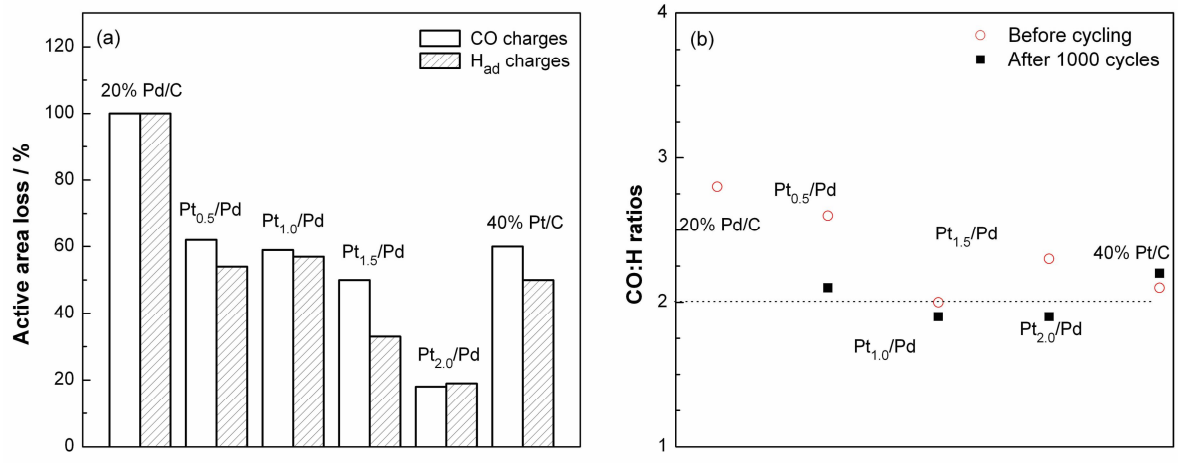

Figure 4- 15 Calculated loss of hydrogen sorbed charges for the voltammograms shown in Figure 4-14.

The change in the voltammogram shape and the decrease in the H and CO charges can be interpreted as being due to the dissolution of Pd during cycling, which leads to a Pt-enrichment of the surface. The electrolyte analysis, as shown in Figure 17(a) and (b) for $Pt_{1.0}$/Pd and $Pt_{2.0}$/Pd, revealed high variations of the level of dissolved Pd, whereas the level of dissolved Pt remained low and nearly constant. The variation of the Pd may be the consequence of Pd deposition on the counter electrode. The results suggest that while Pd was dissolved upon polarization scans, the Pt atoms may have redistributed around the Pd core to give a more complete shell, which explains the appearance of pronounced Pt features in the CV. There was no evidence of dissolution of the Pt shell.

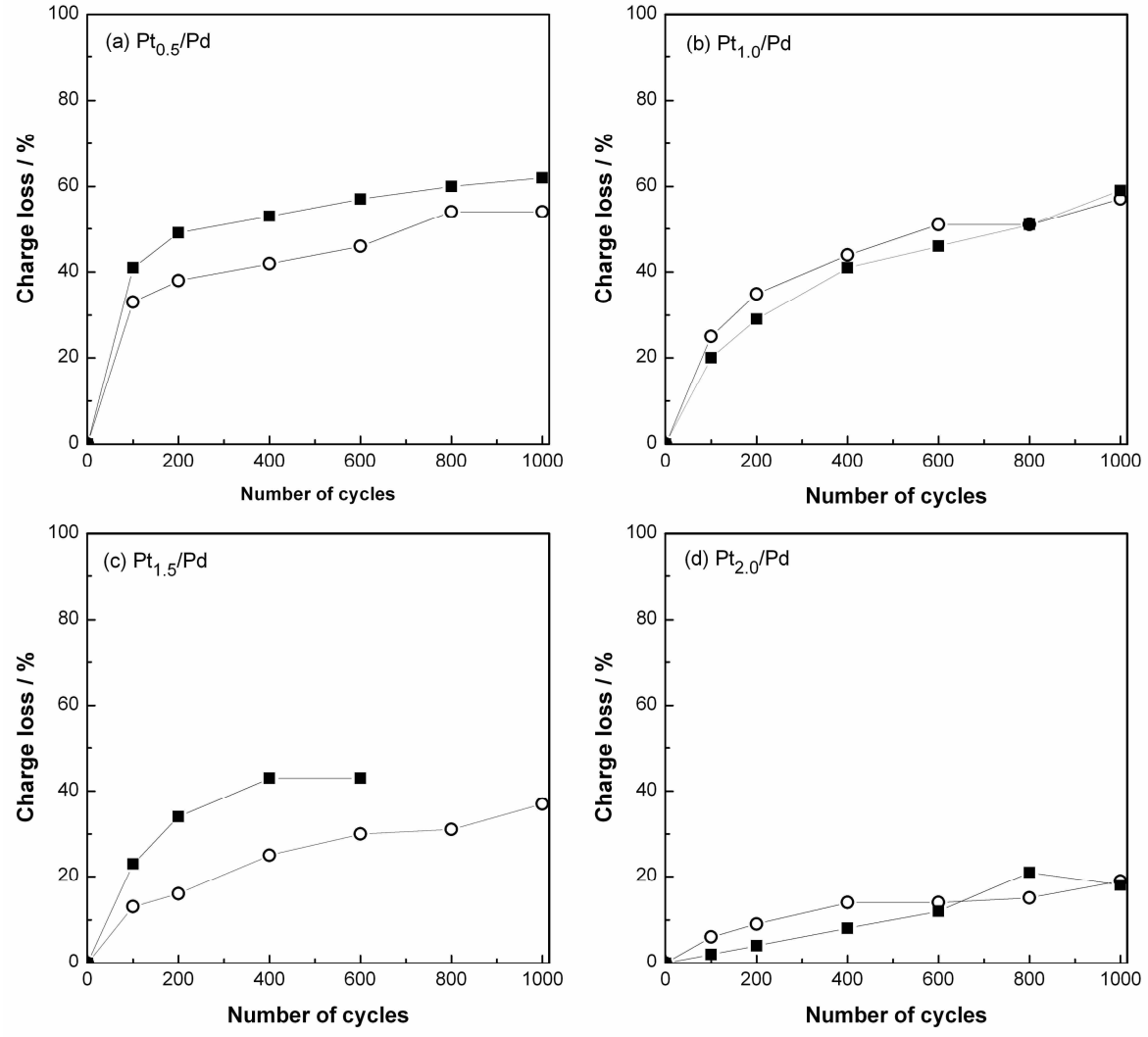

Figure 4- 16 Evolution of H and CO charges as a function of the number of polarisation scans for $Pt_{0.5}$/Pd (a), $Pt_{1.0}$/Pd (b), $Pt_{1.5}$/Pd (c) and $Pt_{2.0}$/Pd (d).

Pd instability can be explained by the contribution of two processes (16): the electrodissolution of Pd and the electrooxidation of Pd, according to equations 4-7 and 4-8, respectively:

$$Pd \rightarrow Pd^{2+} + 2e^{-} \quad \textbf{(4- 7)}$$

$$Pd + H_2O \rightarrow PdO + 2H^{+} + 2e^{-} \quad \textbf{(4- 8)}$$

In the conditions of the experiment (1 M H_2SO_4, 80 °C), the electrooxidation of Pd starts at about 0.72 V vs Pd/H ref. In addition, the rate of Pd electrodissolution is enhanced in sulfuric acid as there is a strong interaction between acid sulphate ions and the polarized Pd surface, which leads to the formation of a highly soluble Pd sulphate species (9, 16).

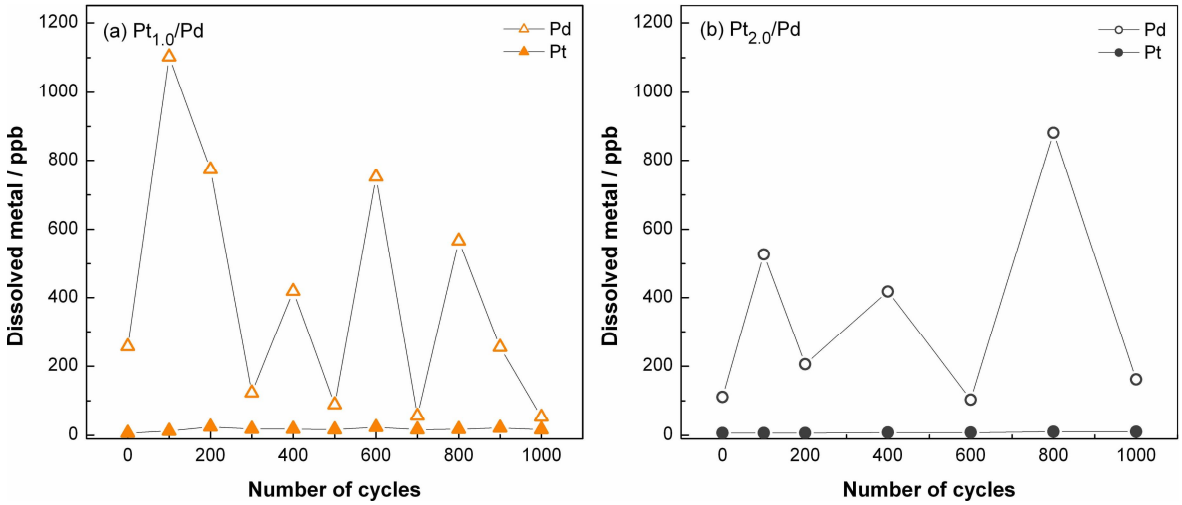

Figure 4- 17 Pd and Pt dissolution during stability test for $Pt_{1.0}/Pd$ (a) and $Pt_{2.0}/Pd$ (b).

4.4.3. Activity for the reduction of oxygen

RDE measurements

Preliminary screening of the ORR activity of the core-shell catalysts was conducted using rotating-disk electrode measurements in 0.1 M $HClO_4$ saturated with oxygen and at ambient temperature. The thin film method has the advantage of allowing control of mass transfer thereby allowing evaluation of the kinetic ORR activity. Figure 4-18 displays the rotating-disk polarization curves at 2500 rpm and the corresponding Levich plots for a 400 to 2500 rpm range of rotation speeds, for the Pt_x/Pd core-shell catalysts, a 20%Pd/C and a standard 40% Pt/C provided by Johnson Matthey Technology Centre. The amounts of catalyst deposited on the electrodes were chosen so that the thickness of the catalyst layers

remained constant between the electrodes to minimise internal mass-transfer limitation (17). Each measurement was performed two to three times to ensure reproducibility of the data. The Pt loadings for the core-shell and 40% Pt/C catalysts are reported in Table 4-9.

The shape of the Pd hydrodynamic curve appeared very different from that of 40%Pt/C and the core-shell catalysts, suggesting a deviation from the mass transport controlled regime. However, this shape was always observed despite changes applied to the catalyst ink composition and the catalyst layer uniformity. A lower value of limiting current is observed for Pd/C, which may indicate that on Pd the ORR may also follow the 2-electron reduction mechanism. As indicated by the positive onset of the reduction of oxygen, the activity of the core-shell surfaces are higher than that of Pd. It is known that Pd exhibits poor catalytic activity compared to Pt for the ORR (1, 18-20).

The comparison of the polarization curves in the kinetic region (from 0.85 V vs Pd/H ref.) showed that the catalytic activity of the core-shells is higher than that of Pd/C and lower than that of Pt/C, except for $Pt_{2.0}$/Pd that showed same activity as Pt/C. This represents a great improvement as $Pt_{2.0}$/Pd contains just half the Pt loading of the Pt/C electrode. It can be noted that the ORR limiting current values were similar for Pt/C and the Pt_x/Pd core-shells. This suggests that the ORR mechanism on the Pt/Pd core-shells follows mainly the 4-electron pathway. The limiting currents should obey the Levich equation to validate the RDE experiment. The straightness of the core-shell and Pt/C Levich plots confirms that the experiment was conducted under mass transport control.

Table 4- 8 Pt loading deposited on RDE electrodes for Ptx/Pd core-shells and 40%Pt/C.

	$Pt_{0.5}$/Pd	$Pt_{1.0}$/Pd	$Pt_{1.5}$/Pd	$Pt_{2.0}$/Pd	40% Pt/C
Pt loading / μg cm^{-2}	3.2	5.4	9.2	11.2	20

Figures 4-18 (c) and (d) show the mass transport-corrected Tafel plots normalized by the electrochemical surface area (per cm^2 Pt) and by the Pt loading (per mg Pt). They were derived from the hydrodynamic curves (Figure 4-18(a)), which were corrected for diffusion to give the kinetic currents using the Koutecky-Levich analysis:

$$\frac{1}{i} = \frac{1}{i_K} + \frac{1}{i_L} \qquad \textbf{(4- 9)}$$

Where i is the experimental value of the current, i_k, the kinetic current and i_L the limiting value of the diffusion current given by the Levich equation (Section 2.6.2).

There are generally two ways of expressing the catalytic activity. These are:

- Mass activity = current / mass of catalyst
- Specific activity = current / surface are of catalyst

The mass activity has economical implications for fuel cells, since the cost of the electrodes depends on the amount of Pt used. The specific activity is more meaningful in terms of structure-sensitivity. The mass activity and the specific activity correspond to the graphs E vs. $log[i/(i_L-i)]/(Pt_{loading})$ and $log[i/(i_L-i)]/EPSA$, respectively. The catalytic activity of the electrocatalysts was determined from the kinetic current at 0.9 V, where the diffusion term in Equation 4-9, is considered negligible.

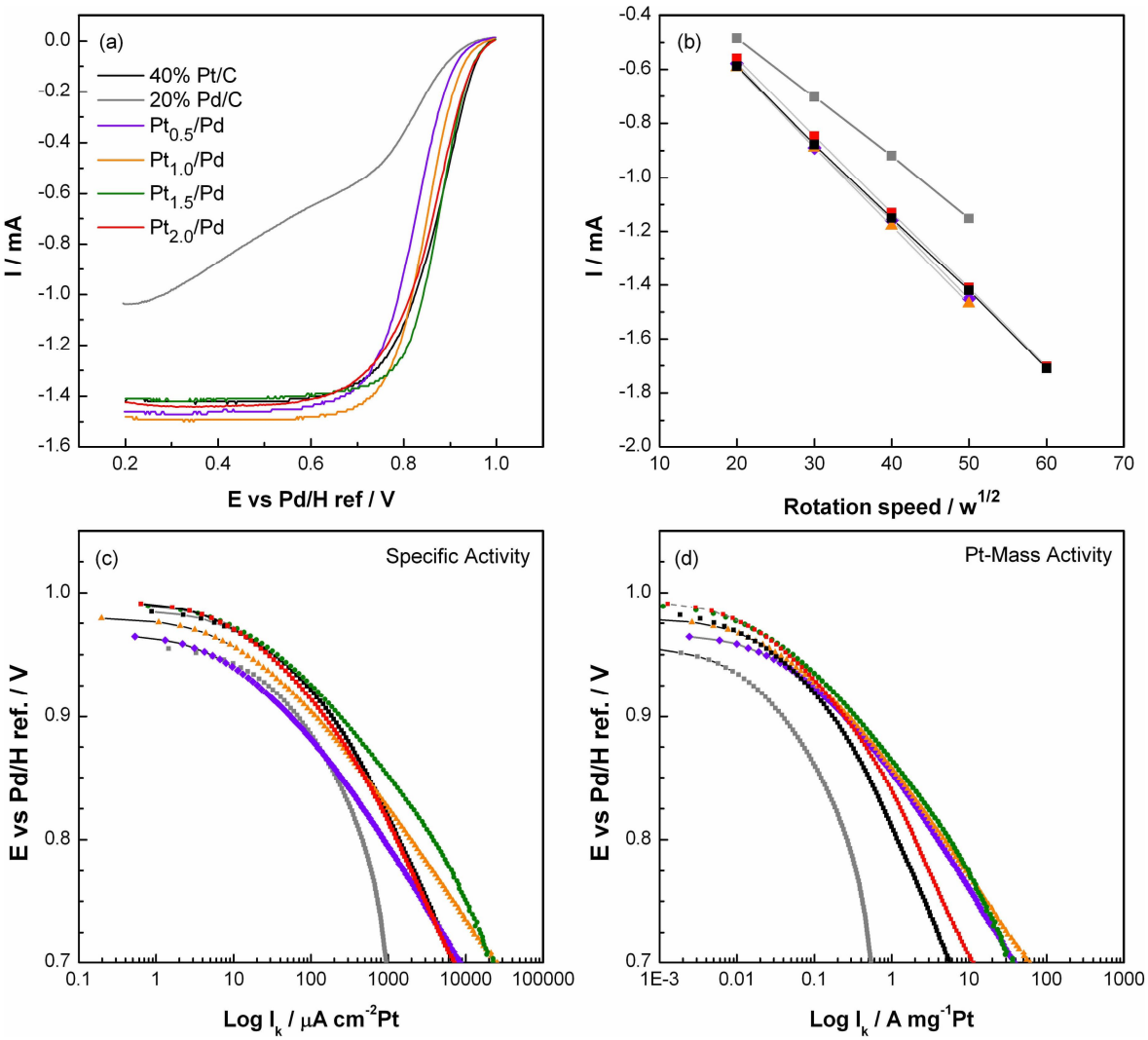

Figure 4- 18 Polarisation curves (backward scans) for the ORR on Ptx/Pd core-shell catalysts and 40% Pt/C (a). Levich plots (b). Tafel plots corrected for the electrochemical area (c) and for the Pt mass (d). Electrode geometric area: 0.196 cm2.

Figure 4-19(a) show the relationship between the Pt coverage and the mass activity at 0.9 V vs Pd/H ref. All the Pt_x/Pd core-shells exhibited greater Pt-mass activity than Pt/C, showing the benefits of the Pt overlayer. In terms of total mass activity, only $Pt_{1.5}/Pd$ and $Pt_{2.0}/Pd$ show equivalent activity to Pt, probably due to a better Pt coverage.

The ORR specific activity with respect to the Pt coverage is shown in Figure 4-19(b). $Pt_{1.5}/Pd$ exhibited the highest specific activity, which agrees with the trend observed earlier for the hydrogen sorption and CO areas of the core-shell surfaces. $Pt_{2.0}/Pd$ was the second most active, followed by Pt.

According to Nørskov's d-band centre model (21), the association of Pt and Pd, either by alloying or overlaying, results in a change of the electron density around Pt atoms by

raising the d-band centre (21). The high activity of $Pt_{2.0}$/Pd and $Pt_{1.5}$/Pd may be a consequence of the changes in the d-band property of the Pt atoms caused by their interaction with the Pd core. The fact that the Pt coverage was incomplete on the core-shells may have benefited the ORR activity by preferentially creating Pd-OH_{ads}, thus keeping more Pt sites available for the reduction of O_2 (22). The roughness of the core-shell surfaces, due to the formation of Pt 3D-islands, may also contribute to the enhanced ORR activity. The low activity of $Pt_{0.5}$/Pd and $Pt_{1.0}$/Pd activities compared to that of Pt can be explained by insufficient Pt-Pd interactions due to poor Pt coverage.

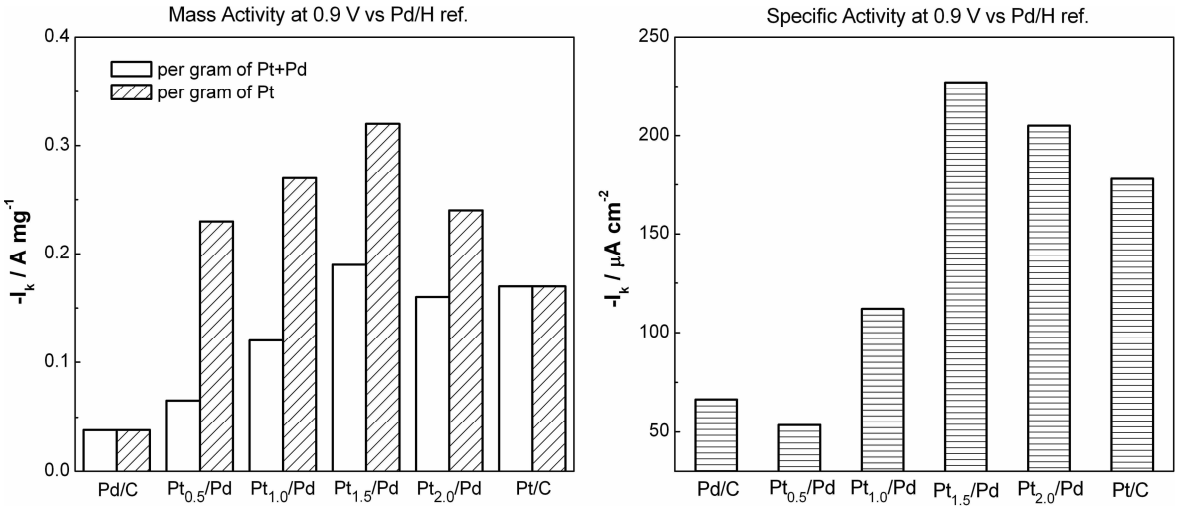

Figure 4- 19 Relationship between the Pt coverage and the ORR mass activity (a) and specific activity (b) at 0.9 V vs Pd/H ref. determined by analysis of the polarisation surves reported in Figure 4-18(a).

Single-cell test

The performance of two MEAs prepared with $Pt_{1.5}$/Pd and $Pt_{2.0}$/Pd as the cathode catalysts with 40% Pt/C as the anode catalyst, were assessed in a hydrogen-oxygen single cell at 0.9 V cell voltage, as shown in Figure 4-20. As described Section 2.6.3, oxygen was flowed to the cathode whereas hydrogen was flowed to the anode Switch to H2/O2 & measure OCVto perform steady state polarisation measurements. The cell was first conditioned by performing fast polarisation curves, where the potential was stepped by 0.05 V every 5 s from 0.95 V to 0.65 V vs. RHE. Then two slow polarisation curves were recorded from 0.95 V to 0.65 V vs. RHE, at a step potential of 0.026 V and a time interval of 30 s. The data were corrected for ohmic losses.

The current density of the MEA with $Pt_{2.0}$/Pd as the cathode catalyst was 45 mA cm^{-2}, the same as that of the MEA prepared with 40wt% Pt/C and operating under the same conditions, whereas that of $Pt_{1.5}$/Pd was 21 mA cm^{-2}. In terms of catalytic activity per milligram of Pt, these values translate into 102, 120 and 154 mA $mgPt^{-1}$ for $Pt_{1.5}$/Pd, 40% Pt/C and $Pt_{2.0}$/Pd, respectively. $Pt_{1.5}$/Pd performance was lower than that of $Pt_{2.0}$/Pt, in constrast to the activity measured by RDE. The results indicate that the Pt/Pd particles could be promising catalysts for the cathodes of PEM fuel cells with a much reduced Pt content but increased catalytic activity.

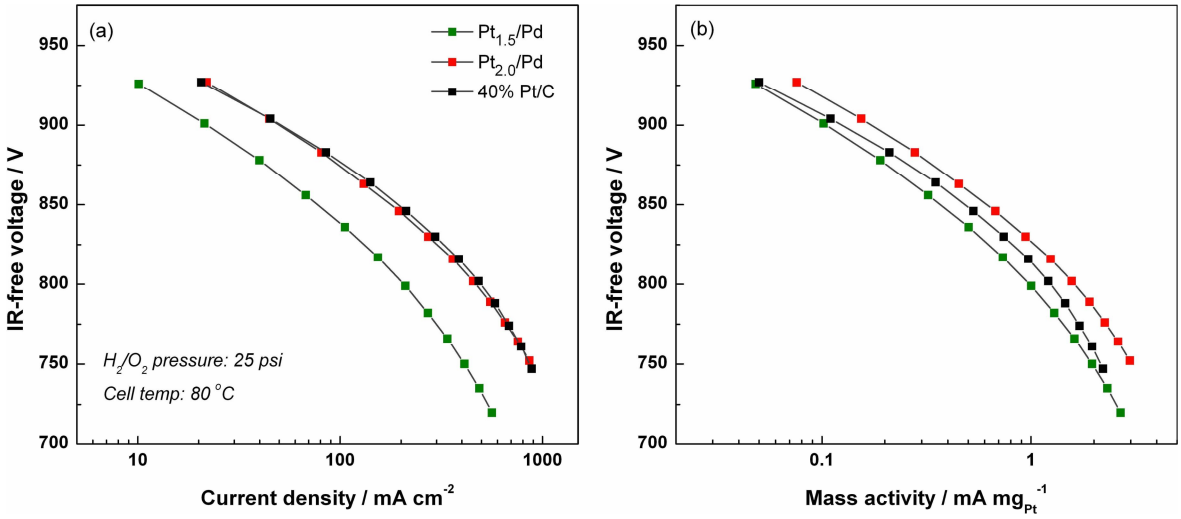

Figure 4- 20 Performances of MEAs prepared with $Pt_{1.5}$/Pd (0.21 mgPt cm^{-2}), $Pt_{2.0}$/Pd (0.29 mgPt cm^{-2}) and 40%Pt/C (0.4 mgPt cm^{-2}) as the cathode catalysts, in H_2/O_2 single cell. The results are presented as cell voltage corrected for the IR drop versus the current density (a) and the Pt-mass activity (b).

4.5. Conclusion

In order to understand the electronic and geometric effect between the Pt (sub)monolayer with the Pd particles on the ORR activity, Pt/Pd core-shell electrocatalysts with different Pt coverage were prepared. To eliminate the particle size effect, the core-shell catalysts were prepared from the same Pd/C catalyst. These catalysts were characterized by various techniques. XRD analysis did not provide much information for the core-shell catalysts due to their small sizes and to the low amount of Pt. However, the analysis of $Pt_{2.0}$/Pd revealed the presence of a Pd-richer PtPd alloy phase with an expanded lattice parameter compared to that of the documented Pd. The change of the lattice

constant may result from the interpenetration of Pd and Pt, which is in agreement with the DFT predictions on segregation phenomenon in Pt/Pd systems. A change in the Pt-Pt and Pt-Pd distances was also observed using EXAFS analysis and supported the XRD results. However, structural changes were not as clearly observed on the lowest Pt-loading core-shell catalysts $Pt_{0.5}$/Pd and $Pt_{1.0}$/Pd. From the aberration-corrected STEM micrographs of $Pt_{2.0}$/Pd, the Pt shell was observed due to the mass contrast between Pt and Pd. The micrographs strongly suggested a preferential deposition of Pt onto the Pd core particle edges. The Pt shell deposited by CSR was identified as 3D Pt islands localised around the low-coordinated sites of the Pd core particles. The actual Pt coverage of $Pt_{2.0}$/Pd was quantified by HS-LEIS and was found to be 65 %. This implies that the core-shell catalysts with less Pt deposited on the Pd surface have a lower Pt coverage.

The results of the stability tests performed on the core-shell catalysts showed a linear relationship between the loss of active area upon cycling and the Pt coverage. It was suggested that Pt atoms rearranged at the surface during cycling while Pd was dissolved away. A more Pt-like electrochemical behaviour was eventually obtained and was attributed to a more complete Pt shell.

A shift of oxygen reduction potential of the core-shell catalysts compared to the Pd core catalyst from CVs and the shift of the Pt 4f peaks from XPS measurements indicated a modification of the electronic structure. This observation is reflected in the ORR activity of the core-shell catalysts measured using RDE. $Pt_{1.5}$/Pd and $Pt_{2.0}$/Pd showed equivalent or greater activity compared to 40% Pt/C with significantly reduced Pt loadings.

References

1. J. H. Yang, J. Y. Lee, Q. B. Zhang, W. J. Zhou and Z. L. Liu, *Journal of the Electrochemical Society*, **155**, B776 (2008).

2. A. Renouprez, J. L. Rousset, A. M. Cadrot, Y. Soldo and L. Stievano, in *5th International School and Symposium on Synchrotron Radiation in Natural Science (ISSRNS)*, p. 50, Poland (2000).

3. H. R. J. ter Veen, T. Kim, I. E. Wachs and H. H. Brongersma, *Catalysis Today*, **140**, 197 (2009).

4. J. F. Moulder, W. F. Stickle, P. E. Sobol and K. D. Bomben, *Handbook of X Ray Photoelectron Spectroscopy: A Reference Book of Standard Spectra for Identification and Interpretation of Xps Data*, Physical Electronics (February 1995) (1995).

5. W. Wang, Q. Huang, J. Liu, Z. Zou, M. Zhao, W. Vogel and H. Yang, *Journal of Catalysis*, **266**, 156 (2009).

6. A. M. Venezia, *Catalysis Today*, **77**, 359 (2003).

7. B. Hammer and J. K. Norskov, *Advances in Catalysis*, **45**, 71 (2000).

8. D. C. Papageorgopoulos, M. Keijzer, J. B. J. Veldhuis and F. A. de Bruijn, *Journal of the Electrochemical Society*, **149**, A1400 (2002).

9. M. Hara, U. Linke and T. Wandlowski, *Electrochimica Acta*, **52**, 5733 (2007).

10. C. Gabrielli, P. P. Grand, A. Lasia and H. Perrot, *Journal of the Electrochemical Society*, **151**, A1937 (2004).

11. A. Czerwinski, R. Marassi and S. Zamponi, *Journal of Electroanalytical Chemistry*, **316**, 211 (1991).

12. L. Birry and A. Lasia, *Electrochimica Acta*, **51**, 3356 (2006).

13. R. Jurczakowskia, B. Łosiewicza and A. Lasiaa, *ECS Transactions*, **2**, 11 (2007).

14. J. Solla-Gullon, V. Montiel, A. Aldaz and J. Clavilier, *Electrochemistry Communications*, **4**, 716 (2002).

15. N. K. Nag, *Journal of Physical Chemistry B*, **105**, 5945 (2001).

16. A. Bolzan, M. E. Martins and A. J. Arvia, *Journal of Electroanalytical Chemistry*, **207**, 279 (1986).

17. Y. H. Shih, G. V. Sagar and S. D. Lin, *Journal of Physical Chemistry C*, **112**, 123 (2008).

18. J. Zhang, Y. Mo, M. B. Vukmirovic, R. Klie, K. Sasaki and R. R. Adzic, *Journal of Physical Chemistry B*, **108**, 10955 (2004).

19. M. B. Vukmirovic, J. Zhang, K. Sasaki, A. U. Nilekar, F. Uribe, M. Mavrikakis and R. R. Adzic, *Electrochimica Acta*, **52**, 2257 (2007).

20. J. J. Salvador-Pascual, S. Citalan-Cigarroa and O. Solorza-Feria, *Journal of Power Sources*, **172**, 229 (2007).

21. A. Ruban, B. Hammer, P. Stoltze, H. L. Skriver and J. K. Norskov, in *1st Francqui Colloquium on Molecular Heterogeneous Catalysis*, p. 421, Brussels, Belgium (1996).

22. J. Zhang, Y. Mo, M. B. Vukmirovic, R. Klie, K. Sasaki and R. R. Adzic, *Journal of Physical Chemistry B*, **108**, 10955 (2004).

CHAPTER 5

EFFECT OF THE Pd CORE SIZE ON THE PROPERTIES OF THE Pt_{SHELL}/Pd_{CORE} ELECTROCATALYSTS

CHAPTER 5: Effect of Pd core size on the properties of the Pt_{shell}/Pd_{core} electrocatalysts

5.1. Introduction

In Chapter 4, it was shown that Pt deposition following the CSR route was influenced by surface defects on the core. Pt deposition was found to be more concentrated at the edges and corners of the Pd particles. In this chapter the effects of the core particle size on the catalyst structure and activity will be developed. As the particle size grows, the surface area decreases and the surface structure changes (1). This should influence both the reactivity and the stability of the particle surface. Large particles (> 4 nm) have a higher proportion of (100) faces which are more sensitive to the adsorbed OH inhibiting effect (2). However, as shown in the previous chapter, the Pt/Pd core-shells prepared by CSR do not have a complete and uniform shell, which may change the relationship between particle size and ORR activity. The electronic effect arising from the Pt shell formation may compensate for the loss in activity of large particles.

The commercial advantage of large core particles is that they use less Pt, relative to the total metal content of the catalyst to form the shell, which is in line with the aim of reducing the Pt loading in ORR electrocatalysts. Given that the electrochemical stability of the Pt/Pd core-shell catalysts was the best with the equivalent of two Pt monolayers (ML), the core-shells prepared for study in this chapter also have two Pt ML. In the following, the catalysts will be denoted as $Pt_{2.0}/Pd_{3nm}$, $Pt_{2.0}/Pd_{5nm}$ and $Pt_{2.0}/Pd_{10nm}$, where the size given for the core was measured by TEM. The electrocatalysts were characterised using a variety of methods and the Pt shell coverage of the core quantified. Their electrochemical properties and ORR activities were assessed.

5.2. Preparation and characterisation of Pd/C core

Different sizes of carbon-supported Pd core particles were obtained by annealing the core catalysts in a furnace at different temperatures. The starting core catalysts had

different Pd contents because they were from different batches. The resulting catalysts were analysed by TEM, XRD and CO chemisorption to evaluate the particle size distributions and dispersion over the carbon support. The Pd core characteristics are summarised in Table 5-1.

Table 5- 1 Physical characteristics of Pd/C catalysts.

	Assay / wt%	Annealing	Pd dispersion* / %	TEM / nm	XRD / nm
Pd_{3nm}	18.5 ± 1.5	200°C	56	3	N/A
Pd_{5nm}	19.5 ± 1.6	500°C	23	4.7	3.6
Pd_{10nm}	18.0 ± 1.4	600°C	18.6	10.5	5.3

*measured by CO chemisorption

The homogeneity of the Pd/C catalysts was investigated by TEM. The micrographs shown in Figures 5-1, 5-2 and 5-3 were taken in the Bright Field Mode, where Pd particles appear darker than the carbon support. The Pd core had a mean particle size of 3.0, 4.7 and 10.5 nm, respectively as shown by their particle size distributions in Figure 5-4. Pd_{3nm} particles seemed well-dispersed on the support. Particles of different sizes can be observed for Pd_{5nm} and the darkest spots can result from the association of several particles.

The particle sizes increased upon annealing under flowing hydrogen. As shown by the TEM histograms of the annealed Pd particles (Figure 5-4), there was a significant broadening of the size distribution upon increasing annealing temperature. The particle size distribution (PSD) for Pd_{3nm} was bimodal and peaked at 3 and 7 nm. The presence of large particles in this sample must originate from the synthetic preparation, as particle agglomeration was not expected at an annealing temperature of 200 °C. A multimodal distribution was obtained for Pd_{10nm}. The mean particle size is not, in this case, very representative of the catalyst. The particle size distribution peaked at 5, 12 and 18 nm, showing that the properties of this catalyst will be an expression of these different sizes.

The particles were more facetted as the particle size increased, as can be seen by comparing Figures 5-2 and 5-3. Annealing allows the catalyst surface to rearrange into more stable surfaces. As a consequence, the defect density decreases and better defined crystal faces are grown.

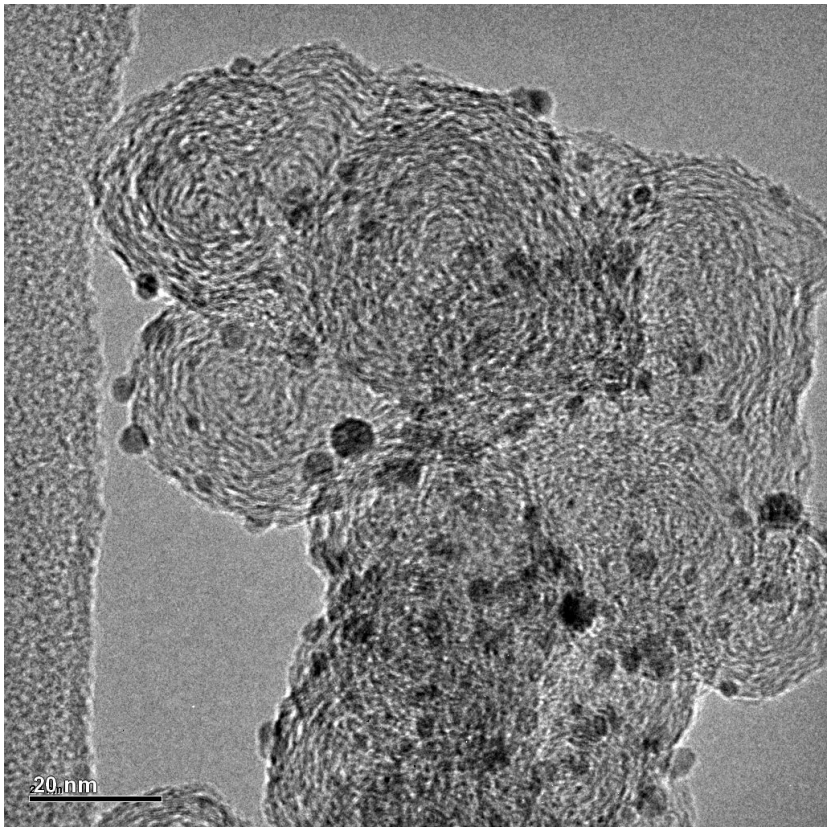

Figure 5- 1 TEM micrograph of carbon-supported Pd_{3nm}. Scale bar: 20 nm.

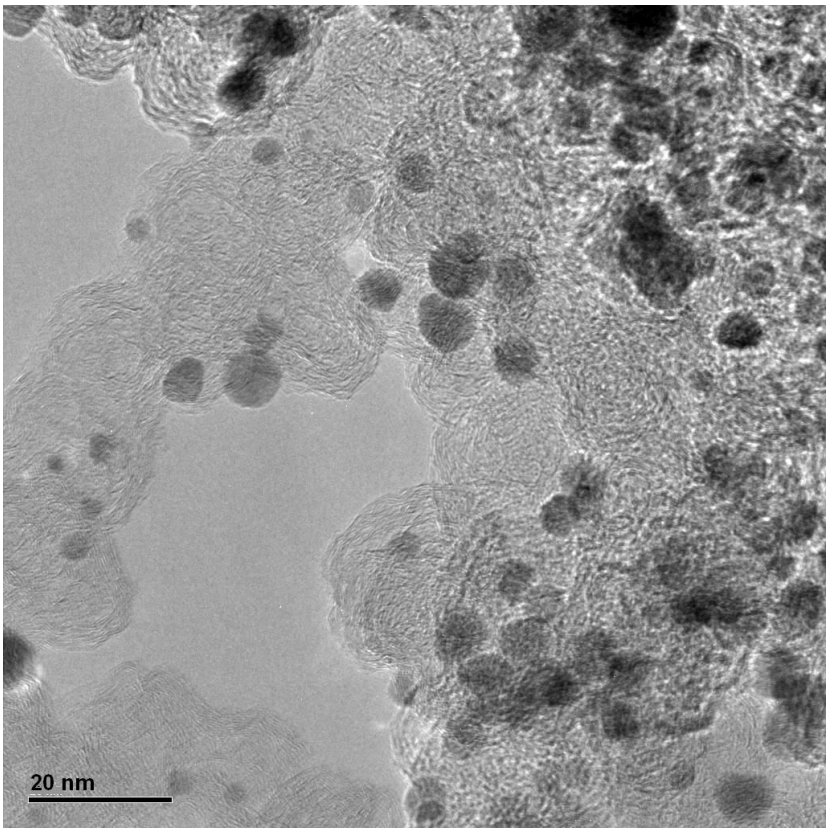

Figure 5- 2 TEM micrograph of carbon-supported Pd_{5nm}. Scale bar: 20 nm.

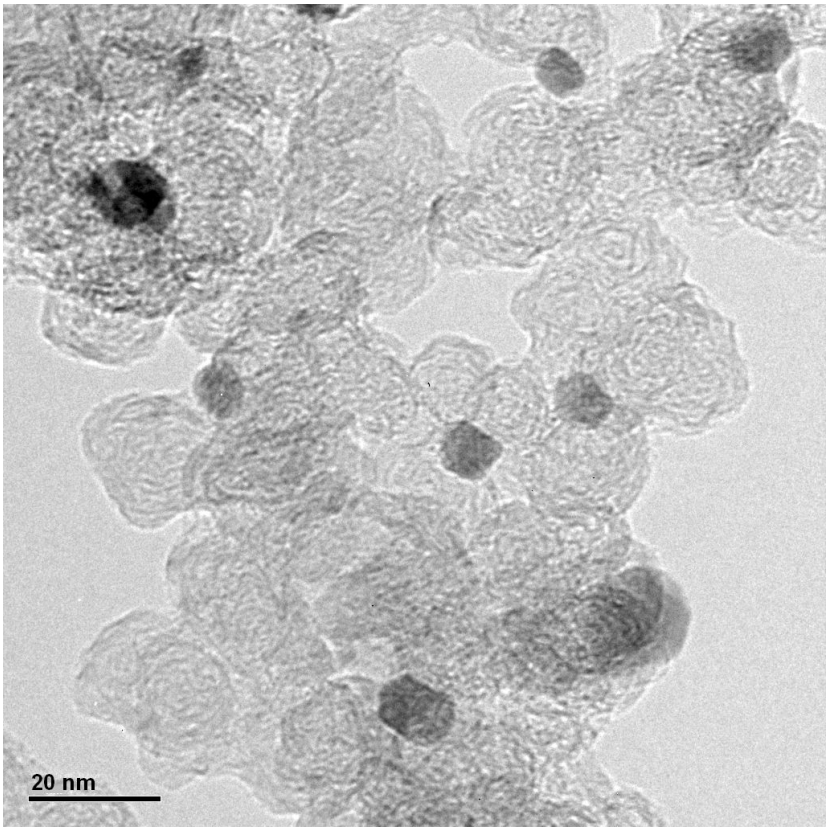

Figure 5- 3 TEM micrograph of carbon-supported Pd_{10nm}. Scale bar: 20 nm.

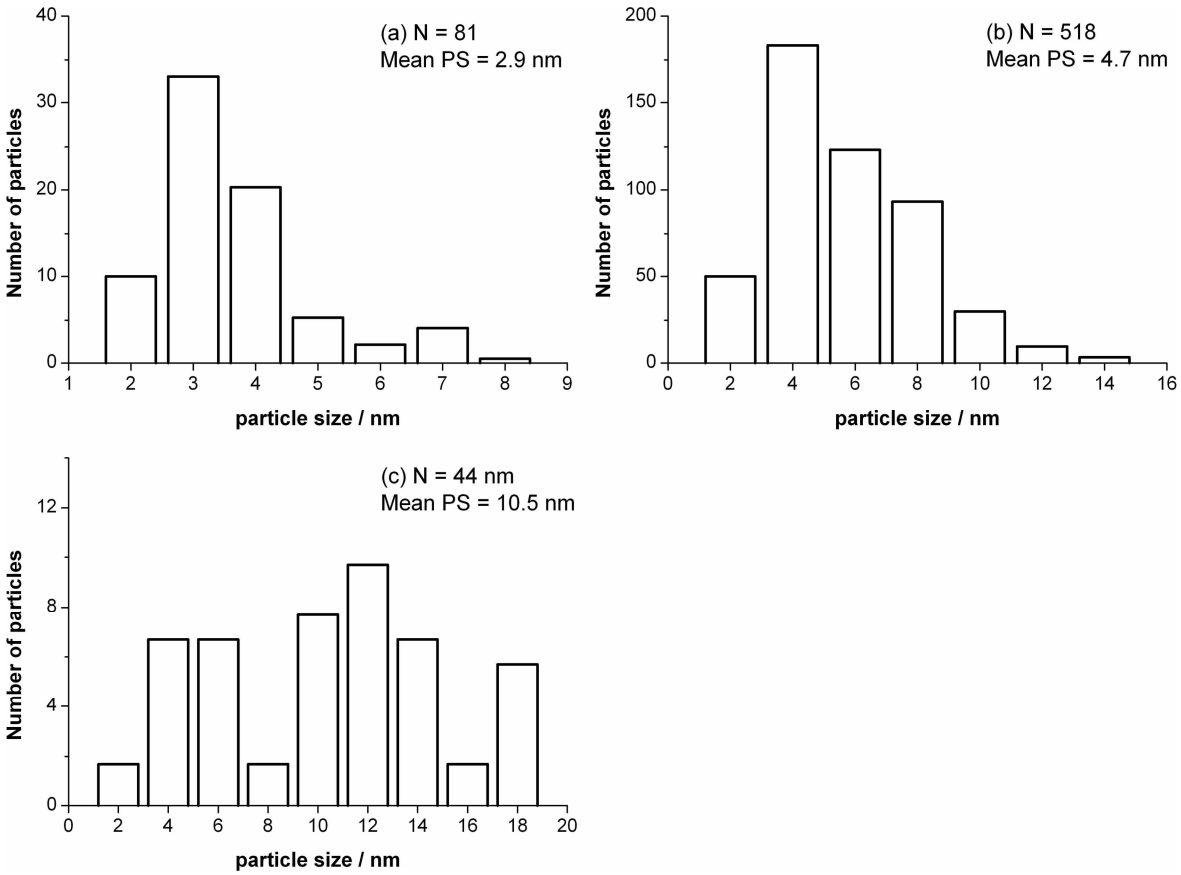

Figure 5- 4 Particle size distribution bar charts for Pd_{3nm} (a), Pd_{5nm} (b) and Pd_{10nm} (c).

When compared to the TEM particle size, the XRD crystallite size can give an idea of the extent of particle agglomeration. The XRD patterns of the Pd catalyst are presented in Figures 5-5 (a), (b) and (c). The crystallite size of Pd_{3nm} could not be calculated due the non-gaussian peak shapes indicating that the Pd phase comprises a range of crystallite sizes. It can be seen that increasing the temperature led to smaller full width at half maximum (FWHM), which corresponds to larger crystalline domains. However, the measured crystallite sizes were still smaller than the corresponding TEM particle sizes, confirming that particle agglomeration was present.

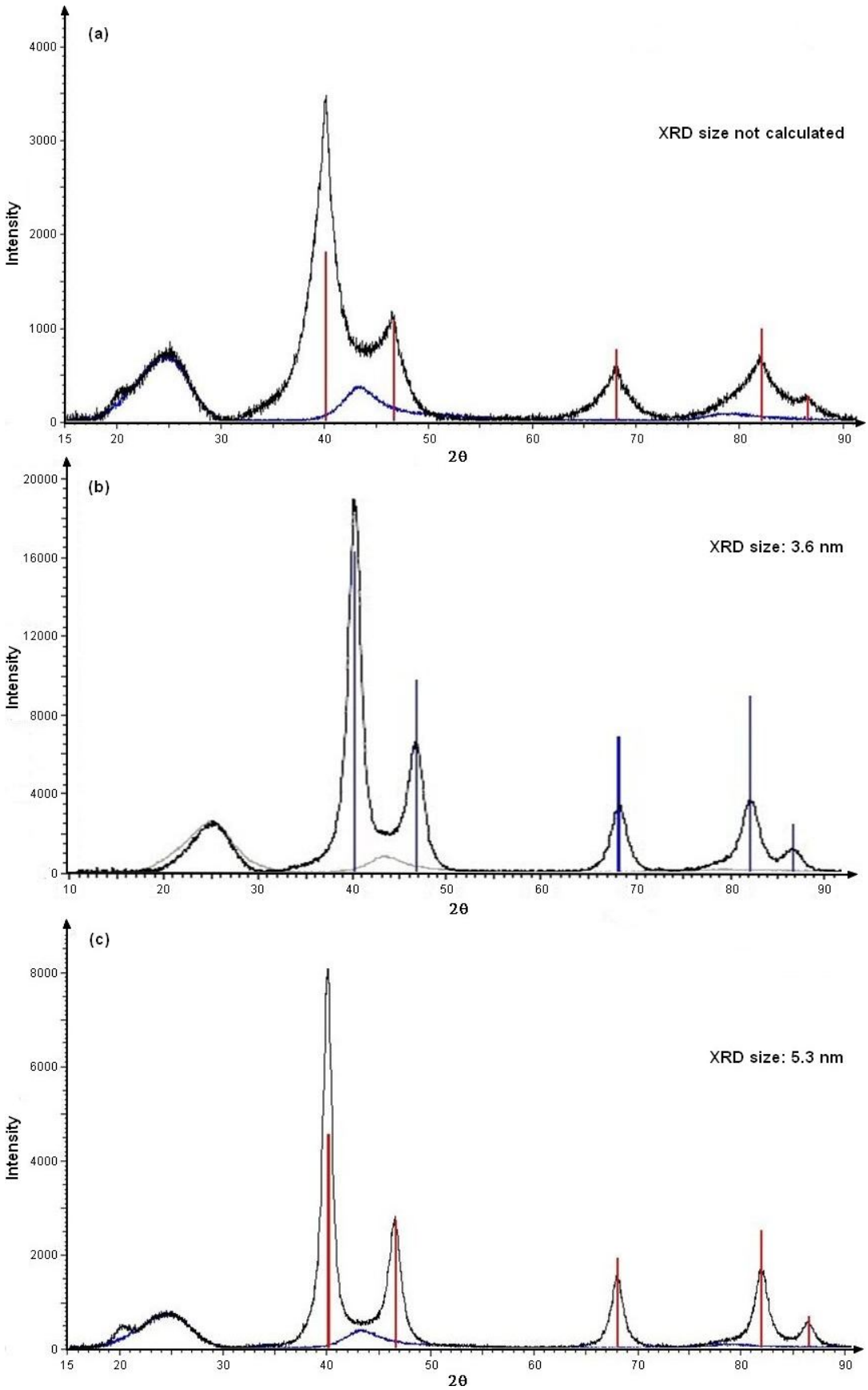

Figure 5- 5 XRD patterns of Pd_{3nm} (a), Pd_{5nm} (b) and Pd_{10nm} (c). The vertical lines represent the documented diffraction peaks of Palladium and the blue pattern represents the carbon contribution.

The particle dispersion as measured by CO chemisorption is presented in Table 5-1. As expected, the Pd dispersion decreased as the mean particle size increased. Based on Equation 2-1, which was used to calculate the necessary amount of $Pt(acac)_2$ to form one Pt ML, it can be seen that the smaller the Pd dispersion the less Pt is needed to form the shell.

5.3. Preparation of $Pt_{2.0}$/Pd core-shell electrocatalysts

The core-shell catalysts were prepared following a layer-by-layer deposition of two Pt MLs. Table 5-2 shows the visual observation and the quantitative ICP-ES analysis results of the reaction filtrates. It can be seen that the Pt deposition was complete for $Pt_{2.0}/Pd_{3nm}$ and $Pt_{2.0}/Pd_{10nm}$, but not for $Pt_{2.0}/Pd_{5nm}$, as indicated by the residual amount of Pt remaining in the toluene after the reaction. For $Pt_{2.0}/Pd_{5nm}$, the filtrate resulting from the second monolayer deposition was reacted again with the catalyst after it was heat-treated at 100 °C in the furnace and passivated to clean the surface from organic residues. An ICP-ES analysis of the filtrate showed that there was < 1 ppm of Pt after the 3rd reaction.

Table 5- 2 Filtrate analysis for the preparation of $Pt_{2.0}$/Pd core-shell catalysts.

	1st deposition		2nd deposition	
Catalyst	**Filtrate**	**Pt / ppm**	**Filtrate**	**Pt / ppm**
$Pt_{2.0}/Pd_{3nm}$	Clear	< 1 ± 0.1	clear	< 1 ± 0.1
$Pt_{2.0}/Pd_{5nm}$	Clear	49 ± 3.9	yellow	300 ± 24
$Pt_{2.0}/Pd_{10nm}$	Clear	7 ± 0.6	clear	< 1 ± 0.1

The composition of the $Pt_{2.0}$/Pd core-shells were determined by ICP-ES and the results are shown in Table 5-3. It can be seen that $Pt_{2.0}/Pd_{5nm}$ experimental Pt content is the furthest from the nominal assay, as anticipated by the filtrate analysis.

Table 5- 3 Experimental and nominal Pt and Pd assays in $Pt_{2.0}$/Pd, and Pt:Pd atomic ratios.

Catalyst	Nominal Pt assay wt%	Actual	Nominal Pd assay wt%	Actual	Pt:Pd atomic ratio
$Pt_{2.0}/Pd_{3nm}$	27.5	25.8 ± 2.1	13.4	12.2 ± 1.0	54:46
$Pt_{2.0}/Pd_{5nm}$	14.2	11.8 ± 0.9	16.7	15.4 ± 1.2	29:71
$Pt_{2.0}/Pd_{10nm}$	10.9	10.1 ± 0.8	16.0	15.6 ± 1.2	26:74

5.4. Characterisation of the Pt shell

5.4.1. XRD analysis

The XRD diffraction patterns of the core-shell catalysts are shown in Figure 5-6 (a), (b) and (c). Table 5-4 summarises the XRD parameters obtained for the $Pt_{2.0}$/Pd core-shells along with the documented values for Pt and Pd crystallites for reference. As explained in Chapter 4, a Rietveld profile was fitted for the $Pt_{2.0}/Pd_{3nm}$ pattern, revealing that the catalyst was mainly composed of a Pd-rich PtPd alloy phase. For $Pt_{2.0}/Pd_{5nm}$ and $Pt_{2.0}/Pd_{10nm}$, there was no clear evidence to indicate the presence of either Pt or PtPd alloy phases. The predominant phase detected was that of Pd. However the calculated lattice parameter was still slightly larger than that expected for a pure Pd phase, which may be due to Pt. The lattice expansion was the largest for $Pt_{2.0}/Pd_{10nm}$, which also had the least amount of Pt. The Pd crystallite size of the core-shell catalysts determined by XRD is very close to the TEM mean particle size found for the corresponding Pd core, but twice that of the Pd core crystallite size determined by XRD.

Table 5- 4 Experimental XRD parameters

	Phases	Crystallite size / nm	Lattice parameter / Å	Cell volume / $Å^3$
Pd	-	-	3.890	58.87
Pt	-	-	3.923	60.38
$Pt_{2.0}/Pd_{3nm}$	PtPd	2.36	3.898	59.23
$Pt_{2.0}/Pd_{5nm}$	Pd	3.96	3.895	59.08
$Pt_{2.0}/Pd_{10nm}$	Pd	9.7	3.900	59.32

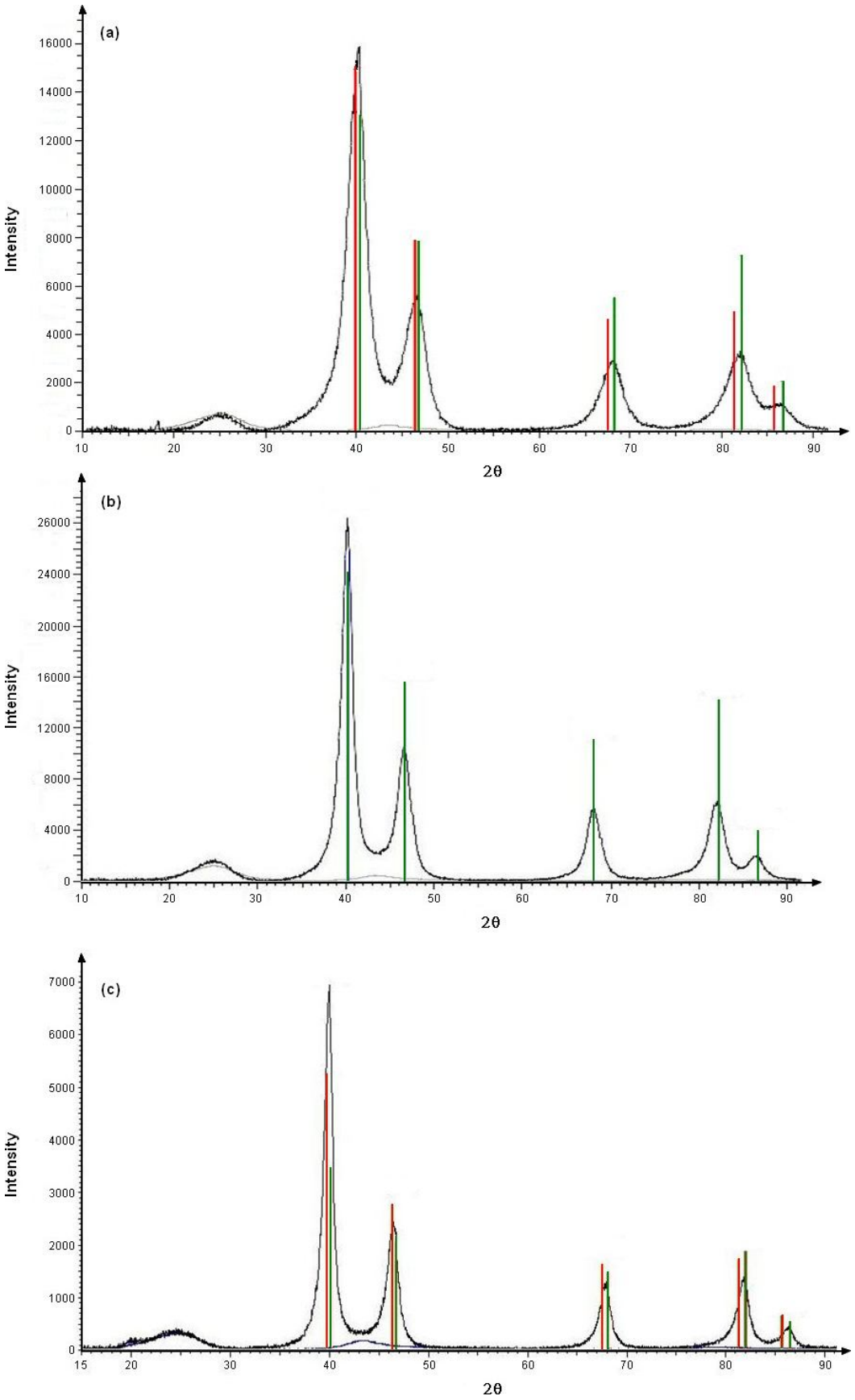

Figure 5- 6 XRD patterns of $Pt_{2.0}/Pd_{3nm}$ (a), $Pt_{2.0}/Pd_{5nm}$ (b) and $Pt_{2.0}/Pd_{10nm}$ (c). The vertical lines represent the documented diffraction peaks of Palladium (in green) and Platinum (in red).

5.4.2. EXAFS analysis

EXAFS spectra of the core-shell catalysts were collected both in hydrogen (at N.S.L.S., Brookhaven) and in air (at S.R.S., Daresbury) atmospheres at the Pt L_{III} edge only. The data analysis was completed using the methods described in Section 2.5.7. The corresponding chi and Fourier transform plots are shown in Figure 5-7 and Figure 5-8 and the EXAFS fit parameters are summarised in Table 5-5.

In hydrogen, the total coordination number increased slightly with the particle size, which is consistent with a decrease in the number of low-coordinated atoms. It can be seen that the Pt-Pt and Pt-Pd distances expanded slightly. In Chapter 4, the expansion in the Pt-Pt and Pt-Pd distances was interpreted as a change in the shell structure with higher Pt coverage. This can be explained by the formation of a PtPd alloy at the interface region. $Pt_{2.0}/Pd_{5nm}$ had the fewest Pt-Pt neighbours and the most Pt-Pd neighbours, indicating a poorer coverage compared to the other two core-shells.

The structure of the $Pt_{2.0}/Pd_{3nm}$ catalyst differed more upon exposure to hydrogen or air than that of the $Pt_{2.0}/Pd_{10nm}$ catalyst. The number of Pt-Pt neighbours dropped while Pt-O bonds were created. The number of Pt-O neighbours was higher for $Pt_{2.0}/Pd_{3nm}$ than for $Pt_{2.0}/Pd_{10nm}$ due to a higher ratio of surface atoms. The number of Pt-Pd neighbours also slightly decreased. There was a greater strain on the Pt-Pd distance, suggesting a significant disruption of the surface structure upon exposure to air. In contrast, the Pt-Pt and Pt-Pd distances in $Pt_{2.0}/Pd_{10nm}$ were similar in air and hydrogen and as were the total coordination numbers.

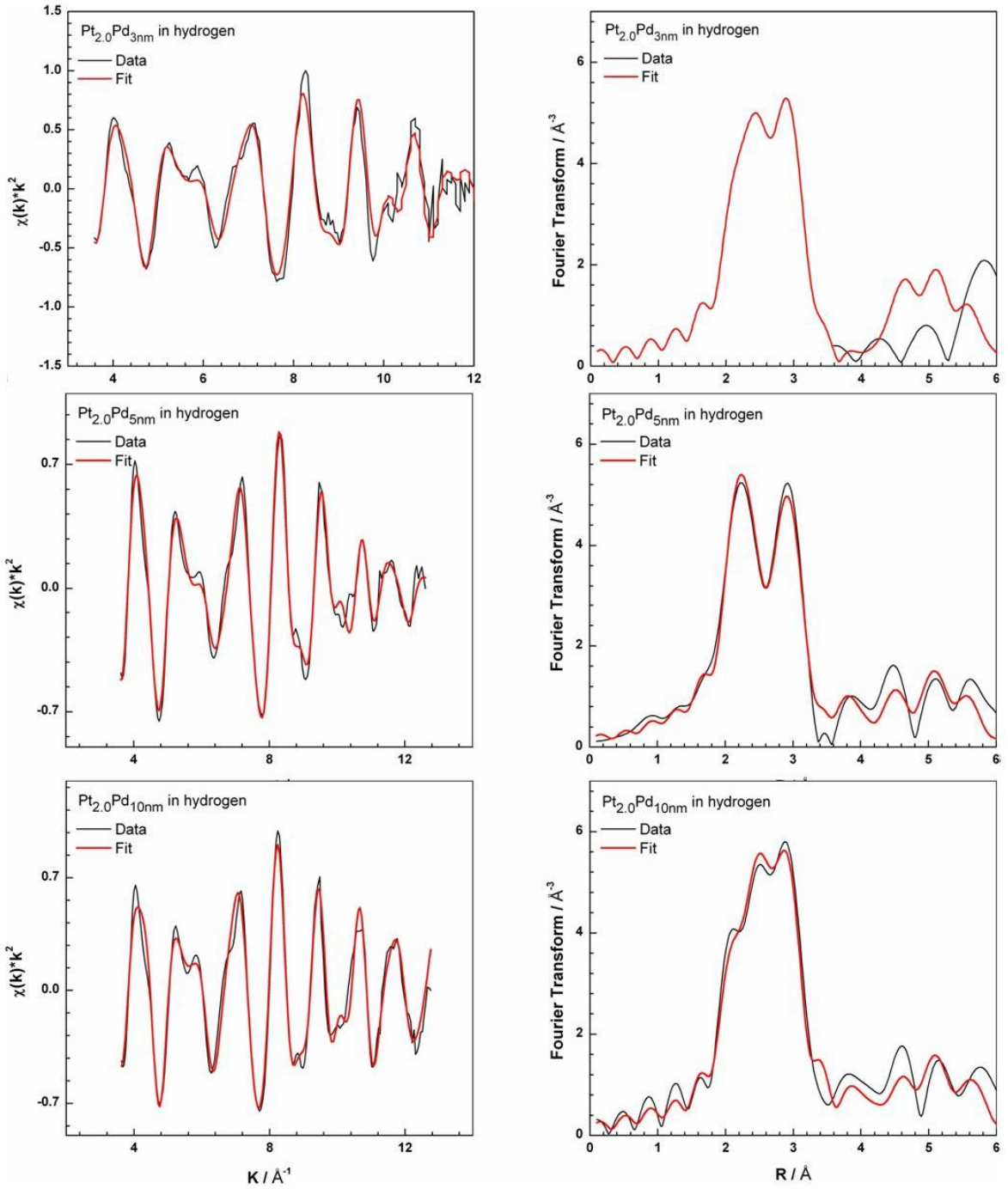

Figure 5- 7 EXAFS plots for $Pt_{2.0}/Pd_{3nm}$, $Pt_{2.0}/Pd_{5nm}$ and $Pt_{2.0}/Pd_{10nm}$. (left) k^2-weighed χ(k) spectra collected at Pt L_{III} edge in hydrogen; (right) k^2-weighed Fourier transforms of the χ (k) data.

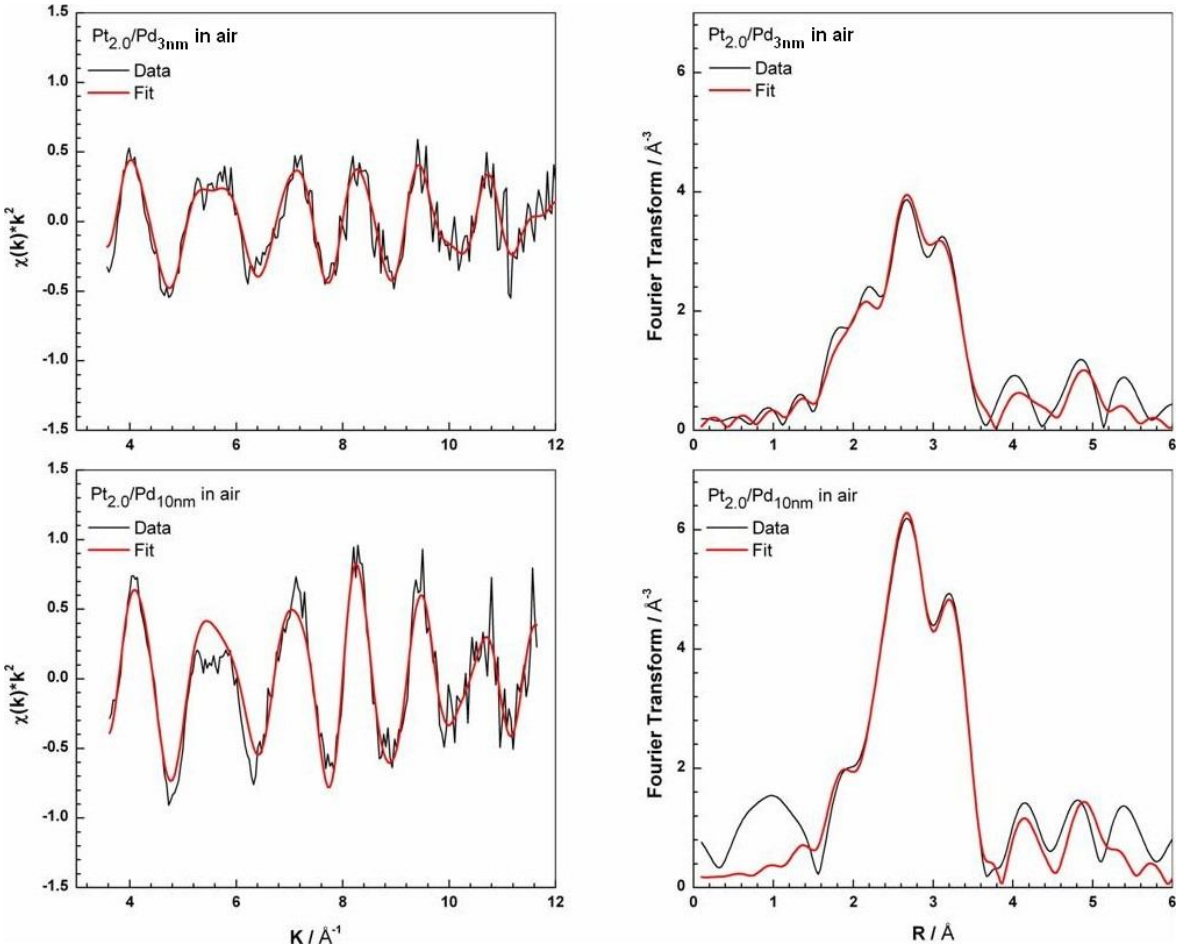

Figure 5- 8 EXAFS plots for $Pt_{2.0}/Pd_{3nm}$, $Pt_{2.0}/Pd_{5nm}$ and $Pt_{2.0}/Pd_{10nm}$. (left) k^2-weighed χ(k) spectra collected at Pt L_{III} edge in air; (right) k^2-weighed Fourier transforms of the χ (k) data.

Table 5- 5 EXAFS fit parameters in air and hydrogen atmospheres

Catalysts	Coordination number	Distance (Å)	Debye-Waller factor $2\sigma^2$ ($Å^2$)	E_f / eV	R_{EXAFS} / %
In hydrogen					
$Pt_{2.0}/Pd_{3nm}$	Pt = 5.68 ± 0.66	2.77 ± 0.01	0.011 ± 0.002	-12.00 ± 1.25	29.0
	Pd = 1.89 ± 0.41	2.78 ± 0.02	0.011 ± 0.003		
Total 1st shell coordination number = 7.4					
$Pt_{2.0}Pd_{5nm}$	Pt = 5.44 ± 0.22	2.76 ± 0.00	0.0113± 0.001	-10.97 ± 0.48	19.5
	Pd = 2.63 ± 0.13	2.75 ± 0.01	0.011 ± 0.003		
Total 1st shell coordination number = 8.1					
$Pt_{2.0}Pd_{10nm}$	Pt = 6.88 ± 0.54	2.76 ± 0.01	0.013 ± 0.002	-10.74 ± 0.99	21.0
	Pd = 1.45 ± 0.38	2.77 ± 0.02	0.014 ± 0.005		
Total 1st shell coordination number = 8.3					
In air					
$Pt_{2.0}/Pd_{3nm}$	O = 0.73 ± 0.19	2.03 ± 0.03	0.014 ± 0.007	-13.48 ± 2.52	37.4
	Pt = 4.44 ± 0.78	2.74 ± 0.02	0.018 ± 0.003		
	Pd = 1.10 ± 0.33	2.80 ± 0.02	0.013 ± 0.004		
Total 1st shell coordination number = 6.3					
$Pt_{2.0}Pd_{5nm}$			N/A		
$Pt_{2.0}Pd_{10nm}$	O = 0.56 ± 0.21	1.99 ± 0.04	0.009 ± 0.010	-12.71 ± 1.47	33.0
	Pt = 6.43 ± 0.60	2.75 ± 0.01	0.011 ± 0.002		
	Pd = 1.34 ± 0.34	2.75 ± 0.03	0.009 ± 0.004		
Total 1st shell coordination number = 8.3					

5.4.3. High resolution TEM and STEM observations

The particle size distributions of the core-shell electrocatalysts were obtained by high-resolution TEM and are shown in Figure 5-9. For $Pt_{2.0}/Pd_{3nm}$ and $Pt_{2.0}/Pd_{5nm}$ the mean particle size slightly increased compared to the particle size of their respective Pd core catalyst. However the histogram profiles of the core-shells did not follow those of the corresponding Pd cores. This was attributed to the fact the catalyst samples used for TEM analysis are generally so small that they are not always representative of the entire catalysts.

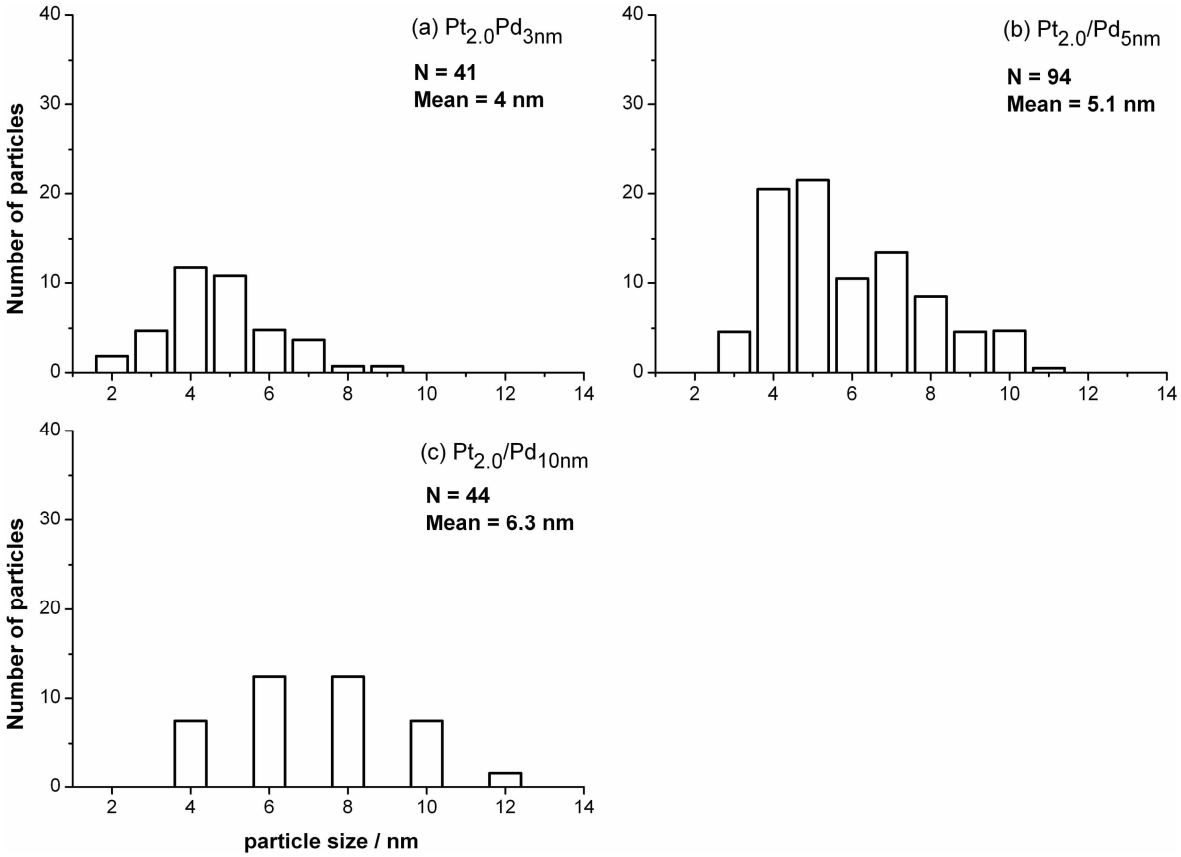

Figure 5- 9 Particle size distribution bar charts for $Pt_{2.0}/Pd_{3nm}$ (a), $Pt_{2.0}/Pd_{5nm}$ (b) and $Pt_{2.0}/Pd_{10nm}$ (c).

An EDX line profile was obtained for each core-shell catalyst sample. The profiles are shown in Figures 5-10, 5-11 and 5-12 for $Pt_{2.0}/Pd_{3nm}$, $Pt_{2.0}/Pd_{5nm}$ and $Pt_{2.0}/Pd_{10nm}$, respectively. The EDX profiles were obtained by recording the intensities of the Pt $M_{\alpha 1}$ (2.70 keV) and Pd $L_{\alpha 1}$ (2.05 keV) emission lines at equally spaced points along a line

across the particle. The relative intensity profiles for Pt and Pd also give an indication of their relative compositions. Note that because only a few individual particles were examined, this method is not representative of the whole catalyst, but it did give some information about the Pt shell continuity and thickness.

For all core-shell catalysts, the Pd curves were not smooth and exhibited variations. This effect was attributed to the interaction of the electron probe with grain boundaries in the particle examined. At grain boundaries, the orientation of the crystalline structure may change and can lead to the diffraction of the electron beam, resulting in a decrease in the emitted X-ray intensities. The high intensity of the Pt signal accompanied by a decrease in the Pd was taken as evidence of a Pt shell. However, the variations of Pt across the particle revealed the discontinuity of the Pt shell. This was more visible on the $Pt_{2.0}/Pd_{10nm}$ EDX profile, where the Pt signal dropped to the background level and then increased again a few times across the particle. The point where the Pt signal count was very low could be interpreted as areas of the Pd core which remained uncovered by the Pt shell.

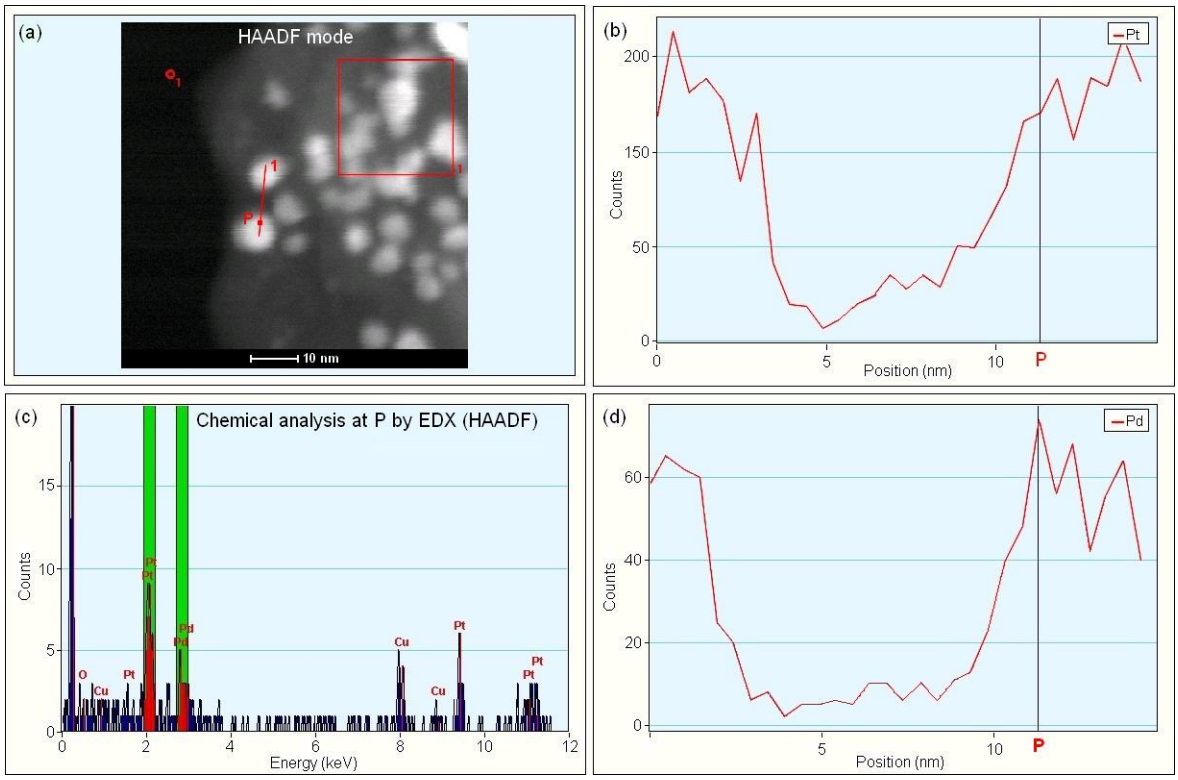

Figure 5- 10 HRTEM micrographs of $Pt_{2.0}/Pd_{3nm}$ particles in HAADF mode (a). EDX Pt profile across two core-shell particles following the red line in picture a (b). Chemical analysis at position P (c). EDX Pd profile across the two core-shell particles (d).

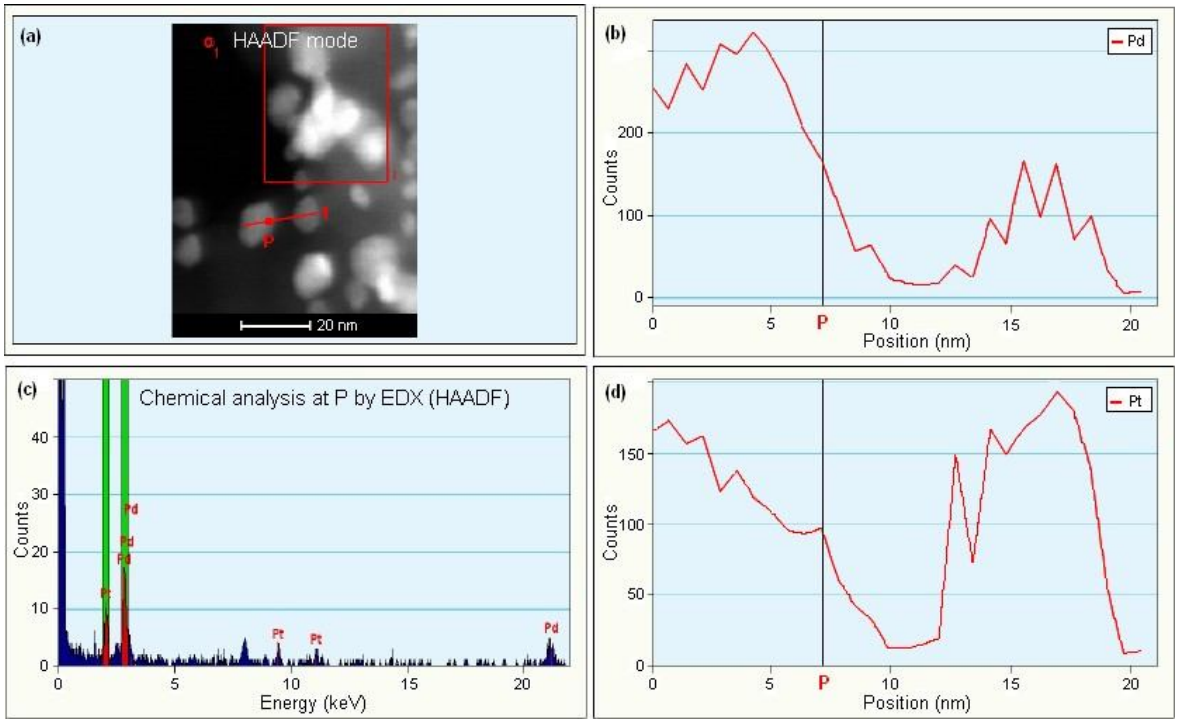

Figure 5- 11 HRTEM micrographs of $Pt_{2.0}/Pd_{5nm}$ particles in HAADF mode (a). EDX Pt profile across two core-shell particles following the red line in picture a (b). Chemical analysis at position P (c). EDX Pd profile across the two core-shell particles (d).

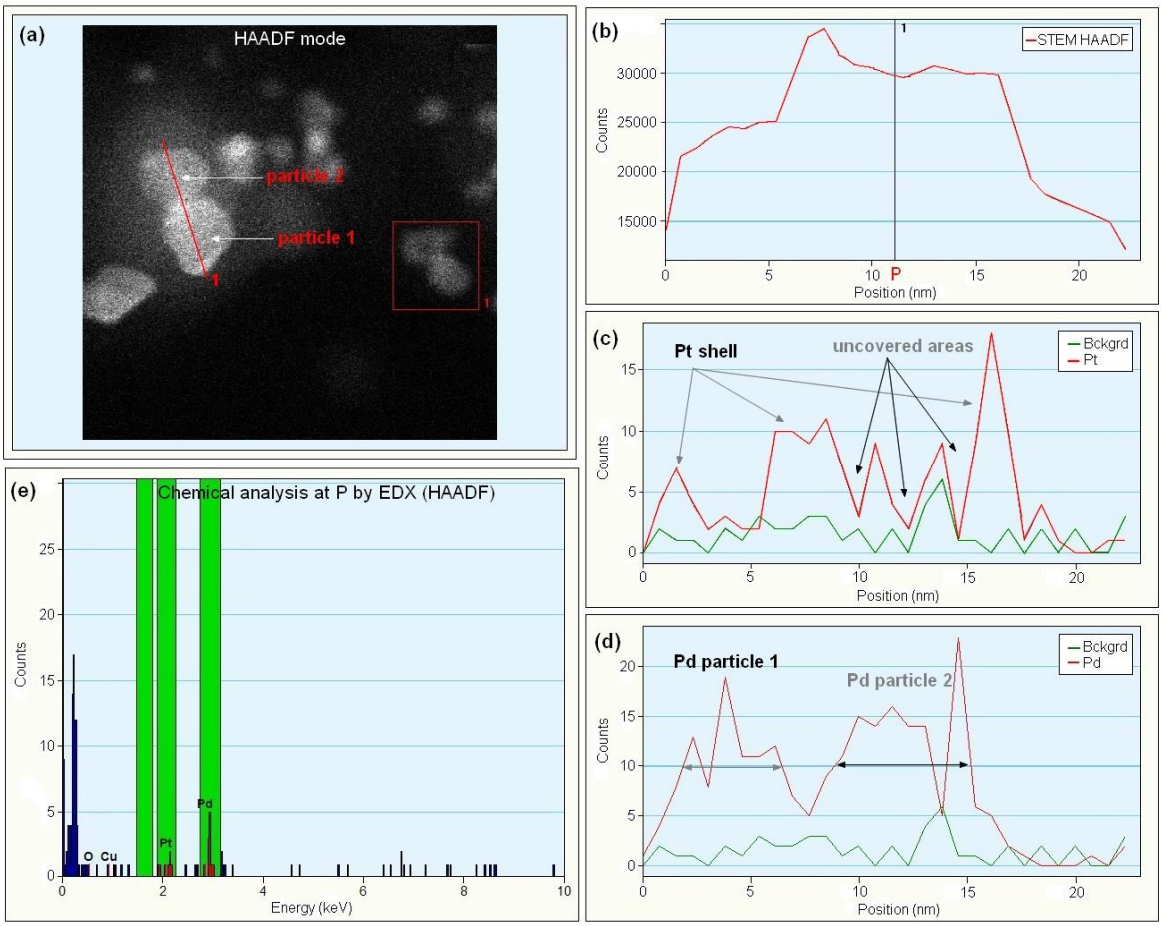

Figure 5- 12 STEM micrographs of $Pt_{2.0}/Pd_{10nm}$ particles in HAADF mode (a). EDX profiles for the sum (Pt+Pd) counts (b), the Pt counts (c) and the Pd counts across the two core-shell particles following the red line in picture a (d). Chemical analysis at position P (e).

5.4.4. HS-LEIS analysis

The LEIS spectrum for the $Pt_{2.0}/Pd$ core-shell catalysts was collected after conditioning the catalyst in hydrogen at ambient temperature. Figure 5-13 (a) shows the 3keV $^{20}Ne^{+}$ LEIS spectra for the catalyst samples $Pt_{2.0}/Pd_{3nm}$ and $Pt_{2.0}/Pd_{5nm}$ after reduction treatment and for the Pd and Pt references. In Figure 5-13 (b) are shown the LEIS spectra of $Pt_{2.0}/Pd_{10nm}$ and a PtPd alloy of same composition. The spectra for the references have been multiplied by 0.001 to aid comparison. The Pd and Pt peaks of the catalysts were integrated and compared to the peaks for the Pd and Pt references. The results of this quantitative analysis are shown in Table 5-6. As expected, the best Pt coverage was observed on the smallest Pd core. The Pt coverage on Pd_{5nm} appeared poorer than on Pt_{10nm}, which may take its origin from the synthesis. During the preparation of $Pt_{2.0}/Pd_{5nm,}$ three reaction steps were needed to deposit most of the Pt and the desired or nominal assay

was not reached. It is interesting to note that for this catalyst the PtPd alloy surface was mainly composed of Pd, which suggests a strong Pd segregation to the surface under a hydrogen atmosphere, in agreement with theoretical calculations (3) and experimental data on PtPd alloys (4, 5). It could be considered that the surface reconstruction observed on extended surfaces cannot occur on small particles because of a high proportion of unsaturated atoms located at edges and corners; the particle size may have to be very large in order to show surface reconstruction.

Table 5- 6 HS-LEIS data extracted from Figure 5-13 (a) and (b).

Catalysts	Surface fraction / %		Atomic composition / %	
	Pt	Pd	Pt	Pd
$Pt_{2.0}/Pd_{3nm}$	0.30	0.16	64.6	35.4
$Pt_{2.0}/Pd_{5nm}$	0.1	0.21	31.6	68.3
$Pt_{2.0}/Pd_{10nm}$	0.08	0.07	52.9	47.1
PtPd alloy	0.07	0.66	9.5	90.5

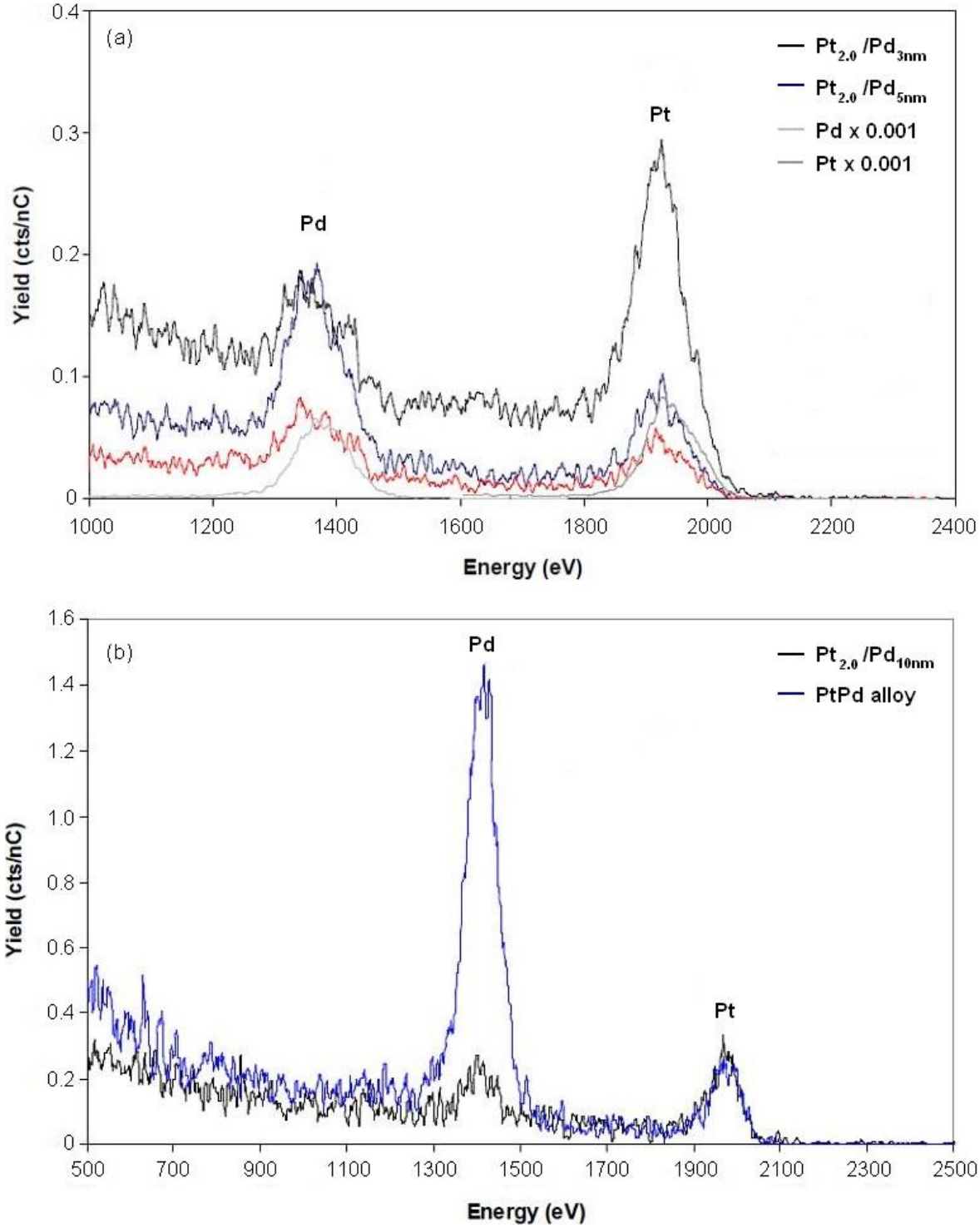

Figure 5- 13 3keV $^{20}Ne^{+}$ spectra of the $Pt_{2.0}/Pd_{3nm}$ and $Pt_{2.0}/Pd_{5nm}$ after the reduction treatment, compared to the spectra for the Pd and Pt reference (a). The spectra for the references have been multiplied by 0.001 to facilitate comparison. 3keV $^{20}Ne^{+}$ spectra of the $Pt_{2.0}/Pd_{10nm}$ and a PtPd of same bulk composition after the reduction treatment (b).

5.4.5. XPS analysis

The XPS normalized spectra obtained for $Pt_{2.0}$/Pd core-shells are shown in Figure 5-14 and the extracted information in Table 5-7. In the Pd 3d and Pt 4d region (325-350 eV) displayed in Figure 5-14 (a), the ratio between the maxima of the Pt $4d_{5/2}$ and Pd 3d peaks increased as the Pd core size decreased, clearly indicating increased Pt-enrichment of the surface. The Pd $3d_{5/2}$ peak showed an additional feature at the high binding energy side around 346-349 eV. This feature was also observed in the Pd/C spectrum and was attributed to an energy loss effect, also referred to plasmon excitation effects. Such plasmon effects are the major inelastic energy losses in a large scale crystalline structure and are more important in metallic materials (6). In brief, plasmon oscillations are caused by a photoelectron traveling through the electronic structure of a material. They result in a broad and weak peak at lower kinetic energy, or higher binding energy than the main peak obtained from the primary photoelectrons. The intensity of this peak was larger for $Pt_{2.0}/Pd_{3nm}$ than for the other two core-shell materials, suggesting a significant change in the electronic environment in the surface region upon Pt addition. One explanation for this can be that the Pt shell is better distributed on the Pd_{3nm} core compared to Pd_{5nm} and Pd_{10nm}, in agreement with a long range ordering of the Pt and Pd atoms at the surface resulting in a detectable signal.

As can be seen in Figure 5-14 (a), the Pd 3d peaks of $Pt_{2.0}/Pd_{5nm}$ and $Pt_{2.0}/Pd_{10nm}$ overlaid well, showing similar oxidation states. In contrast, $Pt_{2.0}/Pd_{3nm}$ exhibited a more prominent shoulder on the high binding energy, revealing a higher proportion of Pd oxide compared to the other two core-shells. This was attributed to a size effect. Small nanoparticles, having a high proportion of low-coordinated atoms, tend to be more readily oxidized than large particles.

The intensity of the Pt 4f peaks, shown in Figure 5-15 (b), increased as the Pd core particle size decreased, confirming that there was a greater fraction of Pt at the surface for small core catalysts. In agreement with the Pd 3d peaks, there was more and more Pt oxide at the surface as the particle size decreased. The binding energy of the Pt $4f_{7/2}$ shifted slightly towards negative binding energies as the Pd core size increased, which can be taken as evidence of an electronic effect of the Pd core on the Pt shell.

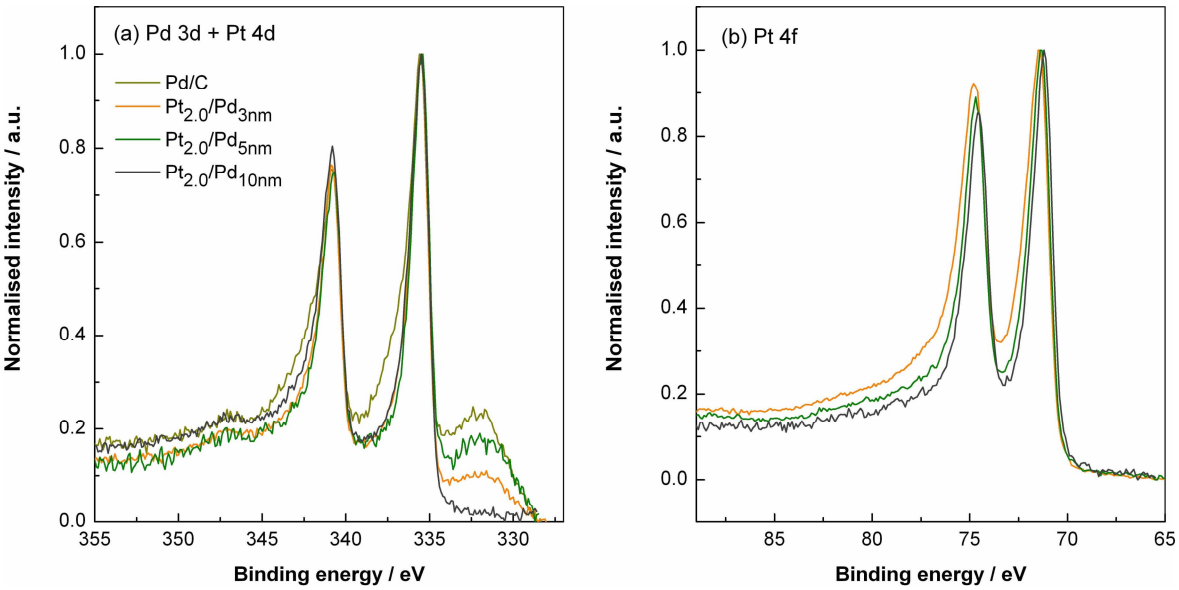

Figure 5- 14 Intensity normalised (a) Pt 4d and Pd 3d and (b) Pt 4f (Shirley-type background substracted) XPS spectra for $Pt_{2.0}/Pd_{3nm}$, $Pt_{2.0}/Pd_{5nm}$, $Pt_{2.0}/Pd_{10nm}$.

Table 5- 7 XPS parameters extracted by curve fitting the spectra shown in Figure 5-15.

Catalysts	Pd $3d_{5/2}$	Pt $4f_{7/2}$	$(Pt:Pd)_{XPS}$	$(Pt:Pd)_{LEIS}$
Pd/C	335.5	-	0:100	
Pt/C	-	71.7	100:0	
$Pt_{2.0}/Pd_{3nm}$	335.6	71.5	75:25	65:35
$Pt_{2.0}/Pd_{5nm}$	335.5	71.4	42:58	32:68
$Pt_{2.0}/Pd_{10nm}$	335.4	71.2	60:40	53:47

5.5. Electrochemical properties

5.5.1. Surface characterisation

The voltammograms of $Pt_{2.0}/Pd_{3nm}$, $Pt_{2.0}/Pd_{5nm}$ and $Pt_{2.0}/Pd_{10nm}$ were compared with that of a 40%Pt/C electrocatalyst and the results are shown in Figure 5-15 (a) and (b). Their electrochemical surface areas (ECA) were calculated assuming no hydrogen absorption by the Pd lattice of the core.

The three core-shell catalysts exhibited different features in the hydrogen region. The magnitude of the peaks is proportional to the surface area of the catalysts as explained in Section 2.6.1. As discussed in the previous chapter, $Pt_{2.0}/Pd_{3nm}$ presented Pd-like spikes

shifted to a lower potential. In contrast, the $Pt_{2.0}/Pd_{5nm}$ voltammogram was less defined. At low potentials, a broad peak was observed with two shoulders around 0.22 V and 0.11 V. The CV for $Pt_{2.0}/Pd_{10nm}$ presented two small peaks at 0.21 V and 0.17 V. The fact that the three core-shells exhibited different voltammograms may indicate that the Pt shell structure was different depending on the core size.

The surfaces of the core-shell catalysts were also characterized by CO stripping voltammetry and the plots are presented in Figure 5-15 (b). All the core-shell CO peaks are positioned between those of the Pt-only and Pd-only electrocatalysts, suggesting a similar synergy between Pt and Pd on all surfaces. However, there was a slight shift of the CO peaks towards negative potentials as the core size increased. It is known that the CO electrooxidation reaction is controlled by the ability of the surface to dissociate water and form adsorbed OH groups (7). As the particles get larger, there is a decrease in the adsorption energy for OH and CO due to a lower number of low-coordinated sites (edges and corners), where binding energies are lower than on terraces (8).

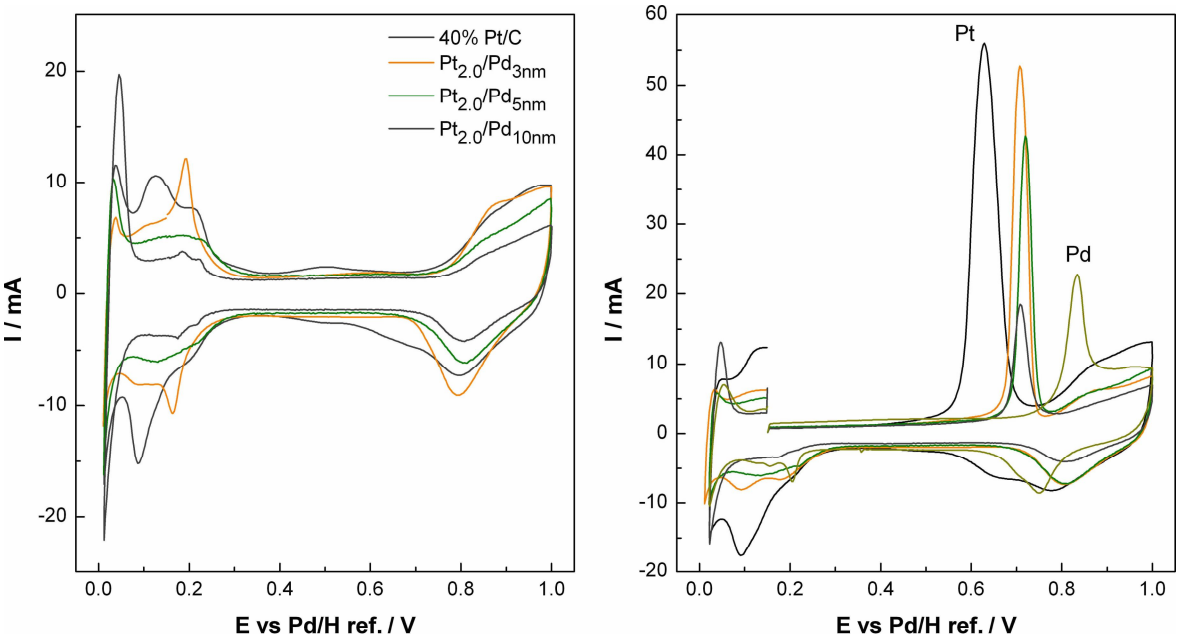

Figure 5- 15 Cyclic voltammograms of $Pt_{2.0}/Pd$ core-shells and 40%Pt/C in 1 dm^{-3} at 80°C, 10 mV s^{-1}.

The ratio between the charges due to hydrogen (Q_H) adsorption and CO oxidation (Q_{CO}) was calculated for the core-shells, (Table 5-8) and compared to those for 20%Pd/C and 20%Pt/C. For a Pt surface this ratio was expected to be close to 2, as the hydrogen adsorption and the CO oxidation processes involve 1 and 2 electrons, respectively. Except

for 20%Pd/C, CO:H equaled 2.1 for the core-shells and 20%Pt/C. 20%Pd/C seemed to generate an excess of CO charges compared to H charges. It was observed that increasing the size of the Pd core did not lead to hydrogen absorption and that CO was single-bonded to the surface atoms. Although the CO electrooxidation experiment is useful for monitoring changes occurring at a catalyst surface, it can not be used to estimate the Pt coverage. The onset of the CO electrooxidation is dependent on the ability of the catalyst surface to adsorb hydroxide groups, which relies on the degree of oxophilicity of the surface. Thus, even if the Pt coverage was complete, the activation of the electrooxidation of CO can still be influenced by the electronic effect existing between the core and the shell.

Table 5- 8 Charges for the hydrogen adsorption and CO electrooxidation processes.

Catalysts	Q_H / $C.mg_{(Pt+Pd)}^{-1}$	Q_{CO} / $C.mg_{(Pt+Pd)}^{-1}$	CO peak potential / mV	Q_{CO}/Q_H	ECA / $m^2\ g^{-1}$
20% Pd	0.06	0.15	834	2.8	50.5
40% Pt	0.13	0.28	629	2.1	61.6
$Pt_{2.0}/Pd_{3nm}$	0.10	0.19	725	2.1	67.3
$Pt_{2.0}/Pd_{5nm}$	0.09	0.19	719	2.1	42.0
$Pt_{2.0}/Pd_{10nm}$	0.04	0.09	708	2.2	20.0

5.5.2. Electrochemical stability

The electrochemical stability of the core-shell catalysts was assessed by cycling the electrodes 1000 times between 0.6 and 1.0 V at 20 mV s^{-1} at 80 ^oC in 1 M H_2SO_4. To follow the changes at the catalyst surfaces upon cycling, CV and CO oxidation voltammograms were performed after every 200 cycles. The successive voltammograms recorded after 0, 200, 600 and 1000 cycles are shown in Figure 5-16. The total H and CO charge losses of the core-shell catalysts, a Pd- and a Pt-only catalysts, after 1000 cycles are shown in Figure 5-17 (a).

It can be seen that for $Pt_{2.0}/Pd_{3nm}$, $Pt_{2.0}/Pd_{5nm}$ and $Pt_{2.0}/Pd_{10nm}$, the peaks at 0.22 V were the first features to disappear in less than 100 cycles. Repetitive polarization scans led to the growth of hydrogen adsorption features and to the positive shift of the oxide removal peaks in the core-shell voltammograms, which eventually resembled the voltammogram of

the carbon-supported Pt catalyst. This was accompanied with a loss of active area measured in the hydrogen region as shown in Figure 5-17.

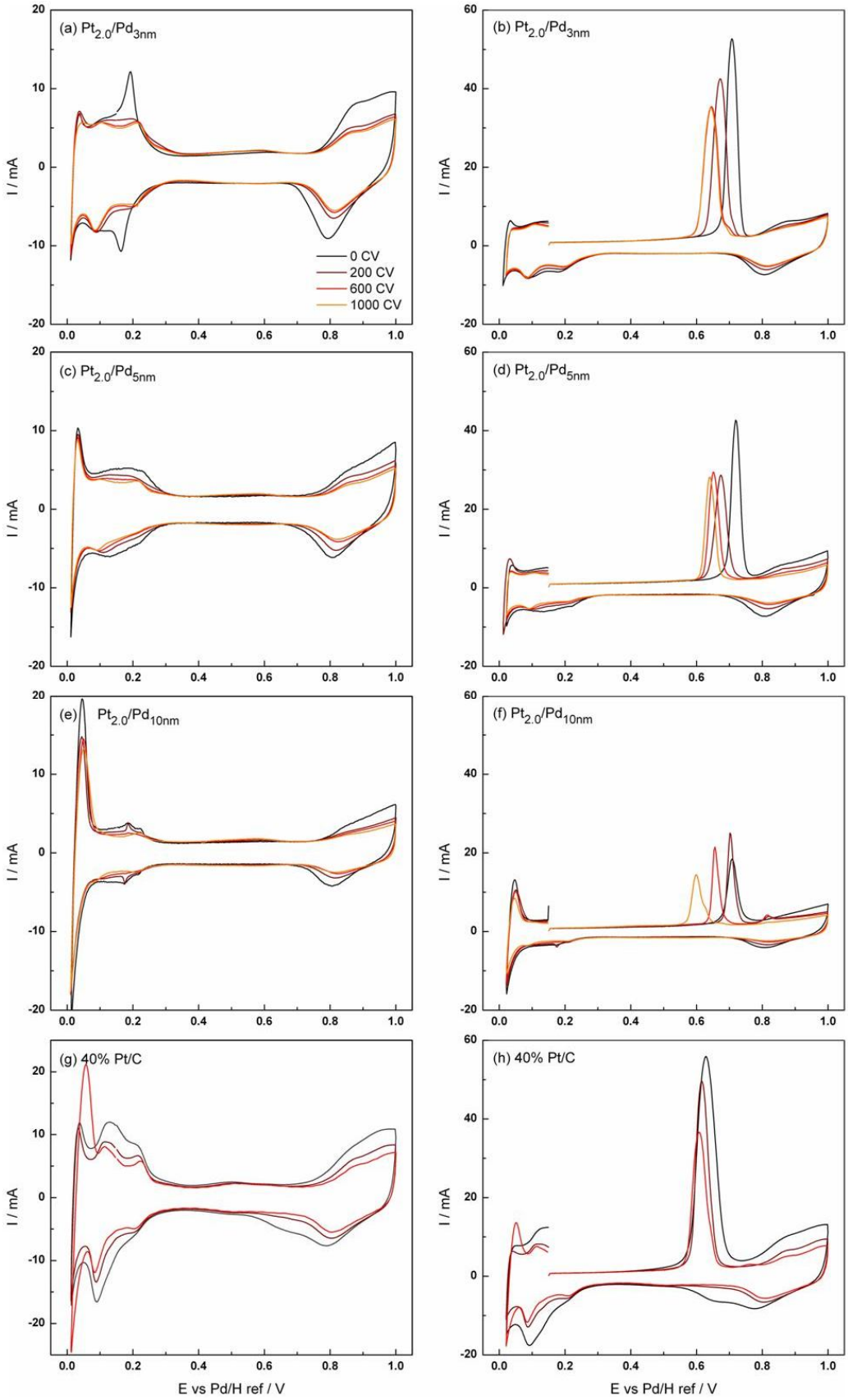

Figure 5- 16 CVs (on the left) and CO electrooxidation voltammograms (on the right) of $Pt_{2.0}/Pd_{3nm}$, $Pt_{2.0}/Pd_{5nm}$, $Pt_{2.0}/Pd_{10nm}$ and 40%Pt/C recorded after 0, 200, 600 and 1000 polarisation scans (0.6-1.0 V) in 1 M H_2SO_4, υ = 10 mV s^{-1}, at 80 °C.

The core-shell CO peaks shifted towards negative potentials, while losing area during cycling. This clearly shows that the surface composition of the core-shells changed upon cycling. It is worth noticing that the CO peaks remained sharp and did not give rise to two peaks. Despite the changes occurring at the surface the synergy between Pt and Pd remained. In Figure 5-17, the Q_{CO}:Q_H ratio of the charges remained close to 2 during the cycling regime for all the core-shell catalysts and the Pt/C catalyst, but not for the Pd/C catalyst, like in Chapter 4. Besides, the H and CO charges decreased at a similar rate for all catalysts, as shown in Figure 5-18. These observations indicate that there was still no excess of hydrogen charge as the Pd core size increased from 2 to 10 nm.

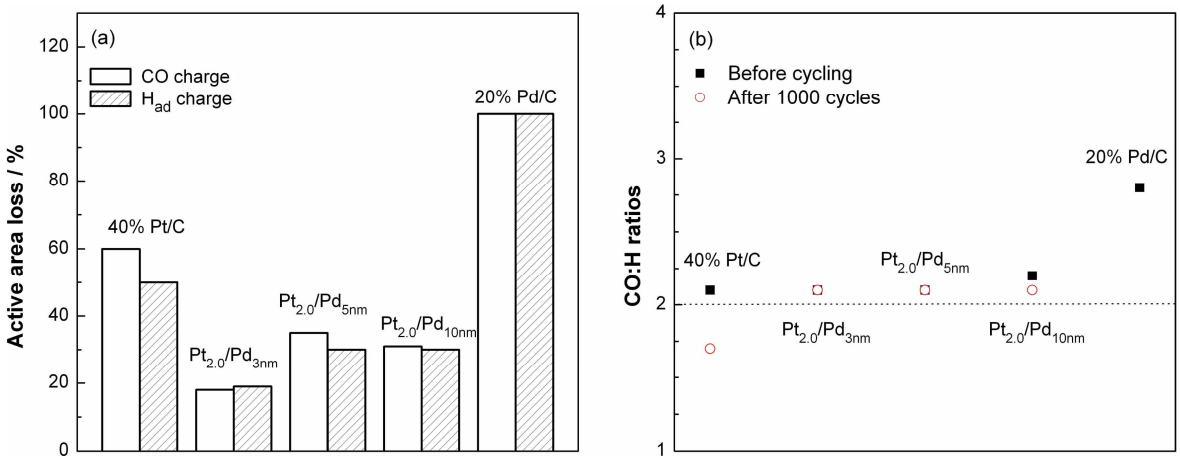

Figure 5- 17 Calculated loss of active area (a) and the corresponding CO:H ratio (b) for the voltammograms shown in Figure 5-16.

The loss of active metal area after 1000 cycles was about 19% for $Pt_{2.0}/Pd_{3nm}$ and 30% for both $Pt_{2.0}/Pd_{5nm}$ and $Pt_{2.0}/Pd_{10nm}$. Although this was an improvement in stability compared to a Pd only catalyst, no stability increase was observed with increasing the size of the Pd core catalyst. The small core-shell was more stable to cycling than the large core-shell and this may be explained by the fact that the Pt coverage is better on the small Pd particles than on large ones. This suggests that the degree of stability of the core-shell could be then related to the amount of Pd exposed on the surface. This is consistent with the fact that the PtPd alloy was less stable than the core-shell catalysts.

ICP-ES analyses of the electrolyte solution indicated that after cycling very low Pt levels (≤ 20 ppb) were found in the electrolyte whereas values of > 1000 ppb were observed for Pd. This suggests that the mechanism of active area loss may be explained by

Pd particles being uncovered upon cycling followed by Pd dissolution, while Pt agglomerates. These two processes, Pd dissolution and Pt particle agglomeration, can be seen as the cause of the observed area loss (9).

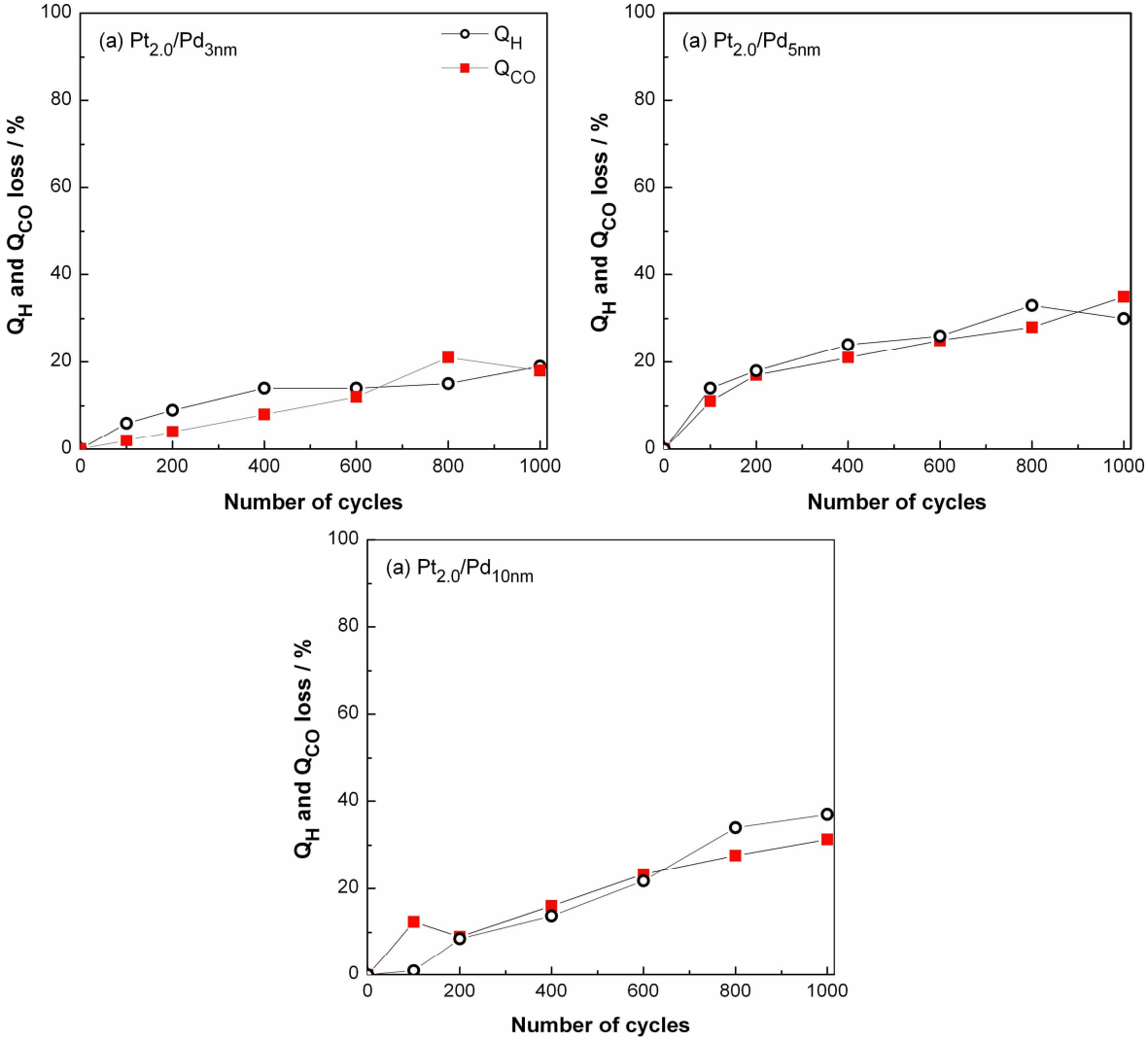

Figure 5- 18 Change in Q_H and Q_{CO} charges as a function of the number of polarisation scans for $Pt_{2.0}/Pd_{3nm}$ (a), $Pt_{2.0}/Pd_{5nm}$ (b) and $Pt_{2.0}/Pd_{10nm}$ (c).

To better understand the mechanism of the core-shell particle degradation, STEM/EDX analyses were performed on $Pt_{2.0}/Pd_{5nm}$ electrode before and after the stability test. An EDX line profile across the core-shell particles before and after the test showed changes in Pt and Pd distribution in the particles and their relative quantities. The pre-cycling TEM analysis, presented in Figure 5-19, showed evidence of a core-shell structure with a very thin Pt shell. The relative intensity of the Pt and Pd signals indicates a predominance of Pd.

The mean particle size was 5.7 nm. From the TEM post-cycling analysis, shown in Figure 5-20, it can be seen that many of the particles had a rich Pt shell and that the Pd cores had mostly disappeared. The Pt signal in this case was more prominent. The mean particle size increased slightly to 6.5 nm.

These results show that both particle agglomeration and metal dissolution occurred during the core-shell degradation. Pd was clearly dissolved away, whereas Pt was agglomerating on the Pd particle surfaces. Pt may have also been dissolved but was then redeposited on the core.

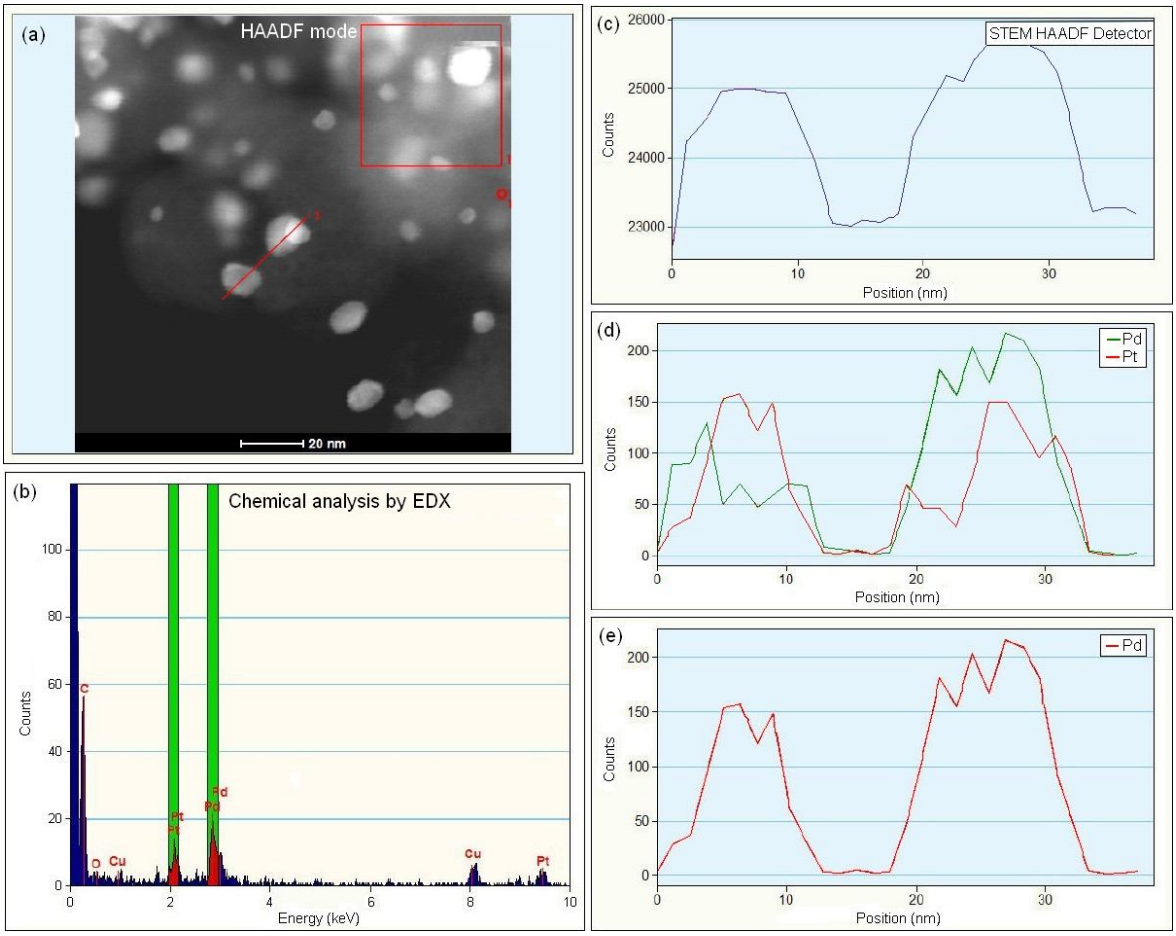

Figure 5- 19 HRTEM/EDX analyses of $Pt_{2.0}/Pd_{5nm}$ electrode before cycling. HRTEM micrographs of $Pt_{2.0}/Pd_{5nm}$ particles in HAADF mode (a). Chemical analysis (b). EDX profiles for total HRTEM signal (c), the Pt and Pd counts (d) and the Pd counts across the two core-shell particles following the red line in picture a (e).

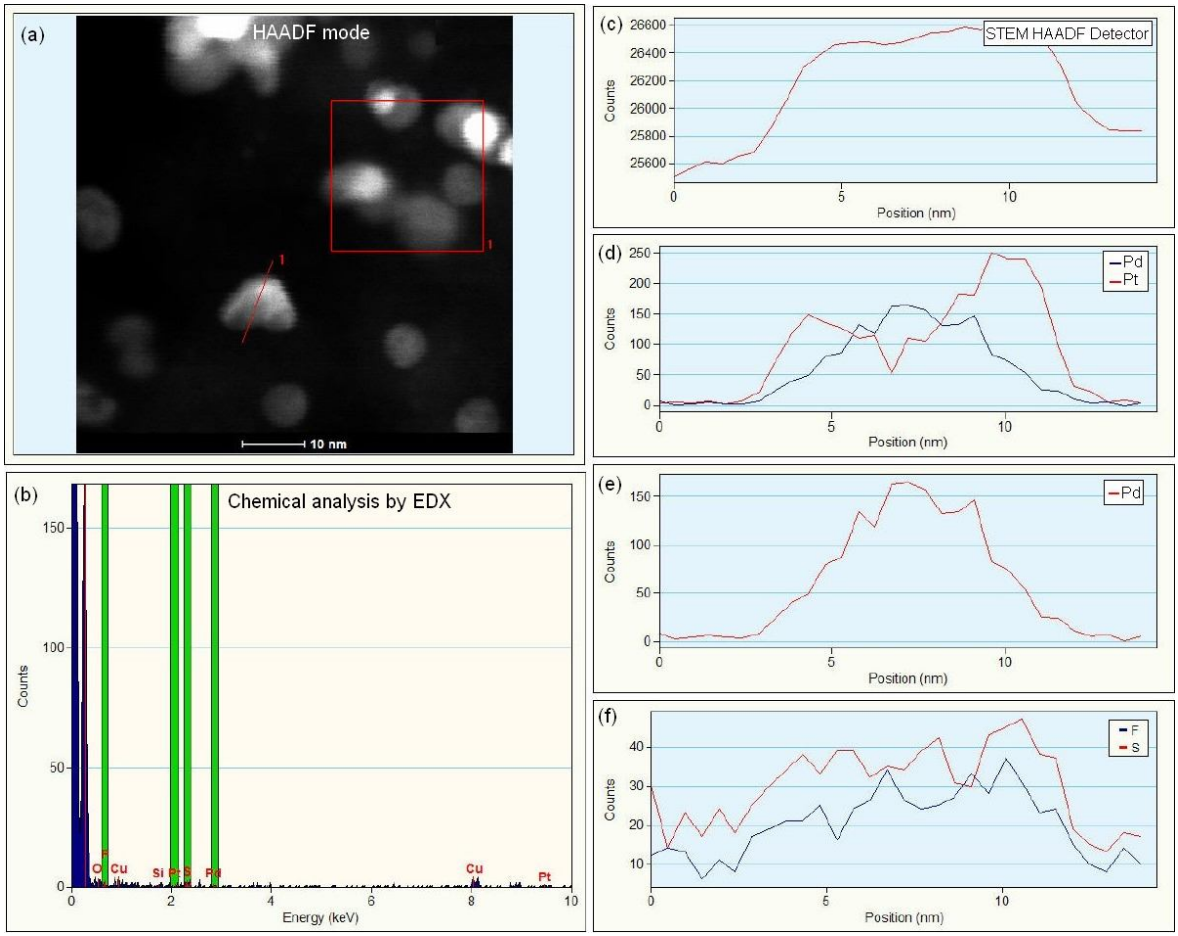

Figure 5- 20 HRTEM/EDX analyses of $Pt_{2.0}/Pd_{5nm}$ electrode after cycling. HRTEM micrographs of $Pt_{2.0}/Pd_{5nm}$ particles in HAADF mode (a). Chemical analysis (b). EDX profiles for total HRTEM signal (c), those of Pt and Pd (d), that of Pd only (e) and those of F and S across the two core-shell particles following the red line in picture (f).

5.5.3. Activity for the reduction of oxygen

Screening of the ORR activity of the core-shell catalysts was conducted using rotating-disk electrode measurements in 0.1 M $HClO_4$ saturated with oxygen and at ambient temperature. Each measurement was performed two to three times to ensure reproducibility of the data. Figures 5-21 (a) and (b) display the rotating-disk polarization curves at 2500 rpm and the corresponding Levich plots for a 400 to 2500 rpm range of rotation speeds, for the Pt_x/Pd core-shell catalysts, a 40% Pt/C and a 20%Pd/C catalysts. The Pt loadings for the tested catalysts are reported in Table 5-9. With fixed catalyst thickness, the electrode Pt loading was reduced as the core size increased. The effect of the Pd core size on the mass and specific activities are expressed by the Tafel plots shown in Figure 5-21 (c) and (d).

Table 5- 9 Pt loading deposited on RDE electrodes for Ptx/Pd core-shells and 40%Pt/C.

	$Pt_{2.0}/Pd_{3nm}$	$Pt_{2.0}/Pd_{5nm}$	$Pt_{2.0}/Pd_{10nm}$	20%Pd/C	40% Pt/C
Pt loading / μg cm^{-2}	11.2	5.7	5.6	10	20

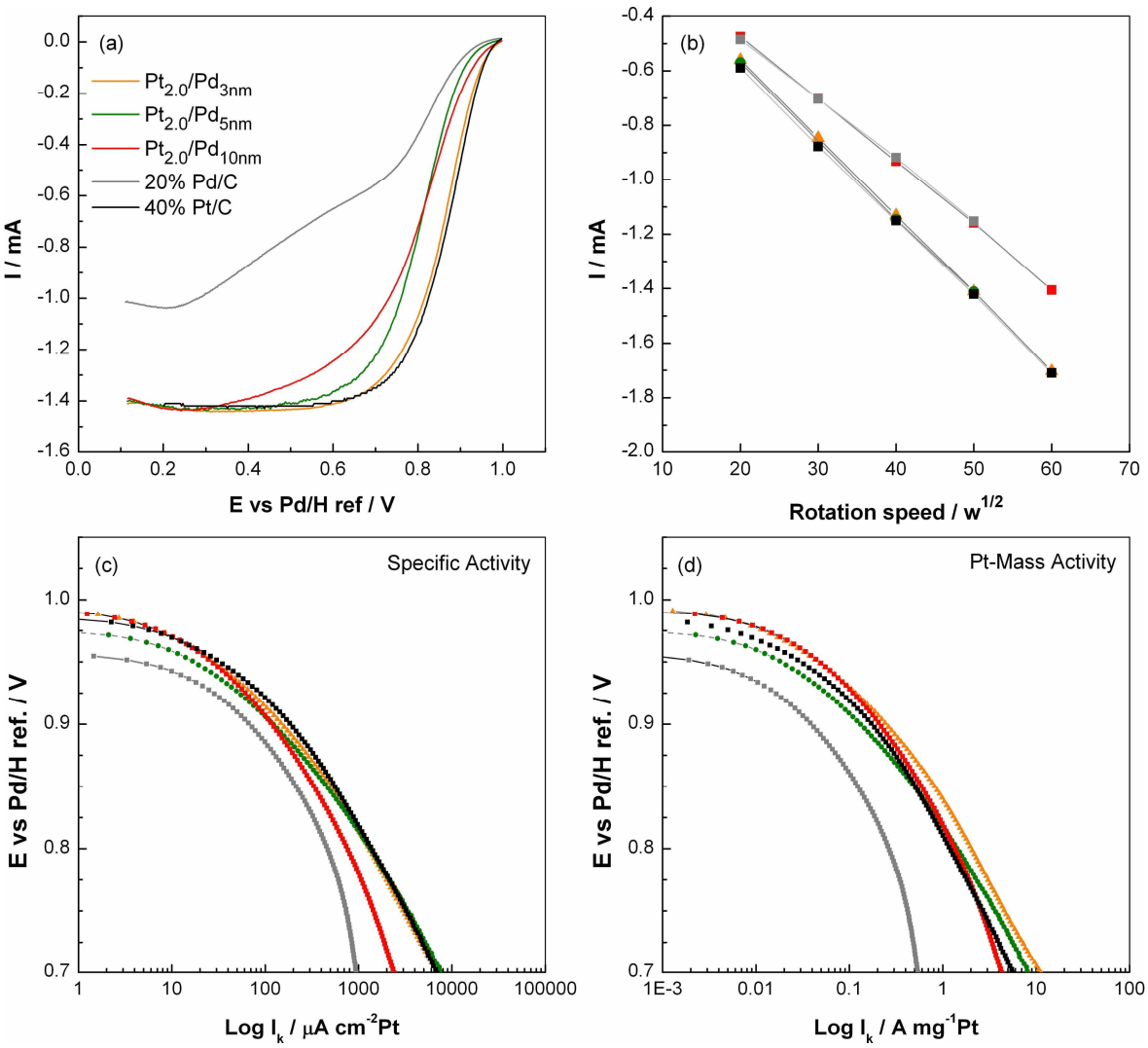

Figure 5- 21 Polarisation curves (backward scans) for the $Pt_{2.0}/Pd$ core-shell, 20% Pd/C and 40% Pt/C electrocatalysts in 0.1 M $HClO_4$. Scan rate of 10 mV s^{-1}. Levich plots (b). Tafel plots corrected for the electrochemical area (c) and for the Pt mass (d). Electrode geometric area: 0.196 cm^2.

It is noted that the ORR limiting current values were close for Pt/C and the $Pt_{2.0}/Pd$ core-shell catalysts. This suggests that the ORR mechanism on the $Pt_{2.0}/Pd$ core-shells follows mainly the 4-electron pathway. The comparison of the polarization curves in the kinetic region (from 0.85 V vs Pd/H ref.) evidenced that the catalytic activity of the core-

shells is higher than that of Pd/C and lower than that of Pt/C, except for $Pt_{2.0}/Pd_{3nm}$, which showed the same activity as Pt/C. This represents a great improvement as $Pt_{2.0}/Pd_{3nm}$ contains just half the Pt loading of the Pt/C electrode. The small core-shell had the best Pt coverage, as indicated by HS-LEIS and STEM analyses, and, out of the three core-shells, was the only one which exhibited observable electronic changes compared to the Pd-only. According to the Nørskov d-band centre model (10), the formation of metal-metal bonds in alloys or in core-shell structures changes the electronic properties of the metal. The high activity of $Pt_{2.0}/Pd_{3nm}$ may be a consequence of the changes in the d-band centre of the Pt atoms caused by their interaction with the Pd core. The fact that the Pt coverage was incomplete on the core-shells may have benefited the ORR activity by preferentially creating Pd-OH_{ads}, thus keeping more Pt sites available for the reduction of O_2 (11).

A bar chart of the values of the mass and the specific activities at 0.9 V vs Pd/H ref for the tested catalysts is shown in Figure 5-22 (a) and (b), respectively. No significant benefit in the Pt mass activity was observed with larger Pd core sizes in $Pt_{2.0}/Pd_{5nm}$ and $Pt_{2.0}/Pd_{10nm}$, compared to $Pt_{2.0}/Pd_{3nm}$. Following the ECA values measured on the ink-painted catalyst electrodes for the surface characterization, the specific activity decreased as the Pd core size increased.

It can be noticed that the least active catalyst was the one which had the poorest Pt coverage. As demonstrated earlier, Pt tended to deposit preferentially at the edges and corners of Pd particles. Because of their high reactivity, Pt atoms at these sites should oxidize first and hence become inactive to the ORR. As documented in the literature, the ORR reaction is more facile on (111) facets in perchloric acid electrolyte (2, 12). The larger particles should have relatively more metal atoms in such facets and, therefore, are predicted to be more active. However, as discussed above, the larger Pd cores were not as well covered by the Pt shell, negating any benefit of their larger diameter and greater number of (111) sites.

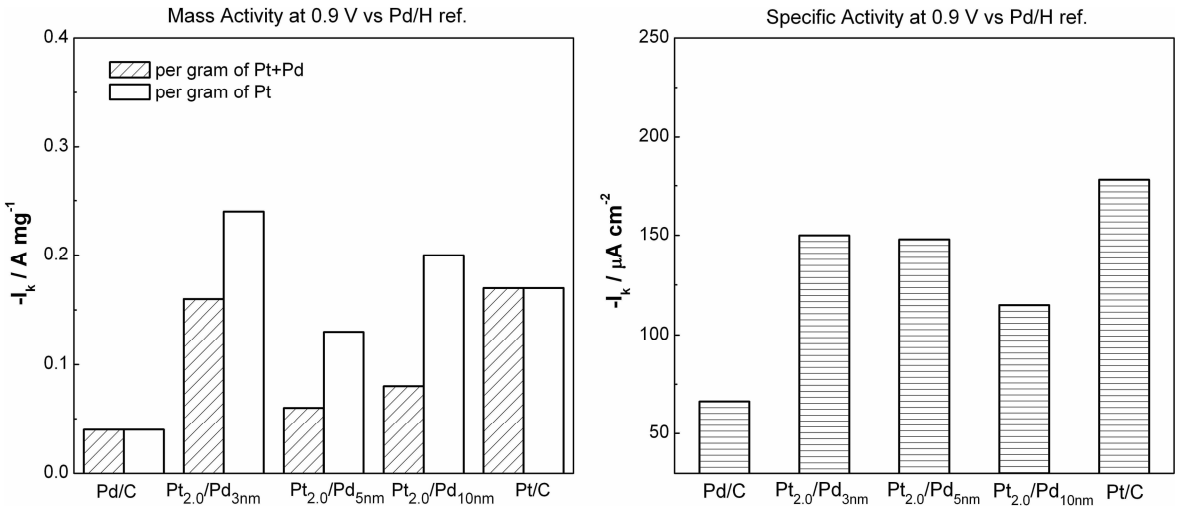

Figure 5- 22 Relationship between the Pt coverage and the ORR mass activity (a) and specific activity (b) at 0.9 V vs Pd/H ref. determined by analysis of the polarisation surves reported in Figure 5-21(a).

5.6. Conclusions

In this chapter, larger Pd core sizes were used for the preparation of the Pt/Pd core-shell, as they were expected to show enhanced stability and further reduced Pt loadings compared to the small Pd core. It was hoped that the 2 ML-Pt shells, although incomplete, would have showed sufficient ORR activity to compensate for the loss in active surface area of large particles.

TEM observations of the Pd cores showed that they had more facetted particles and a multimodal particle size distribution after annealing. The non-uniformity of the Pd core catalyst was then also found in the final core-shell catalysts. The Pt coverage was the highest on the 3nm-Pd core, which in principle should have the most edges and corners at the surface, where the Pt deposition occurred preferentially. As anticipated in Chapter 4, the electrochemical stability of the core-shell catalysts was related to the Pt coverage. This was well illustrated by the case of the $Pt_{2.0}/Pd_{5nm}$ catalyst, for which the Pt coverage, determined by HS-LEIS, was the poorest. This was supported by the EXAFS analysis, according to which $Pt_{2.0}/Pd_{5nm}$ had the lowest N_{Pt-Pt} coordination number. XRD analysis revealed that the lattice parameter of this catalyst expanded the least compared to $Pt_{2.0}/Pd_{3nm}$ and $Pt_{2.0}/Pd_{10nm}$. The $Pt_{2.0}/Pd_{5nm}$ catalyst was then significantly less stable than $Pt_{2.0}/Pd_{3nm}$ upon cycling and slightly less stable than $Pt_{2.0}/Pd_{10nm}$. As a result, the increase in the Pd core size did not show any benefit in the electrochemical stability of the core-

shell catalysts. The degradation mechanism was shown to result from two simultaneous mechanisms: the dissolution of Pd that was not covered with Pt and Pt agglomeration on the core-shell particle surface. The poorer Pt coverage on larger particles also negated any benefit for the ORR activity that could have been gained from their larger diameters.

As shown in Chapter 4, improvements in ORR activity and electrochemical stability of the core-shell catalysts are limited by the Pt coverage. Therefore the Pt shell deposition using the CSR is not suitable for the preparation of core-shell catalysts with large cores obtained by annealing. An interesting experiment would be to prepare core-shell catalysts with large Pd cores having either a controlled rounded-shape or more defects at the surface and observe the effect on the Pt coverage.

References

1. S. L. Gojkovi, S. K. Zecevic and R. F. Savinell, *Journal of Electrochemical Society*, **145**, 3713 (1998).

2. N. Markovic, H. Gasteiger and P. N. Ross, *Journal of Electrochemical Society*, **144**, 1591 (1997).

3. B. Hammer and J. K. Norskov, *Advances in Catalysis*, **45**, 71 (2000).

4. P. P. Wells, E. M. Crabb, C. R. King, R. Wiltshire, B. Billsborrow, D. Thompsett and A. E. Russell, *Physical Chemistry Chemical Physics* (2009).

5. A. Szabo, Z. Paál, A. Szász, J. Kojnok and D. J. Fabian, *Applied Surface Science*, **40**, 77 (1989).

6. J. F. Moulder, W. F. Stickle, P. E. Sobol and K. D. Bomben, *Handbook of X Ray Photoelectron Spectroscopy: A Reference Book of Standard Spectra for Identification and Interpretation of Xps Data*, Physical Electronics (February 1995) (1995).

7. M. Arenz, K. J. J. Mayrhofer, V. Stamenkovic, B. B. Blizanac, T. Tomoyuki, P. N. Ross and N. M. Markovic, *Journal of the American Chemical Society*, **127**, 6819 (2005).

8. F. Maillard, E. R. Savinova and U. Stimming, *Journal of Electroanalytical Chemistry*, **599**, 221 (2007).

9. Y. Shao, G. Yin, Y. Gao and P. Shi, *Journal of the Electrochemical Society*, **153**, A1093 (2006).

10. A. Ruban, B. Hammer, P. Stoltze, H. L. Skriver and J. K. Norskov, in *1st Francqui Colloquium on Molecular Heterogeneous Catalysis*, p. 421, Brussels, Belgium (1996).

11. J. Zhang, Y. Mo, M. B. Vukmirovic, R. Klie, K. Sasaki and R. R. Adzic, *Journal of Physical Chemistry B*, **108**, 10955 (2004).

12. J. Perez, H. M. Villullas and E. R. Gonzalez, *Journal of Electroanalytical Chemistry*, **435**, 179 (1997).

CHAPTER 6

PRELIMINARY RESULTS ON Pt_{SHELL}/Ir_{CORE} ELECTROCATALYSTS

CHAPTER 6: Preliminary results on Pt_{shell}/Ir_{core} electrocatalysts

6.1. Introduction

So far Pt/Pd core-shell electrocatalysts have been investigated for their use as cathode catalysts in PEMFC. However, it was pointed out that Pd was unstable and, as the Pt shell was not complete, Pd leached away into acid solutions upon polarisation scans at 80 °C. These observations contributed to the choice of Ir as an alternative core due to its similar stability to that of Pt. The Pt/Ir core-shell electrocatalysts were expected to show superior durability compared to the Pt/Pd core-shell electrocatalysts although better ORR activity was not anticipated (1, 2). Based on Johnson Matthey PGM price charts (3), the Ir price is currently one third of that of Pt, which is in line with the target of making ORR electrocatalysts cheaper.

In this chapter, two Pt/Ir core-shell catalysts were prepared by CSR using the same Ir core catalyst. The core-shell catalysts contained the equivalent of one and two Pt monolayers, and will be denoted as $Pt_{1.0}/Ir$ and $Pt_{2.0}/Ir$ respectively in the following. The catalysts were characterised with the same physical techniques as in the previous chapters. Particular attention will be paid to their electrochemical stability in very oxidising conditions. Finally, the MEA performance of the $Pt_{1.0}/Ir$ catalyst was evaluated.

6.2. Preparation and characterisation of Ir/C core

The carbon-supported Ir core particles were prepared using a deposition- precipitation route. Iridium trichloride ($IrCl_3$, 53.06% Ir) and $NaHCO_3$ were used as starting materials. As described in Chapter 2 Section 2.2, the carbon was first dispersed in water before addition of the base. The iridium salt was dissolved in warm water prior to addition and then pumped into the reaction mixture, which was refluxed and stirred for about 1 hour.

After being cooled, the catalyst was filtered, rinsed and dried. The dried catalyst was reduced in a furnace at 600 °C for 2 hours in 5% H_2 in N_2.

6.3. Preparation of Pt_x/Ir core-shells

Using the Ir core catalyst prepared above, two Pt/Ir/C core-shell electrocatalysts were prepared by CSR with two different Pt loadings. The amount of $Pt(acac)_2$ weighed exceeded that required for one and two Pt MLs as shown in Table 6-1. To prepare $Pt_{2.0}$/Ir the filtrate was used for a second deposition to complete the reaction.

Table 6- 1 Filtrate analysis for the preparation of $Pt_{1.0}$/Ir and $Pt_{2.0}$/Ir core-shell catalysts.

Catalyst	Excess $Pt(acac)_2$ used	1st deposition		2nd deposition	
		Filtrate	Pt / ppm	Filtrate	Pt / ppm
$Pt_{1.0}$/Ir	0.8 %	clear	6.5 ± 0.5		
$Pt_{2.0}$/Ir	10 %	yellow	240 ± 19.2	clear	< 1 ± 0.1

As shown by the catalyst metal assay in Table 6-2, the experimental Pt assay for $Pt_{2.0}$/Ir was 2.5 wt% below the nominal assay. This Pt loss was due to Pt deposition on the inner tube of the gas inlet, as a visible mirror.

Table 6- 2 Experimental and nominal Pt and Ir assays in Pt/Ir, and Pt:Ir atomic ratios.

Catalyst	Nominal Pt assay wt%	Actual	Nominal Ir assay wt%	Actual	Pt:Ir atomic ratio
38%Ir/C	-	-	40	38 ± 3.0	0:100
$Pt_{1.0}$/Ir	7.15	6.5 ± 0.5	35.3	34.6 ± 2.8	16:84
$Pt_{2.0}$/Ir	14.4	11.9 ± 0.9	32.9	33.8 ± 2.7	26:74

6.4. Characterisation of the Pt shell

6.4.1. CO chemisorption

The Pt/Ir electrocatalyst surface areas were estimated by CO chemisorption and compared with that of the Ir core. It was assumed that one CO molecule was adsorbed per surface atom of Ir. The dispersion (D) was calculated as follows:

$$D = \frac{N_{CO}}{\frac{Ir_{wt\%}}{MM(Ir)} + \frac{Pt_{wt\%}}{MM(Pt)}} \quad \textbf{(6- 1)}$$

Assuming the atomic densities of Pt and Ir at the surface were the same, the electrocatalyst surface areas (S) in square meter per gram of catalyst were determined by the following:

$$S = \frac{N_{CO} \times N_A}{d_S} \quad \textbf{(6- 2)}$$

N_{CO} is the amount of adsorbed CO in mol $g_{catalyst}^{-1}$
N_A is the Avogadro constant (6.023×10^{23})
d_s is the number of metal atoms per cm^2

No significant change in the amount of adsorbed CO between the Ir core and Pt/Ir core-shell catalysts was observed, which supports the assumption of a CO adsorption stoichiometry of 1 CO molecule per 1 surface Ir atom. The dispersion however decreased as a function of the Pt coverage and this may be attributed to an increase in the mean particle size.

Table 6- 3 Calculated dispersion and surface areas determined from the amount of adsorbed CO.

Catalysts	CO / mmol g^{-1}	D / %	Particle size* / nm	Surface area /	
				$m^2\ g_{Ir+Pt}^{-1}$	$m^2\ g_{Pt}^{-1}$
38%Ir/C	0.4084	21	4.5	101.6	
$Pt_{1.0}/Ir$	0.4327	20	4.7	74.8	471.4
$Pt_{2.0}/Ir$	0.4378	18	5.3	68.1	261.7

*calculated from Benfield's cubooacthedron and icosahedron model equation (4)

6.4.2. XRD analysis

Figure 6-1 shows the XRD patterns of the prepared $Pt_{1.0}/Ir$ and $Pt_{2.0}/Ir$ core-shell catalysts along with that of the carbon-supported Ir. A Rietveld analysis was carried out to determine the crystallite sizes and lattice parameters of the phases detected. The XRD data are summarized in Table 6-4.

Regardless of the composition, the three catalysts show similar face cubic centred single phase XRD patterns. The $Pt_{1.0}/Ir$ diffraction pattern indicated the presence of a major amount of poorly crystalline cubic phase very close in lattice parameters to Ir. The profile of the pattern does not indicate whether free Ir or a very Ir-rich Pt/Ir alloy is present. The characteristic non-Gaussian peak profiles indicate a bi-modal crystallite size distribution for the principal phase detected. The lattice parameter and the crystallite size for $Pt_{1.0}/Ir$ could not be determined as Rietveld analysis cannot be accurately applied to bi-modal distributions.

The $Pt_{2.0}/Ir$ diffraction pattern indicates the presence of poorly crystalline Ir and a very poorly crystalline cubic Pt/Ir alloy phase, intermediate in lattice parameters between Pt (3.9231 Å) and Ir (3.8394 Å). Unlike Pd, the Ir diffraction lines are far enough apart from those of Pt, thus making the phase identification easier. The calculated Ir crystallite size is consistent with that of the Ir core catalyst. The diffraction peaks had a clear Gaussian peak shape, indicating the particles are mainly composed of one phase. The absence of a shoulder reveals that isolated Ir particles were not numerous enough to produce a detectable signal. With a Pt bulk atomic composition of 26%, a Pt-containing phase should be detected for $Pt_{2.0}/Ir$, which leads us to the conclusion that the Pt-Ir alloy phase was the predominant phase. Bharadwaj *et al.*(5) determined the phase diagram of the Ir-Pt system and the relationship between the lattice parameter of the Pt-Ir solid solution and the

composition. The alloy phase of $Pt_{2.0}/Ir$ had a lattice parameter of 3.87 Å, corresponding to an atomic composition of 40%Pt and 60%Ir in the near surface region of the core-shell particles. The expansion of the lattice parameter of the alloy phase compared to that of pure Ir arises from the substitution of the smaller Ir atoms by the larger Pt atoms.

Table 6- 4 Crystallite size and lattice parameter calculated by Rietveld analysis.

Catalysts	Phase	Crystallite size / nm	Lattice parameter / Å	Cell volume / Å^3
Pt	-	-	3.9231	60.38
Ir			3.8394	56.60
38%Ir/C		4.2	3.8404	56.64
$Pt_{1.0}/Ir$		N/A	N/A	
$Pt_{2.0}/Ir$	IrPt	1.6	3.870	
	Ir	5.5	3.8374	

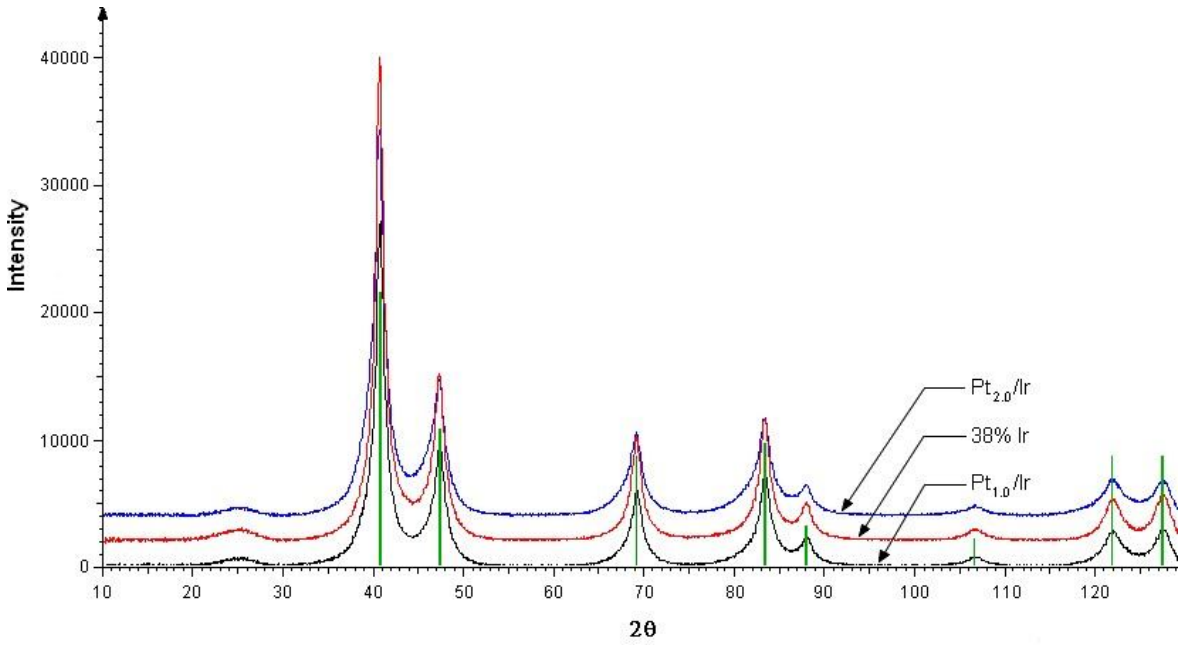

Figure 6 - 1 Overlaid XRD patterns of 38% Ir/C, $Pt_{1.0}/Ir$ and $Pt_{2.0}/Ir$. The green lines represented the documented Ir diffraction lines.

6.4.3. High resolution TEM observations

TEM images were obtained for each of the catalyst materials and representative images are shown in Figure 6-2. The particle size distributions of the core and core-shell electrocatalysts were examined and the histograms obtained by analysis of the images are shown in Figure 6-3. 38% Ir/C showed a wide particle size range, which could be taken as a bimodal distribution skewing around 2 nm and 12 nm. The TEM images of the large particles showed evidence of stacking faults, as seen in Figure 6-3.

The inhomogeinity of the core particle size distribution was also observed in the core-shells. The average particle size of $Pt_{1.0}$/Ir was around 4.2 nm with many large particles of more than 20 nm being found. The $Pt_{2.0}$/Ir sample had a multimodal Pt Ir particle size distribution with an average size of 5.2 nm. The $Pt_{2.0}$/Ir particle size was consistent with the crystallite size, indicating the absence of particle agglomeration. The particles looked facetted.

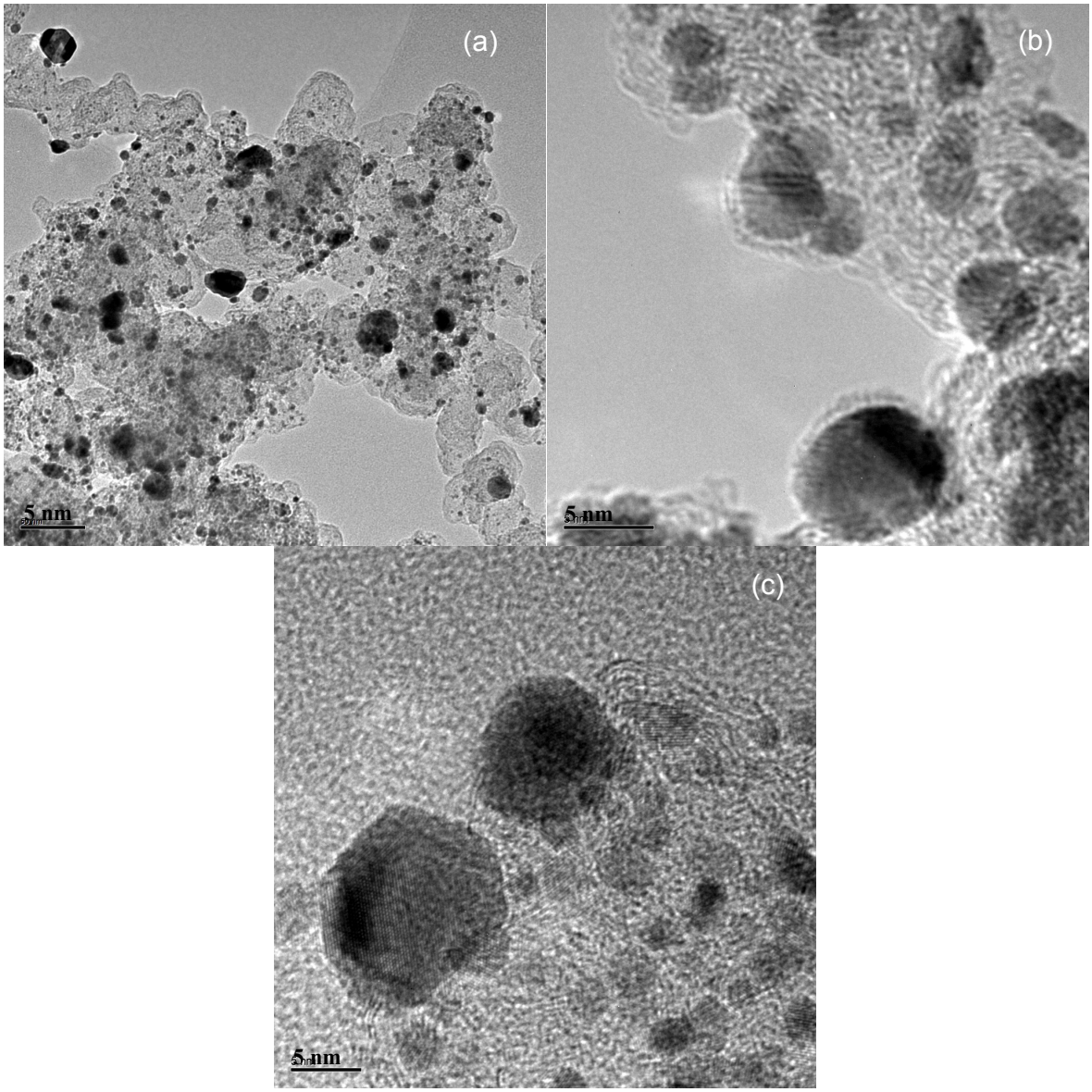

Figure 6 - 2 TEM micrographs of 38%Ir/C (a), $Pt_{1.0}$/Ir/C (b) and $Pt_{2.0}$/Ir/C (c).

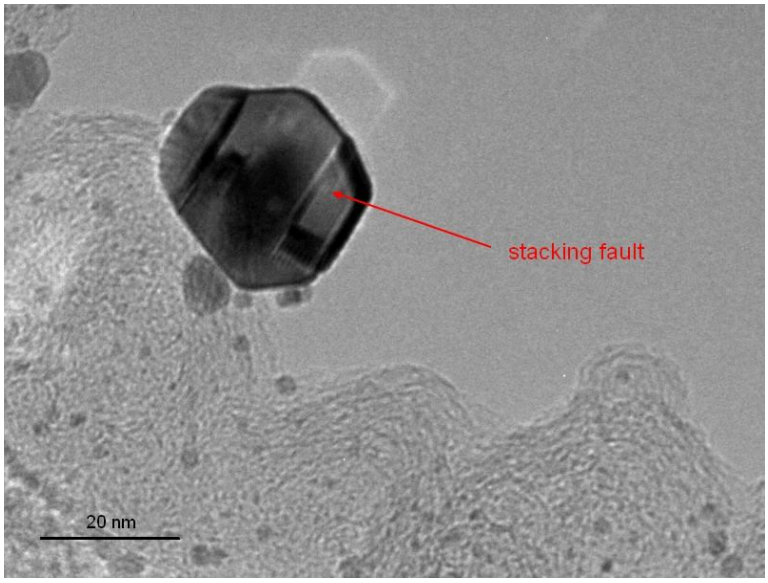

Figure 6 - 3 HRTEM micrographs of 38% Ir/C particles showing a stacking fault.

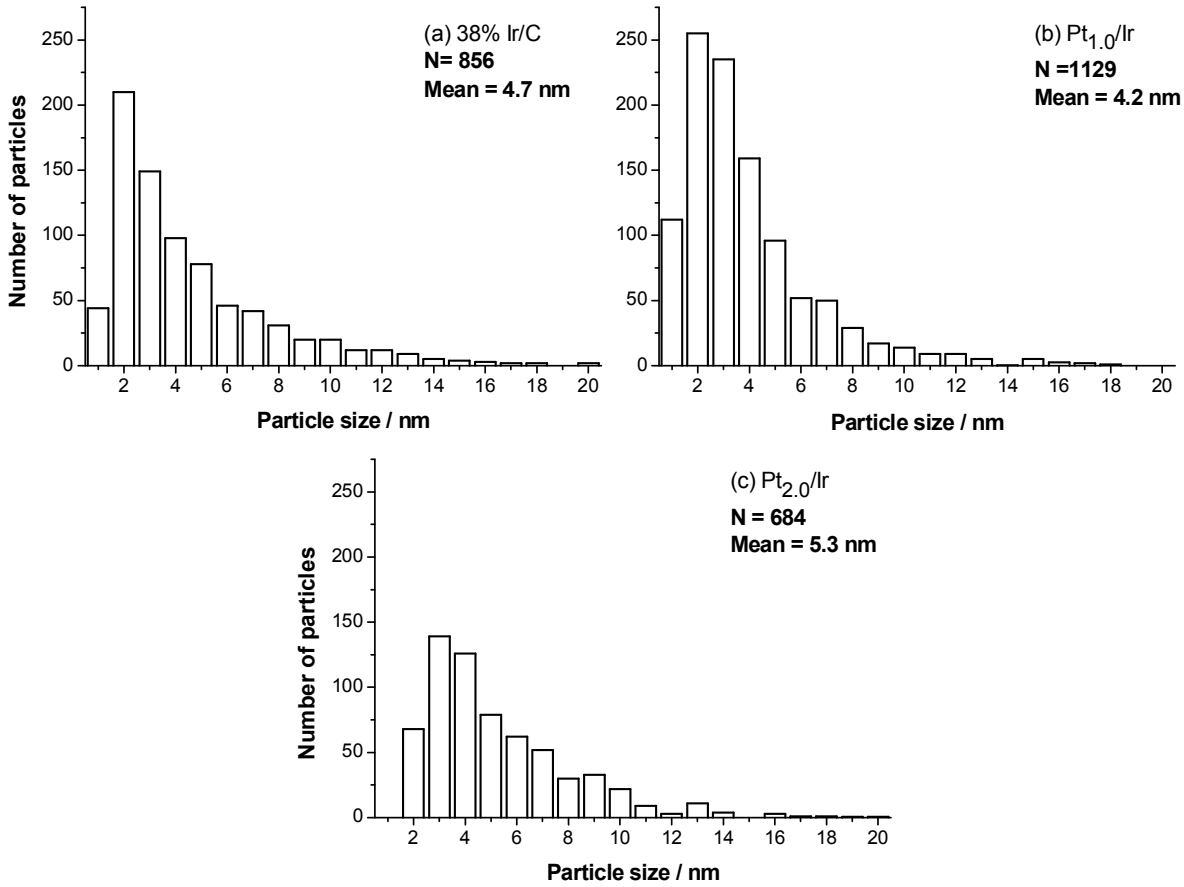

Figure 6 - 4 Particle size distribution bar charts for (a) 38% Ir/C, (b) $Pt_{1.0}$/Ir, (c) $Pt_{2.0}$/Ir.

The EDX profiles, shown in Figures 6-5 and 6-6, were obtained by recording the intensities of the Pt $L_{\alpha 1}$ (9.44 keV) and Ir $L_{\alpha 1}$ (9.17 keV) emission lines at 60 points across the particle. The lines in the K and M series could not be used to analyse the composition because they were too close in energy. The observation of the Pt shell was not possible because of the similarity in weight between Pt (195.08 g mol^{-1}) and Ir (192.22 g mol^{-1}).

For $Pt_{1.0}/Ir$, the Ir and Pt peaks follow each other (almost one to one) as one would expect for an alloyed particle. This may be a consequence of the proximity in energy of the $L_{\alpha 1}$ emission lines. The particle analysed was rather small, about 2.2 nm across, and did not present any sign of agglomeration or dislocations, as shown by the absence of spikes in the signal. The Pt shell could not be distinguished using EDX. The particle analysed in $Pt_{2.0}/Ir$ was larger, about 18 nm across. The EDX line profile resembled again that of an alloy. The Ir and Pt distributions followed each other in trend but not exactly one to one, which suggests localised atomic scale clustering.

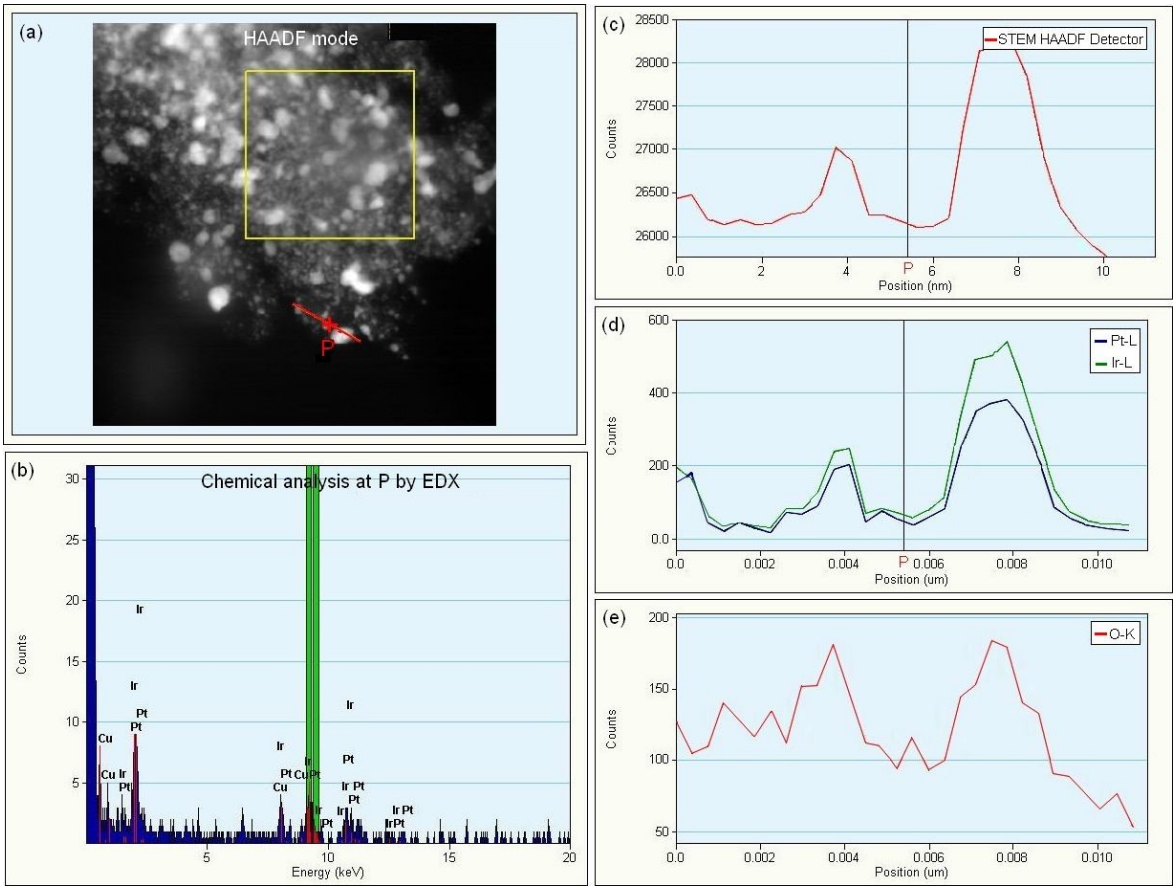

Figure 6 - 5 HRTEM micrographs of $Pt_{1.0}/Ir$ particles in HAADF mode (a). Chemical analysis at position P (b). EDX total count profile across two core-shell particles following the red line in picture a (c). EDX Pt and Ir profiles (d). EDX O profile (e).

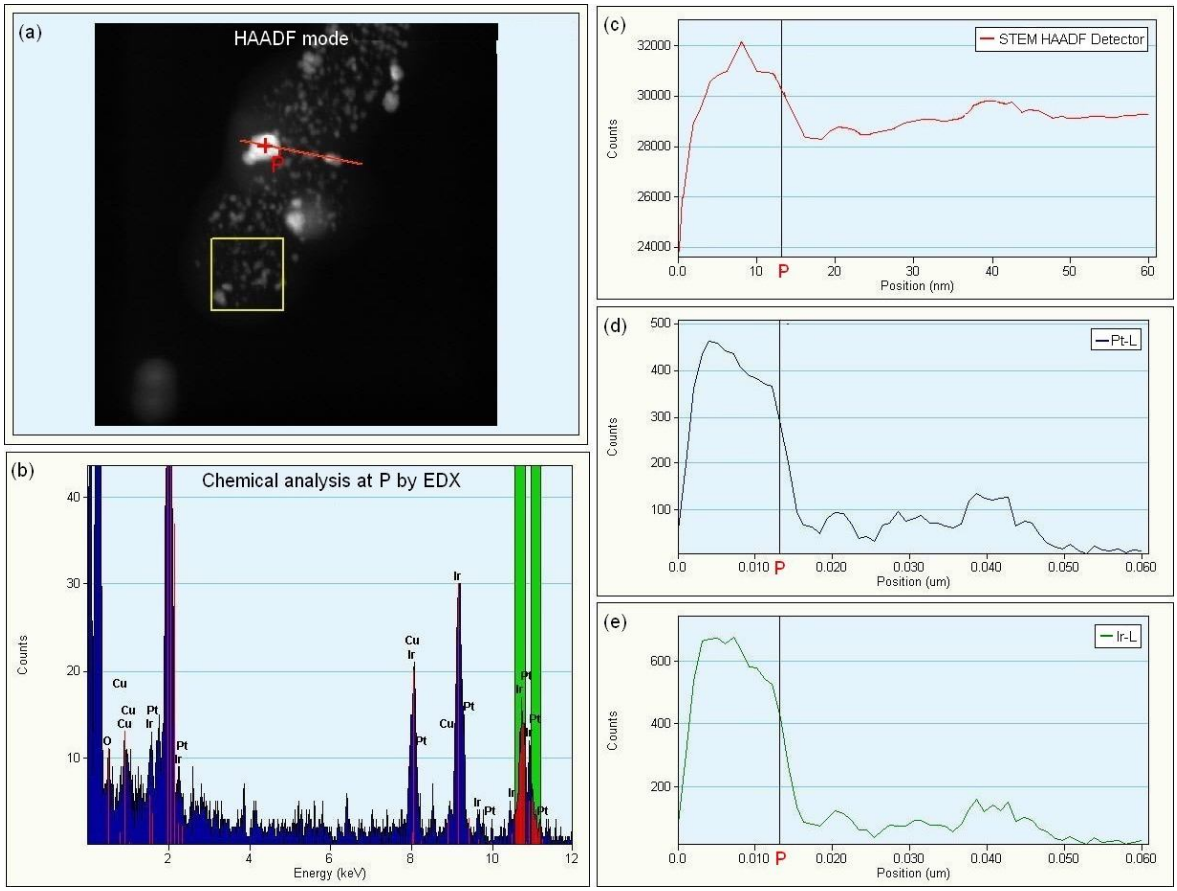

Figure 6 - 6 HRTEM micrographs of $Pt_{2.0}/Ir$ particles in HAADF mode (a). Chemical analysis at position P (b). EDX total count profile across two core-shell particles following the red line in picture a (c). EDX Pt profile (d). EDX Ir profile (e).

6.4.4. HS-LEIS analysis

The HS-LEIS analyses were performed on the Pt/Ir core-shells and the 38% Ir/C for comparison. The samples were analyzed with the Qtac100 instrument since high mass resolution was required to separate the Pt peak from the Ir peak. This was achieved with heavy primary ions $^{84}Kr^{+}$. However, in this case, the secondary ion background needed to be suppressed with the aid of Time-of-Flight filtering. All samples were analysed after a 10 minute treatment with 100 mbar H_2 at room temperature to remove oxygen from the sample surface.

With the Qtac100 instrument, the samples were analysed at 6 different spots with a size of 2x2 mm^2. This kept the sputter damage to the samples limited to less than 1% of a monolayer.

Figure 6-7 shows the 8keV $^{84}Kr^{+}$ ToF Filtered LEIS spectra after background subtraction of the catalyst samples after hydrogen reduction treatment, compared to the scaled spectra

for the clean metal references. It is clear that the spectra for samples $Pt_{1.0}$/Ir, $Pt_{2.0}$/Ir and 38% Ir/C were very similar.

Table 6-5 shows the contribution of Ir to the spectra of the catalyst samples. The results suggested that the core-shell surface did not contain any Pt and the amount of Ir was slightly lower for $Pt_{2.0}$/Ir. The catalyst surface may have been covered with organic species from the synthesis. That would suggest that the hydrogen-heat treatment performed on the core-shell materials was not sufficient to completely clean off the surface. As this was not observed on the Pt/Pd core-shells, it may indicate that the ligands were more strongly bonded to the Pt/Ir surface than the Pt/Pd one. An alternative explanation would be the diffusion of Pt into the Ir lattice, although this was not expected as it does not agree with the DFT predictions. Callejas-Tovar (6) showed that Ir is not expected to segregate to the surface in either the PtIr alloy or core-shell systems under vacuum or in the presence of oxygen.

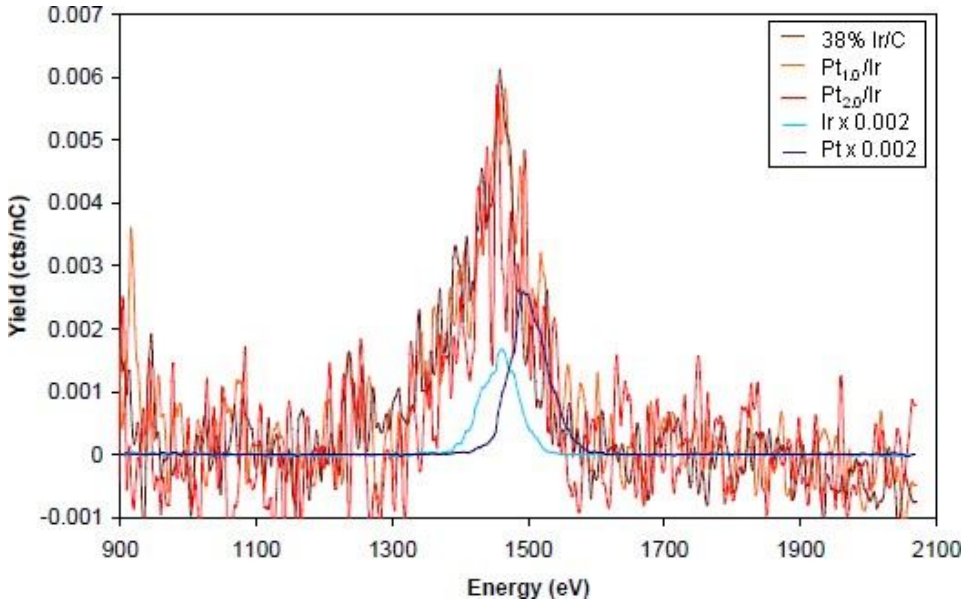

Figure 6 - 7 The 8keV $^{84}Kr^{+}$ ToF Filtered LEIS spectra, after background subtraction, for $Pt_{1.0}$/Ir, $Pt_{2.0}$/Ir and 38% Ir/C.

Table 6- 5 Surface atomic composition extracted from Figure 6-5

Catalysts	Surface fraction / %	
	Pt	Ir
38%Ir/C	0	0.75
$Pt_{1.0}/Ir$	0	0.75
$Pt_{2.0}/Ir$	0	0.6

6.4.5. XPS analysis

To examine the chemical state and composition of the Pt-Ir core-shell catalysts, XPS measurements of Pt 4f and Ir 4f were carried out. The XPS spectra are shown in Figure 6-8. Both iridium and platinum 4f signals appear to be almost entirely due to metal. The binding energies are higher than the reference data for the pure metals, which may be assigned to an alloy effect or the interaction of the carbon support.

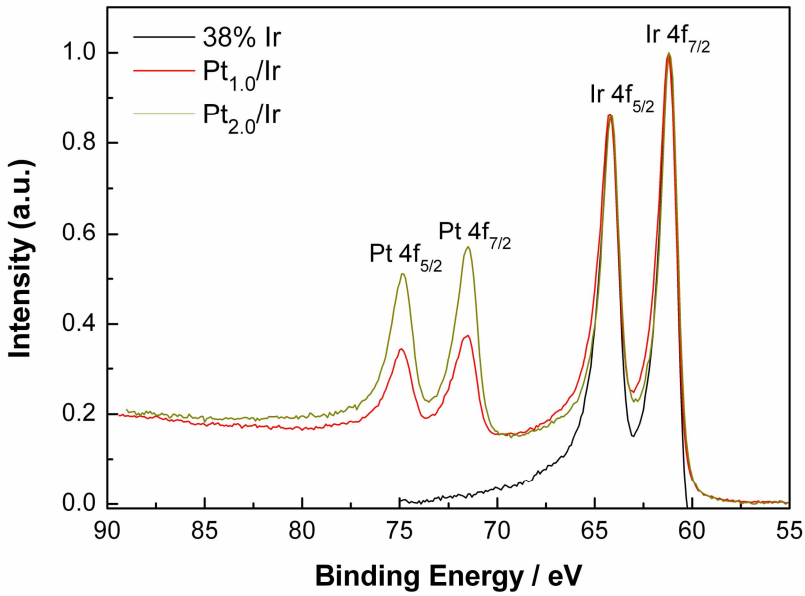

Figure 6 - 8 Normalised Pt 4f and Ir 4f XPS spectra for 38% Ir/C, $Pt_{1.0}/Ir$ and $Pt_{2.0}/Ir$ catalysts.

The Pt:Ir atomic ratios of the near surface were similar to those determined by ICP-ES, allowing for the experimental errors and are shown in Table 6-6. This suggests that the particles were alloyed, even though the temperature was kept low. Another explanation may be that the deposition of Pt was energetically more favourable on Pt-H sites rather than on Ir-H sites, which would lead to a poorer Pt coverage on Ir cores than on Pd cores.

Interestingly, the Pt:Ir surface composition of $Pt_{2.0}$/Ir (31:69) was similar to that of the PtIr alloy phase detected by XRD (40:60). This suggests that, in contrast to the prepared Pt/Pd core-shell catalysts, the Pt/Ir core-shell catalysts present an alloyed surface.

No binding energy shift was observed for both Pt $4f_{7/2}$ and Ir $4f_{7/2}$ peaks, signifying that neither the electronic structure of Pt nor that of Ir was modified. As Pt is more electron rich than Ir, a charge transfer from Pt to Ir would be expected, which would increase the Pt 5d vacancy, and thus the Pt binding energy. The fact that this effect was not observed may be due to the low atomic proportion of Pt compared to Ir.

Table 6- 6 XPS parameters extracted by curve fitting the spectra shown in Figure 6-7

Catalysts	Ir $4f_{7/2}$	Pt $4f_{7/2}$	$(Pt:Ir)_{XPS}$	$(Pt:Ir)_{ICP-ES}$
40% Pt/C	-	71.7	-	100:0
38% Ir/C	61.2	-	-	0:100
$Pt_{1.0}$/Ir	61.2	71.6	20:80	16:84
$Pt_{2.0}$/Ir	61.2	71.5	31:69	26:74

6.5. Electrochemical properties

6.5.1. Surface characterisation

Figure 6-9(a) shows a representative voltammogram for 38%Ir/C in 1 M H_2SO_4 solution at 80 °C. The CV of 60%Pt/C was added for comparison. A similar Ir voltammogram was obtained by K. Lee et al. (7). Iridium displays surface electrochemical behaviour similar to that of Pt. The hydrogen adsorption/desorption peaks, although small, can be observed in the potential range between 0.02 and 0.4 V vs Pd/H ref. There were two peaks around 48 mV and 140-340 mV. They were broad and flat, compared to those of Pt.

Although the amount of oxide formed on Ir was not significant, it is interesting to notice that the onset potential was very low, around 0.45 V compared to 0.7 V on Pt. As a consequence, the double layer region was very narrow covering only a 10 mV potential range.

At potentials above 0.4 V, oxygen is adsorbed and gives rise to an ill-defined and rather flat wave. This may indicate that in the potential range of study (0.01 – 1.0 V), Ir does not

form multiple layers of oxide, as Pt, but a compact oxide monolayer. As shown in Figure 6-10, the initial oxide formation is reversible but becomes irreversible as the anodic potential is increased in agreement with previous studies (10). This is in agreement with the Pourbaix diagram for Iridium at 25 °C at pH 0, where it can be seen that Ir oxide IrO_2 does not form until 1.0 V vs RHE (8). Extending the anodic potential limit to 1.4 V gave rise to a second broad and flat feature between 0.8 and 1.1 V (Figure 6-10), followed by the evolution of oxygen (9). This was accompanied by a negative shift of the oxide removal peak on the cathodic sweep.

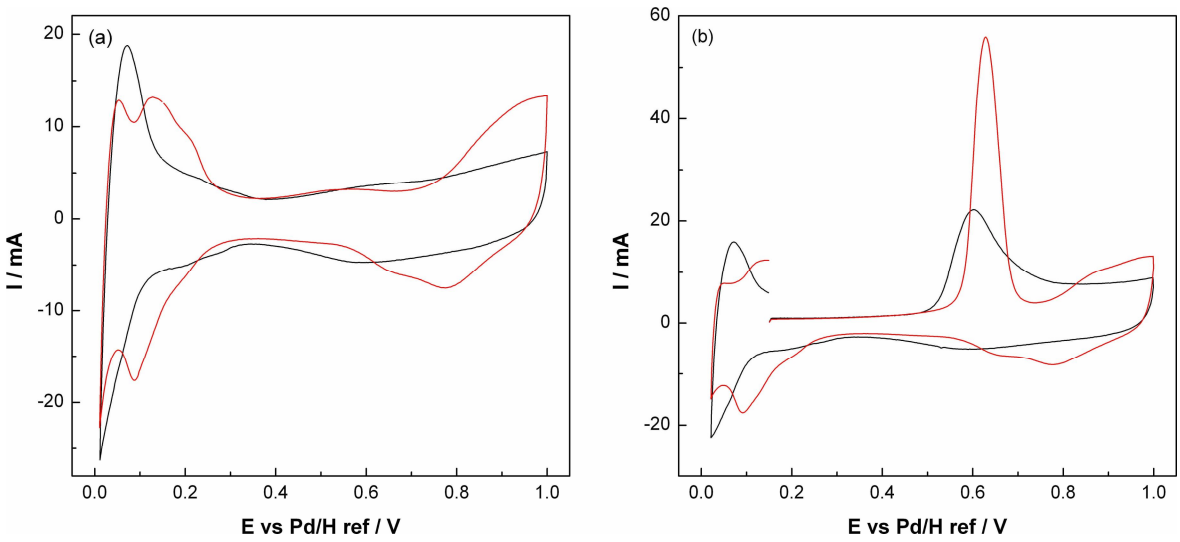

Figure 6 - 9 (a) Cyclic voltammograms and (b) CO electrooxidation voltammograms of 38%Ir/C (black line) and 40%Pt/C (red line) in 1 M H_2SO_4, at 10 mV/s at 80°C. Electrode area: 3.14 cm^2

The electrooxidation of CO occurs at lower potential on Ir, which is consistent with the fact that Ir starts to grow oxide at more negative potentials than Pt. In fact, surface activity towards CO electrooxidation is predominantly influenced by the ability of the surface to dissociate water and to form OH_{ad}. The broadness of Ir CO peak was interpreted as due to the wide particle size distribution of the 38% Ir/C catalyst.

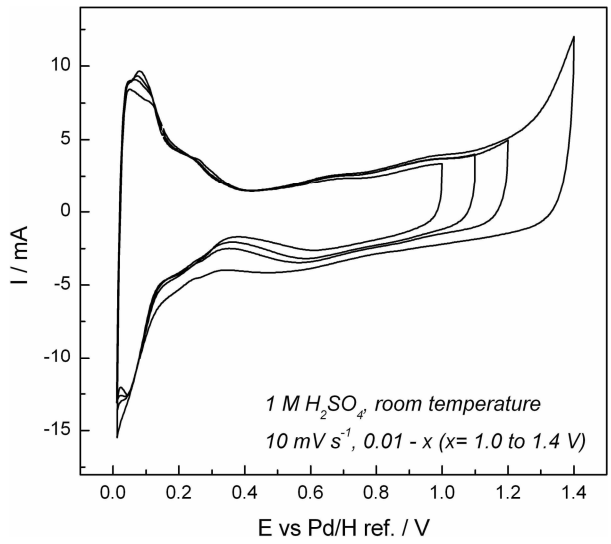

Figure 6 - 10 Window opening experiment on 38% Ir/C, in which the anodic limit was changed (1.0, 1.1, 1.2, 1.4 V), in 1 dm^{-3} H_2SO_4, Scan rate: 10 mV s^{-1}.

The voltammograms of $Pt_{1.0}$/Ir, $Pt_{2.0}$/Ir are compared with 38% Ir/C and 40% Pt/C electrocatalysts and are shown in Figure 6-11(a). The core-shell CVs were very similar to that of pure Ir, which is not surprising as the physical characterisation presented earlier revealed that the core-shell catalyst surfaces were mostly composed of Ir. The voltammograms exhibited a broad feature between 0.15 V and 0.3 V with an early onset of the hydrogen evolution reaction. In the oxide region, the onset of the oxide formation was the same for the Pt/Ir core-shell catalysts and Ir, but a lot more oxide was built up on Pt/Ir. Two features were observable in the cathodic sweep at 0.77-0.79 V and 0.57-0.58 V, and could be assigned to the reduction of Pt oxide and Ir oxide, respectively. In the CO electrooxidation voltammograms presented in Figure 6-9(b), the shape and the position of the core-shell CO peaks were similar to that of 38%Ir/C: low CO electrooxidation onset potential (~0.4 V) and a long tail, the latter suggesting a slow process.

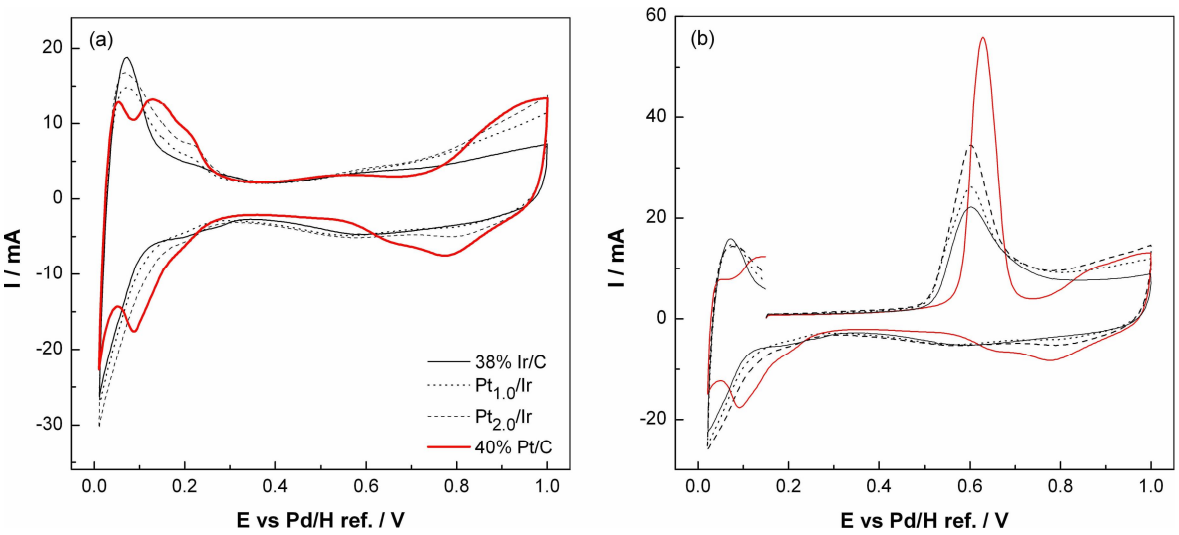

Figure 6 - 11 Cyclic voltammograms of the $Pt_{1.0}/Ir$, the$Pt_{2.0}/Ir$, 40%Pt/C and 38% Ir/C catalysts in 1 M H_2SO_4 at 80°C, 10 mV s^{-1}.

The electrochemical information about the Pt/Ir core-shell catalysts was extracted from Figure 6-11 and is presented in Table 6-7 along with that of 38%Ir and 40%Pt. The electrochemical area (ECA) of the electrocatalysts was determined by the CO electrooxidation charge in the cyclic voltammograms in Figure 6-11. The Faradaic charge for H_{upd} and CO monolayer formation on Ir was assumed to be the same as for Pt, 210 and 420 μC cm^{-2}. The surface areas calculated were consistent with those calculated from the data measured by CO chemisorption. The Q_{CO}:Q_H charge ratios were very high for the Ir-containing catalysts, indicating either an excess of CO charge or a lack of H charge. As the Q_{CO} is limited by the catalyst surface area, the high Q_{CO}:Q_H is more likely to be due to the low Q_H. This suggests that hydrogen is not easily adsorbed on Ir.

Table 6- 7 Electrochemical data extracted from Figure 6-10.

Catalysts	CO charge / C $mg_{(Pt+Ir)}^{-1}$	Q_{CO}:Q_H	ECA* / m^2 $g_{(Pt+Ir)}^{-1}$
38% Ir/C	0.89	19.1	102.4
$Pt_{1.0}/Ir$	0.73	10.6	55.7
$Pt_{2.0}/Ir$	0.72	23.2	54.4
40% Pt/C	0.86	2.1	65.4

*determined by the CO electrooxidation charge

6.5.2. Electrochemical stability

The electrochemical stabilities of the Ir core and the Pt/Ir core-shell electrocatalysts were investigated by repetitive polarisation scans in 1 M H_2SO_4 at 80 °C, following the same procedure as for the Pt/Pd core-shell electrocatalysts. The CVs performed after 0, 200, 600 and 1000 polarisation scans between 0.6 and 1.0 V, are shown in Figure 6-12. During the stability test, the level of dissolved Ir and Pt was monitored by withdrawing 5 mL of the electrolyte and then analysing by ICP-ES. The change in the amount of catalyst dissolved during cycling is presented in Figures 6-13 (b), (d) and (f). The active area loss of the electrocatalysts was determined by measuring the H_{upd} and CO electrooxidation Faradaic charges, Q_H and Q_{CO}, and the results are summarised in Table 6-8.

As the electrocatalysts were cycled, Pt features appeared in the H_{upd} region. After 1000 cycles, the voltammograms exhibit a strong Pt character although they retain the Ir features in the oxide region (Figures 12(a), 12(c) and 12(e)). The change in the voltammogram shape was accompanied by the dissolution of Ir into the electrolyte, while the level of dissolved Pt remained low and almost constant. The area of the core-shell CO peaks decreased in a constant way, but more importantly, the onset of the peaks did not change with cycling. This suggests that the presence of Pt on the surface did not modify the electronic properties of the surface. However, the decrease in the Q_{CO}:Q_H charge ratios towards 2 (Figure 6-14(b)) indicated a Pt-enrichment of the surface.

Table 6- 8 Electrochemical stability results

Catalysts	Q_H loss / %	Q_{CO} loss / %	Potential shift / mV	Q_{CO}:$Q_{H(1000\ cycles)}$
38% Ir/C	51	71	-9	11
$Pt_{1.0}$/Ir	-12	78	-45	2
$Pt_{2.0}$/Ir	-256	65	-39	2.3
40% Pt/C	50	60	-44	2.1

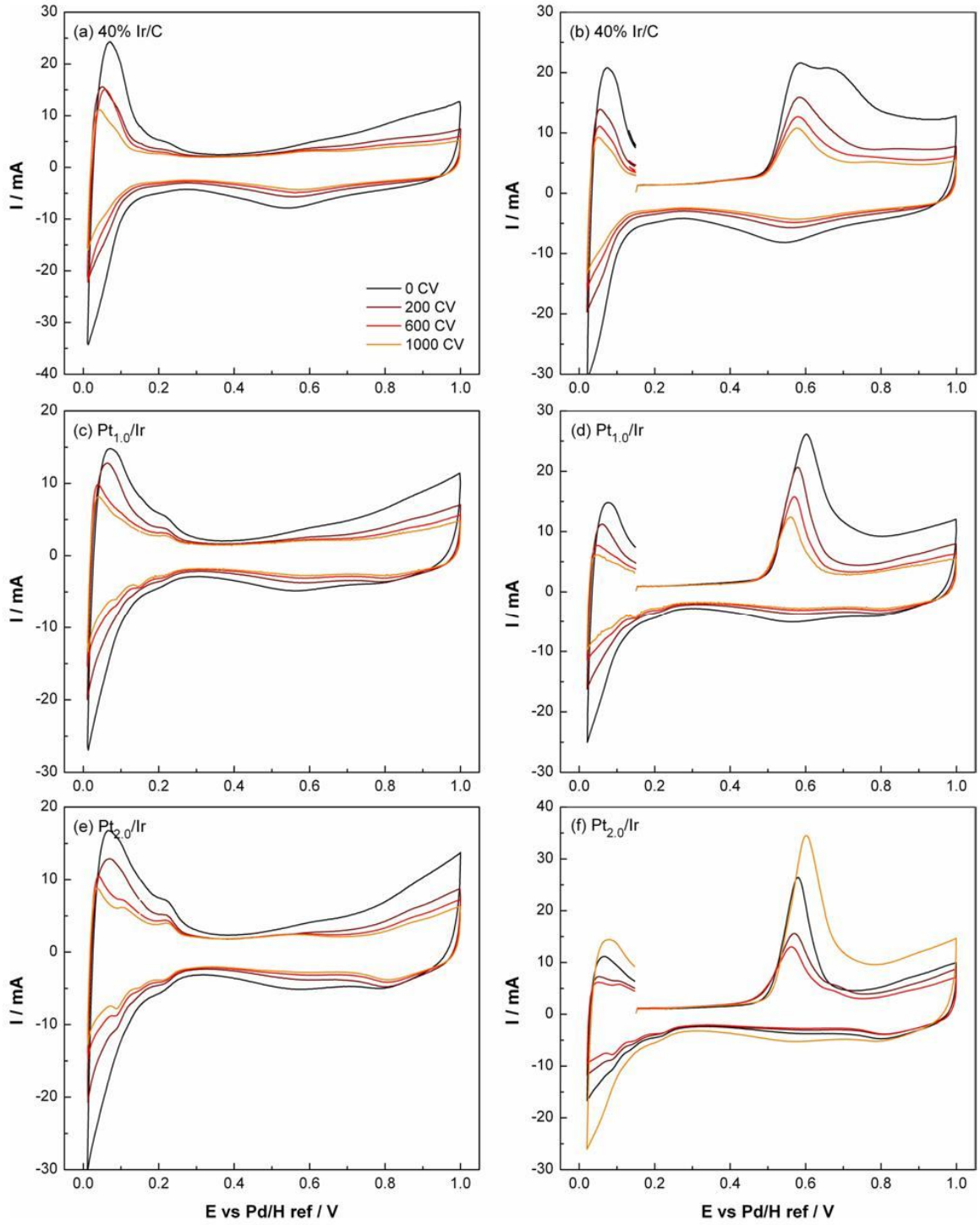

Figure 6 - 12 Cyclic voltammograms (a-b) and CO electrooxidation voltammograms (c-d) recorded every 200 cycles from 0 to 1000 cycles in 1 *M* H_2SO_4, between 0.01 – 1.0 V at 10 mV s^{-1} at 80 ºC for (a-b) 38%Ir, (c-d) $Pt_{1.0}/Ir$ and (e-f)) $Pt_{2.0}/Ir$ electrocatalysts.

Figure 6-13 (a), (c) and (e) shows the change in the Q_H and Q_{CO} charges upon cycling for the Ir/C core, and the Pt/Ir core-shell electrocatalysts. For the Ir/C core, both charges changed in the same way. For the Pt/Ir core-shell electrocatalysts, the Q_H charge loss

decreased significantly before slowly increasing, whereas the Q_{CO} charge loss increased constantly. Until about 400 cycles, there is an excess of Q_{CO} charges compared to Q_H charges, indicating that hydrogen is weakly adsorbed on Ir.

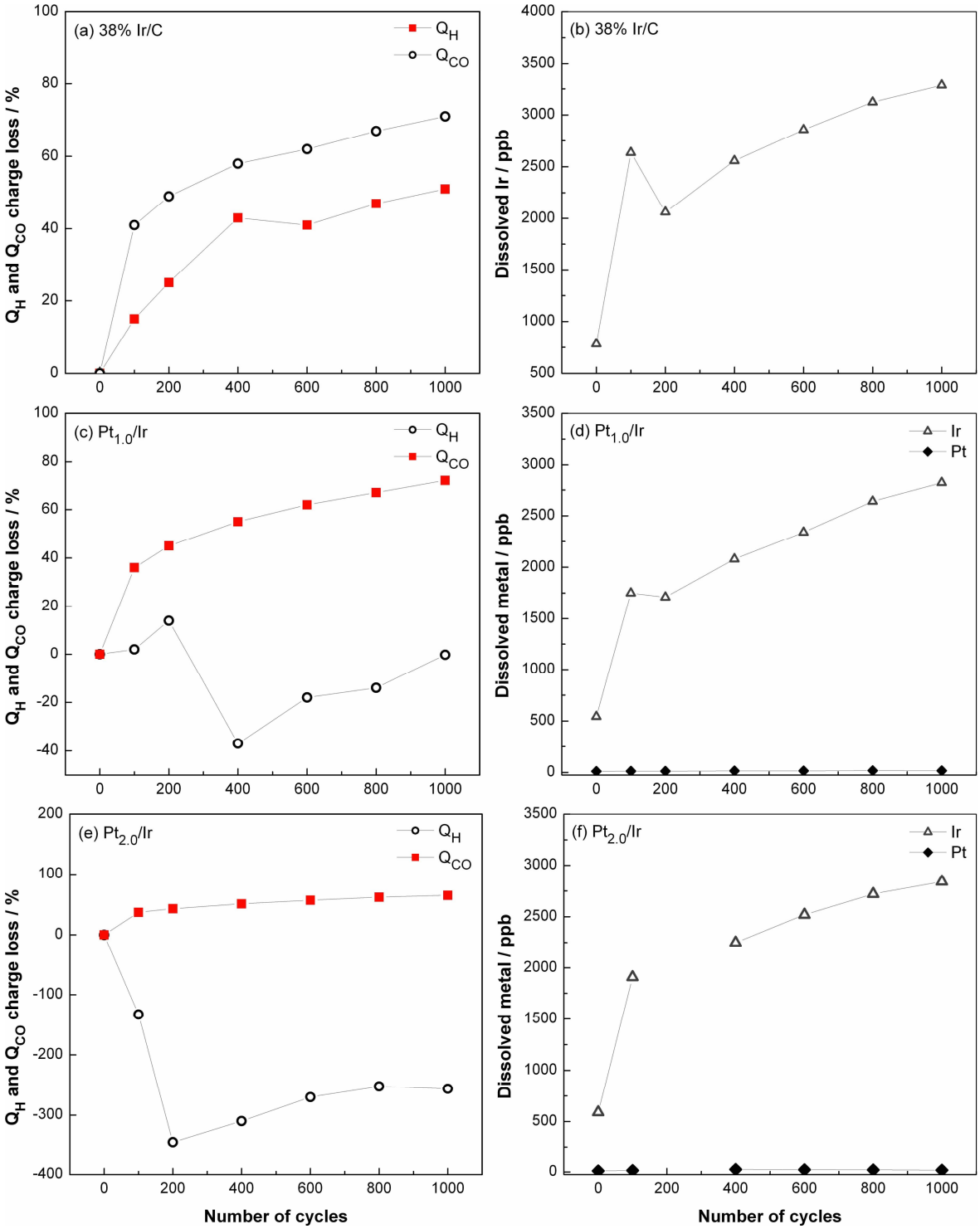

Figure 6 - 13 Change in Q_H and Q_{CO} charges (a, c and e) and in the amount of dissolved Pt and Ir (b, d and f) during the cycling test for 38% Ir/C, $Pt_{1.0}$/Ir and $Pt_{2.0}$/Ir.

Figures 6-14 show that the charges obtained from the integration of the H_{upd} region and the CO peak did not change in the same way. Based on the percentage of Q_{CO} charge loss after 1000 cycles, the $Pt_{1.0}$/Ir/C and $Pt_{2.0}$/Ir/C catalysts lost 72% and 65% of their active areas, respectively. Compared to the Ir core catalyst, whose active area loss is about 71%, the core-shell catalysts did not show a significant improvement in stability. This supports the idea that the Pt coverage on the core-shell electrocatalyst was very low but that during cycling the surface became more Pt-rich, which explains the increase in the H_{upd} Faradaic charges.

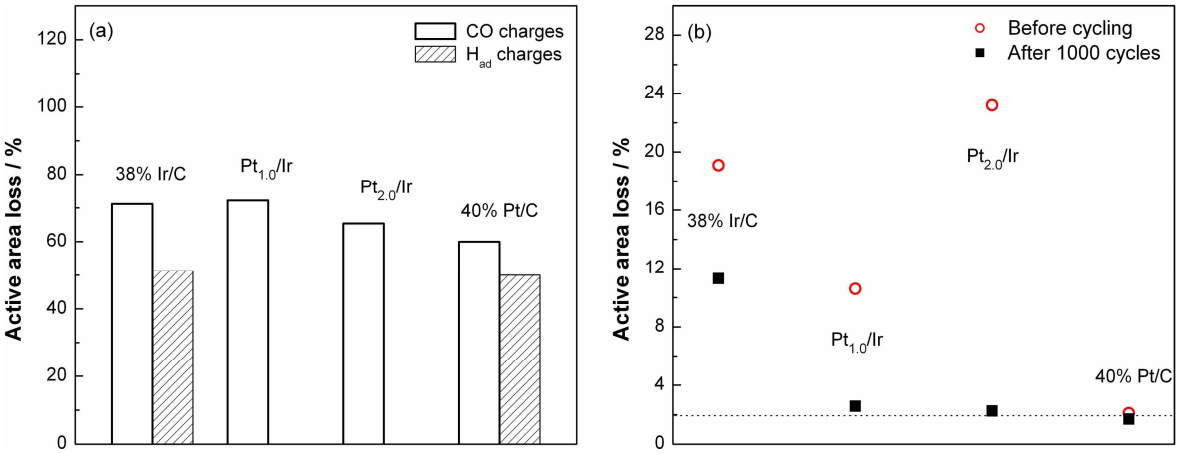

Figure 6 - 14 CO and H charge losses after 1000 cycles (a) and their ratios CO:H before and after 1000 cycles (b)

6.5.3. Activity for the reduction of oxygen

RDE measurements

Due to a lack of time, the ORR activities of the Pt/Ir core-shell catalysts were not tested using the thin film method. However, the activity of Ir core catalyst was assessed and compared to that of 40% Pt. The hydrodynamic voltammograms measured in O_2-saturated 0.1 M $HClO_4$ at 2500 rpm at ambient temperature are shown in Figure 6-15(a).

It can be seen that the onset of the reduction of oxygen occurred at lower potential on Ir than on Pt. The small slope of the Ir voltammogram is indicative of slow ORR kinetics. The mass and specific activities of 38%Ir/C at 0.9 V were respectively $\left(\frac{1}{85}\right)^{th}$ and $\left(\frac{1}{30}\right)^{th}$ of the 40%Pt/C catalyst. The low ORR activity of Ir can be explained by the fact that it

bonds oxygen more weakly than Pt, which makes the oxygen dissociation difficult. In fact, as can be seen in the Ir voltammetry (Figure 6-9), the oxide formation/reduction process was more reversible on Ir than on Pt.

It can be supposed that the Pt/Ir core-shell catalysts would have an intermediate activity between those of Ir and Pt. In fact, Nørskov's DFT calculations predict that the d-band center of a Pt monolayer would be downshifted by the presence of an Ir(111) substrate, which would weaken the bond with oxygen and hinder O_2 dissociation.

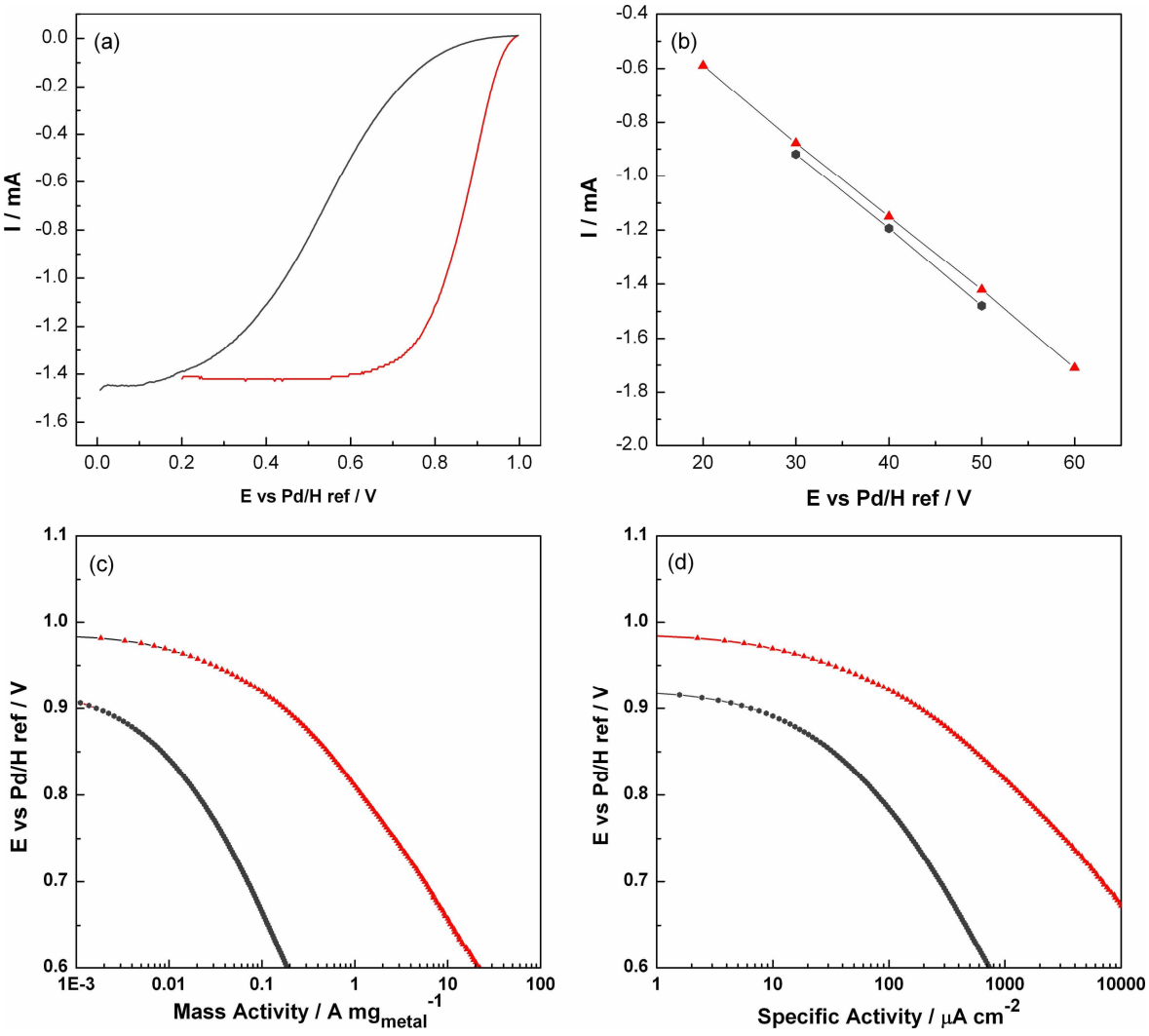

Figure 6 - 15 Activity assessment for 38% Ir/C (grey) and 40% Pt/C (red) in 0.1 M $HClO_4$ at room temperature: (a) Hydrodynamic voltammograms (backward scans) in O_2-saturated 0.1 M $HClO_4$ at 10 mV s^{-1}, 1.0-0 V. (b) Levich plots: limiting currents taken at 0.05 V for 38% Ir/C and 0.2 V for 40% Pt/C. (c) Mass activity per gram of metal at 2500 rpm. (d) Mass activity per cm^2 of active catalyst at 2500 rpm. Electrode area: 0.196 cm^{-2}.

Single cell test

The performance of three MEAs (49 cm^2) prepared with Pt1.0/Ir, $PtIr_3$ alloy and 40%Pt as the cathode catalysts with 40% Pt/C as the anode catalyst, was assessed in a H_2/O_2 single cell at 80 °C, at 50 kPa_{gauge}, at 100 $\%RH_{anode/cathode}$ (relative humidity). Before the test, the resistance across the cell and the hydrogen crossover current were determined. The MEA was then conditioned under H_2/air at 0.5 $A.cm^{-2}$, which was followed by the evaluation of its performance under H_2/O_2. The polarisation curves were corrected for ohmic losses and are shown in Figure 6-16.

$Pt_{1.0}$/Ir core-shell and $PtIr_3$ alloy electrocatalysts had a Pt:Ir surface atomic composition of about 20:80 and 38:62, respectively, and showed equal Pt-mass activity. It is remarkable that at 0.85 V, $Pt_{1.0}$/Ir exhibited 2 times higher Pt-mass activity than 40%Pt with only one sixth of the Pt.

It was suggested that the adsorption of oxygen-containing species onto the catalyst surface can affect the ORR kinetics. A decrease in OH adsorption on Pt results in the enhancement of ORR activity and is achieved by alloying Pt with a more easily oxidised element, such as Ir (11). Surface Ir atoms are likely to be covered by hydroxide groups at more negative potentials than Pt because of a lower onset potential for the oxide formation. That would leave more Pt sites free for the ORR, which may contribute to the enhanced activity.

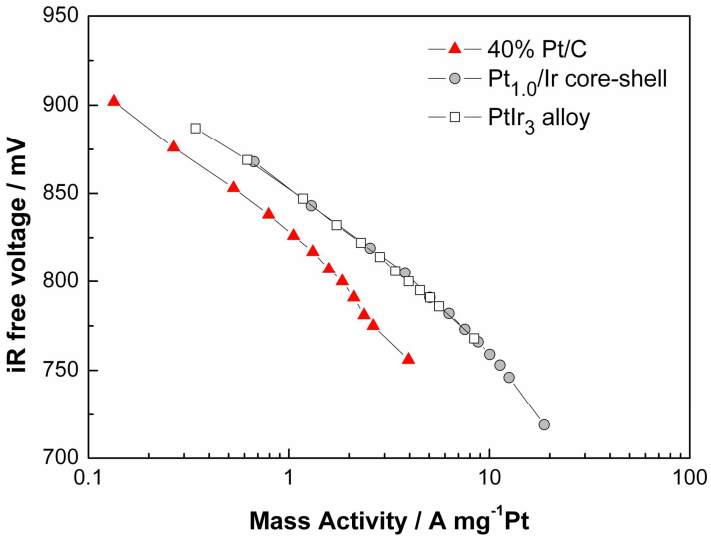

Figure 6 - 16 H_2/O_2 corrected performance of $Pt_{1.0}$/Ir, $PtIr_3$ alloy, and 40% Pt in 49 cm^2 hardware at 50 kPa_{gauge} at 80 °C, 100 % $RH_{anode/cathode}$ (relative humidity)

6.6. Conclusions

Two carbon-supported Pt/Ir core-shell catalysts were prepared by CSR with an equivalent of one and two Pt monolayers, respectively. In particular, completion of the Pt precursor decomposition was more difficult to achieve for $Pt_{2.0}/Ir$. It is possible that the Ir hydride and the Pt hydride in the vicinity of Ir did not have a sufficient reducing capability for the decomposition of $Pt(acac)_2$. Another explanation would be that the first Pt organometallic species deposited on the Ir surface were not completely hydrogenolysed, which would hinder the deposition of additional Pt.

The physical characterization of the Pt shell proved to be more difficult than for the Pt/Pd system because Pt and Ir are very similar elements in terms of weight and electronic structure. Pt and Ir could have been better distinguished by XRD analysis since they have more separated diffraction peaks. However, as mentioned in the previous chapters, the small size and the very poor crystallinity of the catalysts limit the detection of the elements. HRTEM analysis appeared to be unsuitable for the study of the Pt/Ir system for two reasons: (1) there was not enough Z-contrast between Pt and Ir to observe the Pt shell; (2) due to the proximity in energy of the K and M emission lines of Pt and Ir, the less intense L lines had to be used to obtain an EDX profile. Unexpectedly, the surface composition of the Pt/Ir core-shell catalysts measured by HS-LEIS did not show any Pt contribution. This observation was not well understood and it might be explained by the segregation of Pt in the Ir lattice, although this is not energetically favorable according to the DFT predictions. However, the physical characterization suggested in general that the Pt/Ir core-shell catalysts exhibited alloy features, and this observation was supported by cyclic voltammetry. The voltammograms obtained in H_2SO_4 and the CO electrooxidation voltammograms of the Pt/Ir core-shell catalysts were strongly Ir-like. The Pt features appeared only after Ir was leached by conditioning cycles. This behaviour can be attributed to either the low atomic fraction of Pt compared to Ir or the diffusion of Pt into the Ir lattice. Although Ir showed excellent stability to cycling compared to Pd, the Pt/Ir core-shell catalysts did not have improved stability compared to the Ir only-catalyst, which may result from a very poor Pt coverage. The ORR activity of $Pt_{1.0}/Ir$ measured in a MEA was found to be higher than 40%Pt. The origin of the enhanced activity was not completely understood but may partly be attributed to a decline in Pt-OH formation.

References

1. J. Zhang, M. B. Vukmirovic, Y. Xu, M. Mavrikakis and R. R. Adzic, *Angewandte Chemie International Edition*, **44**, 2132 (2005).

2. A. U. Nilekar and M. Mavrikakis, *Surface Science*, **602**, L89 (2008).

3. http://www.platinum.matthey.com/pgm-prices/price-charts/

4. R. E. Benfield, *Journal of the Chemical Society Faraday Transactions*, **88**, 1107 (1992).

5. S. R. Bharadwaj, S. N. Tripathi and M. S. Chandrasekharaiah, *Journal of Phase Equilibria*, **16**, 460 (1995).

6. R. Callejas-Tovara and P. B. Balbuena, *Surface Science*, **602**, 3531 (2008).

7. K. Lee, L. Zhang and J. Zhang, *Journal of Power Sources*, **170**, 291 (2007).

8. L. Gu, N. Luo and G. H. Miley, *Journal of Power Sources*, **173**, 77 (2007).

9. T. Pauporte, F. Andolfatto and R. Durand, *Electrochimica Acta*, **45**, 431 (1999).

10. D. A. J. Rand and R. Woods, *Electroanalytical Chemistry and lnterfacial Electrochemistry*, **55**, 375 (1974).

11. T. Ioroi and K. Yasuda, *Journal of Electrochemical Society*, **152**, A1917 (2005).

CHAPTER 7

CONCLUSION

CHAPTER 7: Conclusion

The aim of this thesis has been to prepare and evaluate Pt-shell electrocatalysts using the CSR route to demonstrate improved performance as cathode catalysts in Polymer Electrolyte Membrane Fuel Cells (PEMFCs) when compared with Pt alone.

A study of the CSR reaction to deposit Pt onto Pd cores showed it is a relatively fast reaction between the Pd-H sites and $Pt(acac)_2$. Provided the reaction takes place at elevated temperature and in the presence of H_2 (purged through the solution), the reaction was complete. The reaction was complete and the deposition of Pt was localised. The absence of isolated Pt clusters on the carbon support was confirmed by EXAFS, XRD, and cyclic voltammetry.

Although all the $Pt(acac)_2$ reacted, the Pt shell was not complete, as revealed by the STEM images and the LEIS analysis. Pt was found to be localised on the outside of the Pd particles but uncovered Pd areas were also visible. The images strongly suggested that Pt deposited preferentially at the low-coordination sites of the Pd particles (edges, corners) and built up there before starting to cover the faces. TEM observations of the Pd cores showed that they had more facetted particles after annealing. Therefore the large Pd cores obtained from annealing of the small Pd cores tended to have lower Pt coverages. The number of low-coordination sites of the Pd core and the ability of Pt element to adsorb hydrogen seem to be the limiting factor for obtaining a complete coverage. The Pt coverage was found to be the highest on the 3nm-Pd core, 65% coverage being obtained. According to cyclic voltammetry, most of the prepared core-shell electrocatalysts did not exhibit strong Pt features in the H_{UPD} region but a broad peak similar to that of a PtPd alloy electrocatalyst.
XRD analysis revealed signs of alloying between Pd and Pt. A change in the Pt-Pt and Pt-Pd distances was also observed using EXAFS analysis and supported the XRD results.

The results of the stability tests performed on the core-shell catalysts showed a linear relationship between the loss of active area upon cycling and the Pt coverage, regardless of the Pd core size as shown in Figure 7-1. The degradation mechanism was shown to result from two simultaneous mechanisms: the dissolution of Pd that was not covered with Pt and

the Pt agglomeration on the core-shell particle surface. It was suggested that Pt atoms rearranged at the surface during cycling while Pd was dissolved away. A more Pt-like electrochemical behaviour was eventually obtained and was attributed to a more complete Pt shell.

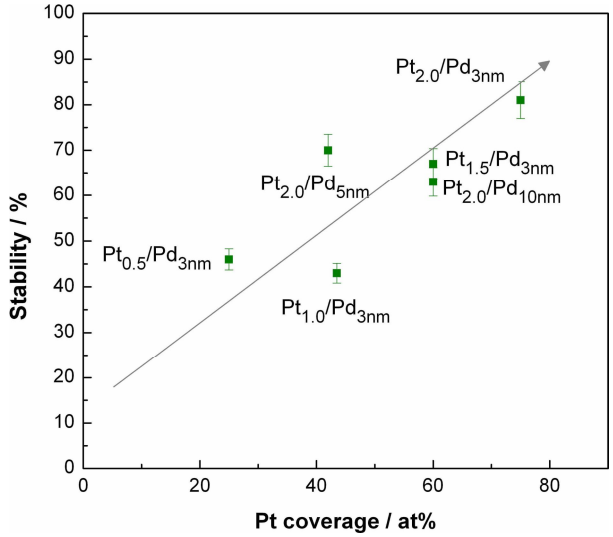

Figure 7- 1 Correlation between the core-shell electrocatalyst stability and their XPS-deduced Pt atomic composition. The stability is defined as the retained active are after 1000 cycles between 0.6 and 1.0 V at 80 °C in 1 M H_2SO_4.

The ORR activity of the Pt/Pd core-shell electrocatalysts was a function of both the Pt coverage and the size of the Pd core. A volcano-type relationship was found between the ORR activity and the Pt coverage on 3 nm Pd cores and the highest ORR activity was observed for the $Pt_{1.5}/Pd_{3nm}$ catalyst, which showed greater activity compared to 40% Pt/C. This suggests that the core/shell interaction responsible for the activity enhancement starts to decay when too much Pt accumulates at the same sites. However, the relationship between the ORR activity and the Pd core size was systematic despite the inconsistency with the Pt coverage. The activity decreased as the Pd core size increased. In Figure 7-2, the specific and the Pt-mass activities of the Pt/Pd core-shell electrocatalysts are plotted against their electrochemical stabilities. The ORR activities presented were measured by RDE and in a single cell, and the stability was a measure of the retained active area after 1000 cycles between 0.6 and 1.0 V at 20 mV s^{-1} at 80 °C. In Figure 7-2(a), the electrocatalysts with either improved specific activity or stability compared to 40% Pt/C, are grouped in the top right quadrant. They have the highest XPS-deduced Pt atomic composition and the 3-nm Pd core. It can be seen that the least stable and active

electrocatalysts, in the bottom left quadrant, are the one with the poorest coverage. The most stable electrocatalysts have ≤ 1.5 Pt ML. In Figure 7-2(b), the Pt-mass activity of the core-shell electrocatalysts is plotted against their electrochemical stabilities. At the top of the graph, the blue line stands for the Pt-mass activity target defined by the Department of Energy in 2006 (1). Most core-shell electrocatalysts exhibit better Pt-mass activity than 40% Pt/C with a half to one sixth of the Pt loading. Although only half the activity target was achieved, a better control of the Pt shell structure may lead to further improvements.

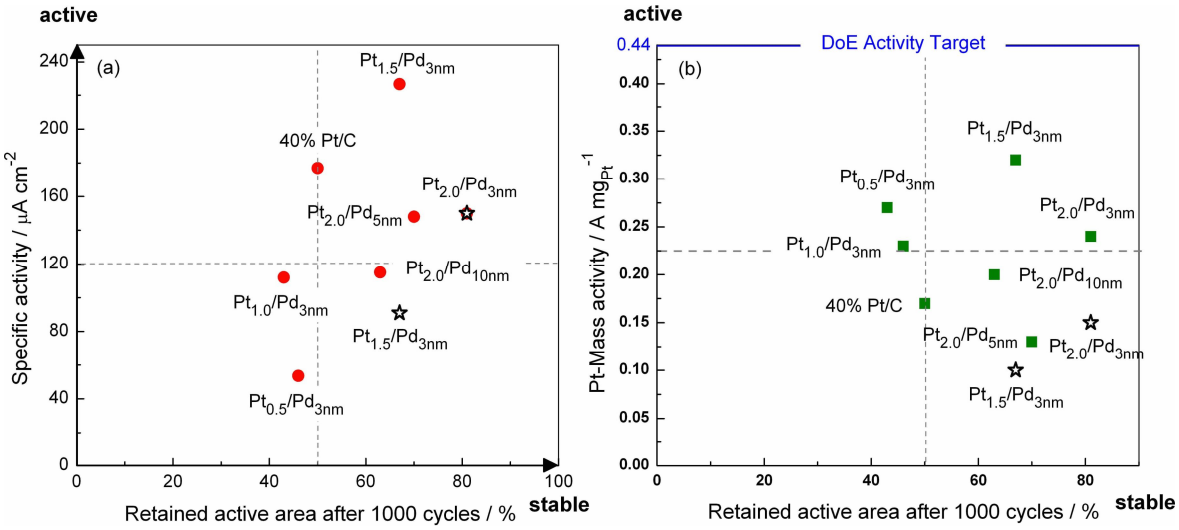

Figure 7- 2 Classification of the Pt/Pd core-shell electrocatalysts by specific activity (a), Pt-mass activity and electrochemical stability. The star symbol signifies the activity was measured in a single cell.

The characterisation of the Pt shell of the $Pt_{1.0}$/Ir and $Pt_{2.0}$/Ir core-shell electrocatalysts prepared by CSR was more difficult due to the similarity between Pt and Ir. The physical and electrochemical characterisation did not show any sign of the presence of a Pt shell but suggested that the Pt/Ir electrocatalyst surfaces were alloyed. While the lattice parameter of the PtIr alloy phase in $Pt_{2.0}$/Ir could be related to a Pt:Ir atomic composition of 40:60, the XPS-deduced ratio obtained was of 31:69, which is close to the bulk ratio 26:74. The EDX line profiles obtained for both $Pt_{1.0}$/Ir and $Pt_{2.0}$/Ir resembled those one might expect for alloy particles. These observations strongly suggested that Pt segregation in the Ir lattice occurred. The presence of Pt was clearly observable by cyclic voltammetry after Ir was leached away during the durability test. Against our expectations, the Pt/Ir core-shell electrocatalysts showed very poor stability. However, an interesting result was the ORR

Pt-mass activity of $Pt_{1.0}$/Ir measured in a MEA, which was found to be double that of 40%Pt.

This work has shown that it is possible to enhance the ORR activity with reduced Pt loadings by using core-shell structured electrocatalysts. As a full Pt coverage could not be obtained using the CSR synthesis route, the question of how much higher the ORR activity and the stability of these electrocatalysts could be if the Pt coverage was complete remains. Could this be achieved by using Pd or Ir cores with a highly roughened surface or a round shape? An alternative to annealing to prepare large sized-cores would be preferable as it favours the growth of the faces, which lead to a poor Pt coverage.

Reference

1. R. Adzic, J. Zhang, K. Sasaki, T. Huang, J. Wang and M. Vukmirovic, in *DOE Hydrogen Program Review, May 23-26* (2005).